



HAL
open science

Search for strongly produced supersymmetric particles with the ATLAS detector and interpretation in the pMSSM

Marija Marjanovic

► **To cite this version:**

Marija Marjanovic. Search for strongly produced supersymmetric particles with the ATLAS detector and interpretation in the pMSSM. High Energy Physics - Experiment [hep-ex]. Université Paris Saclay (COmUE); Univerzitet u Beogradu, 2015. English. NNT : 2015SACLS096 . tel-01327222

HAL Id: tel-01327222

<https://theses.hal.science/tel-01327222>

Submitted on 6 Jun 2016

HAL is a multi-disciplinary open access archive for the deposit and dissemination of scientific research documents, whether they are published or not. The documents may come from teaching and research institutions in France or abroad, or from public or private research centers.

L'archive ouverte pluridisciplinaire **HAL**, est destinée au dépôt et à la diffusion de documents scientifiques de niveau recherche, publiés ou non, émanant des établissements d'enseignement et de recherche français ou étrangers, des laboratoires publics ou privés.

NNT: 2015SACLS096

**THÈSE DE DOCTORAT
DE
UNIVERSITY OF BELGRADE
ET DE
L'UNIVERSITÉ PARIS-SACLAY,
préparé à Université Paris-Sud**

École Doctorale n°576 PHENIICS

Particules, hadrons, énergie et noyau : instrumentation, image, cosmos et simulation

Spécialité de doctorat: Physique des particules

Par

Mme. Marija MARJANOVIĆ

**Search for strongly produced supersymmetric
particles with the ATLAS detector and
interpretation in the pMSSM**

Thèse présentée et soutenue à Orsay, le 16 Novembre 2015

Composition du Jury :

M.	Petar ADŽIĆ	Examineur
Mme.	Sophie HENROT-VERSILLÉ	Co-Directrice de thèse
M.	Andreas HOECKER	Rapporteur
M.	Tilman PLEHN	Rapporteur
M.	Achille STOCCHI	Président du jury
Mme.	Marija VRANJEŠ MILOSAVLJEVIĆ	Co-Directrice de thèse

Abstract

In order to explain all the theoretical and experimental constraints (stability of the Higgs boson mass, existence of dark matter (DM), neutrino masses...), the Standard Model (SM) of particle physics needs not be enlarged. A possible solution is supersymmetry (SUSY) that adds a new symmetry which connects bosons and fermions. This symmetry predicts the existence of new particles, like squarks, gluinos and neutralinos, that can be produced at the LHC. This thesis presents the search for SUSY sparticles in final states with 2-6 jets, no leptons and large missing transverse energy (0-lepton search) with the ATLAS detector. The main remaining background after all the selection process is composed of tau leptons. In order to validate its modeling several validation regions have been designed within this thesis work (for W+jets and top pair production) and further used in the final fit of the data. The description of the tau lepton background has been found to be adequate, thus supporting the final results of this search. Those results, along with the ones of other 21 ATLAS searches, are further interpreted in a 19-parameters framework, the phenomenological minimal supersymmetric standard model (pMSSM), in order to give the most comprehensive limits on SUSY particles masses. This parameter space is modeled by constraints coming from precision measurements, the mass of the SM Higgs boson, the limits from direct DM searches, the upper limit on the cold DM energy density of the Universe and pre-LHC SUSY searches. More than 300 000 SUSY models were analysed and more than 40% of them have been excluded (most of them by the 0-lepton search). The results are interpreted as limits on the SUSY sparticle masses, and the cold DM energy density. It has been found that no particular type of DM candidate is favoured by the actual measurements.

Résumé

Cette thèse présente le travail effectué dans le cadre de la recherche de la supersymétrie (SUSY), avec les données à 8 TeV du Grand collisionneur de hadrons (LHC) enregistrées par le détecteur ATLAS. L'accent est mis sur les états finaux caractérisés par une grande énergie transverse manquante (E_T^{miss}), 2–6 jets et zéro lepton (l'analyse 0-lepton dans ce qui suit) et l'interprétation des résultats est donnée dans le cadre du modèle standard minimal supersymétrique phénoménologique (pMSSM).

Le modèle standard de la physique des particules (SM) est une théorie bien établie et confirmée par de nombreuses observations. Le SM décrit les particules et leurs interactions (à l'exception de la gravité). Malgré ses nombreux succès, le SM est également limité car il ne donne pas d'explication à toutes les observations comme l'existence de matière noire (DM) et les masses de neutrinos. Il y a aussi le problème de la stabilité de la masse du boson de Higgs (le problème de la hiérarchie). SUSY prédit un candidat naturel pour la DM et résout le problème de la hiérarchie.

SUSY permet aussi l'unification des couplages de jauge, ce que n'est pas faisable dans le cadre de SM. Cela fait d'elle une théorie très attirante et c'est la motivation principale des recherches de particules supersymétriques (sparticules).

Elle ajoute une nouvelle symétrie au SM qui associe les fermions et bosons. Selon les transformation de SUSY, à toutes les particules de SM on associe un nouveau partenaire. Leurs nombres quantiques sont les mêmes à l'exception de la valeur du spin. Les valeurs de ce nouveau nombre quantique, la R -parité, dépendent du nombre baryonique et du nombre leptonique aussi bien que de la valeur du spin. La conservation de la R -parité garantit la stabilité du proton, et dans la suite on suppose la conservation de la R -parité.

Le modèle SUSY le plus simple est le modèle de supersymétrie minimal (MSSM), qui associe seulement un partenaire supersymétrique à chaque particule de SM, à l'exception du secteur du Higgs pour lequel l'addition des bosons de Higgs neutres et chargés est nécessaire (H^0, A^0, H^\pm). Chaque quark a son partenaire supersymétrique appelé le squark (\tilde{q}), de même pour les sleptons (\tilde{l}) et les bosons de jauge ont leur partenaires bino (\tilde{B}), winos (\tilde{W}) and higgsinos (\tilde{H}). Ils se combinent pour créer les neutralinos and charginos. Il y a quatre neutralinos ($\tilde{\chi}_i^0, i = 1, 2, 3, 4$) classés par les valeurs de leur masses (le neutralino le plus léger est le $\tilde{\chi}_1^0$). La particule la plus légère (LSP) est le candidate possible pour la DM puisqu'il est électriquement neutre et neutre de couleur. Dans cette thèse la possibilité que le neutralino le plus léger est la LSP est étudiée en détails. Les mélanges des winos et higgsinos chargés donnent quatre charginos ($\tilde{\chi}_i^\pm, i = 1, 2$).

Comme on s'attend à ce que la SUSY soit une symétrie brisée (car on n'a observé aucune particule SUSY jusqu'à maintenant), on a besoin de 105 paramètres pour decrire ce secteur là. Ces paramètres sont les paramètres des masses des sparticules et également les valeurs des couplages. Les matrices de mélange des neutralinos et charginos dépendent de ces paramètres, et dans les cas extrêmes quand le paramètre de masse du bino (M_1), ou du wino (M_2) ou du higgsino (μ) est beaucoup plus petit que les autres, le $\tilde{\chi}_1^0$ est principalement bino ($M_1 \ll M_2, \mu$), wino ($M_2 \ll M_1, \mu$) ou higgsino ($\mu \ll M_1, M_2$).

Pour contraindre les paramètres du MSSM on peut utiliser la mesure de la densité d'énergie de DM issue des données cosmologiques (fond diffus cosmologique, Supernovae, les oscillations

baryoniques) qui peuvent être comparées avec les valeurs attendues calculées dans le cadre d'un modèle SUSY donné. Au tout début l'Univers était chaud et toutes les particules étaient en équilibre thermique. Comme l'Univers est en expansion, il se refroidit et le taux d'interaction entre particules devient de plus en plus petit. Quand le taux d'interaction est devenu trop faible l'équilibre entre les taux de production et annihilation disparaît, et ceci est connu comme le "freeze-out". À ce moment là, le taux d'annihilation est plus faible que le taux de production, et les particules instables disparaissent, tandis que le nombre de particules stables devient constant. Le densité relique de DM froide $\Omega_{\text{CDM}} h^2$ dépend des processus de production ($f\bar{f} \rightarrow \chi\chi$) et d'annihilation ($\chi\chi \rightarrow f\bar{f}$), où χ représente la particule candidat de DM et f représente toutes les particules qui peuvent s'annihiler pour créer la DM. La valeur de la densité relique de DM froide attendue est inversement proportionnelle à la moyenne thermique de la section efficace d'annihilation.

Quand le neutralino est plutôt bino, il n'a pas de coannihilateurs naturels, et il montre une phénoménologie très riche. Le canal d'annihilation de neutralino le plus simple est l'annihilation directe des deux neutralinos pour créer le boson Z , (Z -funnel), le boson Higgs de SM (h -funnel), ou le Higgs lourd (A -funnel), ou la coannihilation de neutralino avec une autre sparticule (comme staus, charginos, squarks, gluinos...). Dans le cas où le neutralino est plutôt wino ou higgsino, il a le chargino le plus léger comme un coannihilateur naturel (puisque leurs masses sont similaires). Ça donne une différence de phénoménologie entre les cas où la LSP est plutôt bino, wino ou higgsino, et dans ce qui suit ces cas vont être discutés séparément.

Puisque le MSSM est décrit par 124 paramètres, on ne peut pas les examiner tous dans les détails. Une solution à ce problème est de réduire le nombre de paramètres. Si on assume l'unification de plusieurs paramètres à l'échelle d'énergie plus large c'est qu'on appelle "le modèle de haut échelle", on peut réduire le nombre de paramètres. Une autre solution est d'étudier "les modèles simplifiés", qui sont une simplification des modèles SUSY réels et qui supposent que seulement certaines sparticules sont accessibles. Ils dépendent seulement des masses de sparticules, leur rapports de branchement et leur sections efficace de production. Les modèles simplifiés permettent d'étudier la SUSY d'une manière modèle indépendante. Dans cette thèse on va étudier les modèles simplifiés qui supposent que juste les squarks et neutralinos sont accessibles, alors que toutes les autres sparticules sont découplées. En ce cas, le squark peut se désintégrer seulement en quark et neutralino, ce qui donne l'état final avec des jets et $E_{\text{T}}^{\text{miss}}$. Ce modèle peut être plus compliqué si le chargino est aussi accessible, et en ce cas la désintégration des squarks passe par des charginos à neutralinos. On a alors plus des jets dans l'état final. Il y a aussi des modèles simplifiés par lesquels les gluinos et neutralinos sont les seules particules accessibles, on ajoute aussi le chargino à ce groupe.

Les modèles SUSY sont spécialement intéressants à étudier au LHC, puisqu'il est possible de produire plusieurs sparticules dans les collisions de protons. Les sections efficaces de production attendues sont très larges pour les squarks et gluinos, puisque on fait l'hypothèse qu'ils sont produits par l'interaction forte. De nombreux états finaux sont possibles dans les désintégrations de sparticules. Le détecteur ATLAS est très bien adapté pour la recherche de nouvelle physique. Le travail présenté dans cette thèse est effectué avec les données enregistrées par le détecteur ATLAS en 2012. Pendant ce temps, la performance était exceptionnellement bonne, le LHC a livré 22.8 fb^{-1} et ATLAS a enregistré 20.3 fb^{-1} .

Cette thèse est concentrée sur les états finaux avec les jets, grand $E_{\text{T}}^{\text{miss}}$ et zéro lepton car ils sont très intéressants pour sonder l'existence de squarks et gluinos. Le veto des événements avec leptons (electrons et muons) est utilisé pour supprimer le bruit de fond, et les états finaux avec leptons sont étudiés avec une autre analyse conçue spécialement dans ATLAS. L'analyse 0-lepton est conçue autour des régions de signal (SR), contrôle (CR) et validation (VR). Les SRs sélectionnent les parties de l'espace de phase où on attend le signal, et l'analyse 0-lepton a 15 SRs. Elles sont définies par les variables discriminantes qui suppriment le bruit de fond

et, en même temps, ont une efficacité de sélection de signal suffisamment grande. La variable discriminante très puissante est la masse effective (m_{eff}), la somme scalaire des impulsions transverses (p_{T}) des jets et $E_{\text{T}}^{\text{miss}}$. Chaque SR exige au moins 2 à 6 jets dans l'état final, et les différentes SR sont optimales pour différents modèles SUSY. Par exemple, les SRs avec un petit nombre des jets sont sensibles à la production des paires de squarks suivie par la désintégration directe, alors que les SRs avec beaucoup de jets sondent la production des gluino et/ou les chaînes de désintégrations plus longues.

On utilise les CR pour mettre des contraintes sur les bruits de fond dominants ($t\bar{t}$, W +jets, Z +jets et multijet), ainsi on a construit quatre CRs pour chaque SR. Chacune est dominée par un type de bruit de fond, et en comparant les données observées dans chaque CR avec ce qui est attendu de la simulation Monte Carlo (MC), il est possible d'estimer la normalisation de ce bruit de fond. C'est fait par le fit de vraisemblance. Les quantités les plus importants sont les facteurs de transfert qui permettent de normaliser le bruit de fond attendu dans chaque SR à partir de ce qui a été mesuré dans les CRs. On assume que la forme des variables utilisée par la sélection est bien reproduit par MC. Les résultats du fit de vraisemblance sont vérifiés dans les VRs, par comparaison entre le nombre d'événements observés dans les données et l'estimation de bruit de fond fait par le fit.

Le bruit de fond dominant dans les SRs après tous les critères de sélection, vient de la désintégration hadronique des leptons tau (plus que 70%). La désintégration du boson W produit par la production de W +jets ou $t\bar{t}$, donne des leptons tau qui peuvent se désintégrer en leptons (electron ou muon) et hadroniquement (au pions). Les désintégrations leptoniques de leptons tau sont supprimées par le véto sur les événements avec leptons, pendant que les leptons tau qui se désintègrent hadroniquement restent.

La désintégration hadronique des leptons tau donne une signature distinctive de jet très collimé avec un nombre de traces caractéristique (une ou trois). Donc on sélectionne les leptons tau à partir des candidats jets avec une seule trace. On utilise aussi le fait que les leptons tau viennent de boson W , que l'on peut reconstruire en utilisant la masse transverse. La masse transverse entre les τ et la $E_{\text{T}}^{\text{miss}}$ est calculée avec le p_{T} de candidate tau, $E_{\text{T}}^{\text{miss}}$ et l'angle entre les deux. On demande qu'elle soit consistante avec la masse du boson W (plus petite que 100 GeV). Cette contrainte supprime les leptons tau mal identifiés, et elle est calculée pour tous les candidates tau dans l'événement.

L'algorithme pour l'identification des leptons tau fonctionne très bien: j'ai vérifié que le taux de faux taus est bas (<0.06) et il ne dépend pas du nombre de jets dans l'événement. Aussi, j'ai fait une étude du taux de leptons tau. On voulait s'assurer qu'il ne dépendait pas de l'empilement. L'étude des taux des leptons taus en fonction du nombre des vertex primaires montre que c'est stable. Ceci démontre que les jets d'empilement ne sont pas identifiés comme des leptons tau.

Afin de vérifier que la modélisation des leptons tau est adaptée, j'ai construit deux VRs: une pour les taus qui viennent de la production de W +jets (VRW) et une pour ceux viennent de la production de $t\bar{t}$ (VRTop). Les VRs sont orthogonales aux CRs et aux SRs. Pour distinguer entre les VRW et VRTop, on ajoute une condition supplémentaire au nombre de jets d'origine de quark b . Dans VRTop au moins un b -jet est exigé, comme il est présent dans la désintégration de top. Le nombre de b -jets attendus dans les désintégrations de boson W est zéro, ainsi dans VRW on ajoute un véto sur les événements avec b -jets.

Après le fit sa prediction est vérifiée dans VRs. On observe un bon accord dans les VRs pour les leptons tau, et ca assure que les leptons tau sont bien modélisés et que les résultats du fit sont fiables. La prochaine étape est de regarder dans les SRs, et là on observe aussi un bon accord entre les données et la prediction de bruit de fond. Comme on n'a observé aucun excès, on peut mettre les limites sur le nombre d'événements qui viennent de processus au-delà de SM, dans les deux cas: modèle dépendant et modèle indépendant. Dans le modèle simplifié

de production de paires de gluinos suivi par la désintégration directe, les gluinos avec les masses au dessous de 1200 GeV sont exclus quand le neutralino est sans masse. De la même façon, les masses des squarks au dessous de 850 GeV sont exclues dans le modèle simplifié de production de paires de squarks qui se désintègrent directement, dans le cas où les 8 squarks légers sont dégénérés en masse, et le neutralino est sans masse. Les résultats sont publiés dans Ref. [1] et [2].

Les résultats peuvent aussi être interprétés dans les modèles SUSY réels. Un cadre très intéressant est le MSSM phénoménologique (pMSSM), pour lequel l'espace de 124 paramètres du MSSM est réduit à 19 paramètres en ajoutant certaines hypothèses: il n'y a pas d'autres sources de violation CP que celles de la matrice CKM, la violation minimale de saveur est imposée à l'échelle électrofaible, les deux premières générations de squarks et sleptons sont de même masses et leur couplages de Yukawa sont négligables, et la LSP est le neutralino le plus léger. Le pMSSM donne une variété d'états finaux, et il y a beaucoup processus de production et de désintégration. Ainsi le pMSSM est intéressant pour l'interprétation de plusieurs analyses d'ATLAS: on inclut 22 analyses pour obtenir le résultat.

Les valeurs des 19 paramètres du pMSSM sont choisies pour pouvoir donner des états finaux accessibles au LHC. Les caractéristiques des modèles sont ensuite calculées et comparées avec les mesures des autres expériences (les désintégrations rares de B, les mesures électrofaibles de précision, les recherches directes de DM) et avec les limites sur les masses des particules de recherches de SUSY avant le LHC. Les modèles sont contraints aussi par la valeur de masse du boson de Higgs. Aussi les résultats de densité résiduelle de DM de la collaboration Planck sont très contraignants. Ils sont pris comme une valeur supérieure car on ne suppose pas que l'ensemble de la DM doit être expliquée par SUSY. En tout, il y avait 500 millions de points choisis dans l'espace des paramètres du pMSSM, et après les contraintes indirectes et l'hypothèse que la LSP est le neutralino le plus léger, ce nombre est réduit à 310 000 modèles analysés.

Afin d'interpréter les résultats des analyses d'ATLAS et d'exclure les modèles pMSSM, plusieurs étapes sont effectuées. La première est que tous les modèles avec une section efficace plus basse qu'une certaine valeur sont considérés comme non observables par ATLAS et sont indiqués non exclus. Le nombre de modèles à analyser a été réduit à 280 000. La prochaine étape était de simuler tous ces modèles au niveau truth et d'exclure les modèles qui donnent des nombres des événements plus hauts que les limites modèle indépendant de chaque analyse. Comme les effets de détecteur sont négligés au niveau truth, il y a un désaccord entre l'analyse au niveau truth et au niveau reconstruit, que l'on prend en compte en ajoutant des marges de sécurité. On n'est pas sûr de bien catégoriser les modèles sur la base des prédictions truth dans cette marge de sécurité et, par conséquent, ils sont reconstruits. La décision finale si le modèle est exclu ou pas, est prise à ce moment là, et 45 000 modèles sont analysés.

On considère le modèle exclu s'il est exclu par au moins une analyse d'ATLAS. Les résultats sont présentés comme les projections d'espace de 19 paramètres du pMSSM projetés dans deux dimensions. Presque tous les modèles avec une masse de gluino inférieure à 1200 GeV et une masse de neutralino inférieure à 500 GeV sont exclus, quand les 22 analyses d'ATLAS sont prises en compte. Chaque analyse a une sensibilité unique, mais il y a aussi des modèles exclus par plusieurs analyses. Quand on prend en compte les 22 analyses d'ATLAS, 40.9% de modèles pMSSM sont exclus. La contribution majeure est celle de l'analyse 0-lepton qui exclut 32.1% des modèles pMSSM (quand la LSP est plutôt bino, elle exclut 35.8% des modèles, 29.7% de modèles avec la LSP plutôt wino et 33.5% pour higgsino). L'analyse 0-lepton exclut aussi une grande partie des modèles qui sont exclus par d'autres analyses qui cherchent des squarks et gluinos (de 0.8 à 0.99), et en même temps elle a une sensibilité unique très grande. Les autres analyses contribuent aussi, particulièrement l'analyse des traces disparues qui exclut 30% des modèles avec la LSP plutôt wino, comme elle est conçue pour chercher les charginos avec une durée de vie très longue. Ces modèles ont une petite différence des masses entre la LSP et le

chargino.

L'étude d'exclusion par l'analyse 0-lepton a permis de faire une comparaison juste entre les limites sur les masses des sparticules dans les modèles simplifiés et dans le cadre du pMSSM. Cette comparaison démontre que les modèles simplifiés ne captent pas tous les aspects phénoménologiques du pMSSM, comme on s'y attend.

L'exclusion de chaque SR d'analyse 0-lepton est aussi étudiée. Elle démontre une belle complémentarité, comme chacune est dominante dans des parties de l'espace de phase différents. Par exemple, les basses masses de gluinos sont exclues par les SRs avec au moins 2 jets, et quand on augmente le nombre minimal de jets les gluinos avec les masses plus hautes sont exclues. C'est très intéressant car les SRs ont été optimisées avec les modèles simplifiés, et ils sont efficaces aussi dans le cadre du pMSSM.

Plusieurs approches statistiques sont étudiées: la plupart des résultats est présentée comme la fraction de modèles exclus, mais aussi les valeurs maximales et minimales de CLs dans certains parties des projections à deux dimensions de l'espace de 19 paramètres du pMSSM sont considérées. Les valeurs maximales et minimales des CLs sont bien définies statistiquement, et donnent des informations supplémentaires et complémentaires. La valeur maximale des CLs donne une indication de quelles parties du plan sont tout à fait exclues. L'information complémentaire vient des valeurs minimales des CLs qui déterminent les parties de plan moins défavorisées. Les hauts valeurs des paramètres des masses de gluino et neutralino sont moins défavorisées.

L'effet des analyses d'ATLAS sur la DM est aussi exploré. Dans cette analyse on ne demande pas que le neutralino sature la densité relique de DM, et seulement les modèles avec la LSP plutôt bino sont capables de saturer la densité relique de DM pour les basses masses de neutralino. Après les contraintes des 22 analyses d'ATLAS, les modèles avec les masses de neutralino inférieure à 800 GeV sont touchées, bien qu'aucune valeur de masse de neutralino soit complètement exclue. Aussi on n'a pas exclu/favorisé une type de LSP plutôt qu'un autre: les fractions comparables de tous sont exclus.

Quand la LSP est plutôt bino, il y a plusieurs mécanismes d'annihilation and de coannihilation presents et ca donne une phénoménologie très riche. C'est intéressant d'étudier quel mechanisme est préféré. La plus haute fraction de modèle est exclue dans le Z and h -funnels, supérieur à 0.7, et c'est aussi bas que 0.2 dans le cas de la coannihilation entre le neutralino et le squark de troisième génération. On n'a pas une conclusion solide pour le mécanisme d'annihilation ou de coannihilation préféré, comme tous les canaux sont toujours ouverts. Si on considère seulement les modèles qui saturent la densité relique de DM, on n'observe pas de changement significatif: tous les modes d'annihilation et de coannihilation sont toujours possibles. Les résultats de l'analyse pMSSM sont publiés dans Ref. [3].

Contents

1	Supersymmetry	2
1.1	Introduction	2
1.1.1	Standard Model of particle physics	2
1.1.2	Limitations of the Standard Model	4
1.1.3	Motivation for SUSY	7
1.2	Supersymmetry	7
1.2.1	SUSY algebra	8
1.2.2	The simplest SUSY model - Wess-Zumino model	8
1.2.3	Interactions of chiral supermultiplet	10
1.2.4	Lagrangians for gauge supermultiplets	11
1.2.5	Supersymmetric gauge interactions	12
1.2.6	SUSY breaking	13
1.2.7	Electroweak symmetry breaking	14
1.3	Minimal supersymmetric standard model - MSSM	14
1.3.1	Superpotential and interaction	14
1.3.2	Soft supersymmetry breaking	15
1.3.3	R -parity conservation	15
1.3.4	Sparticles	16
1.3.4.1	Neutralinos	16
1.3.4.2	Charginos	17
1.3.4.3	Gluino	18
1.3.4.4	Sleptons	18
1.3.4.5	Squarks	19
1.3.4.6	Sfermion mass splittings due to electroweak symmetry breaking	19
1.3.4.7	SUSY Higgs bosons	20
1.4	SUSY models	20
1.4.1	High scale models	20
1.4.1.1	The Minimal Super GRAvity mSUGRA	20
1.4.1.2	GMSB	21
1.4.2	pMSSM	21
1.4.3	Simplified models	21
1.5	Dark matter	22
1.5.1	Cold dark matter energy density	22
1.5.2	SUSY dark matter candidates	23
1.5.3	Neutralino annihilation channels	23
1.6	Simulation of physics processes at the LHC	24
1.6.1	Production processes	24
1.6.2	Production of supersymmetric particles at the LHC	24
1.6.3	Event simulation	27
1.6.4	Generators	27

1.7	Conclusion	28
2	LHC and ATLAS	29
2.1	Large Hadron Collider	29
2.1.1	Acceleration of particles	29
2.1.2	Luminosity	31
2.1.3	LHC operation	31
2.2	ATLAS detector	33
2.2.1	Nomenclature - the ATLAS coordinate system	33
2.2.2	Design of the ATLAS detector	34
2.2.3	The Inner Detector	34
2.2.4	Calorimeters	36
2.2.5	The Muon Spectrometer	38
2.2.6	Magnet system	38
2.2.7	The Trigger system	39
2.2.8	Simulation of the ATLAS detector	40
2.3	Object reconstruction	40
2.3.1	Reconstruction of tracks	40
2.3.2	Primary vertex	42
2.3.3	Jets	42
2.3.4	b-jets	43
2.3.5	Electrons	43
2.3.6	Photons	44
2.3.7	Muons	44
2.3.8	Missing transverse momentum	45
2.4	Conclusion and outlook	45
3	0-lepton	48
3.1	0-lepton analysis strategy	48
3.1.1	Background processes	49
3.1.2	Object definition	50
3.1.3	Discriminating variables	52
3.2	Dataset and Monte Carlo samples	53
3.2.1	Dataset	53
3.2.2	Monte Carlo samples	53
3.2.2.1	Simulation of the pile up	53
3.2.2.2	Background samples	53
3.2.2.3	Signal samples	55
3.3	Event selection	56
3.3.1	Trigger	56
3.3.2	Event cleaning	57
3.3.2.1	Non-collision background	57
3.3.3	Signal region selection	59
3.3.3.1	Event preselection	59
3.3.3.2	Signal regions	59
3.3.4	Control regions	59
3.3.4.1	Control region for multi-jet background	59
3.3.4.2	Control region for $Z \rightarrow \nu\nu + \text{jets}$	61
3.3.4.3	Control region for semileptonic $t\bar{t}$ events	61
3.3.4.4	Control region for $W \rightarrow l\nu$ events	62

3.3.5	Validation regions	62
3.4	Results and interpretation	63
3.4.1	Statistical treatment	64
3.4.2	Systematic uncertainties	64
3.4.3	Results	65
3.4.3.1	Background only fit	65
3.4.3.2	Discovery fit	67
3.4.3.3	Exclusion fit	67
3.5	Conclusion and outlook	70
4	Tau leptons in the 0-lepton analysis	75
4.1	Tau leptons in the 0-lepton analysis and in ATLAS	75
4.1.1	Motivation for considering tau leptons in the 0-lepton analysis	75
4.1.2	Characteristics of hadronically decaying tau leptons	76
4.1.3	Track counting algorithm	77
4.1.4	BDT tau selection	78
4.1.5	Tau Energy Scale	78
4.2	Purity and reliability of the tau selection	79
4.2.1	Transverse mass between tau and E_T^{miss}	79
4.2.2	Tau fake rate	79
4.2.2.1	Tau fake rate estimated from the pure jets samples coming from $Z \rightarrow ee$ and $Z \rightarrow \mu\mu$	80
4.2.2.2	Tau fake rate estimated from the smeared QCD multijet sample	80
4.2.3	Stability of the tau rate with respect to pile up	82
4.3	Validation regions for taus	82
4.3.1	Definition of tau validation regions	83
4.3.2	Transverse mass in events containing taus	83
4.3.3	Other kinematic variables in events containing tau leptons	85
4.3.4	Comparison between track counting and BDT algorithms	89
4.3.5	Signal contamination	89
4.3.6	Agreement between the data and MC expectation in the VRs for τs	90
4.4	Tau veto in Signal regions	90
4.4.1	Effect of the veto on the events containing tau leptons	90
4.4.2	Impact of tau veto on exclusion contours	93
4.4.2.1	Direct squark decay - no systematic uncertainty	94
4.4.2.2	Direct squark decay - systematic uncertainty included	94
4.4.2.3	Onestep gluino decay - systematic uncertainty included	95
4.5	Validation with the 13 TeV data	95
4.6	Conclusion	97
5	pMSSM parameter space and ATLAS SUSY searches	98
5.1	pMSSM parameter space	99
5.1.1	pMSSM parameters	99
5.1.2	pMSSM parameters range	99
5.2	Experimental constraints	101
5.2.1	Electroweak precision data	101
5.2.2	Flavour physics	101
5.2.3	Higgs and pre-LHC collider constraints	101
5.2.3.1	Higgs mass	101
5.2.3.2	Pre-LHC collider constraints	102

5.2.4	Cosmological constraints	102
5.2.5	Direct detection of dark matter	102
5.3	Resulting parameter space	104
5.3.1	Different model sets corresponding to the LSP type	104
5.3.2	Examples of the intertwining between parameters and observables	106
5.3.3	Effects of indirect constraint on pMSSM parameters	109
5.4	ATLAS SUSY searches	112
5.4.1	Inclusive searches	112
5.4.2	Third generation searches	114
5.4.3	Electroweak searches	115
5.4.4	Other searches	115
5.5	Analysis strategy	116
5.5.1	Cross-section calculations	116
5.5.2	Model points at the truth level	116
5.5.3	Model points at the reconstructed level	118
5.5.4	Categorisation of model points	118
5.6	Conclusion	119
6	0-lepton analysis for the pMSSM analysis	120
6.1	Implementation of the 0-lepton analysis at the truth level	120
6.1.1	Truth code	120
6.1.2	Comparison of the analysis at the truth and at the reconstructed level - simplified models	122
6.1.2.1	Simplified model of gluino pair production followed by direct decay	122
6.1.2.2	Simplified model of squark pair production followed by onestep decay	122
6.1.2.3	Lepton efficiencies	124
6.1.2.4	Jet smearing	126
6.1.2.5	Derivation of the r_1 and r_3 values from simplified models	126
6.1.3	Comparison of the analysis at the truth and at the reconstructed level - pMSSM	127
6.1.3.1	Comparison of the yields	128
6.1.3.2	Comparison of shapes	128
6.1.3.3	Jet matching	130
6.2	CLs - yields discussion	132
6.2.1	Comparison between the yields and CLs values - pMSSM model points	133
6.2.2	Predicting CLs value based on the yield at the truth level	133
6.3	Categorisation of pMSSM model points for the 0-lepton analysis	137
6.3.1	Exclusion procedure	137
6.3.2	Results of the categorisation	137
6.4	Conclusion	139
7	pMSSM interpretation	141
7.1	ATLAS SUSY limits	141
7.1.1	ATLAS searches exclusion	142
7.1.2	Sparticle masses	143
7.1.2.1	Gluino - neutralino mass plane	143
7.1.2.2	Lightest squark - gluino mass plane	144
7.1.2.3	Lightest squark - neutralino mass planes	145

7.1.3	Complementarity of ATLAS SUSY searches	148
7.2	0-lepton limits	149
7.2.1	Sparticle masses	149
7.2.1.1	Gluino - neutralino mass plane	149
7.2.1.2	Squark - neutralino mass plane	150
7.2.2	0-lepton signal regions	150
7.3	SUSY parameter space - 0-lepton limits	152
7.3.1	Fraction of excluded model points	152
7.3.2	CLs max	152
7.3.3	CLs min	155
7.3.4	Distinction between $\mu > 0$ and $\mu < 0$	156
7.4	Dark matter	158
7.4.1	Non-saturated dark matter	158
7.4.2	Saturated dark matter	159
7.5	Conclusion	160

Introduction

The Standard Model (SM) of particle physics is a well established theory that fits most of the experimental data. Nevertheless there are hints in the data of Beyond the SM physics such the observations of neutrino oscillations, and the measurement of a large cold dark matter (DM) energy density from cosmological measurements. One of the most popular extensions of the SM is the Supersymmetry (SUSY). Through the inclusion of a new symmetry that connects bosons and fermions, SUSY not only solves partly the SM limitations, but also provides a natural solution to DM.

This thesis concentrates on the 20.3 fb^{-1} of LHC proton-proton collision data collected with the ATLAS detector at $\sqrt{s} = 8 \text{ TeV}$. If SUSY is present in nature, squarks (partners of quarks) and gluinos (partners of gluons) are expected to be produced copiously at this energy, leading to events whose main signature is no electron nor muon, but a large number of jets and missing transverse energy (from the production of the lightest supersymmetric particle (LSP) leaving the detector unseen) denoted the 0-lepton analysis. To be able to set limits on the production of SUSY sparticles one needs to master very precisely the SM backgrounds: the remaining ones, once all the selection cuts of the analysis have been applied, are mainly composed of a tau lepton. The first part of the work presented in this thesis concentrates on the definition of Validation Regions used in the final fitting procedure to better assess this tau background. From this fit, and since no excess has been observed, upper limits on various supersymmetric particles production have been derived within simplified models or SUSY models with low number of parameters.

The exploration of more complicated parameter spaces needed a dedicated resource consuming analysis: it has been done within ATLAS under the 19 parameters phenomenological Minimal Supersymmetric Standard Model (pMSSM) interpretation which not only uses the results of the above mentioned 0-lepton analysis but also other ATLAS searches results. The choice of the parameters and their range of exploration has been done on the basis of non-SUSY experimental results such as the rare B-decays, the mass of the SM Higgs boson, the limits from direct DM searches and the upper limit on the cold DM energy density of the Universe.

The second and main part of this thesis describes the specific 0-lepton analysis that has been performed within the context of the pMSSM interpretation. It starts with the validation of the event selection at the truth and reconstructed levels. Knowing that this is the most constraining ATLAS analysis in the pMSSM parameter space, those checks have been performed with particular care. The constraints obtained with all the analyses on the various sparticle masses is described afterwards, concentrating on squarks, gluinos and neutralinos. The results are discussed for the different natures of the LSP: bino, wino and higgsino. Finally the 0-lepton-only results are described and further explained, first on sparticle mass planes and later on the pMSSM parameters, since only the 0-lepton analysis leads to a well defined statistical procedure that allows to derive properly all those results.

Chapter 1

Supersymmetry

The Standard Model is a theory that successfully describes all the particles that have been observed until now and their interactions (except gravity). It is a great success as it predicted new particles that were later discovered (like Z and W -bosons, top quark. . .). Still, it has its limitations, for example it cannot be valid at very high energies where the gravitational effects are important, and also it does not explain all the matter that is observed in the Universe.

This motivates the building of new theories, whose low energy limit is the Standard Model as it is valid up to energies explored so far. There are many theories that try to describe beyond Standard Model physics, and each has its strengths and weaknesses, as none of them resolves all the problems of the Standard Model. The theory that has gained much attention in the last few decades is Supersymmetry. It predicts the existence of new particles that can explain the matter content of the Universe, and also it allows to stabilize the mass of the already discovered particles. In addition it is an elegant extension of the Standard Model, thus keeping all of its nice features.

This Chapter is a theory introduction to the work that is performed within this thesis. The main goal is to explain the necessary theory concepts, and to present the motivations for the experimental searches that are described later. It relies heavily on Ref. [4, 5].

First a short summary of the Standard Model and its limitations is presented in Section 1.1, then supersymmetry is described in more details in Section 1.2. The minimal supersymmetric extension of the Standard Model is given in Section 1.3. The specific models obtained by imposing certain assumptions on supersymmetry are presented in Section 1.4. The interplay between the supersymmetry and dark matter is explored in Section 1.5. The simulation of events and the production processes of supersymmetric particles are briefly discussed in Section 1.6.

1.1 Introduction

The Standard Model of particle physics is a very successful theory, but it also has its limitations. In this Section first its triumphs are recalled, but also its weak points are discussed.

1.1.1 Standard Model of particle physics

The Standard model (SM) of particle physics [6, 7, 8, 9] is a quantum field theory that describes all known particles and all the forces except the gravitational force. SM is built on the idea that the matter is made from elementary particles (six quarks, six leptons with corresponding antiparticles) and the forces that are present between them (electrodynamics, weak and strong force). Those forces are transmitted by the four particles that transfer interaction (photon, three weak bosons, and gluons). SM also requires the existence of the Higgs boson [10, 11, 12, 13, 14, 15] which explains how particles get their masses.

Interactions between these elementary particles are responsible for the existence of more complex particles, like protons and neutrons. When the SM was first proposed, not all of these particles were observed. And that is where its big success is: it predicted the existence of W and Z -bosons [16, 17, 18], as well as the existence of individual quarks, which were later experimentally confirmed (like top quark [19, 20]).

SM unifies the electrodynamics and weak (into electroweak interaction) and strong interaction. The unification of interactions means that the SM is invariant under local transformations of the gauge group: $SU(3)_C \times SU(2)_L \times U(1)_Y$, where C is colour, L denotes that only the left-handed fermions are subject to the weak interactions and Y is hypercharge. $SU(3)$ is the gauge group of the strong interaction, $U(1)$ is the gauge group of hypercharge, while $SU(2)_L$ represents the weak interaction.

As stated before, the SM encompasses six quarks and six leptons, grouped into three families: first (up and down quark and electron and its neutrino), second (charm and strange quark and muon and its neutrino) and third family (top and bottom quark and tau and its neutrino):

$$Q_i = \begin{pmatrix} u \\ d \end{pmatrix}, \begin{pmatrix} c \\ s \end{pmatrix}, \begin{pmatrix} t \\ b \end{pmatrix} \quad (1.1)$$

$$\bar{u}_i = \bar{u}, \bar{c}, \bar{t} \quad (1.2)$$

$$\bar{d}_i = \bar{d}, \bar{s}, \bar{b} \quad (1.3)$$

$$L_i = \begin{pmatrix} \nu_e \\ e \end{pmatrix}, \begin{pmatrix} \nu_\mu \\ \mu \end{pmatrix}, \begin{pmatrix} \nu_\tau \\ \tau \end{pmatrix} \quad (1.4)$$

$$\bar{e}_i = \bar{e}, \bar{\mu}, \bar{\tau} \quad (1.5)$$

where $i = 1, 2, 3$ is a family index. The particles with and without bars are part of the same fields: the bars denote the right-handed pieces of the fields, while the ones without bars are left-handed. The fields Q_i and L_i are weak isodoublets. The SM fermion Lagrangian density is then:

$$\mathcal{L} = iQ_i^\dagger \bar{\sigma}^\mu D_\mu Q_i + i\bar{u}_i^\dagger \bar{\sigma}^\mu D_\mu \bar{u}^i + i\bar{d}_i^\dagger \bar{\sigma}^\mu D_\mu \bar{d}^i + iL_i^\dagger \bar{\sigma}^\mu D_\mu L_i + i\bar{e}_i^\dagger \bar{\sigma}^\mu D_\mu \bar{e}^i \quad (1.6)$$

where i is the family index, and D_μ the appropriate SM covariant derivative:

$$D_\mu \begin{pmatrix} \nu_e \\ e \end{pmatrix} = [\partial_\mu - igW_\mu^a(\tau^a/2) - ig'Y_L B_\mu] \begin{pmatrix} \nu_e \\ e \end{pmatrix} \quad (1.7)$$

$$D_\mu \bar{e} = [\partial_\mu - ig'Y_{\bar{e}} B_\mu] \bar{e} \quad (1.8)$$

where τ^a ($a = 1, 2, 3$) are the Pauli matrices, $Y_L = -1/2$ and $Y_{\bar{e}} = +1$. g and g' are the coupling constants of the $SU(2)$ and $U(1)$ interactions. The covariant derivative describes the interaction between the fields: the gauge fields that transfer interactions are three $SU(2)$ bosons W_μ^a , $a = 1, 2, 3$ and one $U(1)$ boson B_μ .

If the $SU(3)_C \times SU(2)_L \times U(1)_Y$ symmetry is to be preserved, the W and Z -bosons are supposed to be massless but as their masses have been measured, it is evident that the symmetry is broken. A simple solution consisting of introducing an explicit mass term for the fields is forbidden by the requirement of the gauge invariance. A proposed solution to this is the Higgs mechanism, which can generate their masses through spontaneous symmetry breaking. If one starts from the Lagrangian:

$$\mathcal{L} = (D_\mu \phi)^\dagger D^\mu \phi - V(\phi^\dagger \phi) \quad (1.9)$$

where ϕ denotes a doublet containing one charged (ϕ^+) and one neutral (ϕ^0) scalar field:

$$\phi = \frac{1}{\sqrt{2}} \begin{pmatrix} \phi^+ \\ \phi^0 \end{pmatrix} \quad (1.10)$$

and the potential $V(\phi^\dagger\phi)$ is defined like:

$$V(\phi^\dagger\phi) = \mu^2\phi^\dagger\phi + \lambda(\phi^\dagger\phi)^2 \quad (1.11)$$

For $\mu^2 < 0$ the potential obtains the minimum when:

$$\phi^\dagger\phi = -\frac{\mu^2}{2\lambda} \equiv \frac{v^2}{2} \quad (1.12)$$

where v denotes the vacuum expectation value $v = 246$ GeV. Now one can expand the Higgs field around the minimum v :

$$\phi = \frac{1}{\sqrt{2}} \begin{pmatrix} 0 \\ v + h \end{pmatrix} \quad (1.13)$$

where h represents the perturbative expansion. Inserting this expression into the first term of Eq. 1.9 generates the gauge boson masses:

$$(D^\mu\phi)^\dagger D_\mu\phi^C = \left| \left(\partial_\mu - igW_\mu^a(\tau^a/2) - ig'Y_L B_\mu \right) \frac{1}{\sqrt{2}} \begin{pmatrix} 0 \\ v \end{pmatrix} \right|^2 = \quad (1.14)$$

$$= \frac{v^2}{8} \left| \begin{pmatrix} gW_\mu^a(\tau^a) + igB_\mu \\ 1 \end{pmatrix} \begin{pmatrix} 0 \\ 1 \end{pmatrix} \right|^2 = \frac{v^2}{8} \left| \begin{pmatrix} gW_\mu^1 - igW_\mu^2 \\ -gW_\mu^3 + g'B_\mu \end{pmatrix} \right|^2 = \quad (1.15)$$

$$= \frac{v^2}{8} \left| g^2(W_\mu^1)^2 + (W_\mu^2)^2 + (gW_\mu^3 - g'B_\mu)^2 \right| \quad (1.16)$$

The weak bosons are then defined by:

$$W_\mu^\pm = (W_\mu^1 \mp iW_\mu^2)/\sqrt{2} \quad (1.17)$$

$$\begin{pmatrix} Z_\mu \\ A_\mu \end{pmatrix} = \begin{pmatrix} \cos\theta_W & \sin\theta_W \\ -\sin\theta_W & \cos\theta_W \end{pmatrix} \begin{pmatrix} W_\mu^3 \\ B_\mu \end{pmatrix} \quad (1.18)$$

where θ_W is weak mixing angle (so called Weinberg angle). The W and Z -boson acquire mass (m_W and m_Z), and photon remains massless.

$$m_W = \frac{gv}{2} \quad (1.19)$$

$$m_Z = \frac{v}{2} \sqrt{g^2 + g'^2} \quad (1.20)$$

The Higgs boson mass is then given by:

$$m_h^2 = 2\mu^2 = 2\lambda v \quad (1.21)$$

And the $\cos\theta_W$ and $\sin\theta_W$ can be expressed as follows:

$$\cos\theta_W = \frac{m_W}{m_Z} = \frac{g'}{\sqrt{g^2 + g'^2}} \quad (1.22)$$

$$\sin\theta_W = \frac{g}{\sqrt{g^2 + g'^2}}. \quad (1.23)$$

1.1.2 Limitations of the Standard Model

Despite its predictive power, SM has 19 free parameters that do not have values predicted by the theory, and have to be measured. Those are masses of the particles, parameters of the Cabbibo-Kobayashi-Maskawa (CKM) matrix [21, 22], as well as the gauge couplings and Higgs vacuum expectation value and mass. The large number of free parameters of the SM could be

reduced if there would be gauge couplings unification. As the values of the coupling constants depend on the energy scale they are probed, one can compute their values at higher scales using the renormalisation group equation. The results show that the values approach each other with increasing energy but the unification cannot be accomplished within the SM. This is not really a problem of the SM, but more a hint that there might be some greater symmetry behind it.

The particles of the SM are grouped into three generations, as there is experimental evidence (at least for the number of neutrino generations) that there must be exactly three generations. The SM does not provide any reason that explains why there are exactly three generations.

In the SM the neutrinos are massless particles, while the experiments report the existence of the neutrino oscillations. First evidence that neutrinos are not massless came from the observation of the neutrino oscillations [23, 24] which are consequence of a change of the neutrino flavour in flight that is caused by the nonzero masses and mixing between different neutrino flavours. The SM has to be extended to accommodate them, which leads to introduction of at least nine additional parameters that are needed to account for the neutrino masses and mixing.

Particles of the SM compose only 4.9% of the matter content of the Universe. This means that should be some other form of matter or energy that should account for the remaining. The results of the Planck Collaboration [25] imply that 26.8% of the energy content of the Universe is made of cold dark matter. Within the SM there is no particle that satisfies this requirement, so the SM has to be extended to be able to explain the cold dark matter.

One of the specially prominent problems of the SM is related to the Higgs sector. The mass of the Higgs boson is a free parameter of the SM, but even before it was measured it was shown that it must be of order of 100 GeV, from the precision measurements. The one-loop corrections to the Higgs boson mass are computed using the cut-off regularisation (Λ_{UV} is the ultraviolet cutoff which is interpreted as the energy scale at which new physics shows up):

$$\Delta m_h^2 = -\frac{|\lambda_f|^2}{8\pi}\Lambda_{UV}^2 + \dots \quad (1.24)$$

If one assumes that the SM is valid up to the Planck scale, the correction to the Higgs mass would be of the order of the Planck mass. Thus it is surprising that the Higgs mass remains small even after receiving such large corrections. This is known as the hierarchy problem.

Also at the Planck scale $M_P = (8\pi G_{Newton})^{-1/2} = 2.4 \times 10^{18}$ GeV, the gravitational effects become important, but the SM does not include gravitational interaction: SM has to be extended to include also gravity.

Global fits of the SM were used in the past to predict not measured parameters of the SM, like the Higgs boson mass [26]. After the Higgs boson discovery [27, 28] and the measurement of its mass, the global SM fit became overconstrained thus allowing to take one by one of the observables out from the fit, and use it to predict its value. In Figure 1.1 (taken from Ref. [29]), the comparison of the fit results with the indirect determination in units of the total uncertainty, defined as the uncertainty of the direct measurement and that of the indirect determination added in quadrature. One can observe there is a good agreement between many of the observations and the SM predictions. Still there is some place for new physics.

The effects of new physics (if its scale is too high to be directly observed) can be visible through the effects of virtual particles in loops. They are expected to mostly contribute through vacuum polarization corrections to the electroweak precision observables. The oblique parameters S, T, U [30] are traditionally used to measure the size of the radiative corrections coming from the new physics beyond the SM. In the SM their values are zero, so if they are measured to be different from zero it would be a sign of new physics. The T parameter measures the difference between the new physics contributions of neutral and charged current processes at low energies. The S parameter describes new physics contributions to neutral current processes

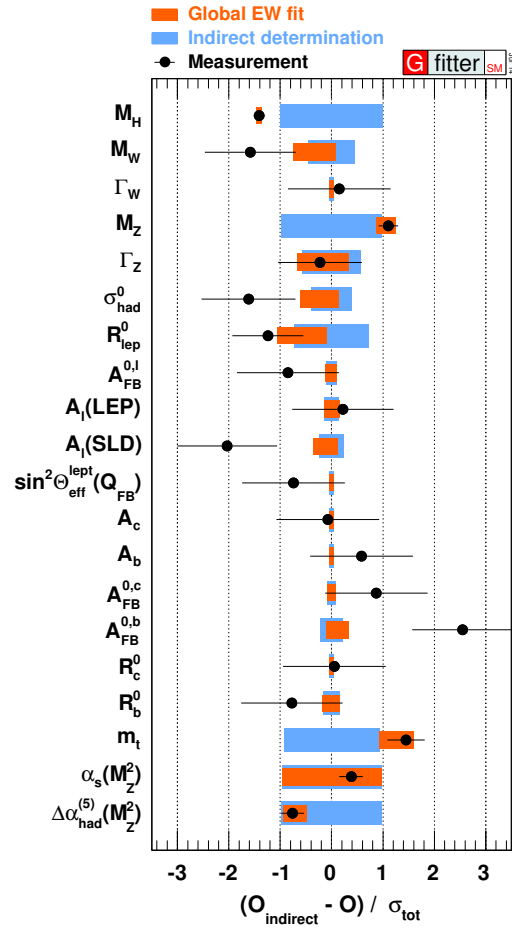


Figure 1.1: Comparison of the global electroweak fit results with the indirect determination in units of the total uncertainty, defined as the uncertainty of the direct measurement and that of the indirect determination added in quadrature. The indirect determination of an observable corresponds to a fit without using the corresponding direct constraint from the measurement. Taken from Ref. [29].

at different energy scales, while (S+U) describes new physics contribution to charged current processes. The U parameter is only sensitive to the W -boson mass and its total width, and is generally small in new physics models.

The value of $\Delta\rho$ is used in the Chapter 5.2 to check the contribution from new physics:

$$\Delta\rho = \alpha\Delta T$$

where $\alpha = 1/128$, and ΔT is the difference between the fitted value from Ref. [29] and the SM value (zero). In the SM the value of ρ should be one, so any deviation from it $\Delta\rho \neq 0$ is a sign of new physics:

$$\rho \equiv \frac{m_W^2}{m_Z^2 \cos^2 \theta_W} = 1 \quad (1.25)$$

1.1.3 Motivation for SUSY

Supersymmetry (SUSY) is a well motivated extension of the SM, as it helps resolving some of its problems. For example, the corrections of the Higgs boson mass coming from the one-loop corrections (mentioned in the previous Section) are easily canceled if there is a new symmetry in nature which connects bosons and fermions: as a result for each correction to the Higgs mass coming from fermions there is a correction with an opposite sign coming from bosons. This protects the Higgs boson mass from large corrections.

One other motivation comes from a possible explanation of the dark matter composition, as the SUSY predicts new particles that are good candidates for the dark matter.

Also, the number of free parameters of the SM can be reduced if there is unification of gauge couplings, which is possible if SUSY is a broken symmetry with the appropriate choice of the breaking parameters - called "soft" breaking terms, and with the masses of SUSY particles below the TeV scale.

One should also be aware that SUSY does not resolves all the problems of the SM, for example the massive neutrinos are not explained in an elegant way.

1.2 Supersymmetry

SUSY is a symmetry that transforms a fermionic state into a bosonic state and vice versa. The particle and its SUSY partner must have the same electric charge, weak isospin and color degrees of freedom, which place them in the same supersymmetric multiplet. The one quantum number that differs is the spin: the SUSY partners have a spin that is different by 1/2, and that is the only property that distinguishes them from the SM particles. The names for the spin-0 partners of the quarks and leptons are constructed by adding an "s" on the beginning of the name, for "scalar". So, they are called squarks and sleptons, or generally sfermions. The superpartners of the vector bosons are the gauginos: the partner of gluon is the gluino, and the superpartners of the electroweak bosons are spin-1/2 winos and bino. The mass of the SUSY particles (sparticles) should be the same as the masses of their SM partners, but none of them is observed up to now, which leads us to the conclusion that SUSY must be broken. The mechanism of SUSY breaking is unknown, and to describe it we have to allow for several free parameters in our theory.

SUSY introduces a new quantum number named R -parity defined by the following relation:

$$R = (-1)^{3(B-L)+2S} \quad (1.26)$$

where B and L are the baryon and lepton numbers, and S is the spin. SM particles have $R = 1$ while SUSY particles have $R = -1$. There are several models that postulate either R -parity conservation or R -parity violation.

1.2.1 SUSY algebra

The supersymmetry transformation is generated by the Q operator defined as:

$$Q|\text{boson}\rangle = |\text{fermion}\rangle \quad (1.27)$$

$$Q|\text{fermion}\rangle = |\text{boson}\rangle \quad (1.28)$$

which must be a spinor. Q^\dagger (the hermitian conjugate of Q) is also a symmetry generator. The operators Q and Q^\dagger are fermionic operators, so they have spin angular momentum 1/2. The algebra of the supersymmetry is given by following relations:

$$\{Q, Q^\dagger\} = P^\mu \quad (1.29)$$

$$\{Q, Q\} = \{Q^\dagger, Q^\dagger\} = 0 \quad (1.30)$$

$$[P^\mu, Q] = [P^\mu, Q^\dagger] = 0 \quad (1.31)$$

where P_μ is the generator of spacetime translations.

1.2.2 The simplest SUSY model - Wess-Zumino model

The simplest SUSY model is a free chiral supermultiplet whose members are a left-handed two-component Weyl fermion ψ and a complex scalar field ϕ . The simplest action that can be written for these fields is just the kinetic energy term for each:

$$S = \int d^4x (\mathcal{L}_{\text{scalar}} + \mathcal{L}_{\text{fermion}}) \quad (1.32)$$

$$\mathcal{L}_{\text{scalar}} = -\partial^\mu \phi^* \partial_\mu \phi \quad (1.33)$$

$$\mathcal{L}_{\text{fermion}} = i\psi^\dagger \bar{\sigma}^\mu \partial_\mu \psi \quad (1.34)$$

where $\partial_\mu = \partial/\partial x^\mu$ and $x^\mu = (t, \vec{x})$. The σ matrices are:

$$\sigma^0 = \bar{\sigma}^0 = \begin{pmatrix} 1 & 0 \\ 0 & 1 \end{pmatrix}, \sigma^1 = -\bar{\sigma}^1 = \begin{pmatrix} 0 & 1 \\ 1 & 0 \end{pmatrix} \quad (1.35)$$

$$\sigma^2 = -\bar{\sigma}^2 = \begin{pmatrix} 0 & -i \\ i & 0 \end{pmatrix}, \sigma^3 = -\bar{\sigma}^3 = \begin{pmatrix} 1 & 0 \\ 0 & -1 \end{pmatrix} \quad (1.36)$$

This model is called the massless, non-interacting Wess-Zumino model [31]. The equation of motion for these fields are $\partial_\mu \phi = 0$ and $\bar{\sigma}^\mu \partial_\mu \psi = 0$.

For the action to be invariant under the supersymmetry transformation i.e.:

$$\delta S = 0 \quad (1.37)$$

the appropriate infinitesimal change of the scalar boson field ($\phi \rightarrow \phi + \delta\phi$) and the fermion field ($\psi_\alpha \rightarrow \psi_\alpha + \delta\psi_\alpha$) should not change the action.

Now one should find the appropriate forms of those infinitesimal changes: ϕ into the fermion field ψ_α . the simplest possibility is:

$$\delta\phi = \epsilon^\alpha \psi_\alpha = \epsilon\psi \quad (1.38)$$

$$\delta\phi^* = \epsilon^\dagger \psi^\dagger \quad (1.39)$$

where the SUSY transformation is parametrised by ϵ^α - which is an infinitesimal, anticommuting, two-component Weyl fermion object (same as ψ). It is assumed to be a constant to start with, as it parametrises a global symmetry, so $\partial_\mu \epsilon^\alpha = 0$ (when one describes local symmetries $\epsilon^\alpha = \epsilon^\alpha(x)$).

The resulting infinitesimal change of the fermion part of the Lagrangian is:

$$\delta\mathcal{L}_{\text{scalar}} = -\epsilon\partial^\mu\psi\partial_\mu\phi^* - \epsilon^\dagger\partial^\mu\psi^\dagger\partial_\mu\phi. \quad (1.40)$$

If the total Lagrangian is to be invariant under the infinitesimal transformations of the fields, the infinitesimal transformations of its scalar and fermion part should cancel each other: $\delta\mathcal{L}_{\text{scalar}} = -\delta\mathcal{L}_{\text{fermion}}$. When one inspects the terms of $\delta\mathcal{L}_{\text{scalar}}$, one can conclude that the $\delta\psi_\alpha$ should be proportional to $\partial_\mu\phi$ and $\delta\psi_\alpha^\dagger$ should be proportional to $\partial_\mu\phi^*$. Another way to see this is also from the supersymmetry operator that turn the fermion field into scalar boson field. The only possibility is:

$$\delta\psi_\alpha = -i(\sigma^\mu\epsilon^\dagger)_\alpha\partial_\mu\phi \quad (1.41)$$

$$\delta\psi_\alpha^\dagger = i(\epsilon\sigma^\mu)_{\dot{\alpha}}\partial_\mu\phi^* \quad (1.42)$$

This leads to the infinitesimal change of the fermion part of the Lagrangian:

$$\delta\mathcal{L}_{\text{fermion}} = \epsilon\partial^\mu\psi\partial_\mu\phi^* + \epsilon^\dagger\partial^\mu\psi^\dagger\partial_\mu\phi - \partial_\mu(\epsilon\sigma^\nu\bar{\sigma}^\mu\psi\partial_\nu\phi^* + \epsilon\psi\partial^\mu\phi^* + \epsilon^\dagger\psi^\dagger\partial^\mu\phi) \quad (1.43)$$

which cancels with $\delta\mathcal{L}_{\text{scalar}}$ up to a total derivative, and the action is indeed invariant under supersymmetric transformation ($\delta S = 0$).

For SUSY to be the symmetry of the theory it is necessary that the algebra closes: that means that the commutator of two supersymmetry transformations is also a supersymmetry transformation:

$$[\delta_{\epsilon_2}, \delta_{\epsilon_1}]\phi = i(-\epsilon_1\sigma^\mu\epsilon_2^\dagger + \epsilon_2\sigma^\mu\epsilon_1^\dagger)\partial_\mu\phi \quad (1.44)$$

$$[\delta_{\epsilon_2}, \delta_{\epsilon_1}]\psi_\alpha = i(-\epsilon_1\sigma_\mu\epsilon_2^\dagger + \epsilon_2\sigma^\mu\epsilon_1^\dagger)\partial_\mu\psi_\alpha + i\epsilon_{1\alpha}\epsilon_2^\dagger\bar{\sigma}^\mu\partial_\mu\psi - i\epsilon_{2\alpha}\epsilon_1^\dagger\bar{\sigma}^\mu\partial_\mu\psi \quad (1.45)$$

Here one can see that the algebra only closes on-shell. An auxiliary field (the field that does not have a kinetic term) can be added, which can allow for the algebra to also close off-shell. One can come to the same conclusion by considering the sum of number of degrees of freedom of the fields on- and off-shell. The additional Lagrangian for this complex scalar field F is just:

$$\mathcal{L}_{\text{auxiliary}} = F^*F \quad (1.46)$$

and its equation of motion is: $F = F^* = 0$, as expected. As this field was introduced to make the supersymmetry algebra close off-shell, its transformation should be proportional to $\bar{\sigma}^\mu\partial_\mu\psi$:

$$\delta F = -i\epsilon^\dagger\bar{\sigma}^\mu\partial_\mu\psi \quad (1.47)$$

$$\delta F^* = i\partial_\mu\psi^\dagger\bar{\sigma}^\mu\epsilon. \quad (1.48)$$

Now the infinitesimal transformation of the part of the Lagrangian that corresponds to the auxiliary field $\delta\mathcal{L}_{\text{auxiliary}}$ can be calculated:

$$\delta\mathcal{L}_{\text{auxiliary}} = -i\epsilon^\dagger\bar{\sigma}^\mu\partial_\mu\psi F^* + i\partial_\mu\psi^\dagger\bar{\sigma}^\mu\epsilon F. \quad (1.49)$$

The infinitesimal transformations of the ψ and ψ^\dagger should be modified to include the terms proportional to F and F^* . New infinitesimal transformations are given by:

$$\delta\psi_\alpha = -i(\sigma^\mu\epsilon^\dagger)_\alpha\partial_\mu\phi + \epsilon_\alpha F \quad (1.50)$$

$$\delta\psi_\alpha^\dagger = i(\epsilon\sigma^\mu)_{\dot{\alpha}}\partial_\mu\phi^* + \epsilon_{\dot{\alpha}}^\dagger F^* \quad (1.51)$$

The goal was to see if the supersymmetric transformation leave the Lagrangian invariant and if their algebra closes off-shell. The addition of the auxiliary field shows that this is possible. Now if one computes the commutator of the supersymmetry transformations applied to each of the fields of the theory $X = \phi, \phi^*, \psi, \psi^\dagger, F, F^*$:

$$[\delta_{\epsilon_1}, \delta_{\epsilon_2}]X = i(-\epsilon_1\sigma^\mu\epsilon_2^\dagger + \epsilon_2\sigma^\mu\epsilon_1^\dagger)\partial_\mu X \quad (1.52)$$

one can see that the supersymmetry algebra closes off-shell also.

1.2.3 Interactions of chiral supermultiplet

In the previous Section a free chiral supermultiplet was considered. The second step towards the definition of the complete theory is to add the non-gauge interactions between particles. To start with, one can find the most general form of renormalisable interactions for fields, described by the interaction Lagrangian (\mathcal{L}_{int}):

$$\mathcal{L}_{\text{int}} = \left(-\frac{1}{2}W^{ij}\psi_i\psi_j + W^iF_i + x^{ij}F_iF_j \right) + \text{c.c.} - U \quad (1.53)$$

where W^{ij} , W^i , x^{ij} and U are polynomials in the scalar fields ϕ_i , ϕ^{*i} with degrees 1, 2, 0 and 4, respectively. If one wants supersymmetry to be the symmetry of the theory, \mathcal{L}_{int} should be also invariant under the supersymmetry transformations, which places certain requirements on its terms. The term $U(\phi_i, \phi^{*i})$ cannot be invariant under the supersymmetry transformation as there is no other term that shows similar transformation with which it can be cancelled, so it cannot be part of the \mathcal{L}_{int} . Neither can the x^{ij} term, for the same reason. So the only possible terms are:

$$\mathcal{L}_{\text{int}} = \left(-\frac{1}{2}W^{ij}\psi_i\psi_j + W^iF_i \right) + \text{c.c.} \quad (1.54)$$

The terms of \mathcal{L}_{int} can be grouped by the parts that are required to cancel mutually:

$$\delta\mathcal{L}_{\text{int}}\Big|_{4\text{-spinor}} = \left[-\frac{1}{2}\frac{\delta W^{ij}}{\delta\phi_k}(\epsilon\psi_k)(\psi_i\psi_j) - \frac{1}{2}\frac{\delta W^{ij}}{\delta\phi^{*k}}(\epsilon^\dagger\psi^{\dagger k})(\psi_i\psi_j) \right] + \text{c.c.} \quad (1.55)$$

The term $\frac{\delta W^{ij}}{\delta\phi_k}(\epsilon\psi_k)(\psi_i\psi_j)$ vanishes because of the Fierz identity:

$$(\epsilon\psi_i)(\psi_j\psi_k) + (\epsilon\psi_j)(\psi_k\psi_i) + (\epsilon\psi_k)(\psi_i\psi_j) = 0 \quad (1.56)$$

if and only if $\delta W^{ij}/\delta\phi_k$ is totally symmetric under interchange of i, j, k . As there is no corresponding identity proportional to the term proportional to $(\epsilon^\dagger\psi^{\dagger k})(\psi_i\psi_j)$, the other possibility is for $\delta W^{ij}/\delta\phi^{*k}$ to be equal to 0, i.e that W^{ij} does not depend on ϕ^{*k} . So W^{ij} has the following terms:

$$W^{ij} = M^{ij} + y^{ijk}\phi_k \quad (1.57)$$

where M^{ij} is a symmetric mass matrix for the fermion fields, and y^{ijk} is the Yukawa coupling of a scalar ϕ_k and two fermions $\psi_i\psi_j$, and it is totally symmetric under interchange of i, j, k . So

$$W^{ij} = \frac{\delta^2}{\delta\phi_i\delta\phi_j}W \quad (1.58)$$

where W is given by:

$$W = \frac{1}{2}M^{ij}\phi_i\phi_j + \frac{1}{6}y^{ijk}\phi_i\phi_j\phi_k \quad (1.59)$$

and is called superpotential.

The next part of \mathcal{L}_{int} to be considered is the one that contains space-time derivative:

$$\delta\mathcal{L}_{\text{int}}\Big|_{\partial} = (iW^{ij}\partial_\mu\phi_j\psi_i\sigma^\mu\epsilon^\dagger + iW^i\partial_\mu\psi_i\sigma^\mu\epsilon^\dagger) + \text{c.c.} \quad (1.60)$$

To turn this expression into a total derivative, one finds:

$$W^i = \frac{\delta W}{\delta\phi_i} = M^{ij}\phi_j + \frac{1}{2}y^{ijk}\phi_j\phi_k \quad (1.61)$$

The full Lagrangian can now be written as:

$$\mathcal{L} = -\partial^\mu\phi^{*i}\partial_\mu\phi_i + i\psi^{\dagger i}\bar{\sigma}^\mu\partial_\mu\psi_i - \frac{1}{2}(W^{ij}\psi_i\psi_j + W_{ij}^*\psi^{\dagger i}\psi^{\dagger j}) - W^iW_i^* \quad (1.62)$$

The scalar potential for the theory in terms of the superpotential is given by:

$$\begin{aligned} V(\phi, \phi^*) &= W^k W_k^* = F^{*k} F_k = \\ &= M_{ik}^* M^{kj} \phi^{*i} \phi_j + \frac{1}{2} M^{in} y_{jkn}^* \phi_i \phi^{*j} \phi^{*k} + \frac{1}{2} M_{in}^* y^{jkn} \phi^{*i} \phi_j \phi_k + \frac{1}{4} y^{ijn} y_{klm}^* \phi_i \phi_j \phi^{*k} \phi^{*l} \end{aligned} \quad (1.63)$$

It is bounded from below, and non-negative. The full Lagrangian is:

$$\begin{aligned} \mathcal{L} &= -\partial^\mu \phi^{*i} \partial_\mu \phi_i - V(\phi, \phi^*) + i\psi^\dagger \bar{\sigma}^\mu \partial_\mu \psi_i - \frac{1}{2} M^{ij} \psi_i \psi_j - \\ &\quad - \frac{1}{2} M_{ij}^* \psi^\dagger_i \psi^\dagger_j - \frac{1}{2} y^{ijk} \phi_i \psi_j \psi_k - \frac{1}{2} y_{ijk}^* \phi^{*i} \psi^\dagger_j \psi^\dagger_k \end{aligned} \quad (1.64)$$

Next one can compute the equations of motion and look in their linearised form:

$$\partial^\mu \partial_\mu \phi_i = M_{ik}^* M^{kj} \phi_j + \dots \quad (1.65)$$

$$i\bar{\sigma}^\mu \partial_\mu \psi_i = M_{ij}^* \psi^\dagger_j + \dots \quad (1.66)$$

$$i\sigma^\mu \partial_\mu \psi^\dagger_i = M^{ij} \psi_j + \dots \quad (1.67)$$

If one then substitute the relevant terms in the equation (for example by keeping only ψ , and substituting ψ^\dagger), the equations get the form:

$$\partial^\mu \partial_\mu \psi_i = M_{ik}^* M^{kj} \psi_j + \dots \quad (1.68)$$

$$\partial^\mu \partial_\mu \psi^\dagger_j = \psi^\dagger_i M_{ik}^* M^{kj} + \dots \quad (1.69)$$

from which one can deduce that the fermions and bosons satisfy the same equations, and so have the same masses. Each chiral multiplet thus contains a complex scalar and a Weyl fermion of equal mass.

1.2.4 Lagrangians for gauge supermultiplets

When the construction of the Lagrangian of fermions and bosons, and the non-gauge interactions leading to their masses, is finished one should also include the gauge interactions. Spin 1 particles are needed to construct a supersymmetric gauge theory. Thus the gauge supermultiplet: a massless gauge boson field A_μ^a and a two-component Weyl fermion gaugino λ^a are added to the particle content of the supersymmetric theory. The index a runs over the adjoint representation of the gauge group ($a = 1, \dots, 8$ for $SU(3)_C$ colour gluons and gluinos; $a = 1, 2, 3$ for $SU(2)_L$ weak isospin; $a = 1$ for $U(1)_Y$ weak hypercharge). The gauge transformations of this vector supermultiplet are given by:

$$\delta_{\text{gauge}} A_\mu^a = \partial_\mu \Lambda^a + g f^{abc} A_\mu^b \Lambda^c \quad (1.70)$$

$$\delta_{\text{gauge}} \lambda^a = g f^{abc} \lambda^b \Lambda^c \quad (1.71)$$

where Λ^a is an infinitesimal gauge transformation parameter, g is the gauge coupling, and f^{abc} are the totally antisymmetric structure constants that define the gauge group. When one counts the degrees of freedom of all fields on and off-shell, it becomes obvious that one will need a real bosonic auxiliary field, D^a , to make SUSY consistent off-shell. It transforms as an adjoint of the gauge group and satisfies $(D^a)^* = D^a$. It has dimension of $[\text{mass}]^2$ and no kinetic term. Now the Lagrangian for a gauge supermultiplet is:

$$\mathcal{L}_{\text{gauge}} = -\frac{1}{4} F_{\mu\nu}^a F^{\mu\nu a} + i\lambda^\dagger \bar{\sigma}^\mu D_\mu \lambda^a + \frac{1}{2} D^a D^a \quad (1.72)$$

where $F_{\mu\nu}$ is the Yang-Mills field strength:

$$F_{\mu\nu}^a = \partial_\mu A_\nu^a - \partial_\nu A_\mu^a + gf^{abc}A_\mu^b A_\nu^c \quad (1.73)$$

with the covariant derivative of the gaugino field given by:

$$D_\mu \lambda^a = \partial_\mu \lambda^a + gf^{abc}A_\mu^b \lambda^c \quad (1.74)$$

One can check that the supersymmetry transformations of the fields given by:

$$\delta A_\mu^a = -\frac{1}{\sqrt{2}}(\epsilon^\dagger \bar{\sigma}_\mu \lambda^a + \lambda^{\dagger a} \bar{\sigma}_\mu \epsilon) \quad (1.75)$$

$$\delta \lambda_\alpha^a = \frac{i}{2\sqrt{2}}(\sigma^\mu \bar{\sigma}^\nu \epsilon)_\alpha F_{\mu\nu}^a + \frac{1}{\sqrt{2}}\epsilon_\alpha D^a \quad (1.76)$$

$$\delta D^a = \frac{i}{\sqrt{2}}(-\epsilon^\dagger \bar{\sigma}^\mu D_\mu \lambda^a + D_\mu \lambda^{\dagger a} \bar{\sigma}^\mu \epsilon) \quad (1.77)$$

leave the Lagrangian unchanged. Like before one should make sure that the algebra of the supersymmetry transformations also closes off-shell, as it was the reason for the addition of the auxiliary field D^a :

$$[\delta_{\epsilon_2}, \delta_{\epsilon_1}]X = i(-\epsilon_1 \sigma^\mu \epsilon_2^\dagger + \epsilon_2 \sigma^\mu \epsilon_1^\dagger)D_\mu X \quad (1.78)$$

where $X = F_{\mu\nu}^a, \lambda^a, \lambda^{\dagger a}, D^a$ are all the fields of the theory.

1.2.5 Supersymmetric gauge interactions

By now it is verified that one can construct a Lagrangian with each of the chiral and gauge supermultiplet that is invariant and that the algebra of supersymmetry transformation close off-shell. The next step is to construct the Lagrangian that will include both multiplets and also their interactions. Let's suppose that the chiral supermultiplets transform under the gauge group in a representation with hermitian matrices $(T^a)_i^j$ that satisfy $[T^a, T^b] = if^{abc}T^c$. Since supersymmetry and gauge transformations commute, the scalar, fermion and auxiliary fields must be in the same representation of the gauge group:

$$\delta_{\text{gauge}} X_i = ig\Lambda^a (T^a X)_i \quad (1.79)$$

where $X_i = \phi_i, \psi_i, F_i$. In order for the Lagrangian to be gauge-invariant, one needs to replace the ordinary derivatives in Eq. 1.34 with the covariant ones:

$$\partial_\mu \phi_i \rightarrow D_\mu \phi_i = \partial_\mu \phi_i - igA_\mu^a (T^a \phi)_i \quad (1.80)$$

$$\partial_\mu \phi^{*i} \rightarrow D_\mu \phi^{*i} = \partial_\mu \phi^{*i} + igA_\mu^a (\phi^* T^a)^i \quad (1.81)$$

$$\partial_\mu \psi_i \rightarrow D_\mu \psi_i = \partial_\mu \psi_i - igA_\mu^a (T^a \psi)_i \quad (1.82)$$

Now one gets the interactions between the supermultiplets: the vector bosons in the gauge supermultiplet couple to the scalars and fermions in the chiral supermultiplets. But maybe there exist other interactions that does not break gauge invariance and also involve the gaugino and D^a fields. As A_μ^a couples to ϕ_i and ψ_i , maybe λ^a and D^a can also couple to it. There are three possible renormalisable interaction terms (meaning mass dimension ≤ 4):

$$(\phi^* T^a \psi) \lambda^a, \quad \lambda^{\dagger a} (\psi^\dagger T^a \phi), \quad (\phi^* T^a \phi) D^a \quad (1.83)$$

If these terms are added to the Lagrangian, there are some changes in the supersymmetry transformation laws that should be made, in order for the Lagrangian to be invariant under the supersymmetry transformations:

$$\delta\phi_i = \epsilon\psi_i \quad (1.84)$$

$$\delta\psi_{i\alpha} = -i(\sigma^\mu\epsilon^\dagger)_\alpha D_\mu\phi_i + \epsilon_\alpha F_i \quad (1.85)$$

$$\delta F_i = -i\epsilon^\dagger\bar{\sigma}^\mu D_\mu\psi_i + \sqrt{2}g(T^a\phi)_i\epsilon^\dagger\lambda^{\dagger a} \quad (1.86)$$

This is achieved by again replacing the ordinary derivatives with the covariant ones.

The complete Lagrangian for a renormalisable supersymmetric theory, that includes both chiral and gauge multiplet is given by:

$$\mathcal{L} = \mathcal{L}_{\text{chiral}} + \mathcal{L}_{\text{gauge}} - \sqrt{2}g(\phi^*T^a\psi)\lambda^a - \sqrt{2}g\lambda^{\dagger a}(\psi^\dagger T^a\phi) + g(\phi^*T^a\phi)D^a \quad (1.87)$$

The interactions between fields are proportional to coupling constants that are fixed by the supersymmetry transformations. The first two interaction terms represent the direct coupling between matter fields and gauginos. From the free term for the D^a field and the last interaction term, one can find the equation of motion of the D^a field:

$$D^a = -g(\phi^*T^a\phi). \quad (1.88)$$

From here one can see that the auxiliary field can be written only in terms of the scalar fields, thus it can be eliminated from Eq. 1.87 and one can find that the complete scalar potential is given by:

$$V(\phi, \phi^*) = F^{*i}F_i + \frac{1}{2}\sum_a D^a D^a = W_i^*W^i + \frac{1}{2}\sum_a g_a^2(\phi^*T^a\phi)^2 \quad (1.89)$$

These terms are called F and D -terms respectively. The F -terms are fixed by Yukawa couplings and fermion mass terms, while the D -terms are fixed by the gauge interactions.

1.2.6 SUSY breaking

If supersymmetry is an exact symmetry of nature the fermions and bosons would have the same masses, and it is excluded experimentally as they have not yet been observed. Thus if it exists, supersymmetry has to be spontaneously broken. The Lagrangian density should be invariant under supersymmetry, while the vacuum state is not.

The breaking of supersymmetry should be done by introducing the terms that have positive mass dimension (so called soft terms). They allow for the hierarchy between electroweak and Planck scale to be preserved. The possible soft supersymmetry breaking terms in the Lagrangian density are:

$$\mathcal{L}_{\text{soft}} = -\left(\frac{1}{2}M_a\lambda^a\lambda^a + \frac{1}{6}a^{ijk}\phi_i\phi_j\phi_k + \frac{1}{2}b^{ij}\phi_i\phi_j + t^i\phi_i\right) + \text{c.c.} - (m^2)_j^i\phi_j^*\phi_i \quad (1.90)$$

$$\mathcal{L}_{\text{maybesoft}} = -\frac{1}{2}c_i^{jk}\phi_i^*\phi_j\phi_k + \text{c.c.} \quad (1.91)$$

where M_a are gaugino masses for each gauge group, $(m^2)_i^j$ and b^{ij} are scalar squared mass terms, a^{ijk} and c_i^{jk} are scalar couplings, and t^i are tad-pole couplings. Possible soft mass terms for the chiral multiplet $m^{ij}\psi_i\psi_j$ are not present as they can be absorbed into the redefinition of the superpotential and the terms $(m^2)_j^i$ and c_i^{jk} .

Supersymmetry is obviously broken by the addition of these terms as there are only scalars and gauginos, but not their superpartners. There are some restrictions on the terms that can be added: the gaugino masses M_a are always possible, while for example terms proportional

Names	spin	R -parity	gauge eigenstates				mass eigenstates			
Higgs bosons	0	+1	H_u^0	H_d^0	H_u^+	H_d^-	h^0	H^0	A^0	H^\pm
squarks	0	-1	\tilde{u}_L	\tilde{u}_R	\tilde{d}_L	\tilde{d}_R	same			
			\tilde{s}_L	\tilde{s}_R	\tilde{c}_L	\tilde{c}_R	same			
			\tilde{t}_L	\tilde{t}_R	\tilde{b}_L	\tilde{b}_R	\tilde{t}_1	\tilde{t}_2	\tilde{b}_1	\tilde{b}_2
sleptons	0	-1	\tilde{e}_L	\tilde{e}_R	$\tilde{\nu}_e$	same				
			$\tilde{\mu}_L$	$\tilde{\mu}_R$	$\tilde{\nu}_\mu$	same				
			$\tilde{\tau}_L$	$\tilde{\tau}_R$	$\tilde{\nu}_\tau$	$\tilde{\tau}_1$	$\tilde{\tau}_2$	$\tilde{\nu}_\tau$		
neutralinos	1/2	-1	\tilde{B}^0	\tilde{W}^0	\tilde{H}_u^0	\tilde{H}_d^0	$\tilde{\chi}_1^0$	$\tilde{\chi}_2^0$	$\tilde{\chi}_3^0$	$\tilde{\chi}_4^0$
charginos	1/2	-1	\tilde{W}^\pm	\tilde{H}_u^\pm	\tilde{H}_d^\pm	$\tilde{\chi}_1^\pm$	$\tilde{\chi}_2^\pm$			
gluino	1/2	-1	\tilde{g}				same			
gravitino	3/2	-1	\tilde{G}				same			

Table 1.1: Particle content of the MSSM.

to $(m^2)_j^i$ can be present only if i, j are such that ϕ_i, ϕ_j^* transform in the complex conjugate representation of each other under all gauge symmetries.

The more general results derived in this Section will be made more specific when these general requirements are applied to a minimal supersymmetric model.

1.2.7 Electroweak symmetry breaking

Electroweak symmetry breaking is also necessary in SUSY models. Like in the SM it is introduced using the Higgs mechanism. The Higgs bosons need to be embedded in supermultiplet. As a consequence there are extra fermionic states that are SUSY partners of the Higgs boson and due to SUSY constraints a single Higgs doublet cannot be used to break the electroweak symmetry and to give mass to all the SM fermions.

1.3 Minimal supersymmetric standard model - MSSM

The minimal supersymmetric standard model (MSSM) is the minimal phenomenologically possible supersymmetric extension of the Standard Model, thus it has only the necessary particles and interactions included.

1.3.1 Superpotential and interaction

The MSSM has 105 new parameters to describe SUSY breaking, on top of the 19 free parameters already present in the SM. These parameters are needed to determine the squarks and sleptons masses and mixing angles, and also to describe CP-violating phases.

The new particles present in the MSSM are given in Table 1.1.

The superpotential for the MSSM is given by:

$$W_{\text{MSSM}} = \bar{u}_\mathbf{y}_\mathbf{u} Q H_u - \bar{d}_\mathbf{y}_\mathbf{d} Q H_d - \bar{e}_\mathbf{y}_\mathbf{e} L H_d + \mu H_u H_d \quad (1.92)$$

$\mathbf{y}_u, \mathbf{y}_d, \mathbf{y}_e$ are 3×3 matrices in family space. The μ parameter is similar to the Higgs boson mass in the SM. Due to SUSY constraints, one has to introduce two Higgs doublets H_u, H_d that couple to up type and down type quarks and leptons.

One usually makes the approximation that only Yukawa couplings to the top, bottom quark and tau lepton are important as they are the heaviest fermions on the SM.

1.3.2 Soft supersymmetry breaking

The soft SUSY breaking terms of the MSSM are given by:

$$\begin{aligned} \mathcal{L}_{\text{soft}}^{\text{MSSM}} = & -\frac{1}{2}(M_3\tilde{g}\tilde{g} + M_2\tilde{W}\tilde{W} + M_1\tilde{B}\tilde{B} + \text{c.c.}) - (\tilde{u}\mathbf{a}_u\tilde{Q}H_u - \tilde{d}\mathbf{a}_d\tilde{Q}H_d - \tilde{e}\mathbf{a}_e\tilde{L}H_d + \text{c.c.}) \\ & - \tilde{Q}^\dagger \mathbf{m}_Q^2 \tilde{Q} - \tilde{L}^\dagger \mathbf{m}_L^2 \tilde{L} - \tilde{u}\mathbf{m}_u^2 \tilde{u}^\dagger - \tilde{d}\mathbf{m}_d^2 \tilde{d}^\dagger - \tilde{e}\mathbf{m}_e^2 \tilde{e}^\dagger - m_{H_u}^2 H_u^* H_u - m_{H_d}^2 H_d^* H_d - (bH_u H_d + \text{c.c.}) \end{aligned} \quad (1.93)$$

M_3, M_2, M_1 are the gluino, wino, and bino mass parameters. Each $\mathbf{a}_u, \mathbf{a}_d, \mathbf{a}_e$ is a complex 3×3 matrix in the family space with dimensions of mass. Each of $\mathbf{m}_Q^2, \mathbf{m}_u^2, \mathbf{m}_d^2, \mathbf{m}_L^2, \mathbf{m}_e^2$ is a 3×3 matrix in the family space that can have complex entries, but they must be hermitian so that the Lagrangian is real. They are squark and slepton mass terms of $(m^2)_i^j$ type (Eq. 1.91). $m_{H_u}^2$ and $m_{H_d}^2$ are squared-mass terms of the $(m^2)_i^j$ type (Eq. 1.91), and they represent SUSY-breaking contributions to the Higgs potential. b is the only squared-mass term of the type b^{ij} (Eq. 1.91) that can occur in the MSSM.

One expects that soft terms are not higher than a few TeV, and that the parameters are of the same order:

$$M_1, M_2, M_3, \mathbf{a}_u, \mathbf{a}_d, \mathbf{a}_e \sim m_{\text{soft}} \sim \text{TeV} \quad (1.94)$$

$$\mathbf{m}_Q^2, \mathbf{m}_L^2, \mathbf{m}_u^2, \mathbf{m}_d^2, \mathbf{m}_e^2, m_{H_u}^2, m_{H_d}^2, b \sim m_{\text{soft}}^2 \sim \text{TeV}^2 \quad (1.95)$$

While supersymmetry by itself does not introduce any new parameters, many of them are added to describe supersymmetry breaking, so this part is really arbitrary.

The values of free parameters are constrained by the flavour physics observables on flavour-changing and CP-violating processes, so most of the parameters cannot be completely arbitrary. For example, it is widely assumed that supersymmetry breaking is mediated by flavour-blind interactions and that the only source of the CP violation comes from the CKM matrix.

1.3.3 R -parity conservation

The MSSM has one undesirable feature: the accidental symmetries that conserve the baryon and lepton numbers in the SM are not present in the MSSM. Those symmetries ensure the stability of the proton. However in the MSSM terms that violate B and L can be added to the superpotential. One can solve this by explicitly imposing a global $U(1)_B$ and $U(1)_L$ symmetry but this is not a satisfactory solution, as the B and L are violated by the non-perturbative processes in the electroweak sector of the SM. In the MSSM this problem can also be solved by introducing the R -parity (Eq. 1.26).

The new quantum number R -parity has an impact on the SUSY phenomenology. The violation of R -parity can lead to too fast proton decay via the exchange of SUSY particles. The appealing properties of the R -parity conserving models are therefore long enough proton lifetime, which makes them preferred models to search for. The conservation of R -parity in scattering and decay processes has an impact on SUSY phenomenology: SUSY particles must be produced in pairs (if we start from an initial state involving SM particles). Their decay must lead (either directly or through cascades) to the production of the stable Lightest Supersymmetric

Particle (LSP), accompanied by SM particles. If the stable LSP is electrically and colour neutral, it is a good candidate for dark matter. It would also go through collider detectors undetected and lead to the well known missing transverse energy signature. In the following, R -parity is assumed to be conserved.

1.3.4 Sparticles

The sparticles predicted by the MSSM are given in Table 1.1, and in this Section a short description of each type of the sparticles is given along with their decay modes.

1.3.4.1 Neutralinos

Neutralinos are electrically neutral fermions, and are mass eigenstates realised by the mixing of the electroweak gauginos (\tilde{B}, \tilde{W}^0) and higgsinos ($\tilde{H}_u^0, \tilde{H}_d^0$) because of the electroweak symmetry breaking. Neutralinos are identical to their antiparticles as they are Majorana fermions.

They are denoted by $\tilde{\chi}_i^0$, $i = 1, 2, 3, 4$ and are labeled in ascending mass. The lightest is $\tilde{\chi}_1^0$, and it is usually assumed to be the LSP, unless there is a lighter gravitino. As it is neutral, it can be a dark matter candidate.

The mass terms corresponding to the neutralino part of the Lagrangian are given by:

$$\mathcal{L}_{\tilde{\chi}^0 \text{mass}} = -\frac{1}{2}(\psi^0)^T M_{\tilde{\chi}^0} \psi^0 + c.c. \quad (1.96)$$

where $\psi^0 = (\tilde{B}, \tilde{W}^0, \tilde{H}_d^0, \tilde{H}_u^0)$, and the mixing matrix is given by:

$$M_{\tilde{\chi}^0} = \begin{pmatrix} M_1 & 0 & -\frac{1}{\sqrt{2}}g'v_d & \frac{1}{\sqrt{2}}g'v_u \\ 0 & M_2 & \frac{1}{\sqrt{2}}gv_d & -\frac{1}{\sqrt{2}}gv_d \\ -\frac{1}{\sqrt{2}}g'v_d & \frac{1}{\sqrt{2}}gv_d & 0 & -\mu \\ \frac{1}{\sqrt{2}}g'v_u & -\frac{1}{\sqrt{2}}gv_u & -\mu & 0 \end{pmatrix} \quad (1.97)$$

The entries M_1 , M_2 and μ are respectively the bino, wino and higgsino mass terms from Eq. 1.93. The terms proportional to g and g' come from the Higgs-higgsino-gaugino couplings. This mixing matrix can also be presented as:

$$M_{\tilde{\chi}^0} = \begin{pmatrix} M_1 & 0 & -\cos\beta \sin\theta_W m_Z & \sin\beta \sin\theta_W m_Z \\ 0 & M_2 & \cos\beta \cos\theta_W m_Z & -\sin\beta \cos\theta_W m_Z \\ -\cos\beta \sin\theta_W m_Z & \cos\beta \cos\theta_W m_Z & 0 & -\mu \\ \sin\beta \sin\theta_W m_Z & -\sin\beta \cos\theta_W m_Z & -\mu & 0 \end{pmatrix} \quad (1.98)$$

with $\tan\beta = v_u/v_d$ (Section 1.3.4.7).

If m_Z is neglected, the neutralino mass eigenstates are very nearly bino-like \tilde{B} , wino-like \tilde{W} and higgsino-like $(\tilde{H}_u^0 \pm \tilde{H}_d^0)/\sqrt{2}$. Depending on a relative values of M_1 , M_2 and μ the LSP can be dominantly bino, wino or higgsino.

Each neutralino has at least a small component of the electroweak gauginos \tilde{B} , \tilde{W}^0 or \tilde{W}^\pm , so they have couplings of weak interaction strength to (scalar, fermion) pairs. To which particle they will decay depend obviously on their masses. They can decay to lepton+slepton pair, as well as to quark+squark pair. Neutralinos also have the gaugino-higgsino-Higgs and $SU(2)_L$ gaugino-gaugino-vector boson couplings. This allows for their decays to lighter neutralino or chargino and a Higgs scalar or an electroweak gauge boson.

$$\tilde{\chi}_i^0 \rightarrow Z\tilde{\chi}_j^0, W\tilde{\chi}_j^\pm, h^0\tilde{\chi}_j^0, \ell\tilde{\ell}, \nu\tilde{\nu}, A^0\tilde{\chi}_j^0, H^0\tilde{\chi}_j^0, H^\pm\tilde{\chi}_j^\mp, q\tilde{q} \quad (1.99)$$

If the neutralinos have a large higgsino component, the decays into third generation quark-squark pairs are significantly enhanced by the top-quark Yukawa coupling.

If all the two-body decays are forbidden, they are forced to decay through three-body decays:

$$\tilde{\chi}_i^0 \rightarrow ff\tilde{\chi}_j^0, ff'\tilde{\chi}_j^\pm \quad (1.100)$$

through the same off-shell gauge bosons, Higgs scalars, sleptons, and squarks. f and f' are distinct members of the same $SU(2)_L$ multiplet.

The decays that result in clean signatures, like leptons, may be important as they are easy to detect. They are more likely if the intermediate sleptons are relatively light. A large mixing in the stau sector can result to larger branching ratios into final states with taus, whose identification efficiency is a lot lower than for electrons and muons.

1.3.4.2 Charginos

Charginos are charged fermions. They are mixtures of charged winos (\tilde{W}^+ , \tilde{W}^-) and higgsinos (\tilde{H}_u^+ , \tilde{H}_d^+) which form mass eigenstates with charge ± 1 .

The chargino mass term of the Lagrangian is:

$$\mathcal{L}_{\tilde{\chi}^\pm \text{mass}} = (\psi^\pm)^T M_{\tilde{\chi}^\pm} \psi^\pm + c.c. \quad (1.101)$$

where $\psi^\pm = (\tilde{W}^+, \tilde{H}_u^+, \tilde{W}^-, \tilde{H}_d^-)$ and

$$M_{\tilde{\chi}^\pm} = \begin{pmatrix} \mathbf{0} & \mathbf{X}^T \\ \mathbf{X} & \mathbf{0} \end{pmatrix} \quad (1.102)$$

$$\mathbf{X} = \begin{pmatrix} M_2 & gv_u \\ gv_d & \mu \end{pmatrix} = \begin{pmatrix} M_2 & \sqrt{2} \sin \beta m_W \\ \sqrt{2} \cos \beta m_W & \mu \end{pmatrix} \quad (1.103)$$

Chargino mass eigenstates are given by:

$$\begin{pmatrix} \tilde{\chi}_1^+ \\ \tilde{\chi}_2^+ \end{pmatrix} = \mathbf{V} \begin{pmatrix} \tilde{W}^+ \\ \tilde{H}_u^+ \end{pmatrix} \quad (1.104)$$

$$\begin{pmatrix} \tilde{\chi}_1^- \\ \tilde{\chi}_2^- \end{pmatrix} = \mathbf{U} \begin{pmatrix} \tilde{W}^- \\ \tilde{H}_d^- \end{pmatrix} \quad (1.105)$$

where the matrices \mathbf{U} and \mathbf{V} are chosen to diagonalise $M_{\tilde{\chi}^\pm}$, and $\tilde{\chi}_1^\pm$ is lighter than $\tilde{\chi}_2^\pm$ by convention.

The charginos have at least a small electroweak gauginos \tilde{W}^\pm component, so they inherit their couplings of weak interaction strength to (scalar, fermion) pairs. Depending on their masses, they can decay to lepton+slepton pair, as well as to quark+squark pair. Charginos also have the gaugino-higgsino-Higgs and $SU(2)_L$ gaugino-gaugino-vector boson couplings. This allows for their decays to lighter neutralino or chargino and a Higgs scalar or an electroweak gauge boson.

$$\tilde{\chi}_i^\pm \rightarrow W^\pm \tilde{\chi}_j^0, Z \tilde{\chi}_1^\pm, h^0 \tilde{\chi}_1^\pm, \ell \tilde{\nu}, \nu \tilde{\ell}, A^0 \tilde{\chi}_1^\pm, H^0 \tilde{\chi}_1^\pm, H^\pm \tilde{\chi}_j^0, q\bar{q}' \quad (1.106)$$

If the neutralinos have a large higgsino component, the decays into third generation quark-squark pairs are significantly enhanced by the top-quark Yukawa coupling.

If all the two-body decays are forbidden, they are forced to decay through three-body decays:

$$\tilde{\chi}_i^\pm \rightarrow ff'\tilde{\chi}_j^0, ff\tilde{\chi}_1^\pm \quad (1.107)$$

through the same off-shell gauge bosons, Higgs scalars, sleptons, and squarks. f and f' are distinct members of the same $SU(2)_L$ multiplet.

As for the neutralinos, the decays of the charginos to leptons leave very clean signatures.

1.3.4.3 Gluino

As the gluino is a colour octet fermion, it cannot mix with any other sparticle. M_3 is the gluino mass parameter. In many models assuming identical SUSY breaking terms for gauginos at the high scale the gluino mass parameter is related to the bino (M_1) and wino (M_2) mass parameters:

$$M_3 = \frac{\alpha_s}{\alpha} \sin^2 \theta_W M_2 = \frac{3}{5} \frac{\alpha_s}{\alpha} \cos^2 \theta_W M_1 \quad (1.108)$$

which leads to the prediction: $M_3 : M_2 : M_1 \approx 6 : 2 : 1$ at the TeV scale. The prejudice that the gluino is much heavier than the neutralinos and charginos comes from here.

The gluino can only decay to squark, either on- or off-shell. The decay $\tilde{g} \rightarrow q\tilde{q}$ is dominant one, if allowed. If stop and/or sbottom are much lighter than other squarks, the decays $\tilde{g} \rightarrow t\tilde{t}_1$ and $\tilde{g} \rightarrow b\tilde{b}_1$ will be prevailing.

If squarks are heavier than the gluino, the decay will go through virtual squarks: $\tilde{g} \rightarrow qq\tilde{\chi}_i^0$ and $\tilde{g} \rightarrow qq'\tilde{\chi}_i^\pm$.

1.3.4.4 Sleptons

Sleptons are the scalar partners of the leptons, as explained previously. They encompass the left and right charged sleptons ($\tilde{e}_L, \tilde{\mu}_L, \tilde{\tau}_L, \tilde{e}_R, \tilde{\mu}_R, \tilde{\tau}_R$) and sneutrinos ($\tilde{\nu}_e, \tilde{\nu}_\mu, \tilde{\nu}_\tau$). Their production cross-sections are not expected to be large at the LHC as they are not strongly interacting. Still, as they are light sparticles in many models, they are maybe the only sparticles that are accessible.

The non-observation of the flavour changing neutral currents leads to the prediction of low mixing angles for most of the sleptons. They are expected to be non-negligible only for third generation slepton - staus. Staus can have very different masses as there are effects coming from the large Yukawa couplings (y_τ) and soft (a_τ) couplings in the RG equations which can lead to large mixing in $(\tilde{\tau}_L, \tilde{\tau}_R)$. Other pairs are largely unmixed: $(\tilde{e}_R, \tilde{\mu}_R)$, $(\tilde{e}_L, \tilde{\mu}_L)$, $(\tilde{\nu}_e, \tilde{\nu}_\mu)$.

Mass matrix for charged sleptons is given, e.g. for stau, by:

$$\begin{pmatrix} m_{\tilde{L}}^2 + m_\tau^2 - m_Z^2 \left(\frac{1}{2} - \sin^2 \theta_W\right) \cos 2\beta & m_\tau (A_\tau - \mu \tan \beta) \\ m_\tau (A_\tau - \mu \tan \beta) & m_{\tilde{E}}^2 + m_\tau^2 - m_Z^2 \sin^2 \theta_W \cos 2\beta \end{pmatrix} \quad (1.109)$$

in the basis $(\tilde{\tau}_L, \tilde{\tau}_R)$. Sneutrinos are massive sparticles:

$$m_{\tilde{\nu}}^2 = m_{\tilde{L}}^2 + \frac{1}{2} m_Z^2 \cos 2\beta \quad (1.110)$$

These masses are given in the three generation notation: if there are flavour mixing states these relations are generalized to 6×6 and 3×3 matrices.

The left and right mixing is proportional to the slepton masses, and therefore it is considered negligible for selectrons and smuons, but possibly significant for staus, especially if $\tan \beta$ is large. This mixing is lowering the mass for the lighter stau. In many models, staus are the lightest sleptons, and the lighter stau is often the lightest sfermion.

As the neutralinos and charginos have a gaugino component, the sleptons can decay into them by following the two-body decays:

$$\tilde{\ell} \rightarrow \ell\tilde{\chi}_i^0, \tilde{\ell} \rightarrow \nu\tilde{\chi}_i^\pm, \tilde{\nu} \rightarrow \nu\tilde{\chi}_i^0, \tilde{\nu} \rightarrow \ell\tilde{\chi}_i^\pm \quad (1.111)$$

If $\tilde{\chi}_1^0$ is bino-like, the right-handed sleptons decay directly ($\tilde{\ell}_R \rightarrow \ell\tilde{\chi}_1^0$), as they do not have a coupling to the $SU(2)_L$ gauginos. The left-handed sleptons cascade decay, through the $\tilde{\chi}_2^0$ or $\tilde{\chi}_1^\pm$ (if $\tilde{\chi}_2^0$ or $\tilde{\chi}_1^\pm$ are mostly wino). This is the consequence of the fact that slepton-lepton-wino interactions are proportional to $SU(2)_L$ gauge coupling g , while the slepton-lepton-bino interactions are proportional to the $U(1)_Y$ coupling g' which is much smaller.

1.3.4.5 Squarks

Squarks are the scalar superpartners of the quarks. The third generation squarks mass matrices are given by:

$$\begin{pmatrix} m_{\tilde{Q}}^2 + m_t^2 + m_Z^2 \left(\frac{1}{2} - \frac{2}{3} \sin^2 \theta_W\right) \cos 2\beta & m_t (A_t - \mu \cot \beta) \\ m_t (A_t - \mu \cot \beta) & m_{\tilde{D}}^2 + m_t^2 + m_Z^2 \frac{2}{3} \sin^2 \theta_W \cos 2\beta \end{pmatrix} \quad (1.112)$$

in the basis $(\tilde{t}_L, \tilde{t}_R)$ and for the bottom squarks:

$$\begin{pmatrix} m_{\tilde{Q}}^2 + m_b^2 - m_Z^2 \left(\frac{1}{2} - \frac{1}{3} \sin^2 \theta_W\right) \cos 2\beta & m_b (A_b - \mu \tan \beta) \\ m_b (A_b - \mu \tan \beta) & m_{\tilde{D}}^2 + m_b^2 - m_Z^2 \frac{1}{3} \sin^2 \theta_W \cos 2\beta \end{pmatrix} \quad (1.113)$$

in the basis $(\tilde{b}_L, \tilde{b}_R)$. The mass matrices for the first two generations are obtained after trivial substitution of quark masses and soft terms. Large mixing is expected in the stop sector, and maybe in the sbottom sector if $\tan \beta$ is large. Because of these mixings and large contributions from the Yukawa couplings in the RGE, third generation squarks are the lightest squarks in many models.

The dominant decay is always $\tilde{q} \rightarrow q\tilde{g}$, if it is kinematically allowed, as it has QCD strength. If it is forbidden, the squark decays to quark and neutralino or chargino.

$$\tilde{q} \rightarrow q\tilde{\chi}_i^0, \tilde{q} \rightarrow q'\tilde{\chi}_i^\pm \quad (1.114)$$

The direct decay to the lightest neutralino is always favoured, and if the squark is right-handed it can dominate as the lightest neutralino is often mostly bino. The left-handed squarks have preference to decay to $\tilde{\chi}_2^0$ or $\tilde{\chi}_1^\pm$, as the squark-quark-wino couplings are much bigger than the squark-quark-bino couplings. As only stops and sbottoms have significant Yukawa couplings, their decays to higgsino-like charginos and neutralinos can be important.

The squark decays can be very long decay chains (cascade decays) as the neutralinos and charginos will decay until the final $\tilde{\chi}_1^0$.

If the $\tilde{t}_1 \rightarrow t\tilde{g}$ and $\tilde{t}_1 \rightarrow t\tilde{\chi}_1^0$ are both kinematically forbidden, the lighter stop decays to chargino ($\tilde{t}_1 \rightarrow b\tilde{\chi}_1^\pm$). If this decay is also not allowed, than it decays to $\tilde{t}_1 \rightarrow c\tilde{\chi}_1^0$ and $\tilde{t}_1 \rightarrow bff'\tilde{\chi}_1^0$.

1.3.4.6 Sfermion mass splittings due to electroweak symmetry breaking

Each squark and slepton Φ will get a contribution Δ_Φ to its squared mass, coming from the $SU(2)_L$ and $U(1)_Y$ D-term quartic interactions. They are model-independent for a given value of $\tan \beta$:

$$\Delta_\Phi = \frac{1}{2}(T_{3\Phi}g^2 - Y_\Phi g'^2)(v_d^2 - v_u^2) = (T_{3\Phi} - Q_\Phi \sin^2 \theta_W) \cos(2\beta)m_Z^2 \quad (1.115)$$

where $T_{3\Phi}$, Y_Φ and Q_Φ are the third component of weak isospin, the weak hypercharge, and the electric charge of the left-handed chiral supermultiplet to which Φ belongs. For example:

$$\Delta_{\tilde{u}_L} = \left(\frac{1}{2} - \frac{2}{3} \sin^2 \theta_W\right) \cos(2\beta)m_Z^2 \quad (1.116)$$

$$\Delta_{\tilde{d}_L} = \left(-\frac{1}{2} + \frac{1}{3} \sin^2 \theta_W\right) \cos(2\beta)m_Z^2 \quad (1.117)$$

$$\Delta_{\tilde{u}_R} = \left(\frac{2}{3} \sin^2 \theta_W\right) \cos(2\beta)m_Z^2 \quad (1.118)$$

These D-term splittings are typically smaller than SUSY contributions but should not be neglected. They split apart the components of the $SU(2)_L$ -doublet sleptons and squarks. The mass splittings for the left-handed squarks and sleptons are governed by model-independent sum rules:

$$m_{\tilde{e}_L}^2 - m_{\tilde{\nu}_e}^2 = m_{\tilde{d}_L}^2 - m_{\tilde{u}_L}^2 = g^2(v_u^2 - v_d^2)/2 = -\cos(2\beta)m_W^2 \quad (1.119)$$

If $\tan \beta > 1$, it follows that $m_{\tilde{e}_L} > m_{\tilde{\nu}_e}$ and $m_{\tilde{d}_L} > m_{\tilde{u}_L}$ with the magnitude of splittings constrained by electroweak symmetry breaking.

1.3.4.7 SUSY Higgs bosons

In the MSSM, the electroweak symmetry breaking is more complicated than in the SM, because there are two Higgs doublets. After the symmetry is broken there are five remaining degrees of freedom (compared to three that are left in the SM), that lead to five massive physical Higgs states: two neutral CP-even (h^0 and H^0), one neutral (A^0) and two charged Higgs bosons (H^+ and H^-). Thus more parameters than in the SM are needed to describe it: $\tan\beta \equiv v_u/v_d$ the ratio of the vacuum expectation values of H_u and H_d , and α the CP-even Higgs mixing angle. So the Higgs sector can be described either with $(\mu, m_{H_u}^2, H_{H_d}^2, b)$ or with $(\mu, m_A, \tan\beta, v)$.

In terms of these parameters, physical Higgs bosons masses are given by:

$$m_{H,h}^2 = \frac{m_A^2 + m_Z^2 \pm \sqrt{(m_A^2 + m_Z^2)^2 - 4m_A^2 M_Z^2 \cos(2\beta)}}{2} \quad (1.120a)$$

$$m_{H^\pm}^2 = m_A^2 + m_W^2 \quad (1.120b)$$

The equation 1.120 implies that the lightest Higgs boson is bounded from above: $m_h < m_Z |\cos 2\beta|$, but these results are valid up to the tree level. This constraint is lifted by the radiative corrections (particularly coming from the stops, depending on their masses and mixing):

$$\Delta m_h^2 \sim \frac{1}{\sin^2 \beta} \frac{3g^2 m_t^4}{8\pi^2 m_W^2} \log \frac{m_t^2}{m_t^2} \quad (1.121)$$

increasing the Higgs mass up to an upper limit of $m_h \leq 135$ GeV if SUSY particles entering the loop have masses lower than ~ 1 TeV.

1.4 SUSY models

As the full MSSM has too many free parameters to be fully explored, some assumptions are needed to reduce the parameter space. There are two approaches that can be considered: a top-down approach when the parameter values are imposed at the high scale and are evolved using the renormalisation group equations to low scales, and a low scale approach where the masses of the sparticles or SUSY breaking term are imposed at low scale.

1.4.1 High scale models

In this class of theories the boundary conditions are imposed at the high scale. As the phenomenology depends a lot on the way SUSY is broken, they are usually explored depending on the nature of the SUSY breaking messenger. In these models the number of parameters is reduced by requiring that some of them are related.

1.4.1.1 The Minimal Super GRAvity mSUGRA

In the supergravity models, the SUSY breaking mechanism is mediated by gravity. Specifically, in the minimal SUGRA model, there are relations between the SUSY breaking parameters at the high scale, reducing their number to five: a universal gaugino mass $m_{1/2}$, a universal scalar mass (slepton, squark, and Higgs masses) m_0 , and a universal trilinear coupling A_0 , all defined at the high scale (typically few 10^{16} GeV), $\tan\beta$, and the sign of μ . $\tan\beta$ is the ratio of the vacuum expectation values of the two Higgs doublets defined at the electroweak scale, and μ is the Higgsino mass parameter. The absolute value of μ is fixed through the requirement of the electroweak symmetry-breaking at the appropriate scale. These parameters are evolved using the renormalisation group equations to get their values at low energy. In most of the mSUGRA parameter space, the LSP is the lightest neutralino, $\tilde{\chi}_1^0$, which is bino.

As explained in Section 1.3.4.3, the gaugino masses are expected to follow these relations: $m_{\tilde{g}} : m_{\tilde{W}} : m_{\tilde{B}} = 6 : 2 : 1$.

1.4.1.2 GMSB

In the gauge-mediated SUSY breaking (GMSB) models SUSY breaking is transmitted to the MSSM via gauge bosons. It results that the gravitino $\tilde{g}_{3/2}$ is a fermion with a mass so small that it can be neglected when considering event kinematics. It is the LSP and has very small couplings to other particles. The lightest neutralino, if it is the NLSP, decays to a gravitino and a photon possibly with a very long lifetime. In the final state there are photons which can be isolated and energetic, as well as all the other particles that are there in other scenarios, as the production and decays are the same. If the $\tilde{\chi}_1^0$ lifetime is so long that it decays outside of the detector, the final state is the same as in the $\tilde{\chi}_1^0$ LSP scenarios. There are some models in which the right-sleptons are lighter than the lightest neutralino, and they decay to a lepton and a gravitino. Depending on the model parameters, this decay might happen outside of the detector and lead to highly ionising particle tracks.

1.4.2 pMSSM

The MSSM has 105 free parameters, but it is understood that not all of them have the same impact on the phenomenology. The phenomenological MSSM (pMSSM) thus explores the possibility to describe large part of the MSSM phenomenology by imposing some assumptions on its parameters and the type of the LSP. Usually the number of considered parameters is 19, and in this thesis this space will be further described in Chapter 5. Here it is important to note that the LSP is assumed to be the lightest neutralino.

As explained before (Section 1.3.4.1) the neutralino can be mostly bino, wino and higgsino and this has big impact on the phenomenology. When neutralino is wino and higgsino-like it is almost always accompanied by a chargino nearly degenerate in mass.

1.4.3 Simplified models

Simplified models are developed as an approach to characterise SUSY phenomenology. They rely on only few sparticles and possible decay chains (others are decoupled). They depend only on sparticles masses, their branching ratios and production cross-sections. They are developed to be easy to constrain and combine. They try to explore in a model independent way a specific feature common to many different theories.

The limits are placed on the cross-section times branching ratios as a function of new particle masses, separately for each event topology. This allows to remove all the assumptions on the relative couplings at each vertex.

The simplified models important for this thesis are the ones of the gluino and squark pair production. In the case of the gluino pair production the subsequent gluino decay may lead to a pair of quarks and a neutralino. The Feynman graph representing this production and subsequent decay is shown in Figure 1.2a. Thus this model is characterised by the masses of the gluino and the neutralino. Another simplified model of the gluino pair production is a bit more complicated: the gluino decay goes through a quark and a virtual squark decaying to a quark and a chargino that give a W -boson and neutralino, as is presented in Figure 1.2b. This simplified model is characterised by the gluino, chargino and neutralino masses.

When one assumes a squark pair production, the simplest decay is to quark and a neutralino, as shown in Figure 1.2c. A bit more freedom is given in the simplified model presented in

Figure 1.2d, where the squark decays to quark and chargino that subsequently decays to W -boson and a neutralino. The parameters of this simplified model are the squark, chargino and neutralino masses.

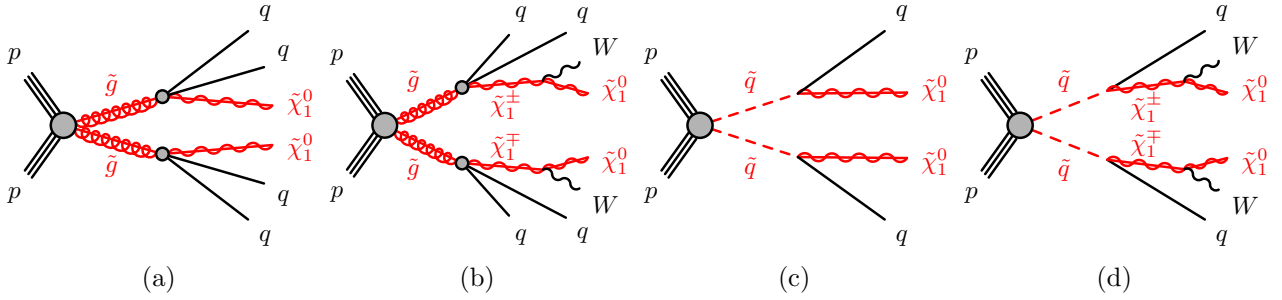


Figure 1.2: Simplified models of: (a) gluino pair production followed by the direct decay to pair of quarks and a neutralino, (b) gluino pair production followed by the gluino decay to a quark and a virtual squark decaying to a quark and a chargino that give a W -boson and neutralino, (c) squark pair production with the squark decaying directly to quark and a neutralino and (d) squark pair production where the squark decays to quark and chargino that subsequently decays to W -boson and a neutralino.

Although one of the possible motivation of the simplified models can be that they are similar to the split SUSY models, they are far too simplified. The simplified models are not realised in nature, but one can hope that by combining interpretation in several of them can constrain a fully specified model.

1.5 Dark matter

First a short introduction to the relation of the supersymmetry and the cold dark matter energy density is given. There are several dark matter (DM) candidates (axions, weakly interacting massive particles, . . .), but here the emphasis is put on the SUSY-DM candidate, so the focus is on the weakly interacting massive particles as thermal relics.

1.5.1 Cold dark matter energy density

The goal of this Section is not to describe in details the thermal history of the Universe: this has been treated in details in the literature and can be found, for instance, in [32, 33], but rather to give hints toward the relation between the annihilation dark matter cross-section that can be computed within a given SUSY model and the cold dark matter energy density extracted from cosmological fits.

In the very early Universe all particles are in thermal equilibrium. At one point, since the universe cools down and expands, the interaction rate becomes small compared to the expansion. This is the moment when the particles "freeze out": the unstable particles disappear from the Universe, and the stable particles numbers become constant. Their thermal relic density today is measured by cosmological probes within the Λ CDM scenario [25]. This evolution is described by the Boltzman equation, and using n as the number density of dark matter particles (hereafter denoted χ), it reads:

$$\frac{dn}{dt} = -3Hn - \langle \sigma v \rangle (n^2 - n_{eq}^2), \quad (1.122)$$

H being the Hubble constant, $\langle \sigma v \rangle$ the thermally averaged annihilation cross-section and n_{eq} is the value of n in thermal equilibrium. On the right hand side of the equation, the first

part is due to the expansion of the Universe, while in the second member of the equation, n^2 is linked to annihilation processes ($\chi\chi \rightarrow f\bar{f}$) and n_{eq}^2 corresponds to production processes ($f\bar{f} \rightarrow \chi\chi$).

Using the appropriate changes of variable, translating the number density in an energy density and the time in temperature, the resolution of Eq. 1.122 leads to [32]:

$$\Omega_{cdm} \sim \frac{\Omega_\gamma}{M_{pl}^* \langle \sigma v \rangle T_0} \quad (1.123)$$

$$\sim \frac{10^{-10} \text{ GeV}^2}{\langle \sigma v \rangle}, \quad (1.124)$$

where T_0 corresponds to the temperature of the Cosmic Microwave Background which has been measured by the COBE experiment and is equal to 2.725K. With $\langle \sigma v \rangle \sim \alpha^2/m_{weak}^2 \sim 10^{-9} \text{ GeV}^{-2}$ one gets: $\Omega_{cdm} h^2 \sim 0.1$ which is close to the value measured by Planck [25].

1.5.2 SUSY dark matter candidates

There are many possible dark matter candidates [34]. They have to be non-baryonic, and stable. The SUSY-DM candidate is the LSP (electrically and colour neutral). There are several sparticles that satisfy these conditions in the MSSM: sneutrino, gravitino and neutralino.

The left handed sneutrino in the MSSM is not a viable dark matter candidate. Given its sizable coupling to the Z boson, sneutrinos either annihilate too rapidly, resulting in a very small relic abundance or give rise to a large detection cross-section and are excluded by direct DM searches. The possibility that is still allowed is for example the addition of the right-handed sneutrinos to the MSSM [35].

The gravitino is the first proposed dark matter candidate [36]. If the R -parity is conserved, the gravitino LSP is stable.

In the following only the possibility of the neutralino being the LSP is explored in details.

1.5.3 Neutralino annihilation channels

The disappearance of neutralinos in the early Universe is governed by direct annihilation, potentially resonant, and possibly co-annihilation with another SUSY particles with similar mass (and so number density).

The SM-like Higgs funnel (h -funnel) It is the region where the mass of the neutralino is about half the mass of the SM-like Higgs boson, so it proceeds through resonant s -channel annihilation. The neutralino mass has to be finely tuned to half the SM-like Higgs mass, as its theoretical width (Γ_h) is $\sim 5 \text{ MeV}$.

The heavy Higgs funnels (A/H -funnels) It is also required that the neutralino mass be half of the A/H -mass, but those are unknown for now. This process is shown in Figure 1.3a.

Stau co-annihilation In this region the neutralino has a mass that is few percent below the $\tilde{\tau}$ mass, so the co-annihilation proceeds through the s -channel, as shown in Figure 1.3b.

Neutralino-chargino co-annihilation is a similar process to $\tilde{\tau}$ co-annihilation but it occurs naturally for wino nad higgsino LSP.

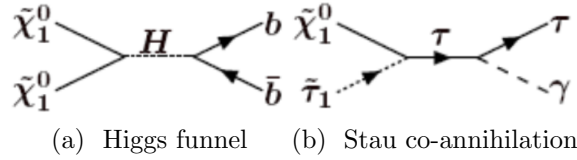


Figure 1.3: Annihilation and co-annihilation processes: (a) heavy Higgs funnel region, (b) Stau-coannihilation region [37]

1.6 Simulation of physics processes at the LHC

This Section briefly describes the theoretical framework for the calculation of physics processes of the proton-proton collisions at the LHC (Section 2.1) and the event generators used for the work presented in this thesis.

1.6.1 Production processes

The proton consists of three valence quarks (uud), gluons and sea quarks, which are quantum fluctuations. Those constituents of the proton are called partons. Factorising the long and short distance scales, the cross-section of particle X production in pp collisions is given by:

$$\sigma_{pp \rightarrow X} = \sum_{ij} \int_0^1 dx_1 \int_0^1 dx_2 \hat{\sigma}_{ij \rightarrow X} f_i(x_1, \mu_F^2) f_j(x_2, \mu_F^2) \quad (1.125)$$

where f_i are the parton distribution functions (PDF), x_1 and x_2 momentum fractions of the partons, and $\hat{\sigma}$ the cross-section of the hard parton-parton event. μ_F is the factorisation scale. The hard cross-section $\hat{\sigma}_{ij \rightarrow X}$ is a function of several parameters:

$$\hat{\sigma}_{ij \rightarrow X} = \hat{\sigma}_{ij \rightarrow X} \left(x_1 p_1, x_2 p_2, \alpha_s(\mu_R^2), Q^2, \mu_F^2, \mu_R^2, \{m\} \right) \quad (1.126)$$

where Q is the energy scale of the interaction, $x_i p_i$ the momentum carried by the particles, μ_R the renormalisation scale and $\{m\}$ the set of masses of the particles involved in the process. The factorisation and renormalisation scales (μ_F and μ_R) are usually considered to be equal to the average mass of the produced sparticles.

The PDF $f_i(x, \mu_F^2)$ is the probability of finding a quark of type i with the momentum fraction x , considered at the factorisation scale μ_F . The parton distribution f_i for gluon and different quarks are presented in Figure 1.4, for $Q^2 = 10 \text{ GeV}^2$ (on the left) and $Q^2 = 10^4 \text{ GeV}^2$ (on the right) [38].

The cross-section of a process is the probability of a given process to happen, and is proportional to the scattering amplitudes which in perturbative theories are calculated using Feynman diagrams, by summing a power series with infinite number of terms. Thus the calculation is performed to some finite order in the perturbative constant. In the case considered here, this constant is α_s .

NLO corrections to the cross-section are accounted for by calculating a k -factor, the ratio between the LO and NLO processes, which can depend on the kinematics of the process. Next-to-leading-logarithmic (NLL) resummation techniques are also employed in the calculation of the cross-sections.

1.6.2 Production of supersymmetric particles at the LHC

The dominant production channels of sparticles at the LHC are squark-squark, squark-gluino and gluino-gluino pair production (strong production processes) and they are presented in Figure 1.5. There are also other production channels like so called mixed production (the associated

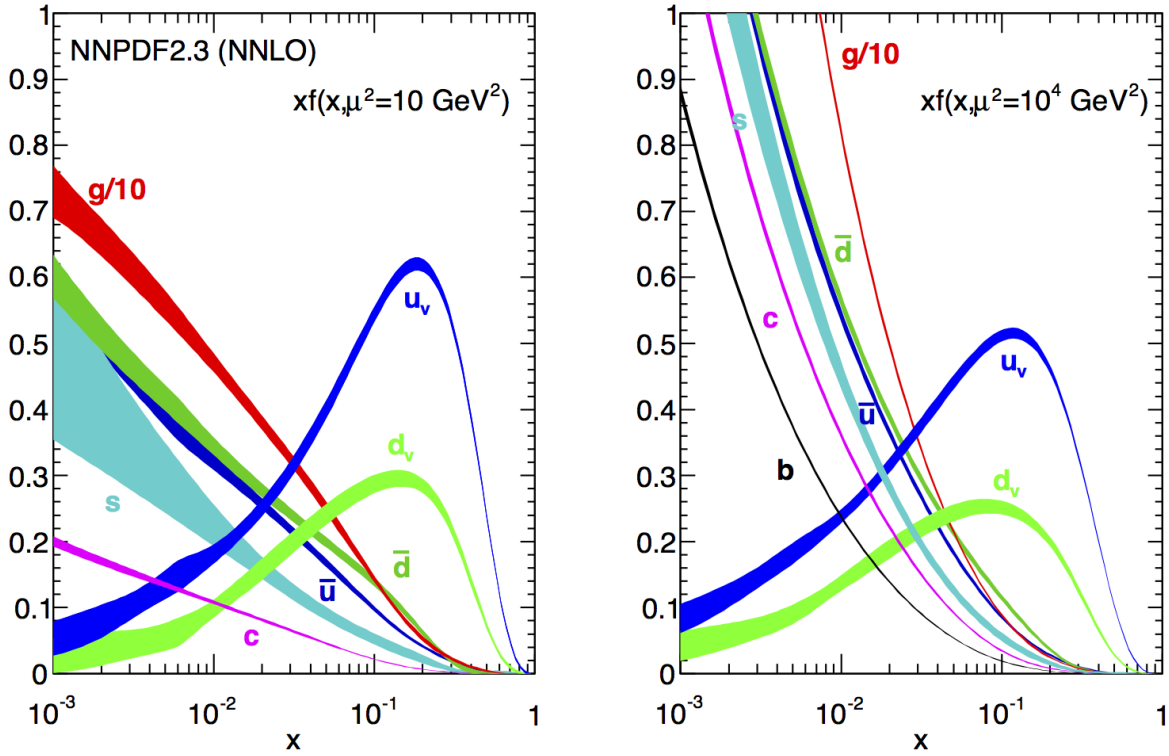


Figure 1.4: The bands are x times the unpolarised parton distribution $f_i(x)$, where f_i represent quarks and gluon, obtained in NNLO NNPDF2.3 global analysis [38].

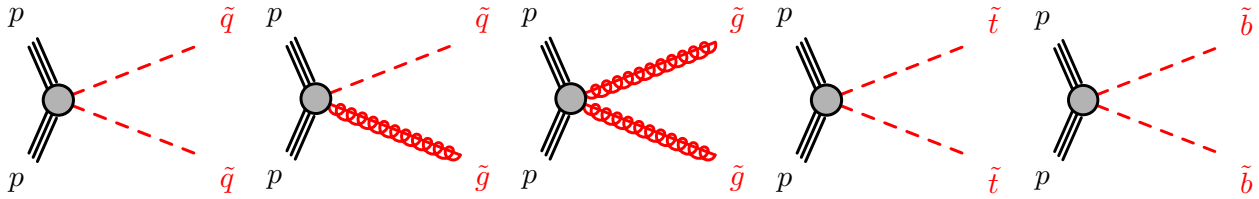


Figure 1.5: Strong production of sparticles at pp colliders.

production of neutralino-squark, chargino-squark, neutralino-gluino, and chargino-gluino) and electroweak production (neutralino-neutralino, neutralino-chargino, chargino-chargino, charged slepton-pair production, sneutrino-pair production, and charged slepton-sneutrino pair production as shown in Figures 1.6 and 1.7). Sometimes the last three production modes are considered separately as the acceptance for slepton pairs can be much higher than for the electroweakinos.

In Figure 1.8 the production cross-section are shown for several types of production, as calculated with `Prospino` [39, 40, 41, 42, 43] at NLO. In Figure 1.8a the production cross-sections as a function of the sparticle mass are presented for pp collisions at a centre-of-mass energy of 8 TeV (as the search presented in this thesis was performed on data from the 8 TeV collisions), while in Figure 1.8b they are shown for pp collisions at a centre-of-mass energy of 13 TeV (as the LHC resumed its operation this year with this energy). The largest cross-section is seen for the strong production of sparticles. The squarks of different chiralities (\tilde{q}_L and \tilde{q}_R) are considered as being equal. Also the squarks from the three generations are treated together, except for the top squark because of the large mixing effects that lead to large differences between masses of \tilde{t}_1 and \tilde{t}_2 . The squarks and gluinos are expected to be produced through the interactions of gluons or valence quarks, as the squarks and gluinos are supposed to be of high mass, and require the interactions of partons that carry a large fraction of the momentum.

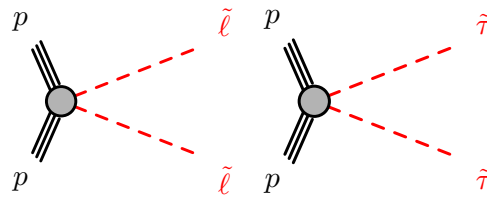
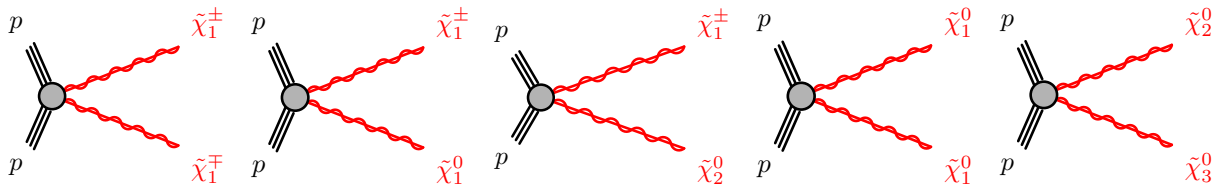
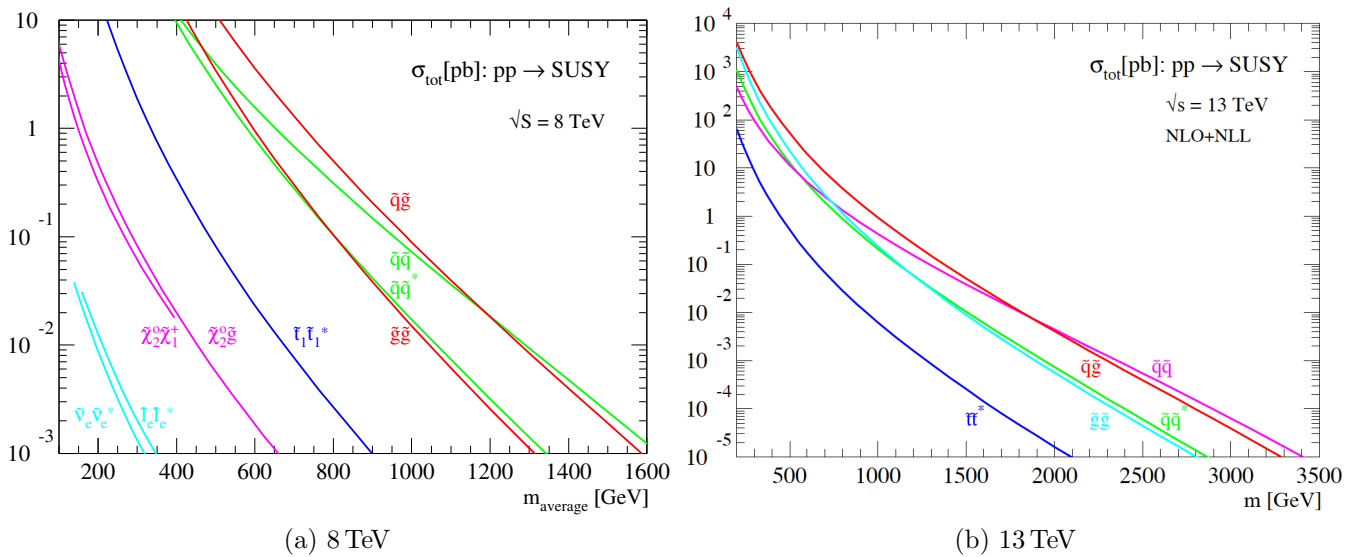
Figure 1.6: Electroweak production of sleptons at pp colliders.Figure 1.7: Electroweak production of electroweakinos at pp colliders.

Figure 1.8: Production cross-section of sparticles at the LHC at 8 TeV and 13 TeV [39, 40, 41, 42, 43].

1.6.3 Event simulation

The generation of events starts with the initial pp collision simulation. Here the hard scatter between the proton constituents is generated. The initial partons are given four-momentum according to the PDF. The matrix elements belonging to the hard process are calculated perturbatively. Each generated event is assigned a weight which corresponds to the differential cross-section, obtained from the matrix element, PDFs and kinematics.

The next step is the parton showering, which consists of the simulation of the gluon radiation from the initial partons (ISR) and from the produced particles (FSR). It can also proceed further to even more gluon radiation and to the formation of the quark-anti-quark pairs, which is also the part of parton shower. Low energy and collinear radiation can not be calculated perturbatively. The ISR is important in the production of heavy and strongly interacting particles: it can give transverse boost to the heavy particle system, thus affecting the event kinematics, and/ or produce additional jets besides the jets originating from the decay of the heavy particles.

After that a simulation of the hadronisation is performed - in which hadrons are formed from the partons. The models of the hadronisation and parton shower have been tuned on data in order to reproduce the observed properties of QCD processes (for example the set of tuned parameters (tunes) is given in Ref. [44]).

The simulated events obtained after all the explained steps of the hard scattering and the parton shower can lead to some double counting when combining multi parton processes. The procedure which solves this issue is known as the matching scheme. All the matching schemes separate the phase space into hard and large-angle emissions (handled by the matrix element) and soft and collinear emission (handled by the parton shower).

To simulate multi parton events, Matrix Element (ME) generators (like `MadGraph`) are used. They generate the full tree-level amplitudes for the heavy particle production plus additional hard partons. But their results do not describe well the events when partons become soft or collinear. In this regime non perturbative QCD mode like Parton Shower (PS) generators (for example `Pythia`) are more appropriate. It describes well the limit of soft and collinear emissions, but breaks down far away from it, i.e for the production of hard and widely separated QCD radiation jets. For a good description of both parts of the phase space, the results of the two generators have to be combined. In that process it is important to eliminate double counting or gaps between different parton multiplicities. The result of the procedure should be smooth distributions. At the end fully inclusive event samples should be generated which give good prediction of physical observables. Therefore there are several schemes - called matching schemes - that are studied in order to ensure a smooth merging of the two generator steps (PS and ME) and the interpolation between the two regimes.

The uncertainty of the event generation comes from the uncertainty of the PDF and is driven by the uncertainty on the distribution on the incoming gluons. To evaluate the theoretical uncertainty, different sets of PDFs are usually considered and compared.

1.6.4 Generators

Different generators have different strategy in event simulation. Some of them, like `SHERPA` [45], `Herwig` [46, 47], and `Pythia` [48], calculate the matrix elements and perform showering themselves. But the latter two are limited as they only take into account $2 \rightarrow 1$ and $2 \rightarrow 2$ processes. Others, like `MadGraph` [49] and `ALPGEN` [50] calculate $2 \rightarrow n$ processes, but rely to other generators to perform showering. There are also generators that calculate matrix elements at NLO with both real and virtual corrections, like `MC@NLO` [51, 52] and `POWHEG` [53, 54, 55], which also have to be interfaced to other generators to perform the showering.

Pythia [48] is a LO general purpose generator, which is able to simulate the hard scattering for the processes with two incoming and one or two outgoing partons ($2 \rightarrow 2$). It is also performing the parton showering and the hadronisation of these events, using string fragmentation. It is mainly used for the simulation of the multi-jet processes, and is often interfaced to matrix element generator to handle the parton showering.

Herwig [46, 47] is also a LO general purpose generator. The difference with respect to **Pythia** is in the method used for the hadronisation - this time it is cluster fragmentation. Also it is often interfaced to matrix element generation to perform the parton shower. **Herwig** [46, 47] is a Fortran generator, with a new version **Herwig++** written in C++. It is interfaced with **Jimmy** [56] for the simulation of the underlying event.

SHERPA [45] is a LO multi parton matrix element generator, and it can handle the parton shower by itself. It is mostly used for the simulation of the vector boson plus jets events.

Alpgen [50] is a LO matrix element generator. It can generate up to six additional partons in the matrix element, which makes it suitable for the generation of the vector boson plus jets events. It doesn't handle the parton showering by itself, so for this task it must be interfaced to **Pythia** [48] or **Herwig** [46, 47].

MC@NLO [51, 52] is a NLO matrix element generator. For the parton showering and hadronisation it must be interfaced to another generator (usually **Herwig** [46, 47]). It is mainly used for the simulation of the $t\bar{t}$ production.

Powheg [53, 54, 55] is also a NLO matrix element generator, which must be interfaced to another generator for the parton showering and hadronisation, usually **Pythia** [48]. Like **MC@NLO** [51, 52] it is used for the $t\bar{t}$ production simulation.

MadGraph [49] a general purpose LO matrix element generator.

AcerMC [57] a LO generator dedicated to the SM processes at the LHC.

Jimmy [56] a generator dedicated to the simulation of the underlying event.

1.7 Conclusion

In this Chapter, supersymmetric extensions of the Standard Model have been presented with a particular emphasis on the Minimal Supersymmetric extension of the Standard Model (MSSM) which is the motivation and framework of interpretation of the work in this thesis. The phenomenological aspects of the MSSM in terms of SUSY particle production at the LHC and dark matter relic density were presented.

Chapter 2

LHC and ATLAS

The main motivations to build the Large Hadron Collider were to answer fundamental questions such as "is there an elementary Higgs boson", and to explore the energy range in the TeV range to explain physics beyond the standard model (BSM). Both the Higgs and BSM particles have been searched for but not found at LEP and at the Tevatron, and going to higher energies was needed. The Large Hadron Collider hosts, among others, the multipurpose ATLAS detector.

This thesis work is performed using the 8 TeV data collected by the ATLAS detector, and its description and performance are necessary for the understanding of the search detailed in the next Chapters. An emphasis is put on the performance of the accelerator and the detector during 2012. The description of the reconstruction and identification of objects follows the procedures developed for the 8 TeV data taking period.

This Chapter first briefly describes the Large Hadron Collider (Section 2.1), and then details the ATLAS detector, and its subdetectors (Section 2.2). The reconstruction and identification of objects is discussed in (Section 2.3).

2.1 Large Hadron Collider

The Large Hadron Collider (LHC) [58] is the world's largest and highest energy circular proton-proton (pp) collider, with a nominal centre-of-mass energy (\sqrt{s}) of 14 TeV, as it is designed to collide two proton beams with energy of 7 TeV each. Also, the heavy ions are part of the LHC program: it can perform lead-lead, as well as the proton-lead collisions. In the following, only the proton program is discussed, as this thesis work is performed with the data collected from the pp collisions.

The designed luminosity of the LHC is $10^{34}\text{cm}^2\text{s}^{-1}$, with the beam crossings separated by 25 ns. The LHC is hosted by the CERN in the 26.7 km tunnel that previously accommodated the Large Electron Positron (LEP) collider. It is situated on the border between France and Switzerland, near Geneva, and lies below the surface (depth varies between 45 m and 170 m). The construction of the LHC started in 1998, and was finished in 2008.

2.1.1 Acceleration of particles

The LHC is the last in line of several machines that are used to accelerate the proton beam, as it is shown in Figure 2.1. Protons are pre-accelerated at several stages before being injected to the LHC. The protons originate from hydrogen atoms that are stripped from their electrons. They are accelerated in the LINAC 2, where their energy reaches 50 MeV. First bunches are formed in the proton booster, and further accelerated to 1.4 GeV. They are then transferred to the Proton Synchrotron (PS) (energy is increased to 25 GeV), and later to the Super Proton

CERN's Accelerator Complex

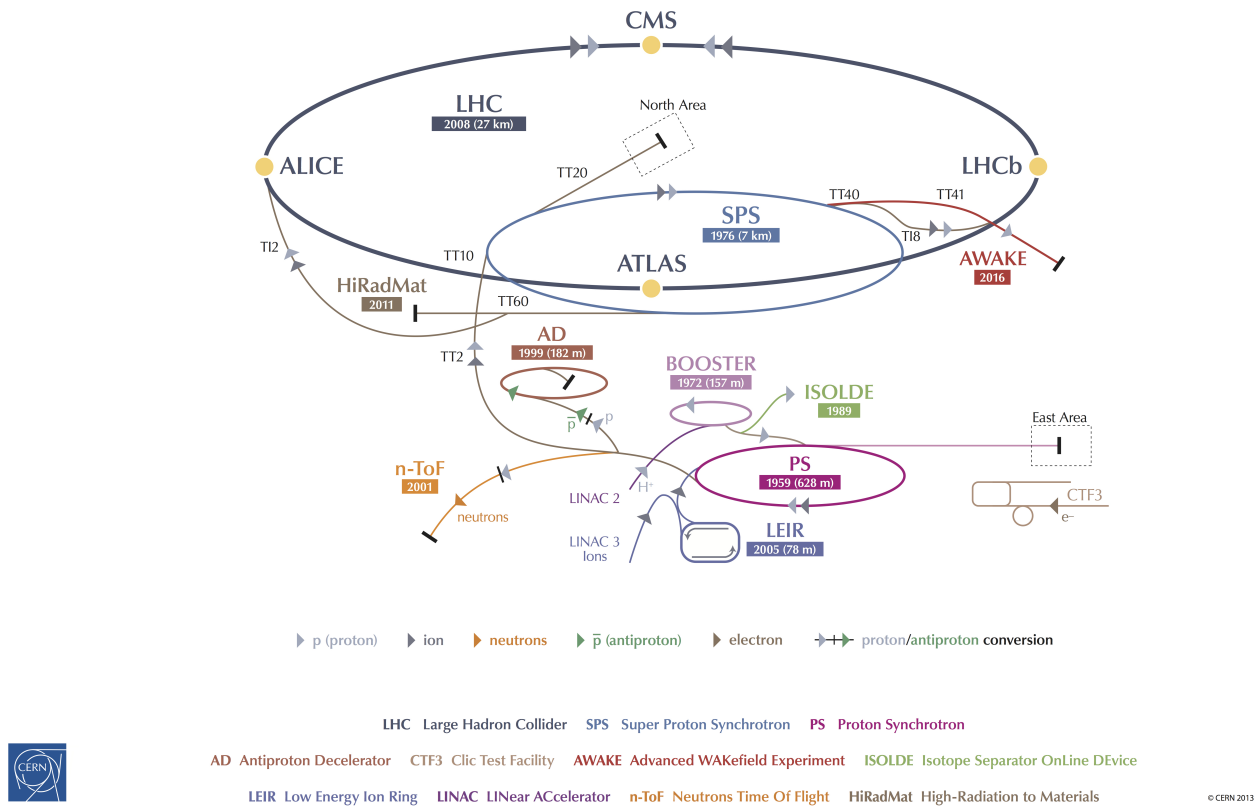


Figure 2.1: CERN's accelerator complex.

Synchrotron (SPS) where their energy reaches 450 GeV. Finally they are injected in the LHC using two different tunnels, and ramped up to their desired energy: 4 TeV in 2012.

The beam of particles is grouped into packets called bunches. Each bunch contains around 10^{11} protons. The length of the bunch is 7.55 cm, and its transverse size is $16.7 \mu\text{m}^2$ at the interaction point. The LHC has been designed to circulate up to 2800 bunches per beam at 25 ns. The beams are accelerated using Radio Frequency cavities, placed in four cryomodules.

The bunches are led by the superconducting magnets along the LHC beam pipe. There are 9593 magnets that are responsible for controlling the proton trajectory and their focus: out of them 1232 are superconductive dipoles producing 8.33 T for 7 TeV beams. Those dipoles operate at the 1.9 K, and the temperature is obtained by embedding them in superfluid helium. The magnet system of the LHC also includes around 390 quadrupoles that are responsible for the beam transverse size. Two separate beam pipes, separated by 194 mm, and two dipole systems are located in the same iron yoke.

The first collisions at the LHC occurred in 2008. It resumed its program in 2010 after the incident that shortly followed. From 2010 to end 2012 (Run 1 of the LHC), it was colliding proton beams first at a 7 TeV and later a 8 TeV center-of-mass energy. From 2013 to 2015 there was a long shut down, and now the operation resumed at a 13 TeV centre-of-mass energy (Run 2 of the LHC).

There are six experiments that are collecting data from the LHC collisions: two general purpose experiments ATLAS [59] and CMS [60], and more specialised experiments like LHCb [61] that is dedicated to B-physics studies, ALICE [62] for the research of the quark-gluon plasma, TOTEM [63], designed for the studies of the elastic scattering and the measurement of the total pp cross-section and LHCf [64], dedicated to the forward production of neutral particles.

2.1.2 Luminosity

The produced number of interaction N , depends on the process considered and the machine instantaneous luminosity \mathcal{L} :

$$N = \mathcal{L} \times \sigma \quad (2.1)$$

where σ is the cross section of the production process. The integrated luminosity L is the integral of the instantaneous luminosity over time: $L = \int \mathcal{L} dt$. If one assumes that the beam distribution is Gaussian:

$$L = \frac{N_{b_1} N_{b_2} n_{b_1} n_{b_2} f \gamma}{4\pi\epsilon\beta^*} F \quad (2.2)$$

where N_b is the number of particles per bunch, n_b is the number of bunches per beam, f is the revolution frequency of the machine, γ is the relativistic factor, ϵ is the normalised transverse emittance and β^* is the beta function at the interaction point. As the particles are not colliding head-on, a factor F , which depends on the crossing angle θ_c between both beams ($\theta_c = 0.85 \mu\text{rad}$ for the LHC), is added.

2.1.3 LHC operation

During the first two years of operation, in 2010 and 2011, the LHC operated at a center-of-mass energy of 7 TeV. In 2012, the energy was increased to 8 TeV. After the long shut down the LHC restarted this year (2015) at an energy of 13 TeV, and will increase to 14 TeV. During Run 1 there was an increase in the number of protons per bunch, as well as the number of bunches injected in the LHC. Also the bunch transverse size was decreased. All of it resulted in the instantaneous luminosity increased from $2.07 \times 10^{32} \text{cm}^{-2} \text{s}^{-1}$ in 2010, to $7.73 \times 10^{33} \text{cm}^{-2} \text{s}^{-1}$ in 2012 (as summarised in Table 2.1 and shown in Figure 2.3b). The LHC operated with a bunch spacing of 75 ns in 2010 and part of 2011, later increasing to 50 ns. The number of bunch crossings increased from 113 in 2010 to 1377 in 2012.

Each proton fill of the LHC can be used for a certain time, as its intensity decreases constantly due to the pp collisions. There are also other effects like the interaction between the beam and the gas left inside the beam pipe, and the local scattering inside the beams. In Figure 2.2 the instantaneous luminosity profile for one representative LHC fill is shown. In green the delivered luminosity is presented, while in yellow the luminosity recorded by the ATLAS detector is shown. The exponential decrease in luminosity is seen in the Figure. A new run starts every 10–20 hours, when the LHC is refilled with the protons. This means that the LHC collides particles about 30% of the time, as also some time is spent on the maintenance.

In Figure 2.14a the integrated luminosity as a function of time is presented for the 7 and 8 TeV centre-of-mass energy in 2011 and 2012, respectively. The integrated luminosity delivered by the LHC is shown in green, while the integrated luminosity recorded by the ATLAS detector is presented in yellow. In 2011 the integrated luminosity delivered was 5.62fb^{-1} , and the ATLAS collected 5.25fb^{-1} , while in 2012 ATLAS collected 21.74fb^{-1} out of 23.25fb^{-1} delivered by the LHC (as summarised in Table 2.1).

There are several pp interactions that happen during the same bunch-crossing, so at the same time as the interesting hard-scattering interaction, there are many additional inelastic interactions taking place: this is called the pile-up. There are two kinds of pile-up: in-time pile-up issued from the particles coming from the collisions within the same bunch crossing, while the out-of-time pile-up originates from the particles coming from different bunch crossing. In Figure 2.4 the mean number of interactions per bunch crossing $\langle N \rangle$ is shown for the data delivered in 2011 and 2012. This number depends on the total inelastic pp cross-section (σ_{pp} , $\sim 70 \text{mb}$ at the LHC), and the instantaneous luminosity \mathcal{L} : $\langle N \rangle = \sigma_{pp} \times \mathcal{L}$.

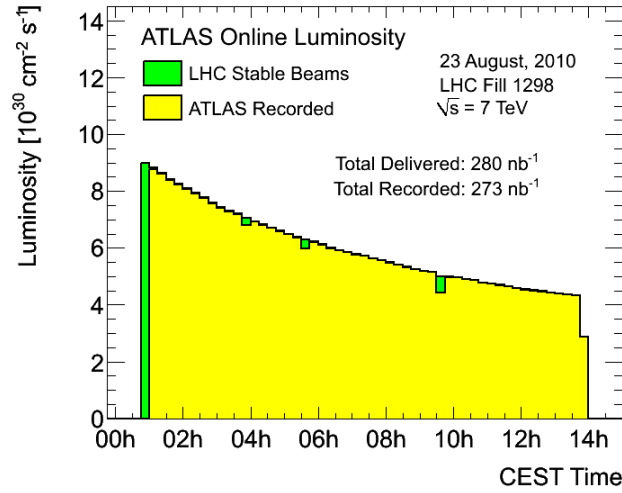
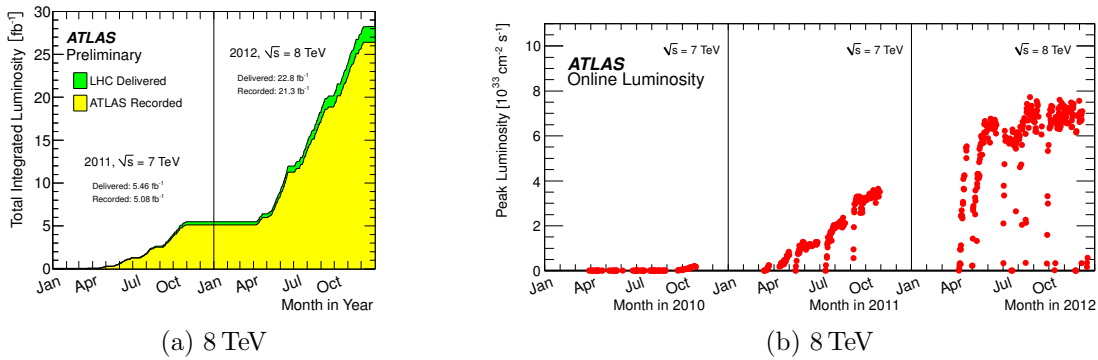


Figure 2.2: ATLAS instantaneous luminosity profile as measured online for representative LHC fill with 7 TeV centre-of-mass energy in 2010. The green shaded curves show the delivered luminosity during stable beam conditions, and the yellow shaded curves give the recorded luminosity with the entire detector available.



(a) 8 TeV

(b) 8 TeV

Figure 2.3: (a) The integrated luminosity versus time delivered to (green), and recorded by ATLAS (yellow) during stable beams and for pp collisions at 7 and 8 TeV centre-of-mass energy in 2011 and 2012. (b) The peak instantaneous luminosity delivered to ATLAS per day versus time during the pp runs of 2010, 2011 and 2012.

	2010	2011	2012	design
\sqrt{s} [TeV]	7	7	8	14
delivered integrated luminosity [fb^{-1}]	0.049	5.62	23.25	80-100
ATLAS recorded integrated luminosity [fb^{-1}]	0.045	5.25	21.74	-
bunch spacing [ns]	75	75/50	50	25
peak instantaneous luminosity [cm^2s^{-1}]	2.07×10^{32}	3.65×10^{33}	7.73×10^{33}	10^{34}
$\langle \mu \rangle$	-	9.1	20.7	19.2
peak μ	3.78	32.21	69.49	-

Table 2.1: The LHC operation during Run 1 and designed values. Several parameters are presented: center-of-mass energy, the integrated luminosity delivered by the LHC, and recorded by ATLAS. Also the spacing between the proton bunches, as well as the peak instantaneous luminosity, and the average number of interactions per bunch crossing and the peak value of the interactions per bunch crossing.

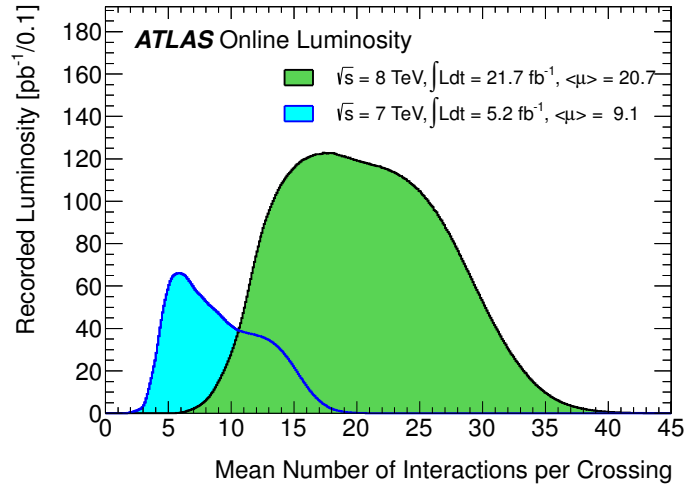


Figure 2.4: The luminosity-weighted distribution of the mean number of interactions per crossing for the 2011 and 2012 data.

2.2 ATLAS detector

The ATLAS detector [59] (A Toroidal LHC ApparatuS) is a multipurpose particle physics detector with a forward-backward symmetric cylindrical geometry and near 4π coverage in solid angle. It is designed to cover the complete range of the LHC program: the precise measurements of the SM processes, the search for the Higgs boson and the measurement of its properties, also an exploration of many of the BSM theories, and the study of flavour physics. It also studies the properties of the quark-gluon plasma resulting from the heavy ion collisions.

2.2.1 Nomenclature - the ATLAS coordinate system

A right-handed coordinate system is used to describe the ATLAS detector. The origin of the coordinate system is at the nominal interaction point (IP) in the centre of the detector and the z -axis points along the axis of the beam pipe. The x - y plane is perpendicular to the beam axis, with the x -axis pointing from the IP to the centre of the LHC ring, and the y axis pointing upward. More often one uses cylindrical coordinates (r, ϕ) in the transverse plane, and the pseudorapidity (η): r is the distance from the beam axis, ϕ is the azimuthal angle around the beam pipe, while $\eta = -\ln \tan(\theta/2)$, θ being the polar angle. The detector is divided in the barrel and end-cap regions.

Several parameters will prove useful for the description of the detector and the reconstruction of physics objects:

d_0 the transverse impact parameter is the distance in the transverse plane ($x - y$ plane) of the closest approach (perigee) to the z -axis of the helix produced by the particle

z_0 the longitudinal impact parameter is the z coordinate corresponding to the perigee

ϕ_0 is the azimuth angle of the momentum at the perigee. It can have values between $-\pi$ and π .

θ_0 is the polar angle of the perigee, values are in range $[0, \pi]$

ΔR is the angular separation in the $\eta - \phi$ plane. $\Delta R = \sqrt{\Delta\eta^2 + \Delta\phi^2}$

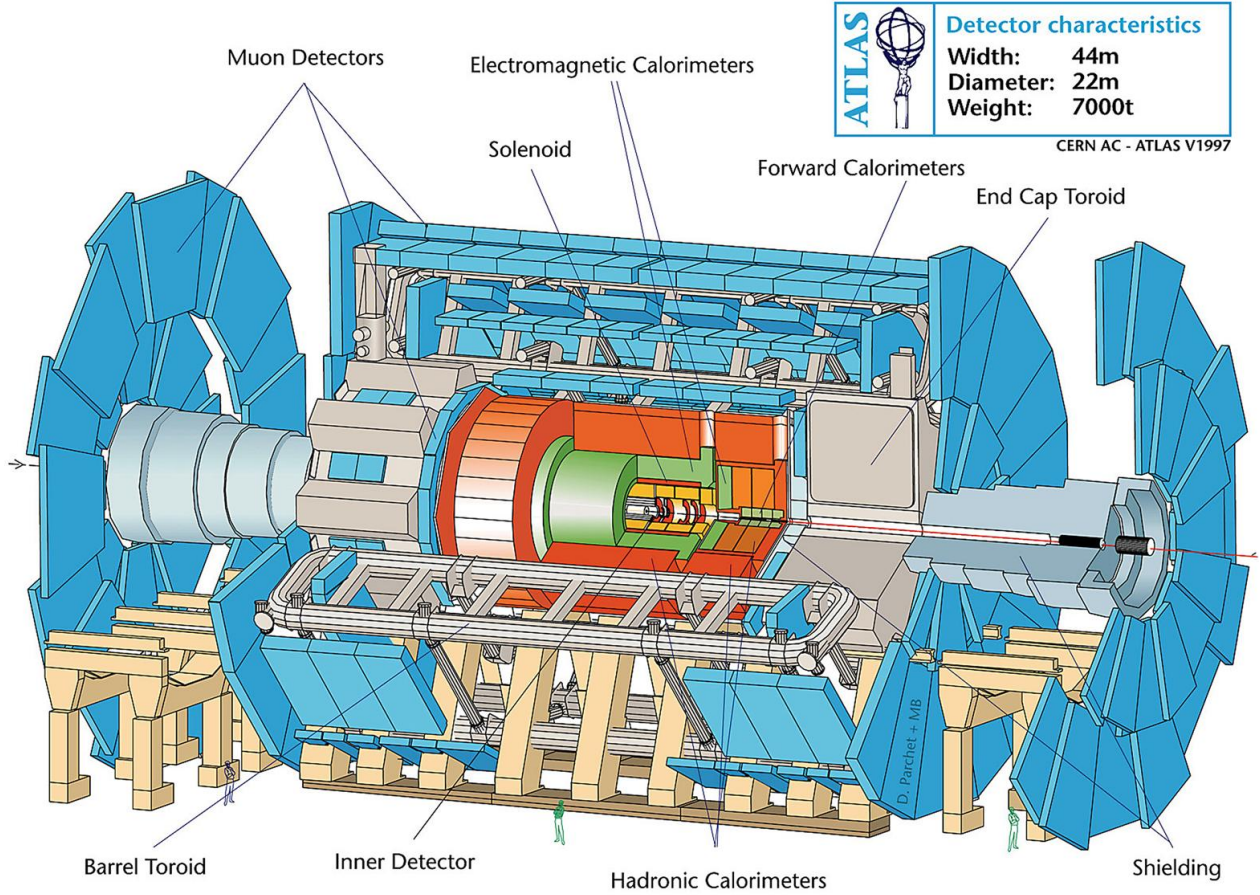


Figure 2.5: ATLAS

2.2.2 Design of the ATLAS detector

The ATLAS detector shown in Figure 2.5 is composed of the following sub-detector systems: the Inner tracking detector, the Electromagnetic Calorimeter, the Hadronic Calorimeter and the Muon Spectrometer.

2.2.3 The Inner Detector

The Inner Detector is located closest to the beam, as its role is to reconstruct the primary and the secondary vertices and the trajectories of the charged particles. It is immersed in the magnetic field produced by the solenoid magnet in order to bend the trajectories of the charged particles. As it is the closest sub-detector to the beam, it should be resistant to the radiation. Nevertheless, its performance degrades with time and with increasing luminosity. The Inner detector is contained within a cylinder whose length is 7 m and with a 1.15 m radius. The designed and measured momentum resolution is:

$$\frac{\sigma(p_T)}{p_T} = 5 \cdot 10^{-4} \cdot p_T \oplus 1\% \quad (2.3)$$

for tracks that have $p_T > 500$ MeV and for $\eta < 2.5$, which is the coverage of the Inner Detector. The first term comes from the intrinsic resolution and dominates in the high p_T regime, while the second term is the consequence of the multiple scattering and dominates for low p_T . As there is a very large density of tracks expected at the LHC, the inner detector needs a very fine-granularity, in order to obtain the needed momentum and vertex resolution. It is composed of three sub-detectors:

The Pixel Detector is the closest to the beam, so its primary role is in the determination of the primary and secondary vertices. Secondary vertices are important as they allow

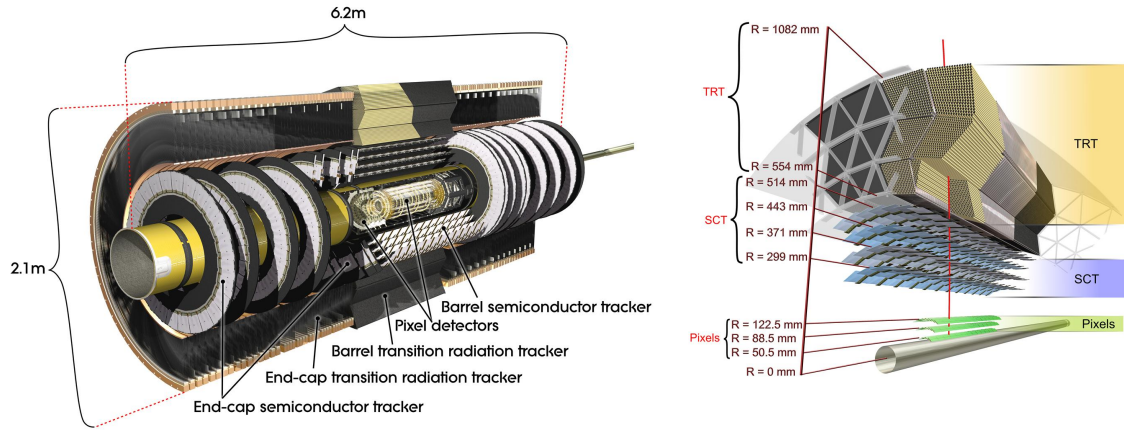


Figure 2.6: The Inner Detector

for the identification of the b -jets. This detector allows for the identification of other short lived particles like τ leptons. This is the highest granularity detector made of semiconductor pixel detectors. There are three pixel layers in the radial direction over the full acceptance, and five disks on each side. There are about 1500 barrel modules, and 700 disk modules. The typical spatial resolution in the $R-\phi$ plane is $\sim 12\mu\text{m}$ and $\sim 66\mu\text{m}$ along the z -axis for the barrel, and $\sim 77\mu\text{m}$ for the end-caps. The thickness of each of three pixel layers is 2.5% radiation length.

The Semi Conductor Tracker (SCT) is designed to precisely measure the tracks, by determining their momentum, and vertex position. It is placed in between 299 mm and 514 mm, from the beam axis. It is also a highly granular system. The technology employed is similar to the Pixel Detector, it is just that it is segmented in strips instead of pixels. It is done to reduce the number of readout channels. There are eight layers of silicon microstrip detectors. The microstrips are 12 cm long and $80\mu\text{m}$ wide. The spatial resolution is $\sim 16\mu\text{m}$ in the $R-\phi$ plane and $\sim 580\mu\text{m}$ in the z direction. The expected number of hits in the SCT system for a passing particle is eight. The barrel modules are supported by four cylinders made of carbon fiber, while the end-caps are supported by nine external disks.

The Transition Radiation Tracker (TRT) is made of straw tubes - cylindrical gas detectors. Their very small diameter and isolation of the sense wire within individual gas volumes, allows them to be efficient in very dense environment. This solution offers a lower material budget, and is less expensive than a silicon detector. It aims at measuring the $R-\phi$ position of the charged particle. The TRT also can identify electrons as the xenon gas is used to detect the transition-radiation photons created in a radiator between the straws. The barrel is made of 50 000 straws and each of them is divided in two to reduce the occupancy. The end-caps are made of 320 000 radial straws. There are two different thresholds defined in order to distinguish between tracking hits (passing the lower threshold) and transition-radiation hits (above the higher threshold). The straws are filled with a non-flammable gas mixture (70% Xe, 20% CO_2 , 10% CF_4). Each straw is 4 mm in diameter, and have a $30\mu\text{m}$ diameter gold-plated tungsten wire, which acts like the anode, while the aluminum which is the internal surface of the straws acts like the cathode. The resolution achieved with the TRT is $\sim 130\mu\text{m}$ in the $R-\phi$ plane, which is less than in the pixel and SCT detector, as expected.

The continuous tracking in TRT with precise position hits in pixel strip provide reliable track recognition and position measurements. The pixels are much more precise, but they

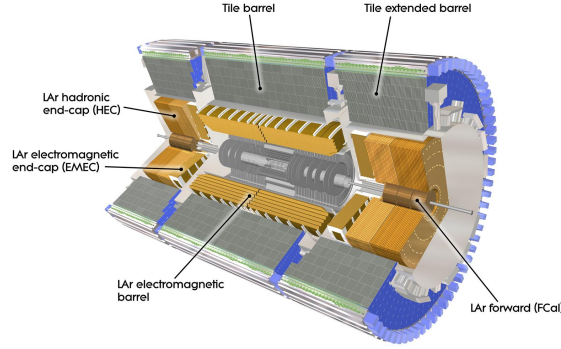


Figure 2.7: The ATLAS calorimeters consist of an electromagnetic calorimeter (LAr) and a hadronic calorimeter (Tile, HEC and FCal). The yellow colour presents the parts of the calorimeters that use LAr, while the grey colour present the tile calorimeter.

cover small area, while the straws cover much larger area with less precision. The combination of both of them allows to measure the momentum precisely.

2.2.4 Calorimeters

The Calorimeters are located around the Inner Detector, and they are shown in Figure 2.7. They measure the energy of electrons, photons and jets, and also their position. They are sampling calorimeters, which means they alternate between the passive and active areas. In the passive areas there is the formation of the shower, which energy is measured in the active areas. The Liquid Argon (LAr) calorimeter is placed in a cylinder with an outer radius of 2.25 m and 13.3 m length, while the outer radius of the Tile calorimeter is 4.25 m and its length is 12.2 m.

The Electromagnetic calorimeter is made of lead (passive) and liquid argon (active), and it has an accordion geometry, as shown in Figure 2.8. This geometry allows for a complete symmetry in ϕ , without any cracks. In front of it (for $|\eta| < 1.8$) there is a presampler detector which is used to correct for the energy lost in the material coming before the calorimeter. Its granularity is 0.025×0.1 in the $\Delta\eta - \Delta\phi$ plane, and its thickness is 11 mm of the LAr in the barrel and 4 mm in the end-caps. The electromagnetic calorimeter is divided into three longitudinal sections, with the active thickness of $6 X_0$, $16 X_0$ and $3 X_0$ respectively (measured at $\eta = 0$). The granularity of the first layer in the $\Delta\eta - \Delta\phi$ is 0.03×0.1 , the second is 0.025×0.025 , and third 0.05×0.025 . The LAr technology is radiation hard. The barrel electromagnetic calorimeter is made of two identical half-barrels which length is 3.2 m, with the internal radius of 1.4 m and is placed in the same barrel cryostat as the solenoid magnet. The end-cap electromagnetic calorimeters are divided into two coaxial wheels. They are located in the end-cap cryostats, as well as the end-cap hadronic calorimeters. The internal wheel radius is ~ 33 cm, and the outer wheel radius is ~ 210 cm.

The energy resolution of the electromagnetic calorimeter is given by:

$$\frac{\sigma(E)}{E} = \frac{a}{\sqrt{E}} \oplus \frac{b}{E} \oplus c \quad (2.4)$$

where a is the stochastic term that describes the fluctuations of the fraction of the shower energy deposited in the sampling medium (LAr) and in the absorber (lead), b is the noise term coming from the electronic noise and out-of-time pile-up, and c is the constant term that takes into account the calibration, mechanical and electrical inhomogeneities.

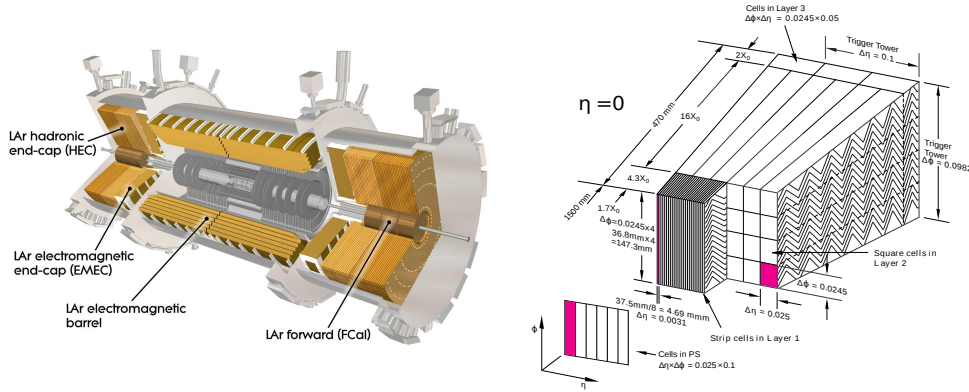


Figure 2.8: Left: the LAr calorimeters. Right: the accordion structure of the electromagnetic calorimeter. The three layers with varying granularity in the ECAL module are indicated,

The electromagnetic calorimeter in the forward region ($3.1 < \eta < 4.9$) is also a LAr calorimeter, which consists of copper rods parallel to the beam axis that are placed into an outer tube with 250 mm LAr gap in between. The rods and the tubes are inserted in the matrix made of copper. The forward electromagnetic calorimeter is exposed to high radiation levels. Each end-cap has 1024 readout channels. The granularity in the $\Delta\eta - \Delta\phi$ is 0.1×0.1 .

The Hadronic calorimeter consists of the Tile calorimeter, Hadronic End-cap (HEC) and Forward hadronic calorimeters (FCAL).

The Tile calorimeter is a cylinder that consists of the central barrel and two extended barrels, and is situated behind the electromagnetic calorimeter. It is a sampling calorimeter with the iron as absorber, and the plastic scintillator plates (tiles) are the active medium. It is made of three layers, and it is divided into 64 modules. The first and second samplings have 0.1×0.1 granularity in $\Delta\eta - \Delta\phi$, and the third sampling has 0.2×0.1 . The barrel has 5760 readout channels. The extended barrels have the same granularity as the barrel, and 1792 readout channels. The samplings are approximately 1.4, 4.0 and 1.8 interaction lengths deep. The scintillating tiles are located in planes that are orthogonal to the beam axis. When the particles pass through the tiles, they emit scintillating light. The fiber collects this light, and takes it to the photomultipliers where it is amplified and further driven to the readout electronics. Several fibers are analysed by the same photomultiplier. The internal diameter of the Hadronic Tile calorimeter is 4.56 m and its external diameter is 8.5 m.

As there is more radiation at the larger pseudorapidities, the LAr technology is employed also for the hadronic end-cap calorimeter. The HEC is made of copper and LAr parallel plates, and the FCAL is again a LAr calorimeter. For the hadronic calorimeter to absorb well the hadronic showers it is 9 interaction lengths thick. The granularity of the forward calorimeter is 0.2×0.2 , and it has 768 readout channels.

The hadronic calorimeter allows for good resolution of the high energy jets. If at the same time it has a large coverage in η , it gives a good E_T^{miss} measurement. The expected energy resolution of the barrel and end-cap system for jets is:

$$\frac{\sigma(E)}{E} = \frac{50\%}{\sqrt{E}} \oplus 3\% \quad (2.5)$$

and for the forward calorimeter it is:

$$\frac{\sigma(E)}{E} = \frac{100\%}{\sqrt{E}} \oplus 10\% \quad (2.6)$$

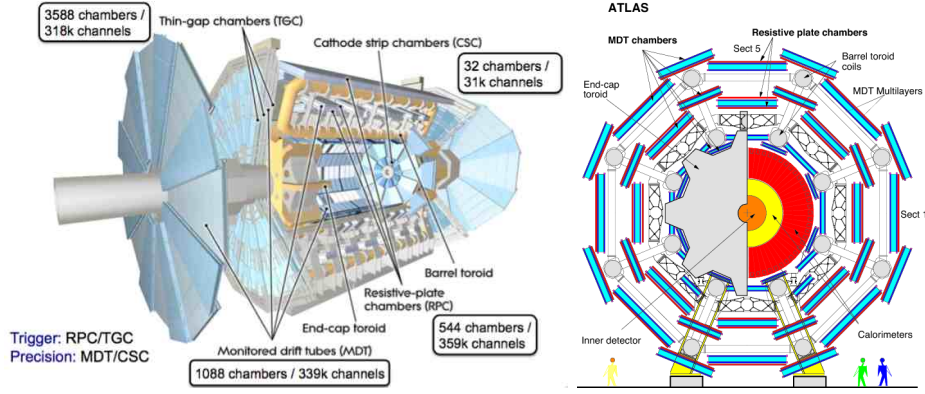


Figure 2.9: The Muon Spectrometer. Right: cross-section of the muon spectrometer in the x-y plane, with the interaction point in the middle.

Both calorimeters are non-compensating which means they have different response depending on the type of the particle: electromagnetic or hadronic. The calorimeters are also part of the trigger system.

2.2.5 The Muon Spectrometer

The Muon Spectrometer is dedicated to the detection and measurement of the properties of the particles that cross the calorimeters unabsorbed, in practice those are muons. The large magnetic field is necessary to provide enough power to bend the trajectory of particles. The most accurately measured coordinate is the η coordinate.

The Monitored Drift Tubes (MDT) are used to measure muon tracks. Each module consists of three layers of drift tubes made of aluminum on both sides. In total there are 400 000 tubes. They are filled with the gas consisting of 93% of Argon and 7% CO_2 . Each tube in the middle has a gold-plated tungsten-rhenium wire, which acts like an anode, while the tube itself acts like a cathode. Tubes are grouped into chambers: there are 1194 chambers in total and $3,7 \cdot 10^5$ readout channels.

The Cathode Strip Chambers (CSC) are used for the end-caps. They have a higher granularity than the MDTs. The CSCs are multiwire chambers filled with an admixture of 80% Ar, 20% CO_2 . Each module is equipped with the rhenium-tungsten anodes that have a diameter of $30 \mu\text{m}$ and are placed parallel to each other. The spatial resolution is $60 \mu\text{m}$.

The Resistive Plate Chambers (RPC) are part of the trigger system and are placed in the barrel. Those are gas detectors that are made of parallel layers of bakelite separated by 2 mm. The gap is filled with a gas consisting of 94.7% tetrafluorethane, 5% isobutane and 0.3% sulfur hexafluorure. When a particle pass through the detector, the avalanche is created by the primary ionisation of the gas under the external electric field. The spatial resolution of the RPC is 10 mm per chamber. There are 1116 RPC in total.

The Thin Gap Chambers (TGC) are multiwire proportional chambers placed in the end-cap, and used in trigger. They are based on the same principle as the CSCs, but have a smaller distance between the wires (1.4 mm) than between wire and anode (1.8 mm). This allows for the drift times shorter than 25 ns (the time between two consecutive bunch crossings). The ϕ coordinate is measured by the radial readout strips, while the η coordinate is measured using the anode wires.

2.2.6 Magnet system

The Magnet system of the ATLAS detector consists of a central solenoid (which provides the magnetic field for the Inner Detector) and three large air-core toroids (that generate the

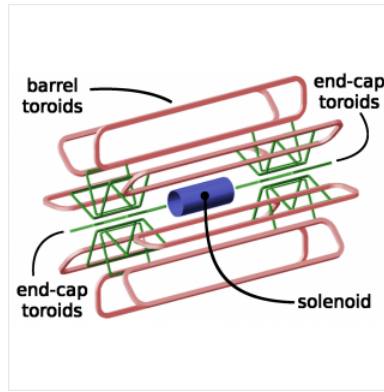


Figure 2.10: The magnet system

magnetic field for the Muon spectrometer): one for the barrel and two for the end-caps.

The central solenoid magnet generates a central field of 2 T. It is made of one coil with 1173 turns, whose axis is the same as the beam axis. The circulating current is 7.73 kA. It is placed around the Inner Detector, and has a length of 5.3 m. In order to achieve the desired performance of the electromagnetic calorimeter, the amount of material in front of it should be as small as possible, and that is why the LAr calorimeter and the central solenoid share one vacuum vessel. The central solenoid coil is as thin as possible.

The toroid magnets Each of the three toroids consists of eight coils. They are all placed radially and symmetrically around the beam axis and generate the magnetic field for the Muon Spectrometer. The end-cap toroid coil system is rotated by 22.5° with respect to the barrel toroid system in order to provide radial overlap and to optimise the bending power in the region between them. Each barrel toroid is 35.3 m long, and 5.4 m wide, wrap by 120 turns. The end-cap toroids have 116 turns. The magnetic field originates from the 22.3 kA current. The peak field is 3.9 T in the barrel, and 4.1 T in the end-caps.

2.2.7 The Trigger system

The 20 millions of collisions that the LHC delivers every second cannot all be read and saved, as the bandwidth, and also the storage facilities are not enough to satisfy the demand. Thus not all the events are retained, and the trigger system is responsible to make a fast decision if the obtained data is interesting and worth to reconstruct, analyse and save.

The Trigger system consists of the three decision levels: level 1 (L1), level 2 (L2) and event filter (EF). Each level relies on the previous one, and refines the selection. L2 and EF are together called High Level Trigger (HLT).

The Level 1 trigger reconstructs the events using the information coming from several sub-detectors, but very rough. It is an initial decision based on the hardware. It uses the information from the calorimeters (but with reduced granularity), and also on the RPC and TGC. It searches for events that have electrons, photons, muons and jets with large transverse momentum (p_T) and also large missing transverse energy (E_T^{miss}). At this level data comes at the 75 kHz rate. The Regions of Interest (ROI) are defined around each object that is triggered and passed to the Level 2 trigger.

The Level 2 trigger uses the full granularity of subdetectors in the ROI to reconstruct the objects, and compares them to predefined requirements. If those are met, the event is transferred to the next trigger level. The Level 2 trigger reduces the rate to 3.5 kHz.

The EF separates the events into different streams based on the triggers that fired. The ones that are used in this thesis are **JetTauEtMiss**, **Egamma** and **Muons**, based respectively on jets and E_T^{miss} , electron and photon, and muon triggers. It reduces the rate to 200 Hz.

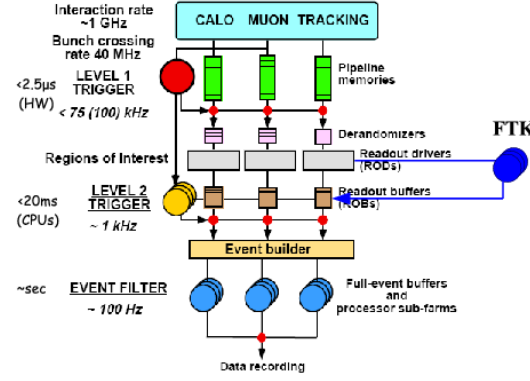


Figure 2.11: The trigger system

The High Level Trigger (L2 and EF) uses the information from the calorimeters, the muon spectrometer, and also from the inner detector to select the events. When the decision is made to keep the event, the informations are passed to the data acquisition system (DAQ), which saves them permanently.

2.2.8 Simulation of the ATLAS detector

The interaction of the particles resulting from the pp collision with the detector is predicted using the a detector simulation implemented in GEANT4 [65]. To model the detector response to this simulated interaction between the particles and detector digitisation is performed. The effect of pile-up is also simulated during digitisation. The last step is the reconstruction of the simulated event using the same setup (algorithms and calibration) as the ones used for the real data events.

The ATLAS detector implementation in GEANT4 is known as the full detector simulation. Alternatively, a fast simulation can be performed, using the ATLAS detector implementation in At1Fast-II [66], which is much faster.

2.3 Object reconstruction

The response coming from the detector is further analysed into reconstructed and identified objects. This Section describes the reconstruction of all the objects that can be detected with the ATLAS detector. In order to perform the analysis described in the subsequent Chapters it is essential to know what are the physics objects one is considering. The reconstruction and identification of each object are achieved by combining the information of several sub-detectors. All physics objects are used in the analyses presented in this thesis, but special attention should be given to jets and E_T^{miss} reconstruction, as well as on τ leptons.

2.3.1 Reconstruction of tracks

Tracks are reconstructed using the information provided by the Inner Detector [67, 68]. When the particles go through the inner detector they leave hits, and those hits are used for the reconstruction of the trajectory. The reconstruction of the trajectory is not straightforward as the particle on its way traverses also the areas of dead material which distorts its path and causes it to lose energy from ionisation and bremsstrahlung. The algorithm that performs the reconstruction of the trajectory has to take into account all these effects. In the events recorded by the ATLAS detector there are also tracks coming from the presence of the pile-up, all contributing to very high density of tracks left in the Inner Detector.

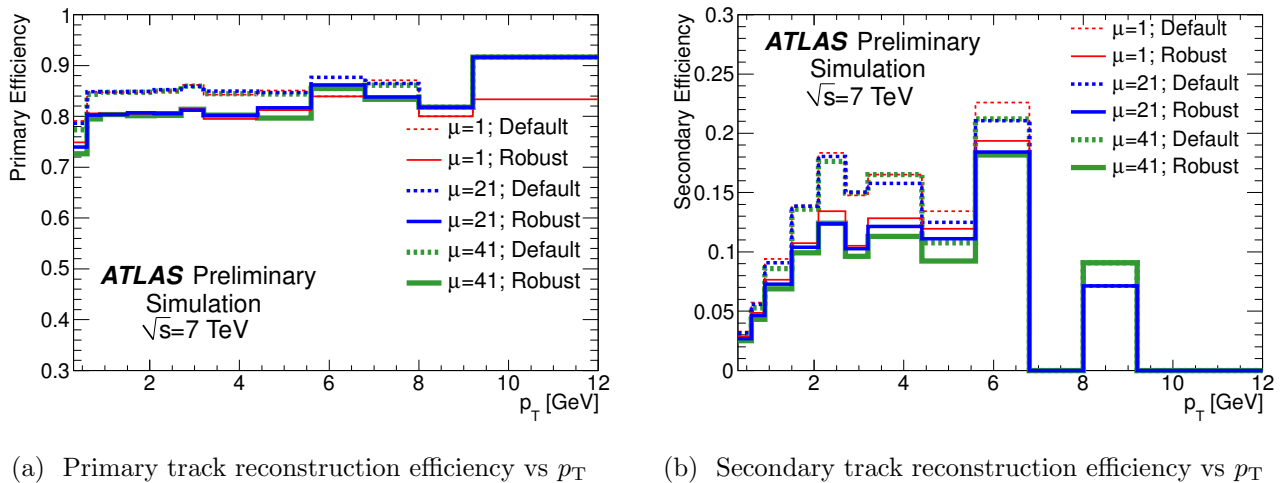
(a) Primary track reconstruction efficiency vs p_T (b) Secondary track reconstruction efficiency vs p_T

Figure 2.12: Track reconstruction efficiency for the (a) primary particles and (a) secondary particles, as a function of the track p_T , shown for different pile-up conditions.

There are two approaches to the reconstruction of tracks depending on whether they originate from primary or secondary particles. The primary particles are produced in the pp collision, or they come from the decay of a particle with a short lifetime. The secondary particles are coming from the decay of a particle with a longer lifetime.

Inside-out tracking is used for the reconstruction of the trajectory of the primary particles.

It takes three-point seeds from the innermost layer of the silicon detectors. The algorithm then makes its way from the interaction point and adds the hits to the trajectory. It takes into account the effects coming from the dead material, and gives the prediction of the trajectory all the way to the external layer of the Inner Detector. The trajectory is then refitted by minimising the χ^2 function of the distance of each hit to the predicted trajectory.

Some of the reconstructed tracks are fake. In order to disentangle real and fake tracks, a ranking system is established. The criteria are the number of hits in the detectors, and also the goodness of the χ^2 fit. If there are missing hits (when compared with the predicted trajectory), and/or the quality of the χ^2 is not satisfactory, the track is likely to be false and is discarded. If there are ambiguities between several tracks, the one with the highest score is retained.

The quality criteria require that each track has a certain number of hits (nine) in the Pixel and SCT, and that there are no missing hits in the b-layer. When the best candidate tracks are chosen in the inner layer of the Inner Detector, they are extrapolated in the TRT by adding the hits that are compatible with the predictions.

This algorithm is efficient in reconstructing tracks with a $p_T > 400$ MeV, as can be seen in Figure 2.12a where the reconstruction efficiency for the minimal bias MC samples is shown as a function of the p_T of the track, for the primary particles. The reconstruction efficiency is defined as the fraction of the primary particles matched to the reconstructed track. The track reconstruction efficiency varies between 0.8 and 0.9 depending on the track p_T . There is also a dependence on the pile-up conditions: the efficiency for various average number of interaction per bunch-crossing μ is shown in red for $\mu = 1$, blue for $\mu = 21$, and green $\mu = 41$. The solid line represents the robust identification, while the dashed corresponds to the default requirements. As expected the reconstruction efficiency is lower for a tighter criteria.

Outside-in tracking is performed for the tracks that are expected not to be efficiently re-

constructed with the Inside-out tracking as they come from secondary particles (from the secondary vertices, or by photon conversion). Also the electrons with high energy loss are also expected to be missed by the Inside-out tracking algorithm. The Outside-in algorithm is performed after the primary vertex (Section 2.3.2) is already reconstructed by the Inside-out algorithm, by performing the pattern recognition starting from the information in TRT and moving backwards to the inner layers of the Inner Detector.

This algorithm efficiency is presented in Figure 2.12b for the minimal bias MC samples as a function of the p_T of the track, for the secondary particles. The dependance of the pile-up is also shown.

2.3.2 Primary vertex

The primary vertex is the place where the hard scattering occurred. As there are many vertices in each event, it is challenging to identify the correct one. For some analyses it is also important to identify the secondary vertices, for example they are used in the identification of b -jets. To find the primary vertex, the algorithm starts from the vertex seeds that are determined from the z coordinate of several reconstructed tracks. The compatibility of a track with a fitted vertex is measured by the goodness χ^2 fit. If a track is more than 7σ away from a fitted vertex, it is removed from the list of tracks associated to that vertex. The resolution of the vertex position is around $30 \mu\text{m}$ in the xy -plane and $50 \mu\text{m}$ in the z direction. For most of the topologies considered in this thesis, the physics processes are hard and the primary vertex is identified with high efficiency.

2.3.3 Jets

The jet algorithm starts from the topological clusters [69, 70] reconstructed in the calorimeters. They are seeded by the cells with the ratio of the energy deposit over the measured noise is above certain threshold. The neighbouring cells are then added to the topocluster, and the energy of the topocluster is determined by summing the energy of all cells.

Jets are reconstructed with the the anti- k_t jet algorithm [71, 72]. The main parameter of this jet reconstruction algorithm is the distance $R_{ij} = \sqrt{\Delta y^2 + \Delta\phi^2}$ between two jet constituents, typically it is 0.4 or 0.6. The algorithm first identifies the cluster with high energy. The clusters with low energy are then added to the previously identified clusters with high energy if they are sufficiently close. If a topocluster does not have other neighbouring topoclusters within a distance $2R$, then it will simply accumulate all the soft cells within a circle of radius R , resulting in a perfectly conical jet. If there exist a topocluster with high energy with $R < \Delta R < 2R$, two hard jets are reconstructed but they are not perfectly conical. The key feature of this algorithm is that the shape of the jet is not influenced by the soft particles, but if there is a hard jet close to it, both of them will have modified shapes. It means that the jet boundaries are not affected by soft radiation.

The energy of the jet calculated by just adding the energy deposited in the cells of the hadronic calorimeter has to be corrected for several effects: calorimeter non-compensation and dead material. The calorimeter non-compensation comes from the fact that the hadrons and electrons of the same energy cause different response of the detector. As mentioned before, the dead material is the material that the particles have to pass through, but which is not the active area of the detector.

The energy corrections are derived from the MC simulation. The local cluster weighting (LCW) calibration method classifies topological clusters by their origin: either electromagnetic or hadronic, and the corrections are different in each case. The correction depend on the p_T and η of the jets. The final jet energy calibration generally referred to as jet energy scale

(JES) is a simple correction relating the calorimeter's response to the true jet energy, and they are applied on top of the LCW corrections. The pile-up influence the jet energy, so there are corrections to be applied. The energy contribution comes from both the same and previous bunch-crossings. The energy corrections depend on the jet η , as well as on the number of the reconstructed vertices in the event and the average number of interactions per bunch crossing and is accounted for using the jet area subtraction method.

The uncertainties on the jet energy scale come from the parametrisation of the dead material, the effects of pile-up, and also theoretical uncertainties coming from the different treatment of the fragmentation and the underlying event, in various MC generators used to evaluate the corrections.

2.3.4 b-jets

The key difference between the light jets and the jets originating from b -quarks is the vertex: B -hadrons have relatively long lifetime so they travel several mm before decaying and producing b -jets. Thus the b -jets originate from a displaced vertex. The algorithms that are used to tag the b -jets rely on the tracking and vertexing information. It employs a neural network that gives a distribution as the output. One can choose an operating point from that distribution. The tagging algorithm should be at the same time efficient at tagging b -jets and also to have a low mistag rate. The b -jets used in this thesis are identified using the MV1 jet tagger at the 70% efficiency operating point [73, 74].

2.3.5 Electrons

The electrons are identified [75, 76] using the information from the Inner Detector (as they are bent by the magnetic field), and the electromagnetic calorimeter, where they deposit their energy. They are identified using an algorithm that matches the clusters formed in the electromagnetic calorimeter with a reconstructed track from the Inner detector. The electrons radiate a significant amount of photons in the Inner Detector, and this too is taken into account by the algorithm. The electrons are reconstructed for $|\eta| < 2.47$ which corresponds to the η values covered by the Inner Detector, except in the region $1.37 < |\eta| < 1.52$ as it is a transition region between the barrel and end-caps where electromagnetic showers are less well measured.

The reconstruction starts from the electromagnetic calorimeter, where the cells are clustered using a sliding window: a rectangular window of 3×5 middle layer cells (size 0.025×0.025 in the $\eta - \phi$) is moved around the layer until it finds 15 cells whose sum of energies is above 2.5 GeV. Those cells are used as a seed cluster, that is matched to a track in the Inner Detector. The tracks are extrapolated from the TRT to the electromagnetic calorimeter. The track is considered matched to a cluster if it points within $\Delta\eta < 0.05$. The energy of the electrons can substantially change due to bremsstrahlung, thus their trajectories change too, but these losses are also taken into account by the algorithm [76]. The algorithm models the losses using the Gaussian Sum Filter (GSF). The electron is considered reconstructed if there is at least one track in the Inner Detector matched to the cluster in the electromagnetic calorimeter. The energy is corrected by adding the estimated energy loss either from the dead material in front of the calorimeter, energy missed during the clustering and also for the possible energy left behind the electromagnetic calorimeter. The energy of the electron is the energy of the cluster, while the η and ϕ coordinates are the coordinates of the track (if it has more than three hits, otherwise the ones of the cluster are taken instead).

At this level, a significant fraction of these electron candidates originates from photon conversion or jet and additional criteria are designed to positively identify it as an electron. To refine the selection, requirements are placed on the informations coming from the Inner Detector

and the calorimeter. Three selections are defined: 'loose++', 'medium++' and 'tight++'. For the loose selection, a requirement on the shower shape is added. The electron identified with medium criteria must have a matched track that passes the following selection: at least seven hits in the pixel and SCT detectors (summed), out of which at least one is in the pixel, $|\eta_{\text{cluster}^{1\text{st layer}}} - \eta_{\text{track}}| \leq 0.01$ and d_0 should be smaller of 5 mm. Additional criteria on the shower shape collected in the first layer of the calorimeter are used. The 'tight' selection is even more stringent as it adds the requirement on the ratio between the energy and momentum of the electron, as well as the information of the transition radiation coming from the TRT. The track distance to the cluster is required to be: $\Delta\phi \leq 0.02$ and $\Delta\eta \leq 0.005$. To further reject photon conversion, a hit in the b-layer is required and a veto on the reconstructed photon vertex is applied. The '++' denotes that there were modification introduced in 2012 to reduce the effects coming from the higher pile-up.

2.3.6 Photons

The reconstruction of photons is very similar to the reconstruction of electrons. The electromagnetic clusters are identified by the same algorithm using the sliding window. Photons can only leave a track in the Inner Detector if they convert to an e^+e^- pair. The absence of the track distinguishes them from the electron. But there are also differences in the shape of the electromagnetic shower: photons have narrower showers. The unconverted photons are difficult to distinguish from π_0 ($\pi_0 \rightarrow \gamma\gamma$), but this is resolved as the first layer of the electromagnetic calorimeter has a high granularity, which allows for the separation of the two photons and subsequent reconstruction of π_0 .

2.3.7 Muons

The muons are mainly reconstructed and identified in the Muon Spectrometer, as they are the only charged particles that reach it. The informations from the Inner Detector and calorimeters are also used. There are several algorithms designed for the reconstruction and identification of muons: stand-alone muons (reconstructed using only informations from the Muon Spectrometer), combined (tracks are reconstructed independently in the Inner Detector and in the Muon Spectrometer, and matched), and segment-tagged muons (the tracks are reconstructed in the Inner Detector and extrapolated to the Muon Spectrometer, where at least one straight track segment is required in the MDTs or CSCs).

Stand-alone muons are reconstructed by an algorithm that starts from the regions identified by the muon trigger chambers. In those regions the hits are identified in all three muon stations, and segments are built out of those tracks. Then the fitting procedure that takes into account the energy losses performs a fit of the track using those segments, and extrapolates it to the interaction region [59]. The coverage of this algorithm is the coverage of the Muon Spectrometer $|\eta| < 2.7$.

Combined muons are muons made from tracks that have been independently reconstructed in the Muon Spectrometer and in the Inner Detector. The algorithm then performs a χ^2 fit to determine the matching between the tracks. The tracks in the Inner Detector are reconstructed using the inside-out algorithm. There are two kinds of fit performed: one does a statistical combination of the inner and the outer tracks by extrapolating the inner track and then combines it with the closest outer track; the other algorithm performs a refit of the track segment in order to get the best global fit of the muon track (it also takes into account the magnetic field and the material in front of the Muon Spectrometer).

Segment-tagged muons do not require a fully reconstructed track in the Muon Spectrometer. This algorithm is optimised for finding muons whose energy is too low to traverse the whole Muon Spectrometer. Those muons only leave a track in the Inner Detector which is later extrapolated to the Muon Spectrometer, and matched to a muon segment reconstructed close to the predicted track position. The goodness of fit is evaluated either with the χ^2 of the distances, or by using a neural network.

More stringent criteria are applied when identifying the muons used for the physics analyses. Further requirements are placed on the number of hits that the track left in the Inner Detector: at least one hit in the Pixel and in B-layer, at least six hits in the SCT. In total, there should not be more than 3 holes in the Pixel and SCT, and in the TRT there must be six hits (for $|\eta| \leq 1.9$, if η is larger, there is no requirement).

2.3.8 Missing transverse momentum

The missing transverse momentum ($\mathbf{E}_T^{\text{miss}}$) is defined as the momentum imbalance in the plane transverse to the beam axis. Along this axis the momentum conservation is expected, so a possible imbalance can be sign of new physics, in the form of the presence of undetected particles. Those can be already known particles like neutrinos, or possible new weakly interacting particles. The $\mathbf{E}_T^{\text{miss}}$ is obtained by summing over the momenta of all particles detected from the pp collision. Its magnitude is denoted by E_T^{miss} .

The sources of fake E_T^{miss} are a limited detector coverage, a finite detector resolution, the presence of dead regions and different sources of noise. The ATLAS calorimeter covers large pseudorapidities to minimise the effect of particles with high energy going undetected in the very forward direction. Despite that, there are transition regions between different calorimeters where the energy measurement is degraded. Dead and noisy readout channels in the detector also produce fake E_T^{miss} , as well as cosmic-ray and beam-halo muons crossing the detector. Selection criteria are applied to clean the data from events affected by all of these sources, and to suppress fake E_T^{miss} , usually by rejecting out-of-time energy deposits in the calorimeters.

To accurately account for the E_T^{miss} in an event, one has to consider all the objects that are produced in the event, using the energy deposits from the electromagnetic and hadronic calorimeters, and the muon spectrometer. Each energy cluster is associated to high- p_T objects in the following order: electrons, photons, jets and muons, in order to replace the initial cluster energy with a more refined calibration [77]. The remaining clusters not belonging to such objects are included in the `SoftTerm` term. The E_T^{miss} is given by the following formula:

$$(E_T^{\text{miss}})_{x(y)} = (E_T^{\text{miss}})_{x(y)}^e + (E_T^{\text{miss}})_{x(y)}^\gamma + (E_T^{\text{miss}})_{x(y)}^{\text{jet}} + (E_T^{\text{miss}})_{x(y)}^\mu + (E_T^{\text{miss}})_{x(y)}^{\text{SoftTerm}} \quad (2.7)$$

where each term is computed from the sum of calibrated cluster energies inside the corresponding objects. The $(E_T^{\text{miss}})_{x(y)}^{\text{SoftTerm}}$ term includes all the energy deposits that are not associated to any objects.

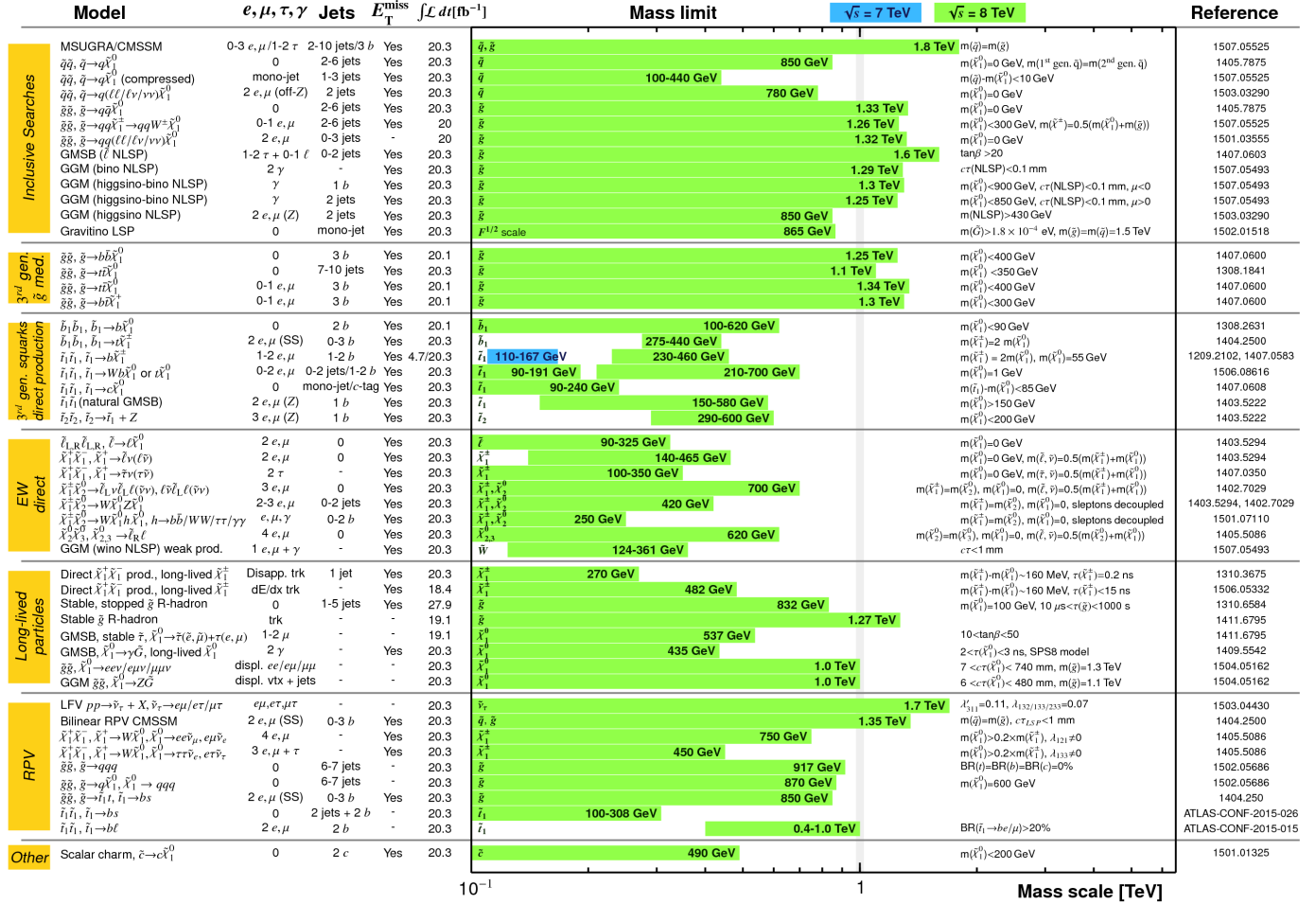
The uncertainties that come from the reconstruction and identification of all the objects influence also the uncertainty of E_T^{miss} .

2.4 Conclusion and outlook

This Chapter was dedicated to the description and the performance of the LHC accelerator as well as the ATLAS detector, both are key in performing the search for the Supersymmetric particles, that is presented in the next Chapter. The LHC is a proton-proton collider, that influence the production of the particles. Also the centre-of-mass energy of 8 TeV at which it

ATLAS SUSY Searches* - 95% CL Lower Limits
Status: July 2015

ATLAS Preliminary
 $\sqrt{s} = 7, 8 \text{ TeV}$



*Only a selection of the available mass limits on new states or phenomena is shown. All limits quoted are observed minus 1 σ theoretical signal cross section uncertainty.

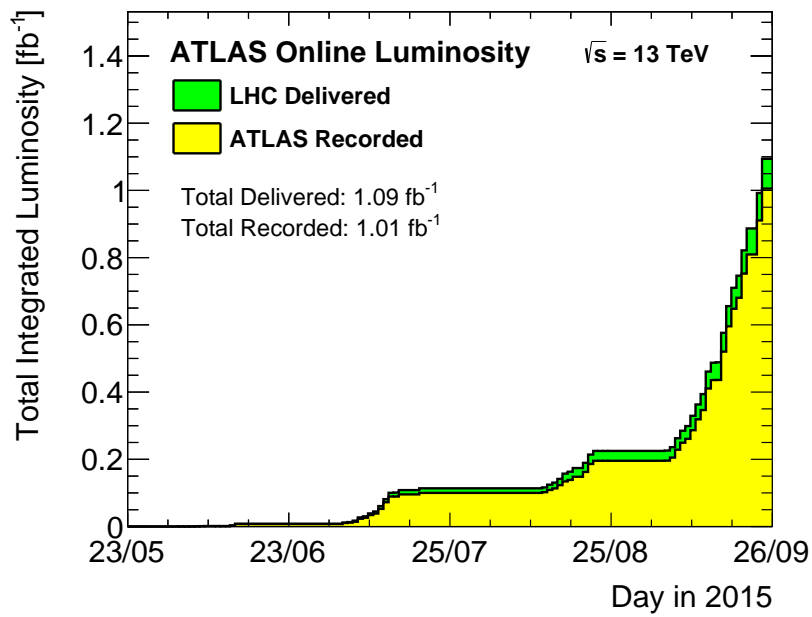
Figure 2.13: Mass reach of ATLAS searches for Supersymmetry. Only a representative selection of the available results is shown.

operated in 2012 along with the other parameters of the accelerator, determines many aspects of the search that is performed with the data collected. The ATLAS detector, along with the all the algorithms developed and specialised for this data-taking period, has an indispensable role when the search is to be designed. Before embarking on a quest for new physics, one should know and understand what are the strong and weak points of the instruments that allow for such a search to happen in the first place.

The full legacy of the Run 1 of the LHC allowed to set limits on the mass reach for SUSY searches: they are shown in Figure 2.13 for ATLAS for mSUGRA and various simplified models. Most of the results presented are performed with 8 TeV data and the masses of several strongly produced supersymmetric particles are already pushed to above 1 TeV. The following Chapters will focus on the analysis that is denoted "2–6 jets" in this summary Table.

During the first shutdown of the LHC, an upgrade of the Pixel Detector has been performed: a new detector, called the Insertable B-layer (IBL) [78], has been installed between the existing Pixel Detector and a new, smaller radius beam-pipe. It improves the tracking, vertexing, and b-tagging performances of the ATLAS detector.

After the shutdown, the LHC resumed its function, and the first new collisions took place in 2015. Figure 2.14 shows the integrated luminosity versus time delivered to (green) and recorded by (yellow) ATLAS during stable beams for pp collisions at a 13 TeV centre-of-mass energy in 2015. One can see that both the LHC and ATLAS detector are performing well under completely new conditions.



(a) 13 TeV

Figure 2.14: The integrated luminosity versus time delivered to (green) and recorded by ATLAS (yellow) during stable beams for pp collisions at 13 TeV centre-of-mass energy in 2015.

Chapter 3

0-lepton

This Chapter presents the search for SUSY in the final state with large E_T^{miss} , 2–6 jets and no isolated electrons or muons with the ATLAS detector, hereafter called 0-lepton. This analysis has been carried out previously within ATLAS [79, 80, 81], and also by the CMS collaboration [82, 83, 84, 85]. This final state is mainly motivated by the possible production of pairs of gluinos and the first or second generation squarks ($\tilde{g}\tilde{g}$, $\tilde{g}\tilde{q}$, $\tilde{q}\tilde{q}$) which have large production cross-sections at the LHC (Section 1.6.2). Possible subsequent R -parity conserving (simplified models) decays of these sparticles ($\tilde{q} \rightarrow q\tilde{\chi}_1^0$, $\tilde{g} \rightarrow q\tilde{q}\tilde{\chi}_1^0$) lead to final states with several jets and large E_T^{miss} , coming from the neutralino. Longer decay chains of squark and gluino can result in the presence of leptons in the final state, but these are covered by different searches within ATLAS. If the squark or gluino decay goes through intermediate particles, the expected number of jets in the final state is even larger. Although the 0-lepton search is designed around the production and decay of squark and gluino, its results constrain any new physics processes that lead to final states with many jets and E_T^{miss} .

This Chapter presents the results of this search using 20.3 fb⁻¹ of LHC proton-proton collisions data at $\sqrt{s} = 8$ TeV collected by the ATLAS experiment in 2012, that are published in Ref. [2] with the supporting internal ATLAS documentation in Ref. [86]. The results are obtained by the 0-lepton analysis team, and they are given as an introduction to this thesis work that is explained in the next Chapter.

Section 3.1 presents the analysis strategy. The dataset and Monte Carlo samples used are given in Section 3.2. Then the selection of events is detailed, for the definition of signal, control and validation regions (Section 3.3). The results of this search and their interpretations are presented in Section 3.4.

3.1 0-lepton analysis strategy

The final states from \tilde{q} and \tilde{g} decays can be produced by several SM processes, so possible signal events can be concealed by them. Separating signal and background events can be done by designing an analysis that targets part(s) of the phase space expected to be dominated by the events coming from signal. This is achieved by defining several signal regions (SR), imposing different selection criteria. The SRs aim at suppressing the expected background coming from the SM processes, while keeping the largest possible amount of signal. Different variables are used for these purposes, and the most effective are the ones that have a different shape for the background and the signal processes (as explained in Section 3.1.3). After imposing all the selection criteria, there are still events coming from the background processes in the SRs. In order to control these events and distinguish them from signal events, it is very important that they are well modelled by the MC generated events. To improve the MC prediction those backgrounds are normalised in dedicated control regions (CR), and then are extrapolated to

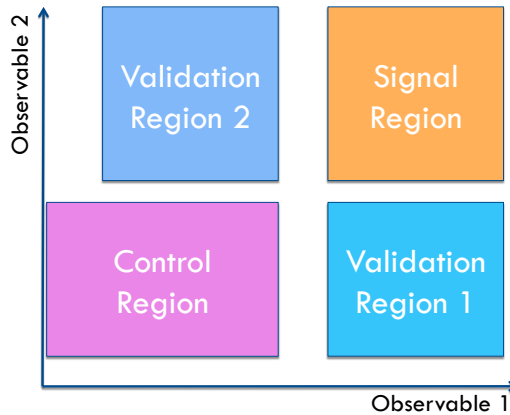


Figure 3.1: 0-lepton analysis strategy.

the SRs. To ensure that this procedure really correctly takes all the effects into account, the normalisation is checked in validation regions (VR). This procedure is summarised by Figure 3.1.

The background estimation in SR proceeds via a likelihood fit that uses the observed number of events in the CRs. The most important quantities are Transfer Factors - the ratios of expected number of events coming from the given background processes in the SR with respect to the CR. They allow to convert the observed number of events in the CR ($N(\text{CR}, \text{obs})$) into the estimate of that background in the SR ($N(\text{SR}, \text{scaled})$):

$$N(\text{SR}, \text{scaled}) = N(\text{CR}, \text{obs}) \times \left[\frac{N(\text{SR}, \text{unscaled})}{N(\text{CR}, \text{unscaled})} \right], \quad (3.1)$$

where $N(\text{SR}, \text{unscaled})$ and $N(\text{CR}, \text{unscaled})$ are the number of events estimated from the MC for the given process in the SR and CR, respectively. The transfer factor is the quantity given in the square brackets. The shape of the variables used for the selection are supposed to be properly reproduced by the MC.

This analysis is designed by imposing consecutive selection criteria (cuts). Then one counts the number of events seen in data and compares with a likelihood analysis that number with the SM prediction left in the SRs after all cuts. If those numbers are in agreement, SM predictions are confirmed and there is no new physics contributing to those SRs. An excess of events in data with respect to the background expectations would be the sign of new physics.

The main backgrounds of the 0-lepton search come from the production of Z or W boson in association with jets, the production of top pairs ($t\bar{t}$) and the multi-jet production. The contribution of these processes to the SR event counts is estimated using dedicated CRs. There are also some backgrounds with a smaller cross-section like diboson and single top production, which do not have dedicated CRs and are taken directly from MC prediction.

3.1.1 Background processes

The main backgrounds of this search are the ones that lead to high- p_T jets and large (possibly fake) E_T^{miss} . High- p_T jets are produced in multi-jet events and, large fake E_T^{miss} can be produced through the mismeasurement of jets. There could be large genuine E_T^{miss} in W , Z or $t\bar{t}$ production but accompanied by lepton. To reduce these backgrounds, a veto on light leptons is introduced. The remaining backgrounds from these processes is thus coming from events with a misidentified light lepton or hadronically decaying taus. All these backgrounds are discussed in this Section.

Multijet production The production cross-section of multijet events at the LHC is very large. They come mostly from two-parton interactions resulting in high- p_T dijet events.

The emission of gluons from both ISR and FSR gives additional jets. Large E_T^{miss} can result from misreconstruction of jets. The fake E_T^{miss} is usually aligned with one of the jets in the event, which helps in reducing this background.

$t\bar{t}$ and single top production come from quark anti-quark interaction ($q\bar{q} \rightarrow t\bar{t}$) or gluon fusion ($gg \rightarrow t\bar{t}$). Gluon fusion dominates. Top quark decays to $W + b$ ($t \rightarrow Wb$), and genuine E_T^{miss} is produced from W leptonic decays. The final state comprises four or more jets.

W +jets production has cross-section that decreases by $1/\alpha_S$ with each additional jet. It contributes to SRs with lower jet multiplicity.

Z +jets production The branching ratio of Z to lepton is much smaller than the leptonic W branching ratio, however $Z \rightarrow \nu\bar{\nu}$ has a 20% branching ratio and constitutes an irreducible background. As for $W + \text{jets}$ production, $Z + \text{jets}$ contributes more to lower jet multiplicity SRs.

Diboson production encompasses WW , WZ and ZZ production and has a much lower production cross-section than W or Z +jets production cross-section.

3.1.2 Object definition

The objects used in the analysis are described in the following. The object selection is outlined here, while the object reconstruction is described in Section 2.3.

Jets are reconstructed with the anti- k_t jet algorithm from the topological clusters reconstructed in the calorimeters with the distance parameter $R = 0.4$. This analysis uses local cluster weighting (LCW) calibration method. Also the jet energy scale (JES) correction is applied. Except for the E_T^{miss} computation, two minimal requirements on the acceptance are imposed: $p_T > 20 \text{ GeV}$ and $|\eta| < 2.8$. When performing overlap removal (Subsection 3.1.2) all jets satisfying this loose selection are considered.

Stringent selection is applied to jets that enter the regions of this analysis: higher p_T requirement and also jet quality criteria. Those are applied to jets after the overlap removal, and the events containing at least one jet which does not satisfy these demands are rejected.

b -jets are identified using the MV1 jet tagger at the 70% efficiency operating point. In this analysis, only jets with $p_T > 40 \text{ GeV}$ and $|\eta| < 2.5$ are tagged as b -jets.

Electrons candidates are reconstructed and identified with the `medium++` purity cuts. In addition to those cuts, the $E_T = E^{\text{clust}} / \cosh \eta$ of electrons should exceed 10 GeV, where η is taken to be η^{track} if the track contains at least 4 silicon hits and η^{clust} otherwise. Furthermore, $|\eta^{\text{clust}}|$ should be less than 2.47. All electrons that fulfill these requirements are considered when the overlapping objects are resolved (Subsection 3.1.2).

More conditions have to be met by electrons entering the CRs selections (referred to as signal electrons) concerning their quality and isolation (Table 3.1).

Muons are reconstructed by an algorithm which performs a combination of a track reconstructed in the muon spectrometer with its corresponding track in the inner detector. In addition, these muon candidates must fulfill a list of quality requirements and be isolated: $\sum p_T(\text{tracks})$ in a cone of $\Delta R < 0.2$ must be less than 1.8 GeV (excluding the muon track). Finally the acceptance cuts of $p_T > 10 \text{ GeV}$ and $|\eta| < 2.4$ are applied. A

Cut	Value/description		
	Preselected Electron	Preselected Muon	Preselected Photon
Acceptance	$p_T > 10 \text{ GeV}$ $ \eta^{\text{clust}} < 2.47$	$p_T > 10 \text{ GeV}$ $ \eta < 2.4$	$p_T > 130 \text{ GeV}$ $ \eta^{s2} < 1.37$ $1.52 < \eta^{s2} < 2.47$
Quality	MediumPP	Loose	Loose
Overlap	$0.2 < \Delta R(e, jet) < 0.4$		
	Signal Electron	Signal Muon	Signal Photon
Quality	TightPP		Tight
Isolation	$\text{ptcone20}/p_T < 0.10$	$\sum p_T \text{ in } \Delta R \text{ cone of } 0.2 < 1.8 \text{ GeV}$	$E_T^{\text{topo40}} < 4 \text{ GeV}$
PV constrains	$ d_0^{PV} < 1 \text{ mm}$ $ z_0^{PV} < 2 \text{ mm}$	$ d_0^{PV} < 1 \text{ mm}$ $ z_0^{PV} < 2 \text{ mm}$	

Table 3.1: Summary of the object selection criteria. The ‘Signal’ object criteria are applied for the selected object to enter CRs.

summary of the muon definition cuts can be found in Table 3.1. These are the muons that are considered for the overlap removal (Subsection 3.1.2).

‘Signal muons’ used for CRs must satisfy additional requirements on quality and isolation (Table 3.1).

Photons candidates are required to pass the `loose` identification criteria and to have a transverse energy of at least 130 GeV to pass the unprescaled single photon trigger requirement. The overlap removal with jets is performed using these preselected photons (Subsection 3.1.2).

‘Signal’ photons must also fulfill ‘tight’ quality criteria, and have to be isolated ($E_T^{\text{topo40}} < 4 \text{ GeV}$), as described in Table 3.1.

Missing transverse momentum The main differences in the E_T^{miss} algorithm used in this analysis with respect to the standard `MET_RefFinal` algorithm are: the absence of the hadronically decaying τ -leptons term, and a slightly redefined muon term which contains only the muons passing the selection defined in this analysis. The lack of a specific `Tau` term means that hadronic taus are included either in the `Jet` term or in the `Soft` term depending on the p_T of their associated jet.

Taus are studied in much more details in Chapter 4. They are reconstructed using a p_T -correlated track counting algorithm as defined in Ref. [87, 88] and only τ candidates with track multiplicity of one are selected. τ candidates that overlap with a medium electron within $\Delta R < 0.2$ are rejected. Only τ candidates with $p_T > 20 \text{ GeV}$ are considered, and in case there are multiple τ candidates the one with the highest p_T is chosen.

Resolving overlapping objects

Some candidate objects defined in the previous Section can overlap with each other, which in most cases is the consequence of the same object being identified with several algorithms (all but one falsely identifying the object). Thus care should be taken when deciding which identification to trust. This has been studied in Ref. [89], and the following classification has been shown to be optimal:

1. If an electron and a jet are found within $\Delta R < 0.2$, the decision is taken that the object is an electron and the overlapping ‘jet’ is ignored.
2. If a muon and a jet exist in distance $\Delta R < 0.4$ of each other, the object is treated as a jet and the muon is discarded.
3. If an electron and a jet are present within $0.2 \leq \Delta R < 0.4$, the object is interpreted as a jet and the nearby ‘electron’ is ignored.
4. If a photon and a jet are within $\Delta R < 0.2$, the object is interpreted as a photon and the overlapping ‘jet’ is ignored.

jet within	$\Delta R < 0.2$	$0.2 < \Delta R < 0.4$	$\Delta R < 0.4$
electron	electron		
muon			muon
electron		jet	
photon	photon		

Table 3.2: Overlap removal table.

3.1.3 Discriminating variables

The discriminating variables are variables that have a different shape for the expected signal and the backgrounds, therefore allowing one to distinguish between them. They are used to suppress the contribution of the SM processes in the SRs.

As the signal is expected to be produced at a high mass, the corresponding final states are expected to contain high- p_T jets, with a jet multiplicity depending on the considered signal. Also large quantity of E_T^{miss} is expected to come from the undetected neutralino. This leads to a first selection of the events with large E_T^{miss} and high- p_T jets.

Next one can try to suppress the multi-jet background: a very effective variable with this respect is the minimum angle in the transverse plane between jets and E_T^{miss} . This background is shown to be at low values for this variable (fake E_T^{miss} in that jet direction).

Many variables were considered when the optimisation of SRs was performed, but it was shown that the effective mass m_{eff} is giving the best results. m_{eff} is defined as the scalar sum of the p_T of the jets in the event and E_T^{miss} .

$$m_{\text{eff}} = \sum_{i=1}^n |p_T^{(i)}| + E_T^{\text{miss}}. \quad (3.2)$$

Two definitions of m_{eff} are used in the 0-lepton analysis: $m_{\text{eff}}(N_j)$ constructed from the leading N jets in the event, and $m_{\text{eff}}(\text{incl.})$ constructed from all jets with $p_T > 40$ GeV is used for the final m_{eff} selection.

Another variable that proves useful is H_T defined as the sum over p_T of the jets:

$$H_T = \sum_{i=1}^n p_T^{(i)}. \quad (3.3)$$

The ratios between E_T^{miss} and m_{eff} , or E_T^{miss} over $\sqrt{H_T}$, when used together with m_{eff} depending on the jet multiplicity of the final state targeted by the SR, have a very performant discriminating power in reducing the remaining background.

3.2 Dataset and Monte Carlo samples

3.2.1 Dataset

The dataset used in this analysis has been recorded by the ATLAS detector, with stable beams and nominal magnetic field conditions in 2012 at a centre-of-mass energy of 8 TeV. In that period the peak instantaneous luminosity increased from 2.74×10^{30} to 7.61×10^{33} $\text{cm}^{-2}\text{s}^{-1}$ and the peak mean number of interactions per bunch crossing increased from 5.9 to 36.53. The total recorded integrated luminosity is 21.7 fb^{-1} . After requiring that all sub-detectors systems are functioning correctly, meaning the data is of good quality, this number falls to 20.3 fb^{-1} . The preliminary uncertainty is $\pm 2.8\%$ based on the calibration procedure described in [90]. The analysis uses data from the `JetTauEtmis` stream in the SRs, while in the CRs the `Egamma` and `Muons` data streams are used.

3.2.2 Monte Carlo samples

All the background processes detailed in Section 3.1.1 are simulated using MC generators to predict the expected number of SM events and the corresponding shapes of the discriminating variables in various regions of the analysis. MC generators are also used for the signal prediction. All samples use $\sqrt{s} = 8 \text{ TeV}$ with a single configuration of the detector corresponding to the beginning of the 2012 data taking. Samples generated for SM processes and mSUGRA signal samples are passed through the `GEANT4` [65] based detector simulation with parameters defined by the central production simulation, while the signal samples for simplified models are passed through the fast detector simulation `AtlFast-II` [66].

3.2.2.1 Simulation of the pile up

To get a realistic description of the events, every background or signal event is overlaid with additional minimum bias events which are generated with `Pythia 8` [48], the `AM2` tune [91] and the leading-order PDF set `MSTW2008LO` [92]. The MC12a pile-up distribution in term of average number of interactions per event $\langle\mu\rangle$ covers a range between $\langle\mu\rangle = 0$ and $\langle\mu\rangle = 40$.

3.2.2.2 Background samples

For every background process two independent event generators are used in order to control their description. One of them is used as baseline and the other as alternative, with a choice based on the post-fit agreement between data and the MC expectation in the CRs for these processes (Section 3.4.3.1). The summary of all the generators that have been used, the order of the cross-section calculation, the set of corresponding tuning parameters (tune) and the PDF set, are outlined in Table 3.3, and further description is given in the following.

W+jets samples were generated using `SHERPA 1.4.0` [45] and `ALPGEN 2.14` [50].

The events generated with `SHERPA`, are generated with the use of the `CT10` [93] next-to-leading order (NLO) parton density function (PDF). Up to four or five extra partons were generated at the matrix-element level. The merging of the hard scatter events with the parton shower description was performed using the `CKKW` prescription [94, 95, 96]. These samples were generated with massive b - and c -quarks thus giving a better description of the flavour composition.

In the case of the `ALPGEN` generator also up to four or five extra partons were generated at the matrix-element level. In this case a different jet matching scheme was used: the `MLM` scheme [97]. Parton shower and fragmentation processes are simulated using

Herwig 6.520 [46, 47] with JIMMY [56] using the AUET2 tune for the description of the underlying event, and the CTEQ6LI [98] as the PDF set.

A generator-level filter ($E_T^{\text{miss}} > 100$ GeV and the leading parton $p_T > 80$ GeV) was applied on these samples to get a higher number of events in the phase space of interest for this analysis. Also the samples were sliced depending on the W p_T to populate tails of the distribution. The processes $W \rightarrow \ell\nu$ are normalised to the reference cross section of 12.19 nb, based on the NNLO prediction [99].

Z/γ^* +jets samples were generated with the same generators as W +jets samples.

$Z \rightarrow \ell\ell$ samples were generated using an invariant mass $m_{\ell\ell} > 40$ GeV. The samples were sliced depending on the Z p_T to populate tails of the distribution. The samples are normalised to NNLO.

γ +jets samples were generated with the same generators as W +jets samples.

They are normalised to the cross-section given by the generator.

Z/γ^* +jets and γ +jets were generated using a very similar setup.

Top quark pair samples were generated with the POWHEG 1.0 [53, 54, 55] and MC@NLO 4.03 [51, 52].

POWHEG-BOX was interfaced to Pythia 6.426 for the fragmentation and hadronisation processes. For the PDF set the CT10 was used, and for the Pythia parameters the Perugia2011C [100, 101] tune. For the generation of these samples the mass of the top quark was fixed to 172.5 GeV.

In generation of the events with MC@NLO 4.03 [51, 52] the CT10 PDF set was used. The production of the underlying event processes was handled by Herwig 6.520 [46, 47] with JIMMY [56].

The $t\bar{t}$ cross-section is calculated to the NNLO in QCD including next-to-next-to-leading-logarithmic (NNLL) resummation of soft gluon terms and it is $253_{-14.5}^{+13.3}$ pb.

Single top samples for s -channel and Wt production were generated using MC@NLO 4.03 [51, 52] with Herwig 6.520 and JIMMY. Since MC@NLO 4.03 does not model well the processes with an initial state b quark, AcerMC 38 [57] was used to generate t -channel events.

The cross sections of these processes are 5.61 ± 0.22 pb for the s channel, $87.76_{-1.91}^{+3.44}$ pb for the t -channel and 22.37 ± 1.52 pb for the Wt channel.

$t\bar{t}$ + W or Z was generated with MadGraph 5.0 [49] interfaced to Pythia 6.426

$t\bar{t}+\gamma$ is not simulated but is partly accounted for with QED FSR from the $t\bar{t}$ sample. $t\bar{t}H$ is completely neglected.

Diboson samples are composed of WW , WZ , ZZ , $W\gamma$ and $Z\gamma$ and they were all simulated with SHERPA 1.40 [45] with up to three partons added at matrix-element level. The b and c quarks were treated as massive except for the processes $W\gamma$ and $Z\gamma$ which were not available with massive quarks at the time of the analysis.

The cross-sections for the processes WW , WZ and ZZ are calculated at NLO.

Triboson samples were generated with MadGraph 5.0 with Pythia 6.426.

Their contribution is found to be negligible thus they were not used in the analysis.

QCD multijet samples were simulated using `Pythia 8.160` with the CT10 PDF set and the AU2 tune[102]. They are not used directly to predict the multijet background in the SR and CR, but were used in the design of the dedicated CR.

Table 3.3: The SM background MC simulation samples used in the 0-lepton analysis. The generators, the order of the cross-section calculations, tunes used for the underlying event and the PDF sets are shown. Samples denoted with (●) are used for the evaluation of systematic uncertainties. For the γ +jets process the LO cross-section is taken directly from the MC generator.

Process	Generator + frag./had.	Order of the cross-section calculation	Tune	PDF set
W +jets	SHERPA-1.4.0 [45]	NNLO [99]	SHERPA default	CT10 [93]
W +jets (●)	ALPGEN-2.14 [50] + HERWIG-6.520 [46, 47]	NNLO [99]	AUET2B [103]	CTEQ6L1 [98]
Z/γ^* +jets	SHERPA-1.4.0	NNLO [99]	SHERPA default	CT10
Z/γ^* +jets (●)	ALPGEN-2.14 + HERWIG-6.520	NNLO [99]	AUET2B	CTEQ6L1
γ +jets	SHERPA-1.4.0	LO	SHERPA default	CT10
γ +jets (●)	ALPGEN-2.14 + HERWIG-6.520	LO	AUET2B	CTEQ6L1
$t\bar{t}$	PowHeg-1.0 [53, 54, 55] + PYTHIA-6.426 [106]	NNLO+NNLL [104, 105]	Perugia [100, 101]	CT10
$t\bar{t}$ (●)	MC@NLO-4.03 [51, 52] + HERWIG-6.520	NNLO+NNLL [104, 105]	AUET2B	CT10
Single top				
t -channel	AcerMC-38 [57] + PYTHIA-6.426	NNLO+NNLL [107]	AUET2B	CTEQ6L1
s -channel, Wt	MC@NLO-4.03 + HERWIG-6.520	NNLO+NNLL [108, 109]	AUET2B	CT10
$t\bar{t}$ +EW boson	Madgraph-5.0 [49] + PYTHIA-6.426	NLO [110, 111, 112]	AUET2B	CTEQ6L1
Dibosons $WW, WZ, ZZ,$ $W\gamma$ and $Z\gamma$	SHERPA-1.4.0	NLO [113, 114]	SHERPA default	CT10

3.2.2.3 Signal samples

Several models are studied in this analysis. The summary of the models used for the optimisation and the interpretation of the 0-lepton analysis results is presented in Table 3.4, along with the parameters that are varied and the MC generator used for the production of the events.

mSUGRA/CMSSM, **SUSY-HIT** [115] interfaced to **SOFTSUSY 3.1.6** [116] is used to generate the mass spectrum for each set of parameters and to calculate the expected decays and to guarantee consistent electroweak symmetry breaking. The mass of the top quark is set to 173.2 GeV for these calculations. The samples were generated with **Herwig++ 2.5.2** [46, 47] with the underlying event tune **UE-EE-3** [117] and the **CTEQ6LI** PDF set. The events are then passed through the full detector simulation. The choice of the $\tan\beta$, A_0 and μ values has been done in order to have a $(m_0, m_{1/2})$ parameter space compatible with the 125 GeV Higgs mass.

Simplified models were generated using **MadGraph 5.0** interfaced to **Pythia 6.426** for the parton shower and SUSY decays. The PDF set used is **CTEQ6LI**. They were generated with one extra parton in the matrix element. The modelling of the ISR and the FSR is important in compressed scenarios as they lead to soft jets. The merging of the matrix element and the parton shower is performed using the MLM procedure [97], with the

matching scale set to $\min(500 \text{ GeV}, m_{\text{SUSY}}/4)$. The generated events are then passed through the fast detector simulation `At1Fast-II` [66].

The signal cross-sections are calculated using NLO calculations and the NLL resummation of soft gluon emission (NLO+NLL) [118, 119, 120, 121, 122]. The nominal cross-section and its uncertainty are calculated using a procedure that averages calculations using various PDF sets, values of α_s and factorisation and renormalisation scales.

Grid Name	Parameters	MC generator
Complex models		
MSUGRA/CMSSM	$\tan \beta = 30$, $A_0 = -2 \times m_0$, $\mu > 0$, $m_0 \in [400, 6000] \text{ GeV}$ with 200 GeV step, $m_{1/2} \in [400, 1000] \text{ GeV}$ with 50 GeV step	HERWIG++
Squark, gluino, neutralino pheno. MSSM	$m(\tilde{q}) \in [400, 4000] \text{ GeV}$ with 200 GeV step $m(\tilde{g}) \in [400, 4000] \text{ GeV}$ with 200 GeV step $m(\tilde{\chi}^0) = \{0, 395, 695\} \text{ GeV}$	MADGRAPH5+ PYTHIA6
Simplified models		
Squark pair production, direct decay $\tilde{q} \rightarrow q\tilde{\chi}^0$	$m(\tilde{q}) \in [87, 1575] \text{ GeV}$, $m(\tilde{\chi}^0) \in [0, 1200] \text{ GeV}$	MADGRAPH5+ PYTHIA6
Gluino pair production, direct decay $\tilde{g} \rightarrow q\bar{q}'\tilde{\chi}^0$	$m(\tilde{g}) \in [87, 1800] \text{ GeV}$, $m(\tilde{\chi}^0) \in [0, 1200] \text{ GeV}$	MADGRAPH5+ PYTHIA6
Squark pair production, 1-step decay $\tilde{q} \rightarrow q(W^\pm\tilde{\chi}^0)$ via an intermediate $\tilde{\chi}^\pm$	$200 < m(\tilde{q}) < 1500 \text{ GeV}$ fixed $m(\tilde{\chi}^0) = 60 \text{ GeV}$ or fixed $x = (m_{\tilde{\chi}^\pm} - m_{\tilde{\chi}^0}) / (m_{\tilde{q}} - m_{\tilde{\chi}^0}) = 0.5$	MADGRAPH5+ PYTHIA6
Gluino pair production, 1-step decay $\tilde{g} \rightarrow q\bar{q}'(W^\pm\tilde{\chi}^0)$ via an intermediate $\tilde{\chi}^\pm$	$200 < m(\tilde{g}) < 1500 \text{ GeV}$, fixed $m(\tilde{\chi}^0) = 60 \text{ GeV}$ or fixed $x = (m_{\tilde{\chi}^\pm} - m_{\tilde{\chi}^0}) / (m_{\tilde{g}} - m_{\tilde{\chi}^0}) = 0.5$	MADGRAPH5+ PYTHIA6

Table 3.4: Settings for the different SUSY signal grids used in this analysis.

3.3 Event selection

This Section describes the selection of events entering the SRs, CRs and VRs of the 0-lepton analysis. A description of the cuts on the quality of the events is first given, then those designed to suppress the backgrounds and select the regions of phase space that are supposed to be sensitive to new physics are described.

First, a selection of good runs and luminosity blocks (periods of ~ 1 -2min of data taking) is applied to real data to ensure that the detector is performing nominally for all events analysed. Then trigger (Section 3.3.1) and event cleaning cuts (Section 3.3.2) are applied. The selection specific to the definition of the SRs is presented in Section 3.3.3. The definition of the CRs corresponding to SRs is given in Section 3.3.4. The VRs used to test the background predictions are outlined in Section 3.3.5.

3.3.1 Trigger

Signal region trigger As this analysis looks at the final states with jets and $E_{\text{T}}^{\text{miss}}$, it is expected to use either jet, $E_{\text{T}}^{\text{miss}}$, or combined trigger. Using only jet trigger is very difficult because of the large rates coming from the SM QCD processes, as a consequence unrescaled jet trigger has very high thresholds.

The baseline trigger for the SRs is a combined jet + E_T^{miss} trigger [123, 124] EF_j80_a4tchad_xe100_tclcw_veryloose. It requires at least one jet with $p_T > 80$ GeV (reconstructed from topoclusters by the anti- k_T algorithm with $\Delta R = 0.4$) and $E_T^{\text{miss}} > 100$ GeV. It uses the LCW calibration scheme. It is seeded by the L1 trigger L1_j50_xe40 and the L2 chain L2_j75_c4cchad_xe55. In Figure 3.2 the efficiency of the considered trigger is shown as a function of the p_T of the leading jet (Figure 3.2a) and the value of E_T^{miss} (Figure 3.2b). Those plots help guiding the offline selection of events, by defining the cuts in such a way that the selected events belong to the plateau of the trigger.

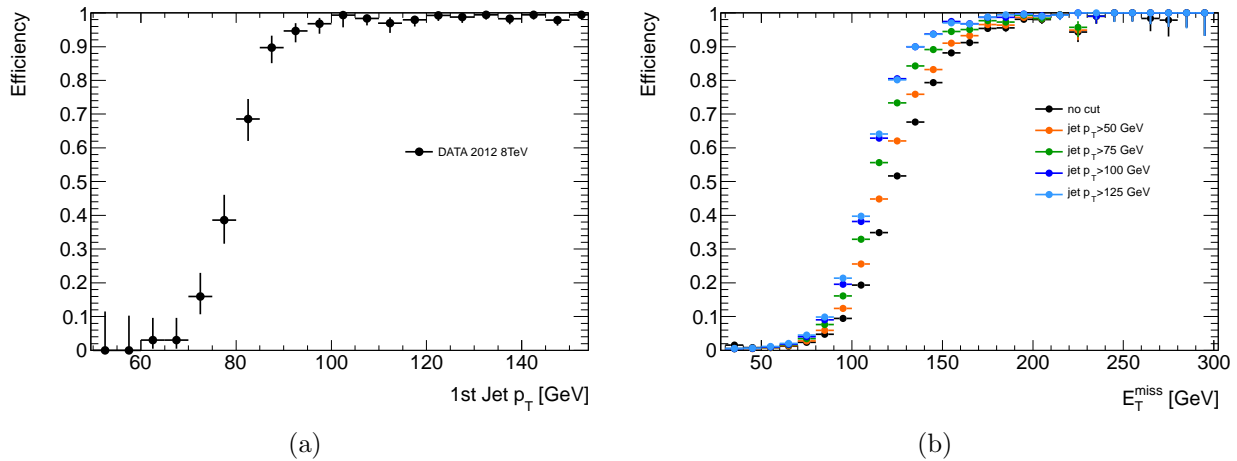


Figure 3.2: Efficiency curves of the jet and E_T^{miss} terms of the EF_j80_a4tchad_xe100_tclcw_veryloose trigger. The E_T^{miss} turn-on is bootstrapped from the EF_xe50_a4tchad, after a cut on jet p_T of 130 GeV has been applied. The jet turn-on is also bootstrapped from the same trigger, and shown for the ‘LCW’ jet calibrations

Control region triggers The CRs selection designed for the estimation of the $W + \text{jets}$ and $t\bar{t}$ backgrounds rely on the presence of leptons. They use unprescaled single-lepton triggers. The same triggers are used for VRZ. The CR that requires photons (CRY) is built around the single photon trigger. The QCD seed events are selected using the nine triggers on single jet with p_T varying from 55 to 460 GeV. They are then weighted with the average prescale for the data taking period they come from.

3.3.2 Event cleaning

The E_T^{miss} in the event can be mismeasured because of non-collision background, bad calorimeter regions and fake muons. As the E_T^{miss} is one of the most important physics objects in the 0-lepton analysis selection, dedicated cuts to reject these are needed.

3.3.2.1 Non-collision background

Some of the events recorded by the ATLAS experiment do not come from the colliding beams - those are referred collectively as the non-collision background. There are several sources of them: coherent noise in the liquid argon electromagnetic calorimeters, spike noise in the liquid hadronic calorimeter, cosmic-rays and beam halo events and also beam gas events. They cannot be trivially rejected when they occur in time with real beam collisions. Several procedures are developed to suppress them.

The events with noise in the electromagnetic calorimeter that have data integrity problems like missing readout elements, or other hardware problems are rejected and the luminosity calculation accounts for this removal. Additionally, the events are not taken into account if they are recorded within the time window of a noise burst, and when there is significant noise detected in the electromagnetic calorimeter. The inefficiency of this selection is found to be negligible.

The effects of the non-collision background may show up as energy deposits in the calorimeters that are reconstructed as jets. The jet properties can be used to disentangle those 'fake' jets from the real ones originating from the hard scattering. The variables that are found useful in this respect are: f_{ch} - jet charged fraction defined as sum of the p_T of the tracks associated to the jet divided by the p_T of the jet, f_{em} - energy fraction in the electromagnetic calorimeter, f_{hec} - energy fraction in the hadronic end-cap calorimeter, t_{jet} jet timing defined as the mean time using energy squared weighting.

First the events that satisfy the Looser jet criteria are vetoed. A so called jet charge fraction quality criteria is also required to reject the jets that originate from cosmics, beam background or detector noise by rejecting the events with a leading jet that satisfies ($f_{ch} < 0.02$ and $|\eta| < 2.0$) or ($f_{ch} < 0.05$ and $f_{em} > 0.9$ and $|\eta| < 2.0$). The inefficiency of this cut is smaller than 1%.

The jets that come from the hard scattering are expected to be reconstructed within $t \sim 0$, while the ones that are the consequence of the non-collision background are reconstructed out of time. Thus one can use this information to eliminate some of the non-collision background. It is incorporated in the energy-weighted mean time of the leading N jets which is defined as:

$$t_{N_j} = \frac{\sum_{i=0}^{N_j} t_i \cdot E_i}{\sum_{i=0}^{N_j} E_i} \quad (3.4)$$

where t_i is the i -th jet timing and E_i is its energy. The events with mean jet time $|t_2| > 4\text{ns}$.

To estimate the remaining non-collision background one defines CRs that are orthogonal to SRs by inverting the timing cut - $|t_{N_j}| < 5\text{ns}$, where N_j is the minimal number of selected jets in each SR. The upper limit on the contribution of this background in SRs with at least two jets is found to be 0.39 events, which makes it completely negligible in this SR. For the channels with higher number of jets, it is found that after $|t_{N_j}| > 4\text{ns}$ and without the imposed criteria on the jet charged fraction, there are no events, which proves that this background is also negligible in higher jet multiplicity channels.

The Tile calorimeter problems manifest themselves through cells and topoclusters with large negative energy. Those events are not rejected by the requirement on the quality of the jets as the topoclusters with large negative energy are not clustered and reconstructed as jets. Those cells instead fall into $(E_T^{\text{miss}})^{\text{Cellout}}$ term, and are subsequently rejected if their contribution to E_T^{miss} is significant:

$$\frac{(E_T^{\text{miss}})^{\text{Cellout}}}{E_T^{\text{miss}}} \cos(\phi((E_T^{\text{miss}})^{\text{Cellout}}) - \phi(E_T^{\text{miss}})) > 0.5 \quad (3.5)$$

The Tile detector had 0.5% to 2% non-operating cells during 2012 - called "dead" regions. If a jet falls into one of these cells it will not be properly reconstructed, that will manifest also like additional E_T^{miss} . This can be corrected by using two methods: one assumes that the "dead" cell has the same energy density like the average of closest cells, while the other estimate the energy loss by shape profile method - the jet shape is obtained from the simulation and used to get the estimate of the energy in the "dead" cells. The latter method is found to perform better and subsequently used. However sometimes this procedure can undercorrect the jet energy and create fake E_T^{miss} . Events are rejected if a corrected jet is aligned to the E_T^{miss} .

The summary of the event cleaning procedure is given in Table 3.5 (cuts 4-8), where the selection criteria common to all SRs of the 0-lepton analysis is summarised.

3.3.3 Signal region selection

3.3.3.1 Event preselection

A veto on light leptons (electrons and muons) is applied to reject $W(\rightarrow l\nu) + \text{jets}$ events and $t\bar{t}$ (cut 9 of Table 3.5). Only leptons with $p_T > 10$ GeV are vetoed as they are expected to be well reconstructed and identified, and also there is a good understanding of the lepton veto efficiency in this case. As a fully efficient trigger is required, only events with $E_T^{\text{miss}} > 160$ GeV and the leading jet $p_T > 130$ GeV are selected (cut 10 and 11 of Table 3.5), see Figure 3.2. Only jets with $p_T > 60$ GeV are considered to define the topology of the event, as those are unlikely to originate from pile-up, this requirement also improves background rejection.

3.3.3.2 Signal regions

The main difference between SRs is in the minimal number of jets they require. The analysis has 5 channels, with at least 2, 3, 4, 5 and 6 jets, which are further differentiated into 15 inclusive SRs. The channels with lower number of jets target models with squark pair production followed by short decay chains, while the channels with higher jet multiplicities are designed to search for gluino pair production and/or longer decay chains.

There are also two SRs requiring two reconstructed hadronic W -bosons. Those are identified either from one high mass jet, or formed from two jets, either way their mass is required to be consistent with the W (cut 17 of Table 3.5) defining two so called "boosted W " SRs.

The next step in the selection is the suppression of the multi-jet background. As explained before (Section 3.1.3) this is achieved by keeping the events which do not have E_T^{miss} aligned on the leading jets. For the channels with the minimal number of jets of two and three, the angle between E_T^{miss} and each of the first two (three) most energetic jets is required to be larger than 0.4. For the other channels, in addition to this, there is also a requirement that $\Delta\phi(j, E_T^{\text{miss}}) > 0.2$, for all the jets in the event with $p_T > 40$ GeV.

Further suppression of the multi-jet background is achieved with Cut 19 of Table 3.6. This cut, together with the last requirement on m_{eff} defines the SRs. The optimisation procedure shows that both Cut 19 and 20 need to be applied together in order to get the most efficient selection and thus the best performing SRs, that cover different parts of the plane and complement each other. Both are shown to be very efficient in suppressing all background processes, thus are used as the final discriminators between the signal and SM processes.

3.3.4 Control regions

Control regions are defined to be kinematically close, but still to be orthogonal to SRs. They are used to normalise the backgrounds that are coming from the SM processes. Each SR has four associated CRs enriched in one of the afore mentioned SM processes in Section 3.1.1: the CR for $Z(\rightarrow \nu\nu) + \text{jets}$ (CRZ), multi-jet (CRQ), $W \rightarrow l\nu + \text{jets}$ (CRW) and $t\bar{t}$ and single top (CRT). The CRs are defined to be close to the SR in order to minimise the uncertainties coming from the extrapolation.

Table 3.7 gives a short overview of the objects used in the selection of the SR and corresponding CRs. A detailed explanation is given later in the text.

Table 3.8 shows the background targeted by each CRs, the process used in its definition and also the selection applied to get a pure sample of the targeted process.

3.3.4.1 Control region for multi-jet background

The multi-jet background is estimated using a fully data-driven method - the jet smearing method [125]. The CR for the multi-jet events (CRQ) is defined by reversing and tightening

Cut	Description	Channel													
		2j				3j	4j				5j	6j			
		2jl	2jm	2jt	2j(W)		4j(W)	4jl-	4jl	4jm	4jt		6jl	6jm	6jt
1	DQ (data)	Run / lumi block appears in SUSY GRL data12.8TeV.periodAllYear _DetStatus-v61-pro14-02.DQDefects-00-01-00_PHYS.StandardGRL.All.Good.xml													
2	Trigger	EF_j80_a4tchad_xel100_tclcw_veryloose													
3	Prim. vtx.	Leading primary vertex with > 4 tracks													
4	Ev. clean - LAr (data)	larError == 0 and tileError!=2 and coreFlag0&x40000 ==0													
5a	Ev. clean - jets Looser (data)	No Looser bad jets after jet-lepton overlap removal with $p_T > 20$ GeV and any η													
5b	Ev. clean - jets (data and MC)	Reject if leading up to 2 selected jets with $p_T > 100$ GeV after overlap removal possess ($chf < 0.02$ and $ \eta < 2.0$) or ($chf < 0.05$ and $emf > 0.9$ and $ \eta < 2.0$)													
5c	Ev. clean - jet timing	Energy-weighted mean time of leading N selected jets after overlap removal in N jet analysis $ \langle t \rangle < 4$ ns.													
6	Ev. clean - Tile data corruption	Veto event if $(MET_CellOut/E_T^{miss}) \times \cos(MET_CellOut.\phi - MET.\phi) > 0.5$													
7a	Ev. clean - cosmics	Only for control regions with muons: no selected muons after overlap removal with ($fabs(mu_staco_z0_exPV) \geq 1$) or ($fabs(mu_staco_d0_exPV) \geq 0.2$)													
7b	Ev. clean Bad muon veto	No selected muons before overlap removal with $\sqrt{mu_staco_cov_qoverp_exPV}/fabs(mu_staco_qoverp_exPV) \geq 0.2$													
7c	Ev. clean Bad muon veto	Veto event if $(MET_MUON/E_T^{miss}) \times \cos(MET_MUON.\phi - MET.\phi) > 0.5$													
8	Ev. clean Dead tile drawers	Veto event if any selected jet with $p_T > 40$ GeV and $BCH_CORR_JET > 5\%$ satisfies $\Delta\phi(j_i, E_T^{miss}) < 0.3$													
9	Lepton veto	No selected e/μ after overlap removal with $p_T > 10$ GeV.													

Table 3.5: Preselection for the SRs used in the 0-lepton analysis. See text for definitions of quantities used in the cuts and their motivations. The channel label 'l-', 'l', 'm', 't', 't+' correspond to 'very loose', 'loose', 'medium', 'tight' and 'very tight' m_{eff} selections respectively.

Cut	Description	Channel														
		2j				3j	4j				5j	6j				
		2jl	2jm	2jt	2j(W)		4j(W)	4jl-	4jl	4jm	4jt		6jl	6jm	6jt	6jt+
10	$E_T^{miss} [\text{GeV}] >$	160														
11	$p_T(j_1) [\text{GeV}] >$	130														
12	$p_T(j_2) [\text{GeV}] >$	60														
13	$p_T(j_3) [\text{GeV}] >$		-			60			60		60			60		
14	$p_T(j_4) [\text{GeV}] >$			-			40		60		60			60		
15	$p_T(j_5) [\text{GeV}] >$				-						60			60		
16	$p_T(j_6) [\text{GeV}] >$				-						-			60		
17	W candidates $60 < m(W) < 100$ GeV		-		$2 W \rightarrow j$		$W \rightarrow j +$ $W \rightarrow jj$									
18	$\Delta\phi(j_{1,2,(3)}, E_T^{miss}) >$ $\Delta\phi(j_{i>3}, E_T^{miss}) >$						0.4									
							0.2									
19	$E_T^{miss}/\sqrt{H_T} >$ $E_T^{miss}/m_{\text{eff}}(N_j) >$	8	15	15			10	10			0.2	0.2	0.2	0.25	0.15	
20	$m_{\text{eff}}(\text{incl.}) [\text{GeV}] >$	800	1200	1600	1800	2200	1100	700	1000	1300	2200	1200	900	1200	1500	1700

Table 3.6: SRs used in the 0-lepton analysis. See text for definitions of quantities used in the cuts and their motivations. Note that the $m_{\text{eff}}(N_j)$ constructed from the leading N jets is used in the $E_T^{miss}/m_{\text{eff}}(N_j)$ cut. The $m_{\text{eff}}(\text{incl.})$ constructed from all jets with $p_T > 40$ GeV is used for the final m_{eff} selection. The channel label 'l-', 'l', 'm', 't', 't+' correspond to 'very loose', 'loose', 'medium', 'tight' and 'very tight' m_{eff} selections respectively.

	jet	e/μ	γ	b-jet	W	new E_T^{miss}
SR	≥ 2	veto baseline	≥ 1	$=0$	$30 \text{ GeV} < m_T(\ell, E_T^{\text{miss}}) < 100 \text{ GeV}$	E_T^{miss}
CRY		veto baseline				$E_T^{\text{miss}} + p_T(\gamma)$
CRW		$=1$				$30 \text{ GeV} < m_T(\ell, E_T^{\text{miss}}) < 100 \text{ GeV}$
CRT		$=1$				$30 \text{ GeV} < m_T(\ell, E_T^{\text{miss}}) < 100 \text{ GeV}$
CRQ		veto baseline				
VRZ		$\geq 2\ell$ OS				$66 \text{ GeV} < m_{\ell\ell} < 116 \text{ GeV}$

Table 3.7: Summary of the objects requirements used in the definition of the SR and corresponding CRs. The calculation of the E_T^{miss} is also highlighted.

CR	SR Background	CR process	CR selection
CRY	$Z(\rightarrow \nu\nu)+\text{jets}$	$\gamma+\text{jets}$	Isolated photon
CRQ	Multijets	Multijets	Reversed $\Delta\phi(j_i, E_T^{\text{miss}})$ and $E_T^{\text{miss}}/\sqrt{H_T}$ or $E_T^{\text{miss}}/m_{\text{eff}}(Nj)$ cuts
CRW	$W(\rightarrow \ell\nu)+\text{jets}$	$W(\rightarrow \ell\nu)+\text{jets}$	$30 \text{ GeV} < m_T(\ell, E_T^{\text{miss}}) < 100 \text{ GeV}$, b -veto
CRT	$t\bar{t}$ and single- t	$t\bar{t} \rightarrow bbq'\ell\nu$	$30 \text{ GeV} < m_T(\ell, E_T^{\text{miss}}) < 100 \text{ GeV}$, b -tag

Table 3.8: CRs used in the analysis, indicating the main SR background targeted, the process used to model the background, and main CR cut(s) used to select this process.

cut 17 from Table 3.6 - the events that have E_T^{miss} aligned with one of the jets. Also the cut 18 of the same Table is reverted, as this was shown to reduce the background coming from $W + \text{jets}$ and $t\bar{t}$ events with tau decaying hadronically. The events selected in this way are seed events. They are then smeared using a smearing function determined in data. The CRQ corresponding to the SR2j is illustrated in Figure 3.3d.

3.3.4.2 Control region for $Z \rightarrow \nu\nu + \text{jets}$

To evaluate the background coming from $Z \rightarrow \nu\nu + \text{jets}$, two processes are considered: the production of $\gamma + \text{jets}$ events (they are supposed to be similar to $Z \rightarrow \nu\nu + \text{jets}$ events when the p_T of Z -boson is much greater than $m(Z)$) and the production of $Z \rightarrow ll + \text{jets}$ events. Consequently two CRs can be defined. The decision of which one to use is based on the expected number of events that are supposed to enter each CR. The CR requiring $\gamma + \text{jets}$ events (CRY) is much more populated, so it is used for estimating $Z \rightarrow \nu\nu + \text{jets}$ background. Nevertheless, the $Z \rightarrow ll$ sample is used to normalise $\gamma + \text{jets}$ to $Z + \text{jets}$, and to validate the results obtained with $\gamma + \text{jets}$. The selection of events is the same as in the corresponding SR, but E_T^{miss} is changed by adding the p_T of the reconstructed photon. The CRY corresponding to the SR2j is illustrated in Figure 3.3a.

3.3.4.3 Control region for semileptonic $t\bar{t}$ events

The CR for $t\bar{t}$ events (CRT) in which one top is decaying leptonically requires a lepton, E_T^{miss} and a reconstructed W -boson which is identified by the transverse mass between the lepton and E_T^{miss} ($m_T(\ell, E_T^{\text{miss}})$). If $m_T(\ell, E_T^{\text{miss}})$ is between 30 GeV and 100 GeV, the event is classified as coming from the top decay. To further enrich the sample of $t\bar{t}$ events at least one jet is required to be a b-jet ($t \rightarrow W + b$). The events that contribute to SRs from $t\bar{t}$ processes contain a lepton that fake jet. This comes either from electron misidentification or when the W decays to hadronically decaying τ identified as jet. The lepton in these events is therefore treated as a jet in the calculation of all the relevant selection quantities which are required to be fulfilled by

	CRW	CRT	VRZ	$\Delta\phi + E_T^{\text{miss}}/m_{\text{eff}}$	ℓ is missing particle	2ℓ	ℓ^+	ℓ^-
VRWf	×			×				
VRWM	×				×			
VRWMf	×			×	×			
VRTf		×		×				
VRTM		×			×			
VRTMf		×		×	×			
VRT2L		×				×		
VRWT+	×	×					×	
VRWT-	×	×						×
VRWTf+	×	×		×			×	
VRWTf-	×	×		×				×
VRZf			×	×				

Table 3.9: Validation regions definitions.

the events entering this CR. Single-top (t -channel, s -channel and Wt) and $t\bar{t} + V$ are taken into account together with $t\bar{t}$ and the same selection of events is applied. The CRT corresponding to the SR2j is illustrated in Figure 3.3c.

3.3.4.4 Control region for $W \rightarrow l\nu$ events

The CR for $W(\rightarrow l\nu) + \text{jets}$ events (CRW) is identical to CRT except that instead of requiring a b -tagged jet, a veto is imposed, which also makes this CR orthogonal to CRT. All the variables used to discriminate the events are recomputed with the lepton considered as a jet, and subsequently the selection of the SR is applied. In this CR also the $Wb\bar{b}$ is accounted for. The CRW corresponding to the SR2j is illustrated in Figure 3.3b.

3.3.5 Validation regions

VRs are used to check the estimation of the background after fit (see Section 3.4.3.1). They are designed to be in between SR and CRs. Their definitions are shown in Table 3.9, where one can see the CR from which their definition is derived, and additional cuts or different treatment of particles applied. For example, VRWMf has the same definition as CRW but with the addition of the $\Delta\phi$ and $E_T^{\text{miss}}/m_{\text{eff}}$ selections applied in the SR, and the lepton is treated as a missing particle instead of being treated as a jet.

The VRs denoted with '+' or '-' are designed to test the lepton charge asymmetry. For example, VRWT+ has the same selection as CRW and CRT, but only considers events with positively charged leptons and has no requirement on b -tagged jets. As W production shows a charge asymmetry, this can be used to statistically separate W and $t\bar{t}$ production.

The VR for $Z \rightarrow \nu\nu + \text{jets}$ (VRZ) selects $Z \rightarrow ll + \text{jets}$ events. It is used to normalise $\gamma + \text{jets}$ to $Z + \text{jets}$, and to validate the results obtained with $\gamma + \text{jets}$. As mentioned before, the production cross-section for this process is much smaller: the branching fraction is three times smaller than for the $Z \rightarrow \nu\nu$ process. Thus the selection of events is looser than in the corresponding SR. The selection is applied to events in which the $p_T(Z)$ was added to E_T^{miss} .

VRT2L is similar to VRZ but with a reversed cut on $m(ll)$ ($m(ll) > 116 \text{ GeV}$). It also requires maximal values of the first and second lepton p_T ($p_T(l_1) < 200 \text{ GeV}$ and $p_T(l_2) < 100 \text{ GeV}$). They are designed to further reject $Z/\gamma^* + \text{jets}$ background. They are sensitive to modeling of the fully leptonic $t\bar{t}$ production.

The VRs for tau leptons are detailed in Section 4.3.

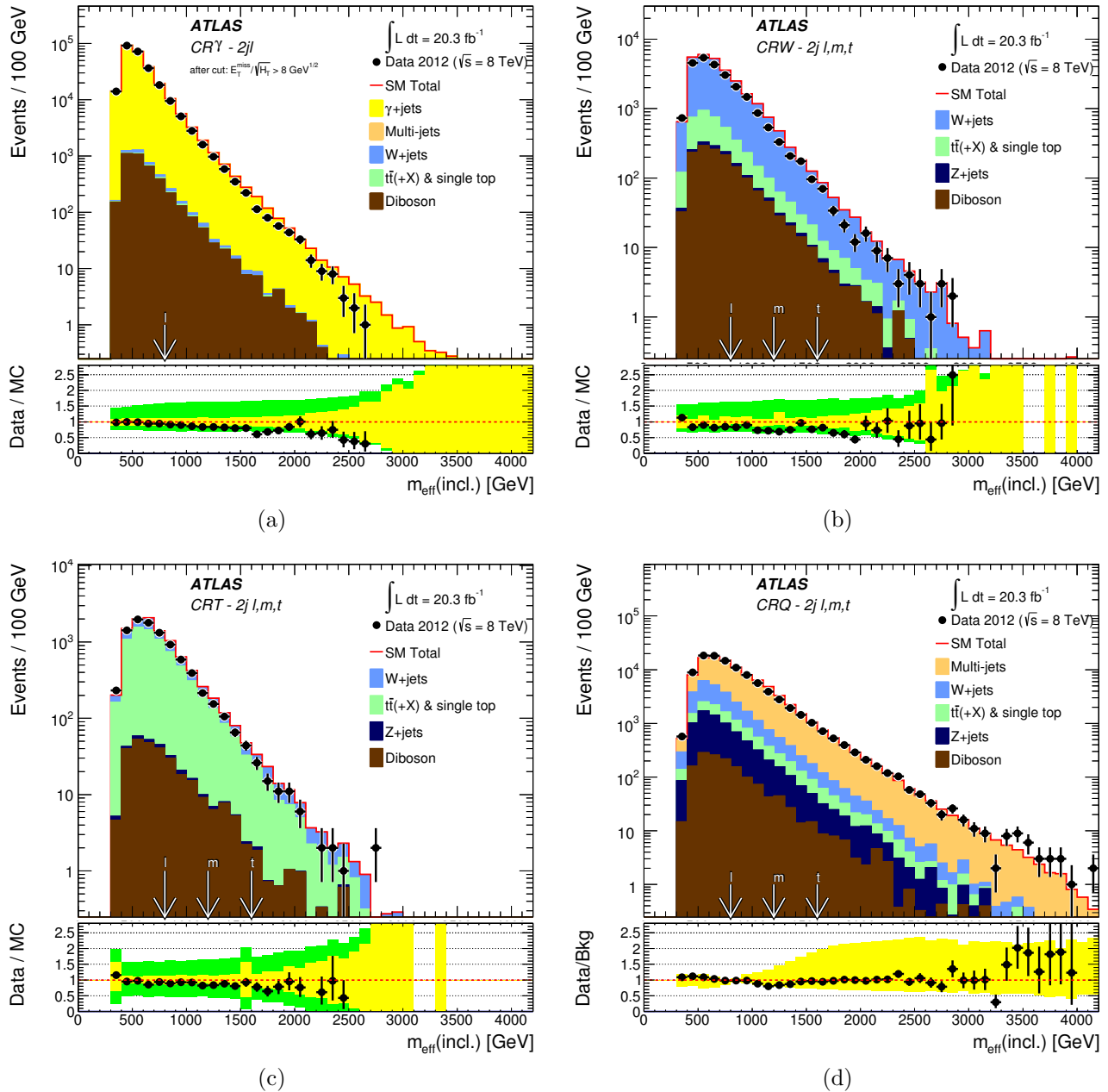


Figure 3.3: Observed $m_{\text{eff}}(\text{incl.})$ distributions in CR γ (top left, for SR 2jl selection criteria only), CRW (top right), CRT (bottom left) and CRQ (bottom right, excluding the requirements on $E_T^{\text{miss}}/\sqrt{H_T}$) corresponding to SRs 2jl, 2jm and 2jt. With the exception of the multi-jet background (which is estimated using the data-driven technique described in the text), the histograms denote the MC background expectations, normalised to cross-section times integrated luminosity. In the lower panels the light (yellow) error bands denote the experimental systematic and MC statistical uncertainties, while the medium dark (green) bands include also the theoretical modelling uncertainty. The arrows indicate the values at which the requirements on $m_{\text{eff}}(\text{incl.})$ are applied.

3.4 Results and interpretation

This Section presents the statistical treatment used to extract the results of the analysis, describes them and discusses their interpretations. The fits rely on the number of expected and observed events in the SRs and CRs that were discussed in the previous Section. The ob-

tained estimates are presented in Section 3.4.3, and are reached by performing several fits: "background", "discovery" and "exclusion fit".

3.4.1 Statistical treatment

The performed statistical tests use a profile log likelihood ratio approach. The ratio obtained from the simultaneous fit of the expected and observed number of events in the SR and the corresponding CRs and the statistical and systematic uncertainties.

The likelihood function is constructed for each SR as a product of Poisson distributions, one for the SR and each of the corresponding CRs, and the probability density function C_{Syst} that constrains the systematic uncertainties:

$$L(\mathbf{n}|\boldsymbol{\lambda}) = P_{\text{SR}} \times P_{\text{CRW}} \times P_{\text{CRT}} \times P_{\text{CRY}} \times P_{\text{CRQ}} \times C_{\text{Syst}}. \quad (3.6)$$

Each Poisson distribution P depends on \mathbf{n} and $\boldsymbol{\lambda}$, where \mathbf{n} denotes the observed number of events in the region, and $\boldsymbol{\lambda}$ represents the expected number of events. The number of expected events in region i (it can be a SR, a CR or a VR), denoted λ_i , can be written as follows:

$$\lambda_i(\boldsymbol{\mu}, s_i, \mathbf{b}, \boldsymbol{\theta}) = s_i(\boldsymbol{\theta}) \cdot \mu_s + \sum_j^{W,Z,t\bar{t},QCD} b_{i,j}(\boldsymbol{\theta}) \cdot \mu_j + b_i^{VV}(\boldsymbol{\theta}) \quad (3.7)$$

where $\boldsymbol{\mu}$ are free normalisation factors, when denoted $\mu_s - s$ refers to the signal, while μ_j refers to the background process. \mathbf{b} represents the expected number of background events, when denoted $b_{i,j}$ it represents the expected number of background events in region i , coming from physics process j , which accounts for the transfer factors when i is a SR. The number of expected events coming from the possible signal are denoted by s_i . $\boldsymbol{\theta}$ are the nuisance parameters that encode the systematic uncertainties (luminosity, JES, ...).

Minor backgrounds like diboson have no associated free parameters, and contribute a fixed amount in the SR and CRs and appears in the $b_i^{VV}(\boldsymbol{\theta})$ term.

The probability density function of the profile log likelihood ration function is calculated in two ways: by employing an asymptotic formula [126] ("Asimov" method), and by considering the MC pseudo experiments. The faster but approximate calculations using the asymptotic formula are used during the optimisation of the analysis and for interpretations in SUSY models. The results obtained with the asymptotic formula and with MC pseudo experiments differ more for SR with a small number of events, as expected.

3.4.2 Systematic uncertainties

There are several sources of systematic uncertainties:

Experimental uncertainties which are related to the reconstruction of the objects. The 0-lepton analysis is mainly sensitive to those related to jets and $E_{\text{T}}^{\text{miss}}$ like: the jet energy scale (JES) and the jet energy resolution (JER) which affect jets and consequently also the $E_{\text{T}}^{\text{miss}}$ calculation. There are also uncertainties coming from the luminosity determination. Other sources of experimental uncertainties are the ones related to b -jets (those are present only in CRT and CRW, but are translated through TF also to SR).

Theoretical uncertainties come from the MC prediction of the signal and background processes. These are assessed by varying the PDF, and factorisation and renormalisation scales. Also the choice of the matrix-element, parton shower, hadronisation and jet matching algorithms are included as uncertainty by comparing two MC generators (baseline and

alternative). One important source of this kind of uncertainties for the signal is ISR that can be large for the models with a small mass difference between sparticles, since the corresponding SR rely on ISR to provide enough boost to produce large enough E_T^{miss} and jet p_T .

Uncertainties on the extrapolation from CR to SR is a statistical uncertainty that comes from the finite statistics available in the CRs, which is translated into an uncertainty on the TF.

As mentioned in Section 3.4.1 those uncertainties are included using the $C_{\text{Syst}}(\theta^0, \theta)$ where θ^0 are the nominal values, which is simply taken as a product of the nuisance parameters in the 0-lepton analysis. The nuisance parameters can be treated as: fully correlated across different regions are physics processes (JES, luminosity, ...); fully correlated across different regions but completely independent per process (MC modelling of different backgrounds, ...); fully uncorrelated (statistical uncertainties) and partially correlated (like it is considered for diboson theoretical uncertainty). Some of them have a negligible impact like luminosity, electron, muon and photon energy scales.

By convention, for the signal the systematic uncertainties on the cross-section, the PDF and the renormalisation and factorisation scales are not included in the likelihood. Instead they are taken into account as variations of the exclusion contour.

3.4.3 Results

The number of observed events in the CRs, direct expectations from simulation and expectations from the fit results are listed in Table 3.10. The quality of the fit prediction for the background is assessed by a "background fit". The compatibility of the results with the SM prediction in SR is quantified by a "discovery fit". Last, "exclusion fits" are performed.

3.4.3.1 Background only fit

First the "background fit" is performed. It normalises all background processes to the data observed in their corresponding CRs with the signal normalisation factor μ fixed to zero. It is used to cross-check the normalisation procedure by comparing the observed number of events in the VRs to the post-fit predictions. However it is not used to estimate the number of expected background events in the SR.

In Figure 3.4 the results of the background fit are shown for the CRs and VRs corresponding to SR2jl. The pull is defined as $(n_{\text{obs}} - n_{\text{pred}})/\sigma_{\text{tot}}$ where n_{obs} is the observed number of events in the VR, n_{pred} is the number of predicted events from the fit in the same region and σ_{tot} is the total uncertainty (systematics and statistics) in the corresponding VR.

The results obtained for all VRs corresponding to all SRs show a good agreement between the number of events estimated from the background processes and the number of observed events in the VRs, which gives good confidence in the fit procedure, as can be seen in Table 3.10.

In Figure 3.5 the observed $m_{\text{eff}}(\text{incl.})$ distributions are shown for the 2-jet (Figure 3.5a), 3-jet (Figure 3.5b), 4-jet (4jl- and 4jl in Figure 3.5c) and 6-jet SRs (Figure 3.5d), before the final selection on this quantity. The different MC samples for the electroweak backgrounds are normalised with the theoretical cross-section. The multi-jet background is estimated using the data-driven method. Examples of SUSY signal (for several points of the simplified models described in Table 3.4) are shown for illustration. The data and the MC predictions do agree within the uncertainties, although the agreement gets slightly worse with the increase of $m_{\text{eff}}(\text{incl.})$.

In Figure 3.6 the comparison between the observed data and the expected yields from the background processes is presented for all the SRs of the 0-lepton analysis. In Figure 3.6a the

Table 3.10: Numbers of events observed in the SRs used in the analysis compared with background expectations obtained from MC prediction and after having performed the fits described in the text. When a dash is shown, the entry is less than 0.01. Combined uncertainties on the predicted background event yields are quoted as symmetric except where the negative uncertainty reaches down to zero predicted events, in which case the negative uncertainty is truncated. The p-values (p_0) for the background-only hypothesis are truncated at 0.5 and are also interpreted in terms of the equivalent Gaussian significance (Z). Also shown are 95% CL upper limits on the visible cross-section ($\langle\epsilon\sigma\rangle_{\text{obs}}^{95}$), the observed number of signal events (S_{obs}^{95}) and the number of signal events (S_{exp}^{95}) given the expected number (and $\pm 1\sigma$ excursions on the expectation) of background events. Limits are evaluated using MC pseudo-experiments as well as asymptotic formulae.

Signal Region	2jl	2jm	2jt	2jW	3j
MC expected events					
Diboson	879	72	13	0.41	0.36
Z/γ^* +jets	6709	552	103	1.2	5.5
W +jets	5472	303	59	0.82	3.1
$t\bar{t}$ (+EW) + single top	1807	54	9	0.14	0.85
Fitted background events					
Diboson	900 ± 400	70 ± 40	13 ± 6	0.41 ± 0.21	0.36 ± 0.18
Z/γ^* +jets	5900 ± 900	430 ± 40	65 ± 8	0.4 ± 0.4	1.7 ± 1.0
W +jets	4500 ± 600	216 ± 26	40 ± 6	1.0 ± 1.0	2.5 ± 0.9
$t\bar{t}$ (+EW) + single top	1620 ± 320	47 ± 8	6.5 ± 2.2	$0.4^{+0.8}_{-0.4}$	$0.4^{+0.5}_{-0.4}$
Multi-jets	115^{+140}_{-120}	$0.4^{+1.4}_{-0.4}$	$0.1^{+0.4}_{-0.1}$	0.03 ± 0.03	$0.03^{+0.06}_{-0.03}$
Total bkg	13000 ± 1000	760 ± 50	125 ± 10	2.3 ± 1.4	5.0 ± 1.2
Observed	12315	715	133	0	7
$\langle\epsilon\sigma\rangle_{\text{obs}}^{95}$ [fb]	60	4.3	1.9	0.16	0.40
$\langle\epsilon\sigma\rangle_{\text{obs}}^{95}$ [fb] (asymptotic)	62	4.0	1.8	0.12	0.40
S_{obs}^{95}	1200	90	38	3.2	8.2
S_{obs}^{95} (asymptotic)	1300	80	37	2.5	8.1
S_{exp}^{95}	1700^{+600}_{-500}	110^{+40}_{-30}	32^{+11}_{-10}	$4.0^{+1.7}_{-0.7}$	$6.4^{+2.9}_{-1.3}$
S_{exp}^{95} (asymptotic)	1600^{+600}_{-400}	110^{+40}_{-30}	31^{+12}_{-8}	$4.1^{+2.4}_{-1.4}$	$6.3^{+3.2}_{-2.0}$
p_0 (Z)	0.50 (0.0)	0.49 (0.0)	0.29 (0.5)	0.50 (0.0)	0.24 (0.7)
Signal Region	4jl-	4jl	4jm	4jt	4jW
MC expected events					
Diboson	175	70	7.2	0.34	2.1
Z/γ^* +jets	885	333	30	2.9	11
W +jets	832	284	16	1.2	6.1
$t\bar{t}$ (+EW) + single top	764	167	4.0	0.6	3.1
Fitted background events					
Diboson	180 ± 90	70 ± 34	7 ± 4	0.34 ± 0.17	2.1 ± 1.0
Z/γ^* +jets	660 ± 60	238 ± 28	16 ± 4	$0.7^{+0.8}_{-0.7}$	5.9 ± 2.1
W +jets	560 ± 80	151 ± 28	10 ± 4	0.9 ± 0.4	2.7 ± 1.6
$t\bar{t}$ (+EW) + single top	730 ± 50	167 ± 18	4 ± 2	0.6 ± 0.6	3.2 ± 3.1
Multi-jets	$1.7^{+4.0}_{-1.7}$	$0.7^{+1.6}_{-0.7}$	-	-	-
Total bkg	2120 ± 110	630 ± 50	37 ± 6	2.5 ± 1.0	14 ± 4
Observed	2169	608	24	0	16
$\langle\epsilon\sigma\rangle_{\text{obs}}^{95}$ [fb]	13	4.5	0.52	0.15	0.68
$\langle\epsilon\sigma\rangle_{\text{obs}}^{95}$ [fb] (asymptotic)	13	4.3	0.45	0.12	0.63
S_{obs}^{95}	270	91	10	3.1	14
S_{obs}^{95} (asymptotic)	270	87	9	2.5	13
S_{exp}^{95}	240^{+90}_{-70}	103^{+34}_{-29}	16^{+6}_{-4}	$4.0^{+1.8}_{-0.9}$	11^{+5}_{-3}
S_{exp}^{95} (asymptotic)	240^{+90}_{-70}	97^{+35}_{-25}	15^{+6}_{-4}	$4.0^{+2.4}_{-1.4}$	11^{+5}_{-3}
p_0 (Z)	0.35 (0.4)	0.50 (0.0)	0.50 (0.0)	0.50 (0.0)	0.34 (0.4)
Signal Region	5j	6jl	6jm	6jt	6jt+
MC expected events					
Diboson	16	9	4	1.6	0.21
Z/γ^* +jets	51	18	7	1.8	2.1
W +jets	54	26	12	2.1	3.4
$t\bar{t}$ (+EW) + single top	52	80	19	2.2	3.4
Fitted background events					
Diboson	16 ± 8	9 ± 4	4 ± 2	1.6 ± 0.8	0.2 ± 0.1
Z/γ^* +jets	31 ± 8	9 ± 4	3 ± 2	0.6 ± 0.6	$0.6^{+0.8}_{-0.6}$
W +jets	28 ± 8	15 ± 7	9 ± 5	1.2 ± 0.9	$0.3^{+1.2}_{-0.3}$
$t\bar{t}$ (+EW) + single top	51 ± 9	76 ± 7	16 ± 4	1.8 ± 0.6	3.7 ± 1.7
Multi-jets	$1.0^{+2.6}_{-1.0}$	$1.7^{+3.0}_{-1.7}$	$0.4^{+0.8}_{-0.4}$	$0.01^{+0.03}_{-0.01}$	$0.3^{+0.4}_{-0.3}$
Total bkg	126 ± 13	111 ± 11	33 ± 6	5.2 ± 1.4	4.9 ± 1.6
Observed	121	121	39	5	6
$\langle\epsilon\sigma\rangle_{\text{obs}}^{95}$ [fb]	1.7	1.9	1.2	0.32	0.39
$\langle\epsilon\sigma\rangle_{\text{obs}}^{95}$ [fb] (asymptotic)	1.6	1.8	1.1	0.30	0.36
S_{obs}^{95}	35	39	25	6.6	7.9
S_{obs}^{95} (asymptotic)	32	37	22	6.1	7.3
S_{exp}^{95}	37^{+13}_{-10}	31^{+12}_{-6}	20^{+6}_{-4}	$6.2^{+2.6}_{-1.3}$	$6.6^{+2.6}_{-1.6}$
S_{exp}^{95} (asymptotic)	35^{+13}_{-10}	30^{+12}_{-8}	18^{+7}_{-5}	$6.3^{+3.1}_{-2.0}$	$6.4^{+3.2}_{-2.0}$
p_0 (Z)	0.50 (0.0)	0.27 (0.6)	0.25 (0.7)	0.50 (0.0)	0.36 (0.4)

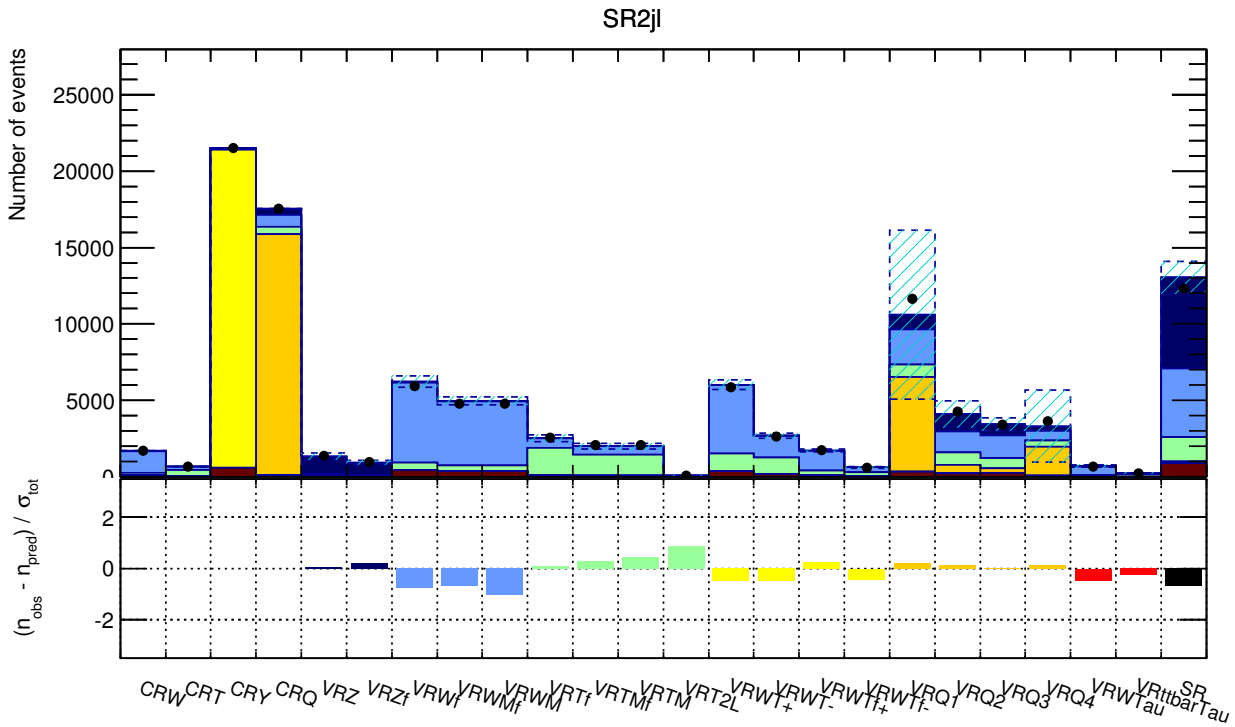


Figure 3.4: Observed and expected event count comparisons in the different VRs corresponding to SR2jl. The VRs are defined in Section 3.3.5. The green error band combines both statistical and fitted background uncertainties on n_{pred} . The lower part of the Figure shows pull results obtained from event counts. σ_{tot} is correlated between regions, so no simple chi2 test should be performed.

comparison is shown prior to the fits, while in Figure 3.6b the normalisation is done with the results of the fit. In Figure 3.6a, as in previously shown $m_{eff}(incl.)$ distributions, there are slight differences between the MC predictions and the observed data in all SRs. After performing the background fit, these are compensated, and there is better agreement between the background expectations and the observed data, as can be seen in Figure 3.6b. The most significant observed excess is in SR3j.

3.4.3.2 Discovery fit

In this fit the SR is added to the fit configuration with no signal contribution ($\mu \equiv 0$). The agreement between SM fit prediction and observed number of events in the SR is quantified via a p-value $p_b = P(q \leq q_{obs}|b)$ where q_{obs} is the observed value of the profile log likelihood that is given as well as its translation in terms of the significance Z in Table 3.10.

No statistically significant excess is observed in any of the SRs, thus the limits are set on the new physics contribution to SRs (Table 3.10).

3.4.3.3 Exclusion fit

The expected number of signal events in each SR and CR is estimated from the MC. The signal normalisation factor μ has the initial value equal to one. For "exclusion" tests, the $CL_s \equiv p_{s+b}/(1 - p_b)$ prescription [127] is used to compute the significance of the test. The penalty factor $1/(1 - p_b)$ is introduced to protect against a faked sensitivity due to a downward statistical fluctuations with respect to the SM prediction. The exclusion is computed in several slices of the SUSY parameter space. For each model point considered, the result of the exclusion fit for the best expected SR is used, calculated with the asymptotic formula. Expected limits

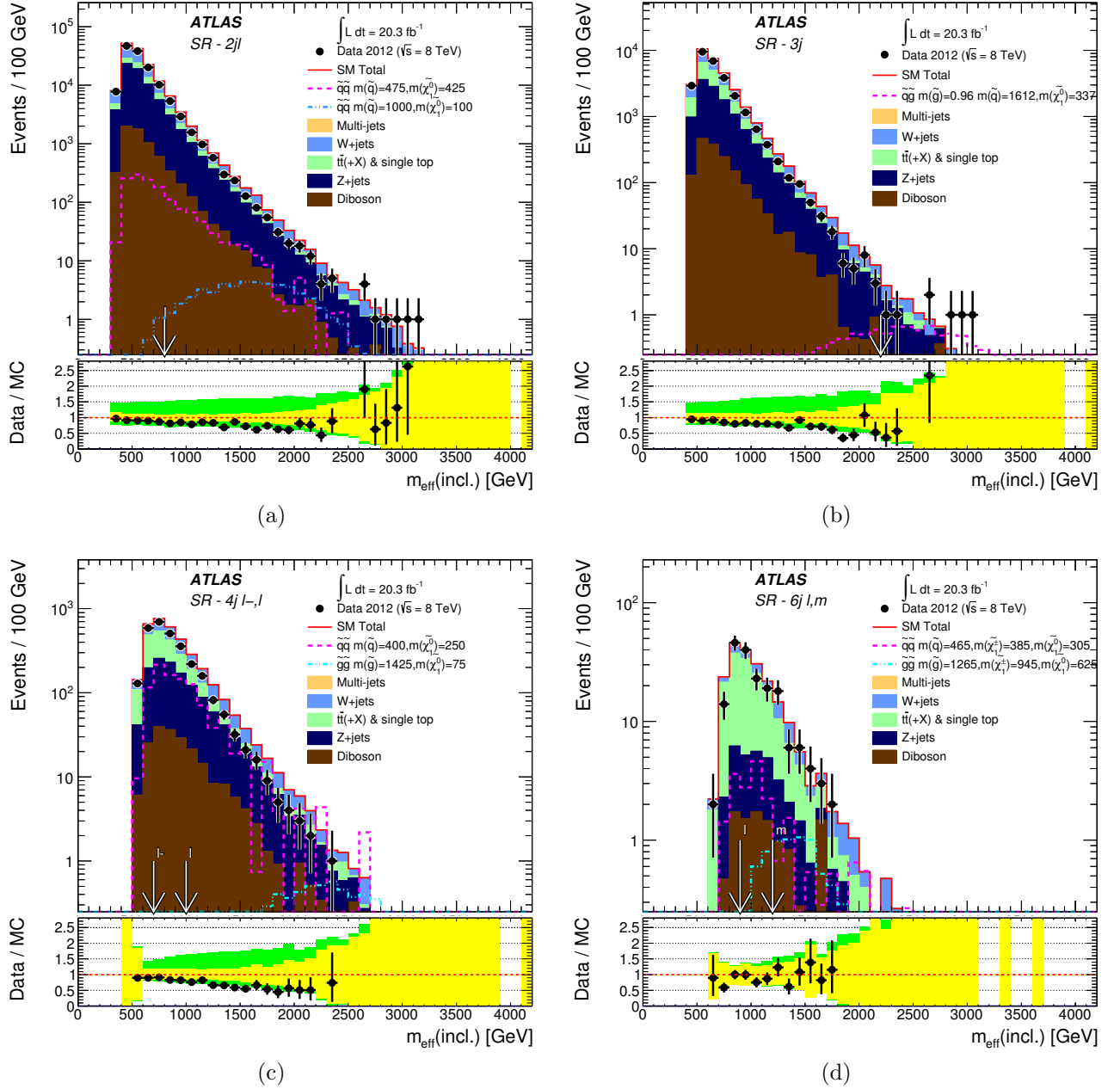


Figure 3.5: Observed $m_{\text{eff}}(\text{incl.})$ distributions for the 2-jet ((a)), 3-jet ((b)), 4-jet (4j $l-,l$) and 4j l in (c) and 6-jet SRs ((d)). With the exception of the multi-jet background (which is estimated using the data-driven technique described in the text), the histograms denote the MC background expectations prior to the fits described in the text, normalised to the cross-section times the integrated luminosity. In the lower panels the light (yellow) error bands denote the experimental systematic and MC statistical uncertainties, while the medium dark (green) bands include also the theoretical modelling uncertainty. The arrows indicate the values at which the requirements on $m_{\text{eff}}(\text{incl.})$ are applied. Expected distributions for benchmark model points are also shown for comparison (masses in GeV).

are estimated by fixing n_{obs} the expected background. Observed limits are calculated from the observed yields in the SR. Both expected and observed limits are recalculated when the signal cross-section is varied within the corresponding uncertainty.

For the interpretation of the results several simplified models are considered, as well as mSUGRA. In Figure 3.7 the exclusion reach is presented for two simplified models: in Fig-

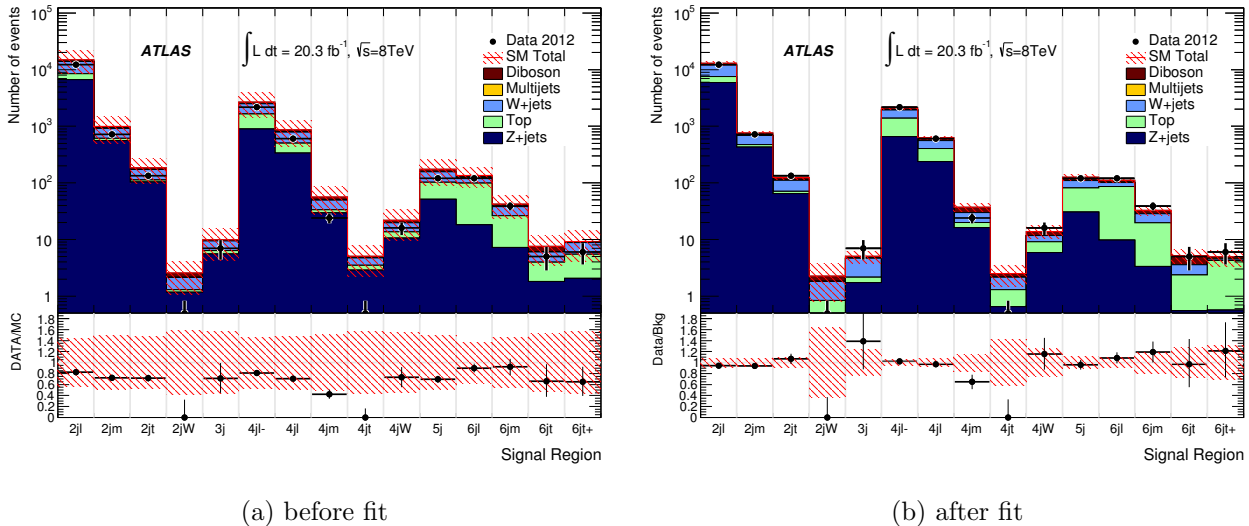


Figure 3.6: Comparison of the observed and expected event yields as a function of the SR. The background expectations are those obtained from MC samples, (a) prior to the fits and (b) after the fits described in the text. In SRs 2jW and 4jt no events are observed in the data.

Figure 3.7a the direct production of gluino pairs with decoupled squarks is considered, while in Figure 3.7b the light-flavour squarks with decoupled gluinos are assumed to be pair produced. As all other sparticles are put to higher masses, the squark is forced to decay to quark and a neutralino, and gluino is required to decay to a pair of quarks and a neutralino. The best performing SRs are those that require at least five jets. From Figure 3.7a, one can see that for a massless neutralino, gluino with masses of up to 1350 GeV are excluded. In Figure 3.7b two scenarios are shown: when eight degenerate light-flavour squarks ($\tilde{q}_L + \tilde{q}_R$) are assumed, and when only one non-degenerate light-flavour squark is expected. As the expected number of jets in this simplified model is rather low, the SRs requiring at least 2jets show the best sensitivity. The exclusion limits differ depending on the assumption: for the massless neutralino the eight degenerate squarks with masses up to 850 GeV are excluded, while if there is only one squark accessible, its mass is constrained to be higher than 440 GeV.

In Figure 3.8 the simplified model assuming pair-produced gluinos decaying through an intermediate chargino to two quarks a W and a neutralino is presented. The exclusion limits are derived in two planes: in Figure 3.8b the neutralino mass is fixed to 60 GeV while the mass difference between the chargino and the neutralino, relative to that between the gluino and neutralino (defined as $x = (m_{\tilde{\chi}_1^\pm} - m_{\tilde{\chi}_1^0}) / (m_{\tilde{g}} - m_{\tilde{\chi}_1^0})$) is varied. Gluinos with masses below 1100 GeV for massless neutralino are excluded in this scenario. In Figure 3.8a, $x = 1/2$ is fixed, while the neutralino mass is left unconstrained.

Figure 3.9 shows the results interpreted in a constrained pMSSM models when the gluino and the light-flavour squark masses are varied, for three values of the neutralino mass. Figure 3.9a presents the exclusion obtained in the squark - gluino mass plane when the neutralino mass is fixed to zero, while Figure 3.9b and Figure 3.9c consider neutralinos of mass of 395 GeV and 695 GeV respectively. All other sparticles are decoupled (their masses are set to very high values). When the neutralino is massless (Figure 3.9a), for very high gluino masses (around 1800 – 2000 GeV) it is de facto decoupled, the sensitivity of the search comes from the sensitivity to the squark production, and thus the most performing SRs are those that require low jet multiplicities. The exclusion reach is quite similar for the case when the neutralino mass is assumed to be zero, and when it is set to 395 GeV. The equal mass light-flavour squarks and gluinos are excluded below 1650 GeV.

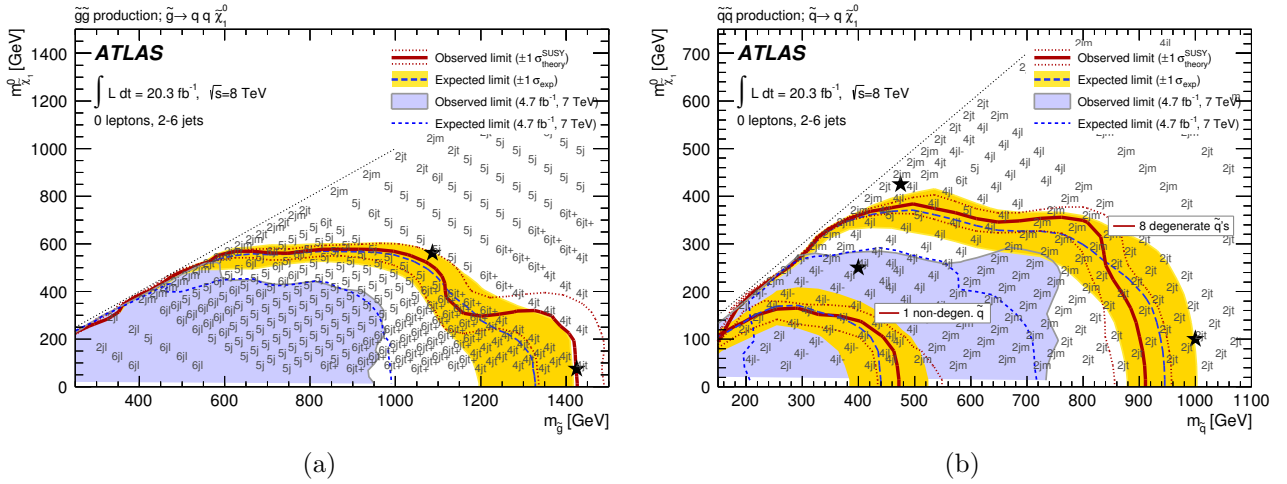


Figure 3.7: Exclusion limits for direct production of (a) gluino pairs with decoupled squarks and (b) light-flavour squark pairs with decoupled gluinos. Gluinos (light-flavour squarks) are required to decay to two quarks (one quark) and a neutralino LSP. In Figure (b) limits are shown for scenarios with eight degenerate light-flavour squarks ($\tilde{q}_L + \tilde{q}_R$), or with only one non-degenerate light-flavour squark produced. Exclusion limits are obtained by using the SR with the best expected sensitivity at each point. The blue dashed lines show the expected limits at 95% CL, with the light (yellow) bands indicating the 1σ excursions due to experimental and background-only theory uncertainties. Observed limits are indicated by medium dark (maroon) curves, where the solid contour represents the nominal limit, and the dotted lines are obtained by varying the signal cross-section by the renormalisation and factorisation scale and PDF uncertainties. Previous results from ATLAS [79] are represented by the shaded (light blue) areas and light blue dotted lines. The black stars indicate the benchmark models. The SRs providing the best expected sensitivity at a selection of model points are indicated.

In Figure 3.10 are shown the limits in a slice of the mSUGRA parameter space with $\tan\beta = 30$, $A_0 = -2m_0$, $\mu > 0$. In Figure 3.10a the $m_0 - m_{1/2}$ parameter plane is presented, while in Figure 3.10b the $\tilde{g}-\tilde{q}$ mass plane is shown. This slice accommodates the measured Higgs boson mass [128]. For high m_0 values the most performant SRs are those with six jets as here the gluino pair production dominates, while for the low m_0 - where squark pair production dominates - the exclusion comes mostly from 2-jet SRs. The light-flavoured squarks and gluinos of the same mass are excluded below 1650 GeV in this model.

3.5 Conclusion and outlook

This Chapter describes the 0-lepton search performed with the 20.3 fb^{-1} of 8 TeV data collected in 2012. First the strategy of the analysis is outlined, the processes contributing to the background are mentioned, along with the variables that are designed to suppress them. The main objects that are the basis of the selection are described, and the selection criteria leading to the definition of the control, validation and signal regions. The fit that takes all of them into account is described, leading to the final results of this search - the number of observed events in the signal regions. Those are then interpreted in terms of the limits on the sparticle parameters and masses in mSUGRA and several simplified models.

In the very beginning of the Run 2, 0-lepton analysis will be very close to the one performed with the Run 1 data, and use the well known strategy and variables described in this Chapter. That should allow for the fast understanding of the Run 2 conditions. The first collisions

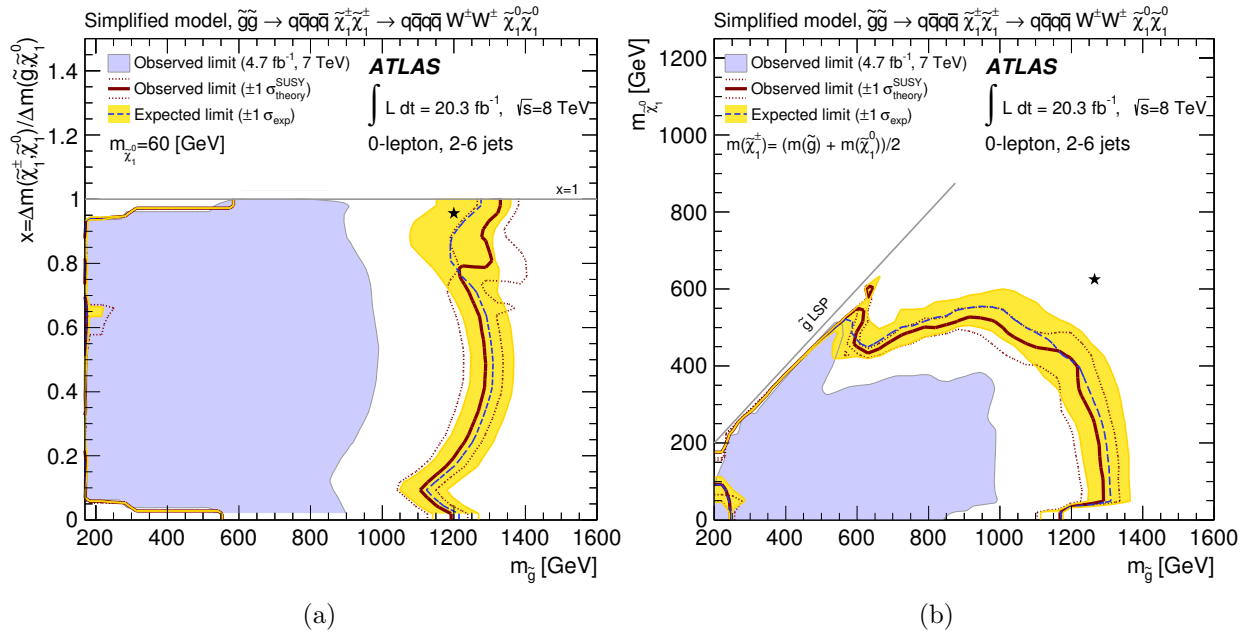


Figure 3.8: Exclusion limits for pair-produced gluinos each decaying via an intermediate $\tilde{\chi}_1^\pm$ to two quarks, a W boson and a $\tilde{\chi}_1^0$. The (b) show results for models with fixed $m(\tilde{\chi}_1^0) = 60$ GeV and varying values of $x = (m_{\tilde{\chi}_1^\pm} - m_{\tilde{\chi}_1^0}) / (m_{\tilde{g}} - m_{\tilde{\chi}_1^0})$. The (a) plot show results for model with a fixed value of $x = 1/2$ and varying values of $m_{\tilde{\chi}_1^0}$. Exclusion limits are obtained by using the SR with the best expected sensitivity at each point. The blue dashed lines show the expected limits at 95% CL, with the light (yellow) bands indicating the 1σ excursions due to experimental and background-only theory uncertainties. Observed limits are indicated by medium dark (maroon) curves, where the solid contour represents the nominal limit, and the dotted lines are obtained by varying the signal cross-section by the renormalisation and factorisation scale and PDF uncertainties. Previous results from ATLAS [79] are represented by the shaded (light blue) areas. The black stars indicate benchmark models used in Figure 3.5.

at 13 TeV have been looked at and a comparison between data and MC predictions has been performed with the first 78 pb^{-1} : the example of the $m_{\text{eff}}(\text{incl.})$ distribution in control region for $t\bar{t}$ background is given in Figure 3.11. The control regions for $W + \text{jets}$ and $Z + \text{jets}$ have also been looked at and are described in Ref. [129].

Finally the expected exclusion reach for up to 10 fb^{-1} has been studied for different simplified models [130]. For instance for a gluino pair production, when $\tilde{g} \rightarrow q\bar{q}\tilde{\chi}_1^0$, p_0 for discovery is shown as a function of the gluino mass for 20% uncertainties on the total background prediction. Within those hypothesis, a 3σ evidence can be obtained with a gluino mass between 1300 and 1350 GeV for 2 fb^{-1} .

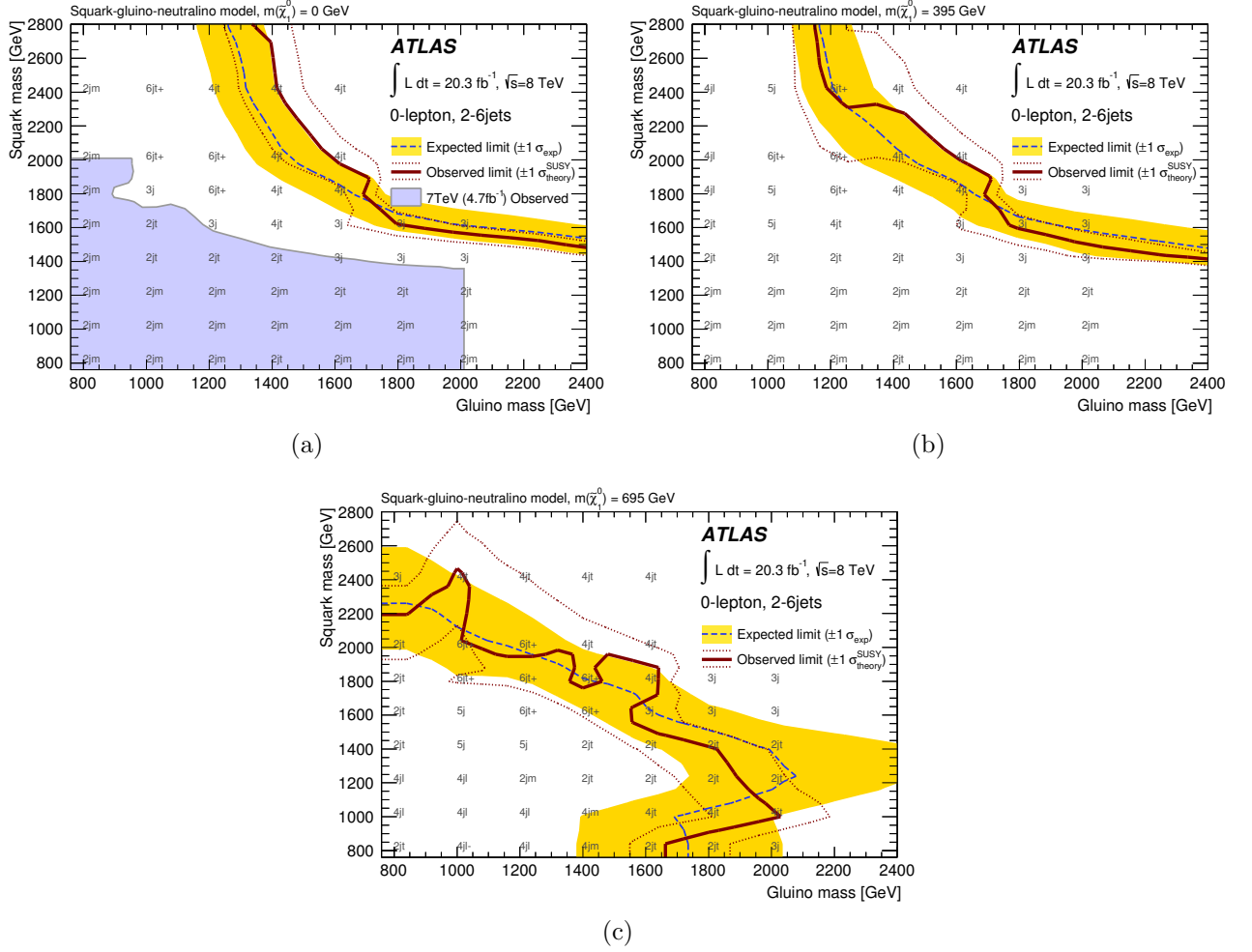


Figure 3.9: Exclusion limit for a simplified pMSSM scenario with only strong production of gluinos and first- and second-generation squarks (of common mass), with direct decays to quarks and lightest neutralinos. The mass of the lightest neutralino is set to zero ((a)), 395 GeV((b)) or 695 GeV ((c)). Exclusion limits are obtained by using the SR with the best expected sensitivity at each point. The dashed line shows the expected limit at 95% CL, with the light (yellow) band indicating the 1σ experimental and background-only theory uncertainties. The observed limit is indicated by the solid curve. The dotted lines represent the observed limits obtained by varying the signal cross-section by the renormalisation and factorisation scale and PDF uncertainties. Previous results for $m_{\tilde{\chi}_1^0} = 0$ from ATLAS at 7 TeV [79] are represented by the shaded (light blue) area. Results at 7 TeV are valid for squark or gluino masses below 2000 GeV, the mass range studied for that analysis. The signal regions providing the best expected sensitivity at a selection of model points are indicated.

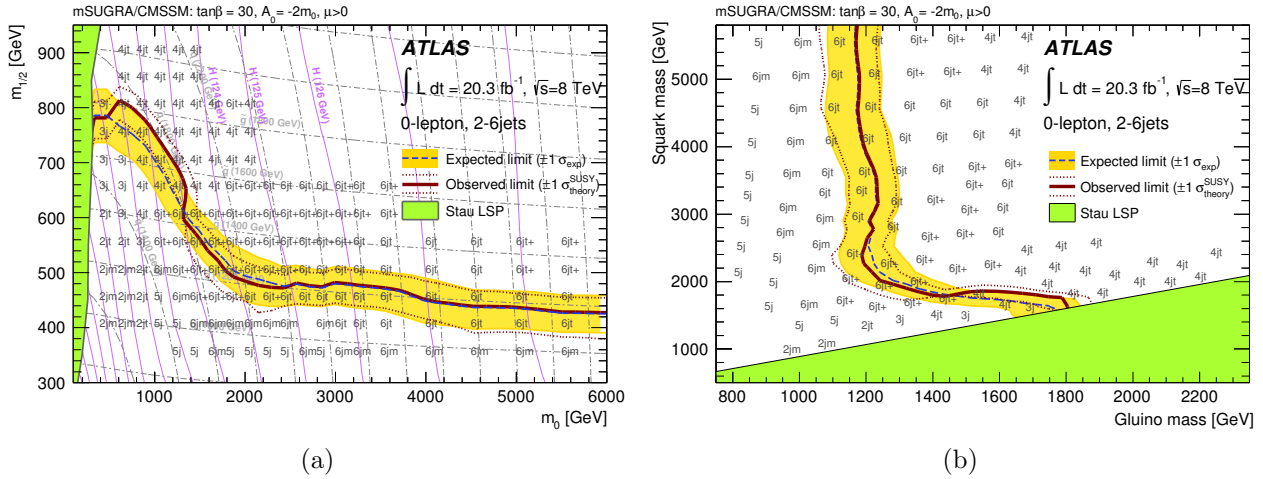


Figure 3.10: Exclusion limits for mSUGRA/CMSSM models with $\tan\beta = 30$, $A_0 = -2m_0$ and $\mu \geq 0$ presented (a) in the $(m_0, m_{1/2})$ -plane and (b) in the $(m_{\tilde{g}}, m_{\tilde{q}})$ -plane. Exclusion limits are obtained by using the signal region with the best expected sensitivity at each point. The blue dashed lines show the expected limits at 95% CL, with the light (yellow) bands indicating the 1σ excursions due to experimental and background-only theory uncertainties. Observed limits are indicated by medium dark (maroon) curves, where the solid contour represents the nominal limit, and the dotted lines are obtained by varying the signal cross-section by the renormalisation and factorisation scale and PDF uncertainties. The signal regions providing the best expected sensitivity at a selection of model points are indicated.

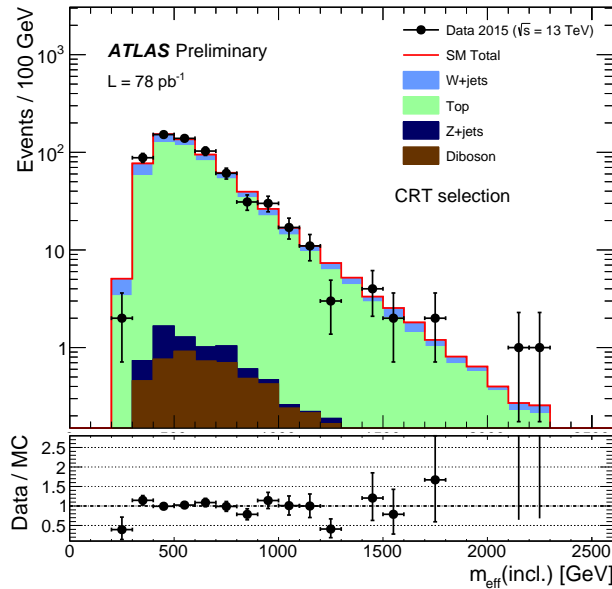


Figure 3.11: The distribution of the observed $m_{\text{eff}}(\text{incl.})$ in CRT after requiring an isolated electron or muon with $p_T > 25 \text{ GeV}$, at least two jets with $p_T > 100, 60 \text{ GeV}$ respectively, $E_T^{\text{miss}} > 100 \text{ GeV}$ and $30 \text{ GeV} < m_T(\ell, E_T^{\text{miss}}) < 100 \text{ GeV}$. The total MC background expectation is normalised to data. In the lower panels the ratio of data to total MC background expectation is presented. The contribution from the multi-jet production is found to be negligible. Only statistical uncertainties are shown, without any experimental or theoretical systematic uncertainties.

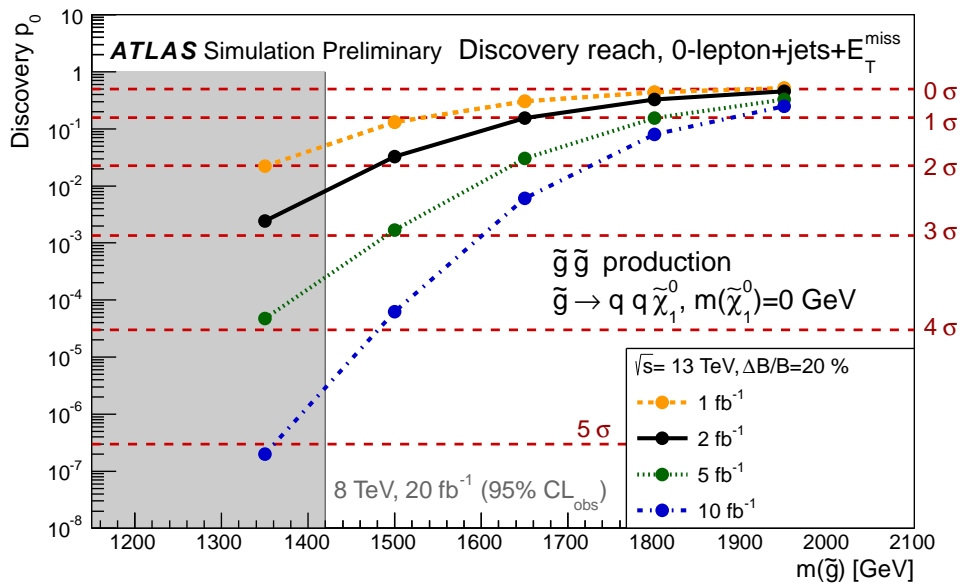


Figure 3.12: Discovery p_0 values as a function of the gluino mass in the gluino-pair production models at a given integrated luminosity of 1, 2, 5, or 10 fb^{-1} (from inner to outer lines) with a hypothesis of 20% uncertainties on the total background prediction. For each integrated luminosity scenario, one baseline signal region is optimised for one target signal point with a hypothesis of 20% uncertainties on the total background prediction.

Chapter 4

Tau leptons in the 0-lepton analysis

The remaining Standard model backgrounds in the 0-lepton analysis signal regions are mainly composed of τ leptons. In order to improve the control over these background processes, the τ identification has been investigated. Two ways are pursued:

- Defining a control/validation region to better constrain the background composition in the final fit for the limit settings and/or check a posteriori that the Monte Carlo prediction for τ can be relied upon.
- Implementing a veto on events containing τ leptons in the signal region definition to improve the final exclusion reach, taking into account the additional systematic uncertainties that come with the τ identification.

The work of this thesis presented in this Chapter is documented in Ref. [1] and Ref. [2], with the definition of the validation regions further used as a cross check to prove that the analysis is well under control for each kind of backgrounds.

In Section 4.1 the τ algorithms that have been developed within ATLAS and that are used in this chapter are described: the track counting and the BDT methods. The effect of the tau energy scale is also discussed in this section. In Section 4.2 are detailed the systematic checks that have been done on the track counting algorithm for the 0-lepton analysis. This was the only available τ identification method at the time this analysis was performed. The τ identification is then used to define two validation regions in Section 4.3. Finally the illustration of what can be gained from vetoing on events containing τ leptons for the signal regions definition is shown in Section 4.4. For the validation region and signal region sections a comparison is performed with the BDT τ identification that came out later.

4.1 Tau leptons in the 0-lepton analysis and in ATLAS

4.1.1 Motivation for considering tau leptons in the 0-lepton analysis

As it is shown in Table 4.1 most of the remaining backgrounds in the SRs of the 0-lepton analysis come from τ leptons. This table illustrates the leptonic flavor composition of backgrounds for each SR done at the truth level. The τ lepton stands for the primary τ lepton independently of its decay mode. The numbers denote percents of the considered final states per production process. In the case of the $t\bar{t}$ and $W\bar{t}$ decays one can have up to two τ s coming from the W boson decay, those are considered as the $\tau + \tau/l$, to emphasise that there is at least one τ in the final state.

The SM background that dominates in each SR after applying the full analysis selection depends mainly on the number of jets that are required, as was shown in Chapter 3. The SRs

with low jet multiplicities are dominated by the $W + \text{jets}$ background, while the ones with higher jet multiplicities are dominated by the $t\bar{t}$. As top quarks mainly decay to a W boson and a b quark ($t \rightarrow Wb$), both backgrounds are in fact dominated by the decays of W bosons. Since, in addition, the 0-lepton analysis vetoes on events that have at least one isolated light lepton, the remaining background comes from the $W \rightarrow \tau\bar{\nu}_\tau$ decays. In parallel, τ leptons do have leptonic decay modes, $\tau \rightarrow e\bar{\nu}_e\nu_\tau$ and $\tau \rightarrow \mu\bar{\nu}_\mu\nu_\tau$ which account for $\sim 17.9\%$ and $\sim 17.4\%$ respectively [131], but they are efficiently suppressed by the light lepton veto. The main hadronic τ decay modes are $\tau \rightarrow \pi^-\nu_\tau$ ($\sim 11\%$), $\tau \rightarrow \pi^-\pi^0\nu_\tau$ ($\sim 25.5\%$), $\tau \rightarrow \pi^-2\pi^0\nu_\tau$ ($\sim 11\%$) and $\tau \rightarrow \pi^-\pi^+\pi^-\nu_\tau$ ($\sim 9\%$), and those are the dominant remaining component of the backgrounds and are the subject of this study.

It should be noted that τ leptons also appear in the final states of some of the SUSY models considered by the 0-lepton analysis, like mSUGRA, so one has to be careful not to suppress possible signal events while trying to reduce background when the events containing τ s are vetoed.

		Channel															
		2j				3j	4j				5j	6j					
		l	m	t	W	t	l-	l	m	t	W	m	l	m	t	t+	
$t\bar{t}$	$\tau + \tau/l$	7.6	10.5	17.9	30.8	6.7	4.9	7.9	7.2	8.5	5.7	9.5	4.8	7.8	11.0	13.1	
	$\tau + \text{jets}$	59.2	54.8	52.3	16.7	59.7	61.0	57.7	56.2	51.2	53.7	58.4	63.1	60.9	45.7	43.7	
	$l + l$	1.4	1.9	0.9	0.0	0.0	0.8	1.3	1.1	0.0	0.0	1.0	0.8	1.3	3.3	5.8	
	$e + \text{jets}$	12.9	10.4	7.0	0.0	8.7	14.5	13.2	12.6	11.1	13.5	13.5	16.7	15.2	15.4	13.1	
	$\mu + \text{jets}$	18.8	22.4	21.9	52.5	24.9	18.8	19.9	22.9	29.2	27.1	17.6	14.5	14.7	24.5	24.3	
	jets	0.0	0.0	0.0	0.0	0.0	0.0	0.0	0.0	0.0	0.0	0.0	0.0	0.0	0.0	0.0	
$W\bar{t}$	$\tau + \tau/l$	9.1	8.8	0.0	x	0.0	8.0	11.0	0.0	0.0	0.0	16.4	12.3	19.2	0.0	0.0	
	$\tau + \text{jets}$	61.5	61.4	45.9	x	0.0	59.7	53.5	41.8	0.0	0.0	34.2	55.9	28.7	0.0	12.1	
	$l + l$	0.4	0.0	0.0	x	0.0	0.4	0.0	0.0	0.0	0.0	0.0	0.0	0.0	0.0	0.0	
	$e + \text{jets}$	9.8	7.2	0.0	x	0.0	11.7	12.1	0.0	0.0	0.0	10.9	11.0	7.9	0.0	37.0	
	$\mu + \text{jets}$	19.0	22.6	54.1	x	100.0	20.3	23.3	58.2	100.0	100.0	38.6	20.8	44.1	100.0	50.9	
	jets	0.2	0.0	0.0	x	0.0	0.0	0.0	0.0	0.0	0.0	0.0	0.0	0.0	0.0	0.0	
t (s - chan)	e	19.4	10.1	0.0	x	x	16.4	52.8	x	x	x	20.9	x	x	x	x	
	μ	18.9	24.1	27.7	x	x	13.4	8.4	x	x	x	0.0	x	x	x	x	
	τ	61.8	65.8	72.3	x	x	70.2	38.8	x	x	x	79.1	x	x	x	x	
t (t - chan)	e	16.2	6.6	0.0	x	x	22.3	33.3	0.0	x	x	36.5	0.0	0.0	x	x	
	μ	24.5	34.5	82.1	x	x	24.5	13.4	100.0	x	x	63.5	0.0	0.0	x	x	
	τ	59.4	58.9	17.9	x	x	53.2	53.3	0.0	x	x	0.0	100.0	100.0	x	x	
$W + \text{jets}$	e	19.5	13.6	12.6	16.5	2.5	16.2	17.1	20.5	6.4	21.5	16.3	11.3	12.6	20.7	30.7	
	μ	20.1	22.9	22.9	8.8	21.1	19.6	19.5	19.5	18.1	16.8	17.0	19.8	14.3	13.1	11.1	
	τ	60.4	63.5	64.5	74.7	76.3	64.3	63.3	60.1	75.6	61.7	66.7	68.9	73.1	66.1	58.1	
$Z + \text{jets}$	e^+e^-	0.0	0.0	0.0	0.0	0.0	0.0	0.0	0.0	0.0	0.0	0.0	0.0	0.0	0.0	0.0	
	$\mu^+\mu^-$	0.1	0.1	0.2	0.2	0.6	0.2	0.1	0.1	0.0	0.0	0.1	0.0	0.1	0.3	0.0	
	$\tau^+\tau^-$	0.7	0.3	0.4	0.8	1.9	0.6	0.5	0.1	0.7	0.1	0.7	0.8	0.2	0.8	0.5	
	$\nu\bar{\nu}$	99.2	99.5	99.4	99.1	97.5	99.2	99.3	99.9	99.3	99.9	99.1	99.2	99.7	99.0	99.5	

Table 4.1: Leptonic flavor composition of the main remaining backgrounds for each SR where τ indicates that the primary lepton is a τ independently of its decay mode. x denotes that no event was selected in the corresponding region. Numbers are in percent.

4.1.2 Characteristics of hadronically decaying tau leptons

The distinct features of the τ decays are used in the identification process. Hadronically decaying τ leptons are most similar to jets. To reconstruct them, one therefore selects calorimeter jets reconstructed with the anti- k_t algorithm with a distance parameter $R = 0.4$, from topological clusters of calorimeter cells. Only candidates with transverse momentum $p_T > 20$ GeV are considered. The main task then is to successfully disentangle τ s from jets. Since there are charged pions in the hadronic decays of τ s, one can use the number of charged tracks detected by the tracker. Selecting candidates with one or three charged tracks proves to be a reliable criteria for identifying τ s. Another discriminating feature of the τ s with respect to jets is that they have a relatively narrow clustering of tracks and depositions in the calorimeters. Both of those characteristics are used in the τ identification. The difficulty of the τ reconstruction comes from the fact that at the LHC the cross-section for the multijet production is much higher than the cross section for weak processes leading to τ leptons, therefore it is challenging to reduce the number of jets falsely identified as τ leptons. Other objects that can be misidentified as

hadronic τ decays, are electrons and also muons, but to a smaller degree. They can sometimes leave the same signature as τ leptons decaying to one charged hadron. The neutral and charged hadrons represent the visible products of the τ lepton.

There are several algorithms developed by the Tau Working Group [87, 88] to identify τ leptons: a cut-based identification, a projective likelihood, and boosted decision trees (BDT) [132, 133]. Those three methods have different performances and identification efficiencies. The choice of which method is the most suitable depends on the part of the phase space that the analysis explores. For the 0-lepton analysis it is important to be efficient in the high p_T region. In the following two algorithms are tested: one is the cut based track counting algorithm, and the other is the BDT. It should be noted that the BDT is used only as a cross check in what follows: it wasn't available in the version of the NTUP_SUSY tag p1328 used for the 0-lepton paper [134]. It was introduced a posteriori using NTUP_SUSY tag p1512. Therefore the discussion in the next sections is mainly focused on the track counting algorithm.

4.1.3 Track counting algorithm

The algorithm that is described in this Section has been developed by the Tau Working Group. It is called the p_T -correlated track counting algorithm, and is defined in Ref. [87]. Tracks that are considered by this algorithm have to pass the following criteria:

- $p_T > 1$ GeV
- Number of pixel hits in B-layer ≥ 1
- Number of pixel hits ≥ 2
- Number of pixel hits + number of SCT hits ≥ 7
- $|d_0| < 1.0$ mm
- $|z_0 \sin \theta| < 1.5$ mm

where $|d_0|$ is the distance of the closest approach of the track to the reconstructed primary vertex of the event in the transverse plane, and $|z_0|$ is the longitudinal distance to the closest approach. The first four requirements ensure the quality of track reconstruction, while the last two impose additional constraints on the primary vertex, which suppresses contribution from pile-up, underlying event and gluon radiation. The tracks in the outer cone of the τ candidate ($0.2 < dR < 0.6$, $dR = \sqrt{d\phi^2 + d\eta^2}$), are only counted as belonging to the τ candidate if they satisfy: $p_T^{core}/p_T^{can} \times dR < 4.0$ (here dR stands for the distance between the τ candidate direction and the outer track) where p_T^{core} is defined as the sum of the p_T of the tracks in the inner cone ($dR < 0.2$), and p_T^{can} is for the tracks in the outer cone. The algorithm counts the number of tracks within $dR < 0.2$ of the τ candidate and adds up those within $0.2 < dR < 0.6$ that satisfy this relative p_T sliding cut (tracks far away have a tighter p_T cut), in order to avoid selecting tracks from underlying or pile up events. The τ identification is limited by the tracking reconstruction efficiency. Figure 4.1 shows the number of tracks calculated for the $W \rightarrow \tau \bar{\nu}_\tau$ MC sample on the left, and similarly for the multijets production on the right. No analysis specific selection criteria is applied. Those plots support the expectation that τ s have a characteristic number of tracks of one or three, while the QCD jets are characterised by a much higher number of tracks. In the following, only τ candidates with a track multiplicity of one are selected. This choice was made in the 0-lepton analysis, as it was seen that adding three track τ candidates didn't bring enough improvement while it introduced many falsely identified τ s.

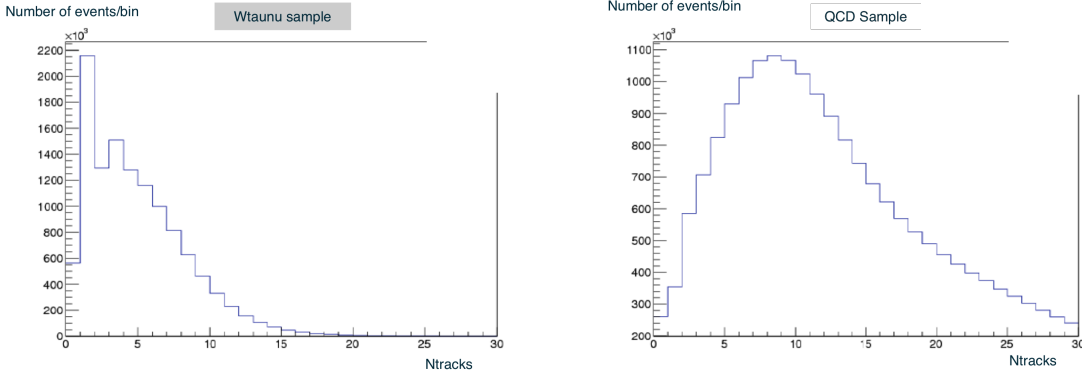


Figure 4.1: The number of tracks calculated by the track counting algorithm for τ leptons for the $W \rightarrow \tau\nu$ MC sample (on the left), and for the QCD multijet MC sample (on the right).

As mentioned before, electrons can sometimes be misidentified as τ s. To avoid cases when one object is at the same time identified as electron and τ , τ candidates that are within $dR < 0.2$ of an identified electron are discarded.

4.1.4 BDT tau selection

The Boosted Decision Tree (BDT) [132, 133] is a technique used to discriminate signal (here τ) from background (here jets) more sophisticated than just applying consecutive cuts on different variables. This method makes use of the correlations between them to increase the separation power of their combination. Several variables are used: six for τ s with one track, and eight for τ s with more than one track. Those are: the electromagnetic shower radius, the track radius, the leading track momentum fraction, the core energy fraction, the electromagnetic fraction, the cluster mass (for τ candidates with one track) and additionally the track mass, and the transverse flight significance (for τ candidates with three tracks) [87]. Different BDTs are trained separately on the τ candidates with one and with three tracks, in separate categories defined by the number of reconstructed primary vertices. There are also BDTs for rejecting electron falsely identified as τ s, but they are not used in the 0-lepton analysis, since an overlap removal between τ candidates and baseline electrons is performed (Section 4.1.3), and the events with baseline electrons are in any case rejected by this analysis. Three working points are defined corresponding to different τ identification efficiency values ('tight', 'medium' and 'loose'), and it is left to the analysis to choose the optimal one. In what follows, it has been chosen to use loose BDT selection, as the aim is to get the highest possible efficiency in selecting τ s.

4.1.5 Tau Energy Scale

Although the τ candidates are built from the calorimeter jets, the reconstructed energy of the τ candidate is not taken from the calibrated seed jet. Instead it is calculated as a sum over the uncalibrated energies of the cells, within $dR < 0.4$ of the seed jet axis. As in the hadronic τ decays there is a mixture of charged and neutral pions, the energy scale is calibrated independently of the jet energy scale by applying a correction to the reconstructed energy at the electromagnetic energy (EM) scale. The correction factors are derived by determining the response functions $R(p_T^{EM})$ of the EM scale p_T compared to the true generated p_T of the hadronic τ decays in MC samples:

$$R(p_T^{EM}) = \frac{p_T^{EM}}{p_T^{gen}} \quad (4.1)$$

The τ candidates are calibrated to the tau energy scale (TES) by applying the inverse of the response function to the p_T :

$$p_T^{TES} = \frac{1}{R(p_T^{EM})} p_T^{EM} \quad (4.2)$$

The uncertainty on the tau energy scale is evaluated using MC simulations with alternative variations. Several kinds of variations are considered: changing the MC events generator and underlying event model, the hadronic shower model, the amount of detector material, the topological clustering noise thresholds, the EM energy scale and non-closure of the calibration method [87]. The topocluster noise thresholds are varied by 10% to estimate the uncertainty due to calorimeter noise. Non-closure assesses the difference between the energy of the τ at the reconstructed and the truth level when applying the calibration to the same sample it was derived from. The total uncertainty on the τ energy calibration scale is calculated by adding in quadrature the relative differences from all systematic sources from the nominal calibration in p_T and η bins. Also it depends on the topology of the event: in this case on the number of tracks of the τ candidate. The variations of the TES are applied to the p_T of the τ candidate.

4.2 Purity and reliability of the tau selection

In this Section the systematic checks that have been performed during this thesis within the context of the 0-lepton analysis on the τ fake rate and the τ rate are presented. The use of the transverse mass to increase the τ purity is presented beforehand. In all the following the identified τ refers to a τ candidate to which only one track has been associated, according to the track counting algorithm.

4.2.1 Transverse mass between tau and E_T^{miss}

As it was shown in Section 4.1.1, the main source of τ leptons in the 0-lepton analysis is the decay of W boson: so one way to enhance the purity of the sample of the events containing τ s is to reconstruct the W . The transverse mass between the τ candidates and the E_T^{miss}

$$m_T(\tau, E_T^{\text{miss}}) = \sqrt{p_T^\tau \times E_T^{\text{miss}} (1 - \cos \theta(\tau, E_T^{\text{miss}}))} \quad (4.3)$$

is calculated and is required to be consistent with the mass of the W boson (less than 100 GeV). This constraint is used to further suppress falsely identified τ candidates, as it is calculated for each identified τ in the event and only those that satisfy it are tagged as τ . The distribution of $m_T(\tau, E_T^{\text{miss}})$ is discussed in Section 4.3.2.

4.2.2 Tau fake rate

The τ fake rate is defined as the ratio between the number of identified jets mis-identified as τ s and the number of jets, therefore giving an indication of the purity of the τ identification when estimated on data samples which do not contain τ s. Since the 0-lepton analysis deals with a large number of jets, one wants to study the behaviour of the τ fake rate in different situations:

- for the pure jets samples coming from the jets accompanying $Z \rightarrow ee$ and $Z \rightarrow \mu\mu$
- for the smeared QCD multijet sample.

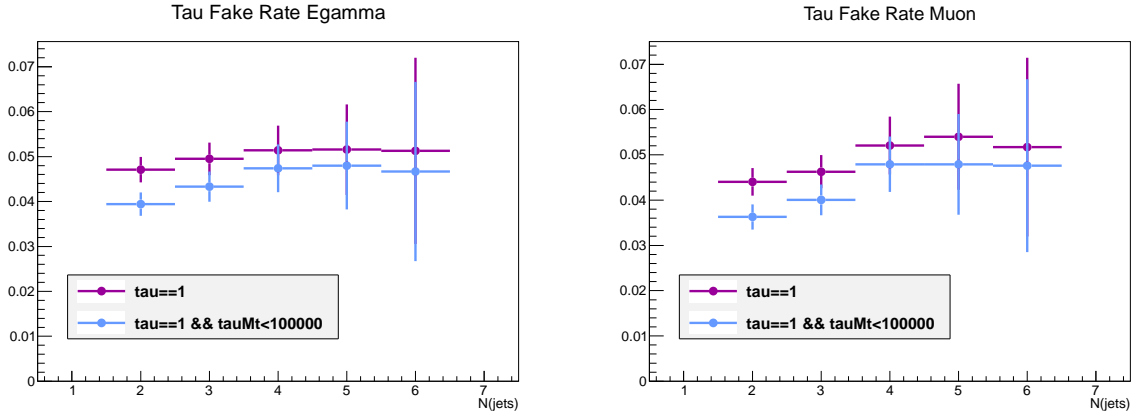


Figure 4.2: The τ fake rate as a function of the number of jets in Egamma (on the left) and Muons stream (on the right) with and without a cut on $m_T(\tau, E_T^{\text{miss}}) < 100$ GeV. It is calculated on the sample of events that have two same flavour light leptons with an invariant mass compatible with the Z .

4.2.2.1 Tau fake rate estimated from the pure jets samples coming from $Z \rightarrow ee$ and $Z \rightarrow \mu\mu$

As explained before, the vast majority of fake τ s are jets. To estimate the τ fake rate one needs a pure sample of jets (in which there are no real τ s). The τ selection is then applied on that sample to estimate the number of events that have jets faking τ s. To get a pure sample of jets, the events are selected from $Z \rightarrow ee$ and $Z \rightarrow \mu\mu$ events (only events that have two same flavour isolated light leptons with a mass compatible with the Z boson are considered). This sample is expected to be quite pure as the cross section for the electroweak WZ production is much lower than for the strong production of Z +jets. The events are selected within two data streams: Egamma and Muons. The selection is the same as applied in CRZ 3.3.4. The used triggers are respectively EF_e24vhi_medium1 or EF_e60_medium1, and EF_mu24i_tight. The τ fake rate is studied after the cut on the jet p_T of 40 GeV. Figure 4.2 shows the distributions of the τ fake rate as a function of the number of jets for those two streams: one with just requiring a τ candidate with one track (in violet), and the other when adding the constraint on the $m_T(\tau, E_T^{\text{miss}}) < 100$ GeV (in blue). As expected, the τ fake rate is smaller when there is an additional selection criteria on $m_T(\tau, E_T^{\text{miss}})$. In general, it is stable with the number of jets and is around 0.04.

4.2.2.2 Tau fake rate estimated from the smeared QCD multijet sample

To study the τ fake rate one can also consider the QCD seeds used for the prediction of the multijet background. As explained in Section 3.3.4.1 the 0-lepton analysis relies on a data driven method to estimate the multijet background. The τ fake rate on QCD seeds is studied after the cut on the p_T of the jets that pass the 0-lepton selection, but without the trigger and E_T^{miss} requirements. It is supposed that the probability of finding two τ s in the event is negligible. The distribution of the τ fake rate as a function of the number of jets is shown in Figure 4.3. The τ selection that requires one track is shown in black, while the addition of the $m_T(\tau, E_T^{\text{miss}}) < 100$ GeV requirement is shown in blue. It is seen that the value of the τ fake rate is compatible with the value obtained from the $Z \rightarrow ee$ and $Z \rightarrow \mu\mu$ events. In Figure 4.4, the dependance of the τ fake rate on the jet $\langle p_T \rangle$ (on the left) and $\langle \eta \rangle$ (on the right) of all the jets in the event is shown. The τ fake rate is stable with respect to $\langle p_T \rangle$ in the event, except maybe for the very low and very high p_T values, but for high p_T values there is very limited statistics. Also, it is stable as the function of $\langle \eta \rangle$.

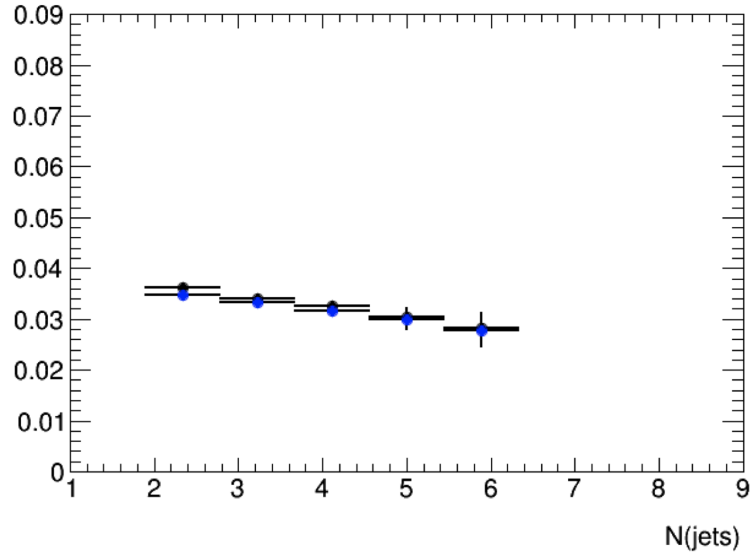


Figure 4.3: The τ fake rate as a function of the number of jets done for the QCD smeared sample, shown after the cut on p_T of the jets that pass the 0-lepton selection, but without the trigger and E_T^{miss} cuts. τ is defined as the τ candidate with one track (in black), and with additional requirement on $m_T(\tau, E_T^{\text{miss}}) < 100$ GeV in blue.

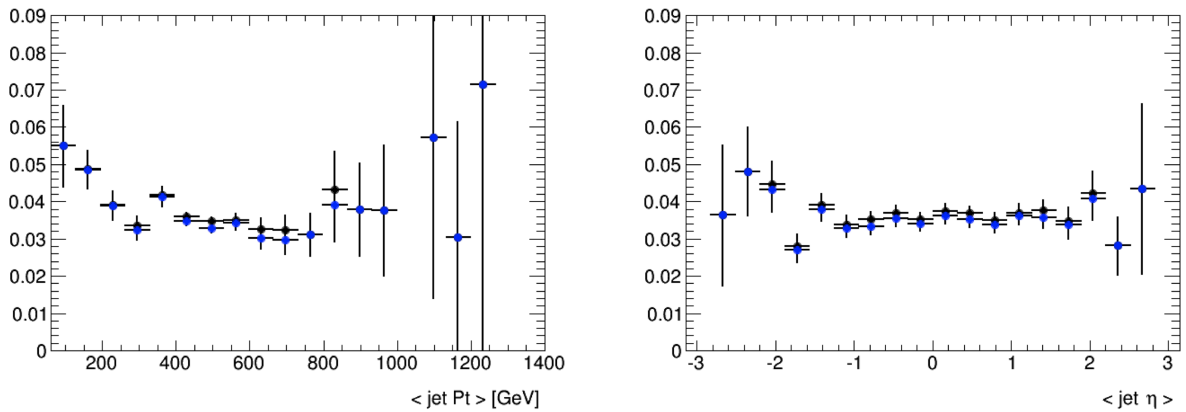


Figure 4.4: The τ fake rate as a function of the mean p_T of all the jets in the event (on the left) and of the mean η of all the jets in the event (on the right) done for the QCD smeared sample, shown after the cut on the p_T of the jets that pass the 0-lepton selection, but without trigger and E_T^{miss} cuts. The τ are defined as the τ candidate with one track (in black), and after $m_T(\tau, E_T^{\text{miss}}) < 100$ GeV in blue.

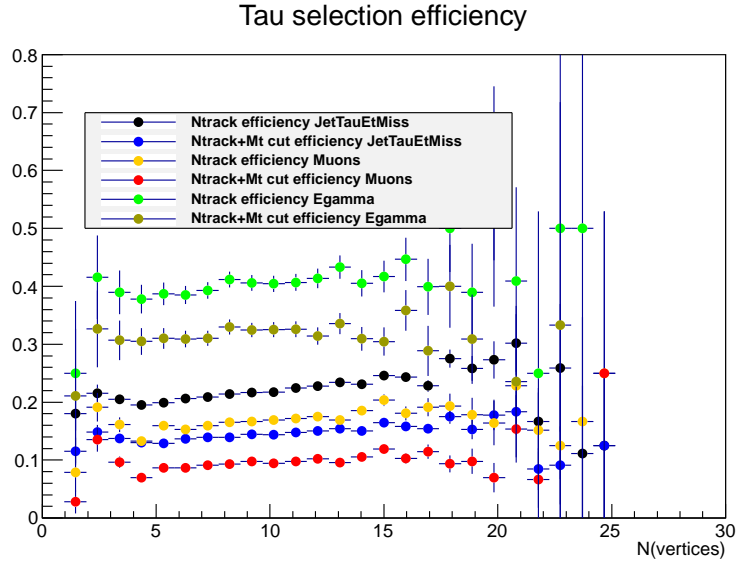


Figure 4.5: The τ rate as a function of the number of reconstructed primary vertices for all the possible different configurations: τ identified with the track counting algorithm, with and without the $m_T(\tau, E_T^{\text{miss}})$ cut, and for all the streams (JetTauEtMiss, Muons and Egamma). The plot is made after $E_T^{\text{miss}} > 160$ GeV, 1^{st} jet $p_T > 160$ GeV and 2^{nd} jet $p_T > 60$ GeV requirements, and a veto on events containing electron or muon.

4.2.3 Stability of the tau rate with respect to pile up

The τ rate is here defined as the ratio between the number of events with identified τ and the total number of events. It is studied as a function of the number of primary vertices hereafter. As explained in Section 4.1.3, when selecting τ s only tracks that are associated to the primary vertex are considered, so all tagged τ s are also coming from the primary vertex. The τ rate was calculated in all data streams (JetTauEtMiss, Muons and Egamma stream). In Figure 4.5, they are shown for τ s defined as the τ candidate with one track, and separately for τ s with one track and $m_T(\tau, E_T^{\text{miss}}) < 100$ GeV. The plot is made after $E_T^{\text{miss}} > 160$ GeV, 1^{st} jet $p_T > 160$ GeV and 2^{nd} jet $p_T > 60$ GeV requirements, and a veto on events containing electron or muon. The plot shows that the τ rate is stable as a function of the number of primary vertices, thus with pile up. This remains true for all data streams, and also regardless of the additional requirement on the $m_T(\tau, E_T^{\text{miss}}) < 100$ GeV. The τ rate is around 0.15 - 0.20 for JetTauEtMiss and Muons streams, for τ identified only with the track counting algorithm, and it goes down to 0.10 with the addition on the $m_T(\tau, E_T^{\text{miss}})$ cut. It is a bit higher in Egamma stream, which is probably due to misidentified electrons.

One can see that the efficiency of the τ identification doesn't depend on the number of the primary vertices, which indicates that there are no falsely identified τ s coming from the pile-up events.

4.3 Validation regions for taus

Both VR and CR could be built using the τ selection described in the previous Section. By simply adding an additional CR for processes with τ in the final state, the fit would become overconstrained. In order not to redesign the full 0-lepton analysis from Ref. [1], it was chosen to rather define VRs: they are described below. In this Section the $m_T(\tau, E_T^{\text{miss}})$ and the distributions of other kinematic variables are presented. The comparison with the BDT algorithm is performed, and the estimation of potential signal contamination. Finally the pull plots of the 0-lepton analysis making use of the τ VRs are shown. There are two VRs for each SR, thus 30

VRs in total, and throughout this section everything is illustrated on VRWTau corresponding to SR2jl and VRttbarTau corresponding to SR6jl. The small discrepancies between the plots presented hereafter come from different inputs used, but the conclusions remain the same.

4.3.1 Definition of tau validation regions

Two VRs are designed for each SR to validate the description of the background with τ leptons: one for those coming from $W + \text{jets}$ (VRWTau), and the other for $t\bar{t}$ (VRttbarTau) background. They are designed to select events that have at least one identified τ with one track and $m_T(\tau, E_T^{\text{miss}}) < 100 \text{ GeV}$. As discussed in Section 3, those VRs should also be orthogonal to both SRs and CRs. That imposes the requirement $0.2 < \Delta\phi(j_i, E_T^{\text{miss}}) < 0.4$ for the first three most energetic jets (as SRs have $\Delta\phi(j_i, E_T^{\text{miss}}) > 0.4$, and CRQ has $\Delta\phi(j_i, E_T^{\text{miss}}) < 0.2$). A looser requirement of $0.1 < \Delta\phi(j_i, E_T^{\text{miss}}) < 0.2$ is applied to all remaining selected jets with $p_T > 40 \text{ GeV}$, for the VRs with more than three jets in the final state. To keep these VRs as kinematically close as possible to SRs, the same $E_T^{\text{miss}}/m_{\text{eff}}$ and $m_{\text{eff}}(\text{incl.})$ cuts are used as in Table 3.6. These two VRs are most similar to VRQ3 that validates the multijet production.

As for the CRW and CRT (Section 3.3.4), VRWTau and VRttbarTau differ by an additional requirement on the number of b -tagged jets (nBjets). For the VRWTau nBjets is required to be zero, since no b -jet is expected in the decay. For the VRttbarTau on the contrary, nBjets ≥ 1 , as a b -jet comes from top quark decay ($t \rightarrow Wb$). The b -jets are identified using the MV1 jet tagging algorithm at the 70% efficiency operating point, they are also required to have $p_T > 40 \text{ GeV}$ and $|\eta| < 2.5$ as in the other 0-lepton CRs.

4.3.2 Transverse mass in events containing taus

As mentioned in Section 4.2.1, in order to make the region more pure in τ s an addition of the requirement on the $m_T(\tau, E_T^{\text{miss}})$ is explored. In Figure 4.6 the distribution of the $m_T(\tau, E_T^{\text{miss}})$ is shown for the VRttbarTau2j before applying the selection criteria on $\Delta\phi(j_i, E_T^{\text{miss}})$ and m_{eff} (cuts 18 and 20 of Table 3.6). The various backgrounds are given in different colours: for this discussion it is important to note that the light blue and light green are events with τ s coming from the $W + \text{jets}$ and $t\bar{t}$ processes respectively. One can see that even at this level of selection, the constructed VRs are enriched in τ s.

- In Figure 4.6a the $m_T(\tau, E_T^{\text{miss}})$ distribution is shown for both data and MC prediction.
- In Figure 4.6b the distribution of the $m_T(\tau, E_T^{\text{miss}})$ reconstructed from the visible τ decay products ($m_T(\text{tauV})$) at the truth level is shown. The visible τ decay products are all products but neutrinos. It is evident there are limitations coming from the E_T^{miss} reconstruction, as in the ideal case, the W boson mass could be reconstructed much more precisely. The tail to high $m_T(\tau, E_T^{\text{miss}})$ value is coming from the E_T^{miss} reconstruction.
- In Figure 4.6c the distribution of the $m_T(\tau, E_T^{\text{miss}})$ calculated from the τ s reconstructed with one track that are matched to τ s at the truth level ($m_T(\text{tauT})$), is presented. They successfully give $m_T(\tau, E_T^{\text{miss}})$ that is consistent with the W boson mass. This distribution shows that the τ s that give $m_T(\tau, E_T^{\text{miss}})$ below 100 GeV are coming from real τ s, so those are retained and tagged as τ s.
- In Figure 4.6d the $m_T(\tau, E_T^{\text{miss}})$ reconstructed from the τ s that are falsely identified as τ s ($m_T(\text{tauF})$) is shown. Falsely identified τ are those that can't be matched to any truth τ . They give a much less peaked $m_T(\tau, E_T^{\text{miss}})$ distribution.

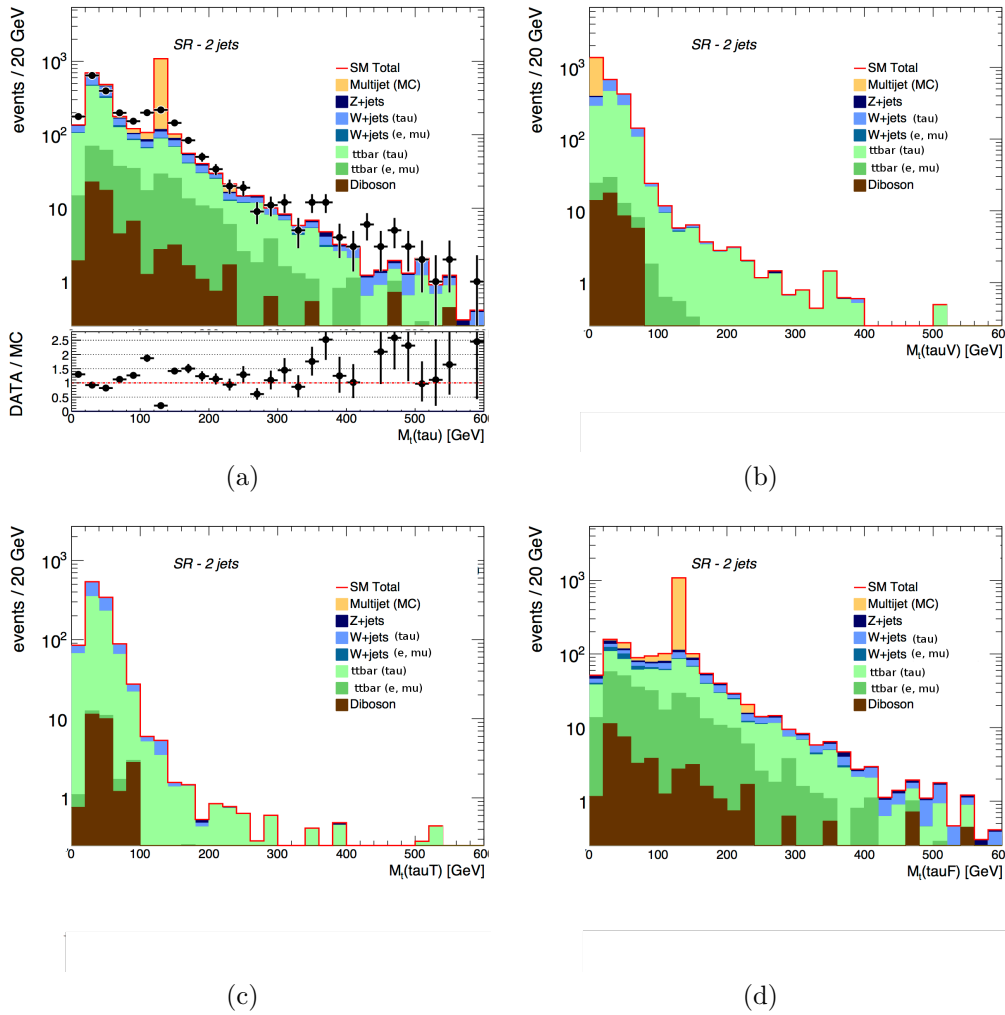


Figure 4.6: In Figure (a) data and expected MC background $m_T(\tau, E_T^{\text{miss}})$ distributions normalised to luminosity before the $\Delta\phi(j_i, E_T^{\text{miss}})$ and $m_{\text{eff}}(\text{incl})$ cut for the VRttbarTau2j, are shown. In Figure (b) the distribution of $m_T(\tau, E_T^{\text{miss}})$ calculated with the visible products of the τ decay at the truth level and E_T^{miss} ($m_T(\text{tauV})$). In Figure (c) and (d) the same distributions are shown but this time calculated with E_T^{miss} and the τ s matched to the τ at the truth level ($m_T(\text{tauT})$) and τ s that can't be matched to any truth τ ($m_T(\text{tauF})$) respectively. The legend is missing for the dark and light green, which are representing background coming from $t\bar{t}$, decaying to electron or muon (in dark green), and to τ lepton (in light green).

In these plots the multijet background is estimated directly from the MC, which is limited in statistics, resulting in several events with large normalisation weights appearing as spikes on the plots. Thus it can be regarded just like an indication where those events would be, but the prediction of their number can not be relied upon. When comparing 4.6b and 4.6c the difference comes from the τ identification, and shows limits one is facing when using τ s, as the E_T^{miss} used in calculating both $m_T(\tau, E_T^{\text{miss}})$ is the same. It is especially prominent at low $m_T(\tau, E_T^{\text{miss}})$ values, so for τ s with small p_T and/or that is in the same direction as E_T^{miss} , possibly faking it.

There is an obvious disagreement between data and MC for $m_T(\tau, E_T^{\text{miss}})$ between 100 and 150 GeV seen in Figure 4.6a. A similar feature is also observed in the analysis that searches for SUSY in events containing τ s which originate from the decays of SUSY particles in their CR for QCD. Two sources have been investigated to explain it: the all hadronic decay of top quark and the multijet background. The first one is exemplified in Figure 4.7 where the data and expected MC background distribution of $m_T(\tau, E_T^{\text{miss}})$ is shown. In red the contribution

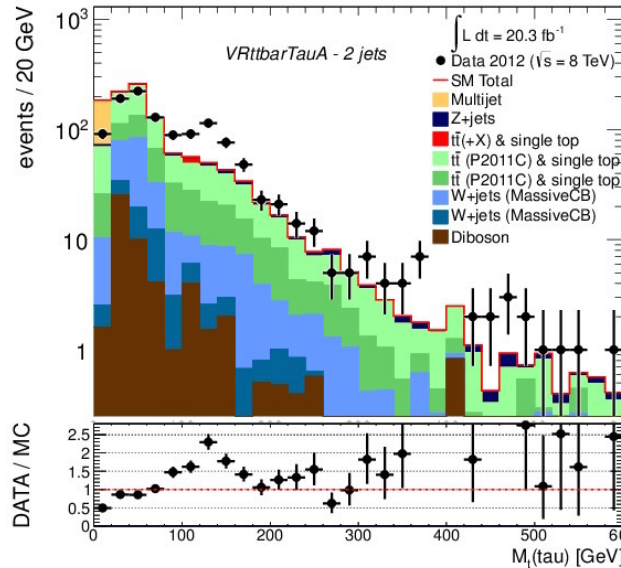


Figure 4.7: Data and expected MC background distribution $m_T(\tau, E_T^{\text{miss}})$ is shown, and in red the contribution from the all hadronic top decay is shown.

from the all hadronic top decay is presented. Although the events are really contributing to the exact place in the $m_T(\tau, E_T^{\text{miss}})$ distribution, their number is almost negligible.

The second possible source of the disagreement between the data and MC has been tested using different cut values on E_T^{miss} . In Figure 4.8 the two requirements on the minimal E_T^{miss} values are considered. On the left plot the $m_T(\tau, E_T^{\text{miss}})$ values calculated for events with $E_T^{\text{miss}} > 160$ GeV is presented, and on the right plot for events with $E_T^{\text{miss}} > 200$ GeV. The events that are mostly contribution to the bump are at low E_T^{miss} values.

The fake τ s do come from events that have low values of both E_T^{miss} and p_T (as in this region the τ are not identified). When the τ is in the direction of E_T^{miss} (E_T^{miss} faked by τ), the multijet events are at low $m_T(\tau, E_T^{\text{miss}})$. With a lower E_T^{miss} cut of 160 GeV and $p_T(\tau)$ of 20 GeV this gives $m_T(\tau, E_T^{\text{miss}}) \sim 80$ GeV. In the case when the E_T^{miss} that is faked by another jet, τ can point in any other direction. For $E_T^{\text{miss}} = 200$ GeV and $p_T(\tau) = 40$ GeV (τ back to back with E_T^{miss}), it gives the $m_T(\tau, E_T^{\text{miss}}) \sim 125$ GeV, which is in the right range of the observed bump. This is pointing towards the direction that it comes from the multijet background. Fake τ s from other processes would probably also contribute to the region where the bump is present. Thus only τ s that give $m_T(\tau, E_T^{\text{miss}}) < 100$ GeV are tagged as τ s.

4.3.3 Other kinematic variables in events containing tau leptons

In Figure 4.9 the data and expected MC background $\Delta\phi(j_i, E_T^{\text{miss}})$ distributions normalised to luminosity before the $\Delta\phi(j_i, E_T^{\text{miss}})$ cut are shown for VRWTTau2jl and VRttbarTau6j. One can see there is some contamination coming from the multijet background (here estimated from the MC) that contributes to the event count in these VRs.

The τ fake rate calculated in Section 4.2.2.2 can be used to get the estimation of the QCD background in the regions where the τ s are selected. Ideally one would predict the multijet background in these regions by using seeds with fake τ candidates and the corresponding resolution function, but there is not enough of these seeds available. To get an estimate of the multijet background, a correction by a factor 0.035 times the number of jets is applied after computing the usual normalisation of the multijet background. As this factor is an upper limit on the τ fake rate this gives an overestimate of the multijet background in τ enriched regions.

In Figure 4.10 the distributions of $m_{\text{eff}}(\text{incl.})$ before the cut on the ratio between E_T^{miss} and $m_{\text{eff}}(N_{\text{jets}})$ (on the left), and that ratio (on the right) with no $m_{\text{eff}}(\text{incl.})$ cut applied are shown

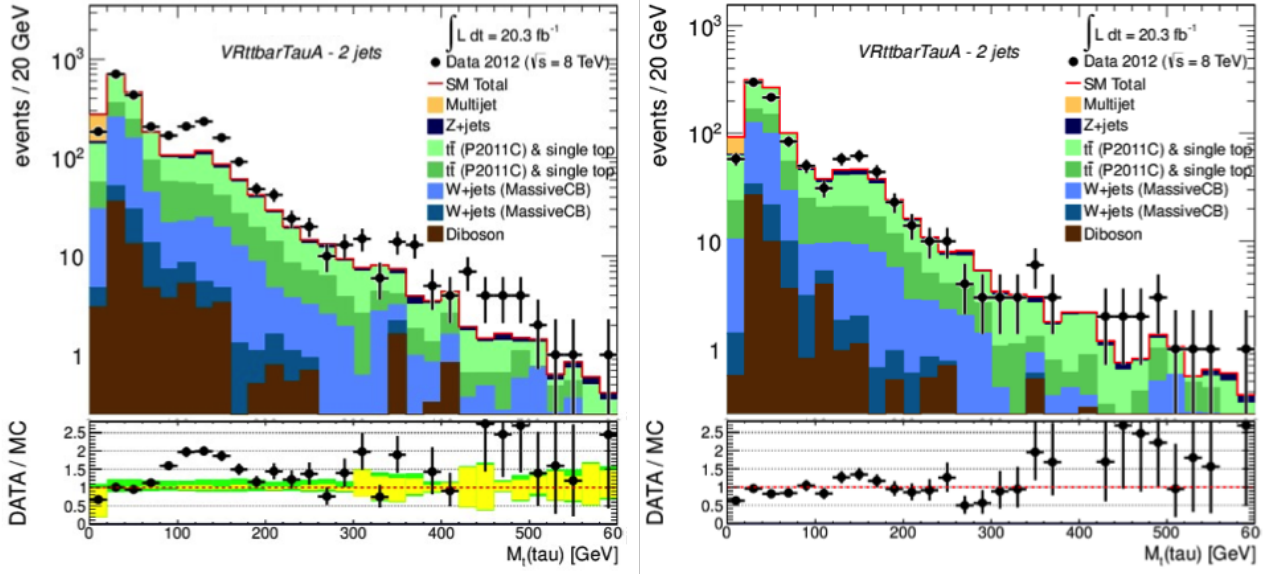


Figure 4.8: On the left plot, data and expected MC background $m_{\text{eff}}(\text{incl.})$ distribution normalised to luminosity in the VRttbarTau2j, is shown, for events with $E_{\text{T}}^{\text{miss}} > 160$ GeV, and on the right plot for events with $E_{\text{T}}^{\text{miss}} > 200$ GeV.

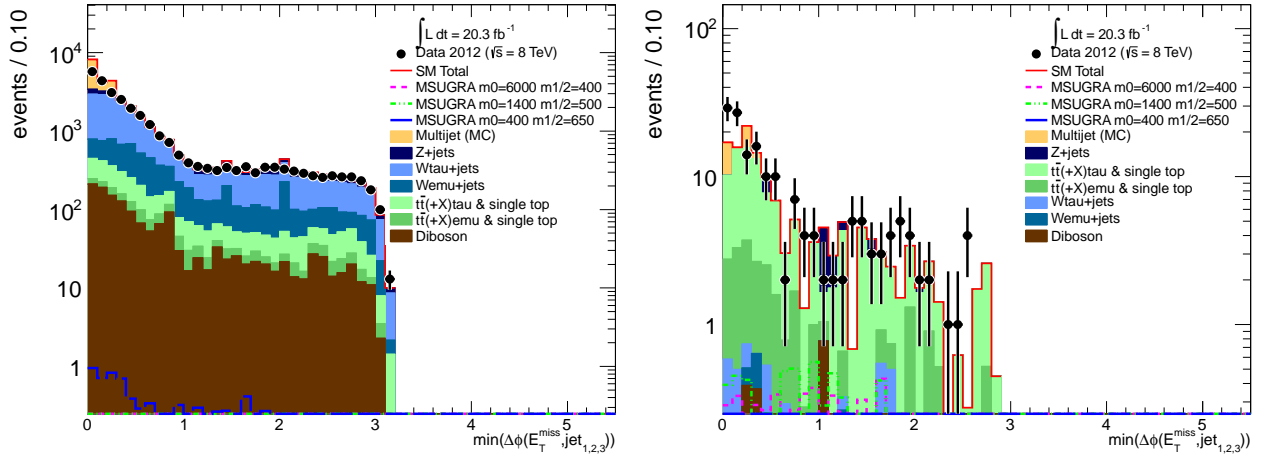


Figure 4.9: Data and expected MC background $\Delta\phi(j_i, E_{\text{T}}^{\text{miss}})$ distributions normalised to luminosity before the $\Delta\phi(j_i, E_{\text{T}}^{\text{miss}})$ cut are shown, with the τ identified with the track counting algorithm. On the left the VRW2j is shown and on the right VRttbar6j. The QCD background is estimated from the MC samples.

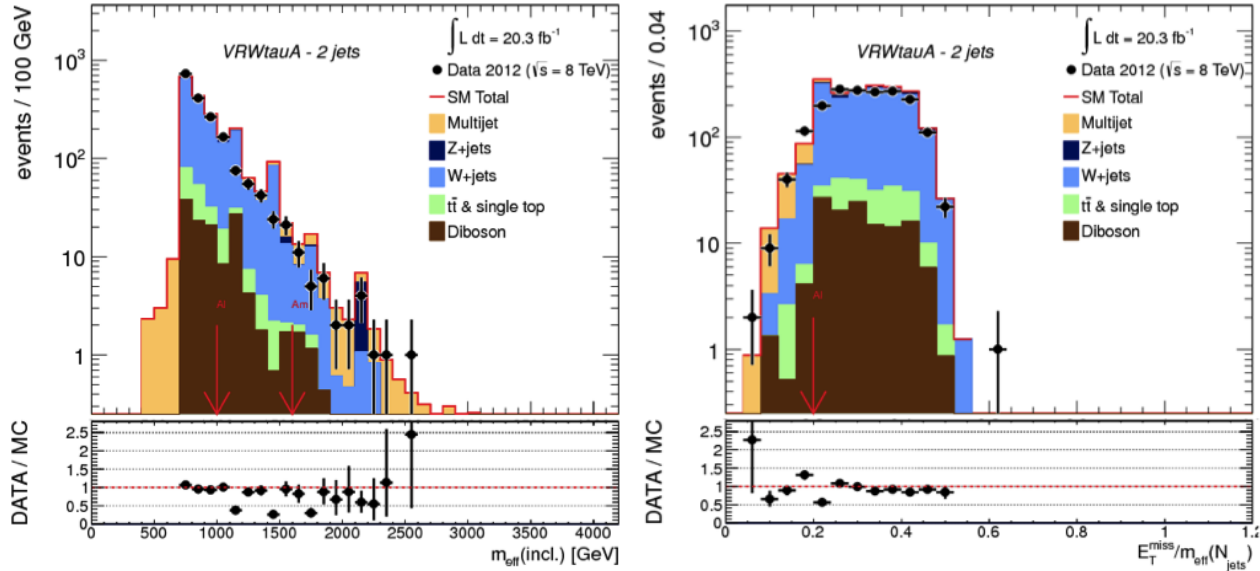


Figure 4.10: The distribution of the $m_{\text{eff}}(\text{incl.})$ before the cut on the ratio between E_T^{miss} and m_{eff} (on the left) and that ratio (on the right) with no $m_{\text{eff}}(\text{incl.})$ cut for the VRWtau2j. In these plots the multijet background is estimated using the QCD smeared multijet sample and the fake τ estimation as described in Section 4.2.2.2.

Process	Region														
	2jl	2jm	2jt	2jW	3j	4jvl	4jl	4jm	4jt	4jW	5j	6jl	6jm	6jt	6jvt
W	71	67	55		57	74	71	74	50	73	71	74	78	69	72
$t\bar{t}$	74	62	65	75	80	94	74	65	90	61	72	74	74	83	76

Table 4.2: The number of events that have τ at the truth level divided by the total number of events in VRWtau and VRttbarTau, after all VR selection criteria. The numbers are in percent.

for the VRWtau2j. In these plots the multijet background is estimated using the QCD smeared multijet sample and fake τ estimation. One can see that there is a good agreement between expected events and the data, and here especially that the QCD smeared multijet sample does describe well the data. Multijet background is well placed at the low $E_T^{\text{miss}}/m_{\text{eff}}(N_{\text{jets}})$ values, and after the $E_T^{\text{miss}}/m_{\text{eff}}(N_{\text{jets}})$ cut at the value of 0.2, almost all multijet background is suppressed. That is why the plot on the left shows the $m_{\text{eff}}(\text{incl.})$ distribution before the $E_T^{\text{miss}}/m_{\text{eff}}(N_{\text{jets}})$, as only without this cut one can see where would the multijet background be. Its contribution placed at the $m_{\text{eff}}(\text{incl.})$ lower than 700 GeV and the lack of other backgrounds in the same region is coming from the different preselection requirement on the $m_{\text{eff}}(\text{incl.})$ applied to the inputs. The multijet background is found negligible in this VR after applying all analysis criteria. In Figure 4.11 the same is shown for the VRttbarTau6j region, and the same conclusion is reached.

In Figure 4.12 one can see the $m_{\text{eff}}(\text{incl.})$ distributions for VRWtau2jl and VRttbarTau6j. There is good agreement between data and MC prediction in both regions. As explained before $m_{\text{eff}}(\text{incl.})$ is the last discriminating variable, and here one can see that after all analysis selection criteria, the VRs for $\tau\tau$ are clearly enriched in $\tau\tau$. In Table 4.2 the number of events that have τ at the truth level divided by the total number of events of that VR, after all the VR selection criteria, is given in percent as a proof of the enrichment.

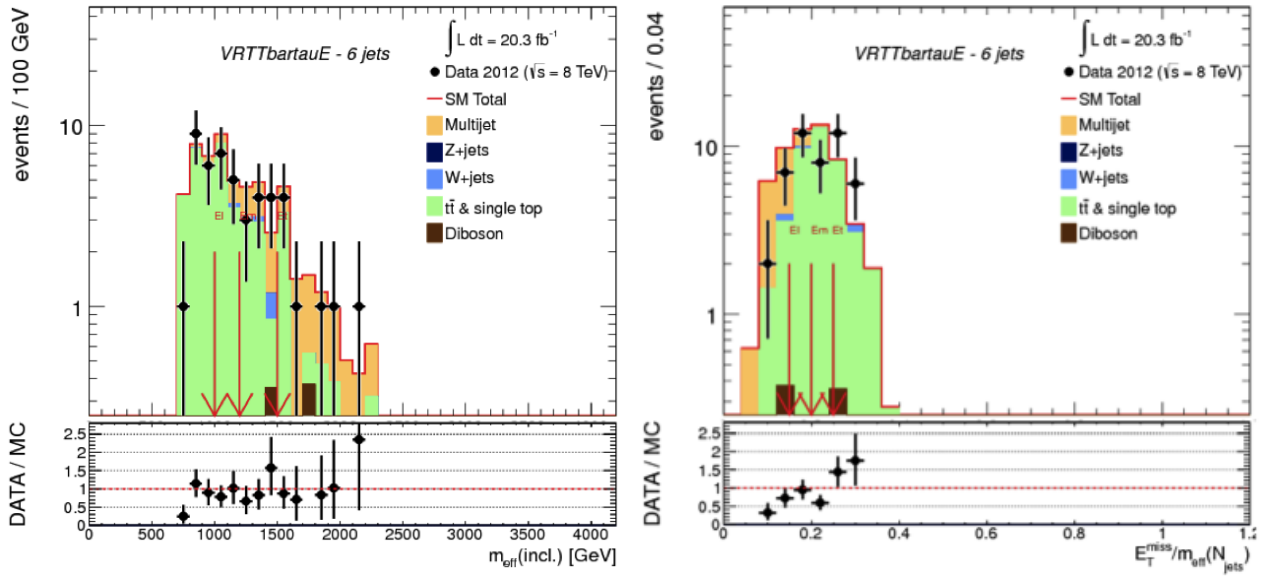


Figure 4.11: The distribution of the $m_{\text{eff}}(\text{incl.})$ before the cut on the ratio between E_T^{miss} and m_{eff} (on the left) and that ratio (on the right) with no $m_{\text{eff}}(\text{incl.})$ cut for the VRttbarTau6j. In these plots the multijet background is estimated using the QCD smeared multijet sample and fake τ estimation as described in Section 4.2.2.2.

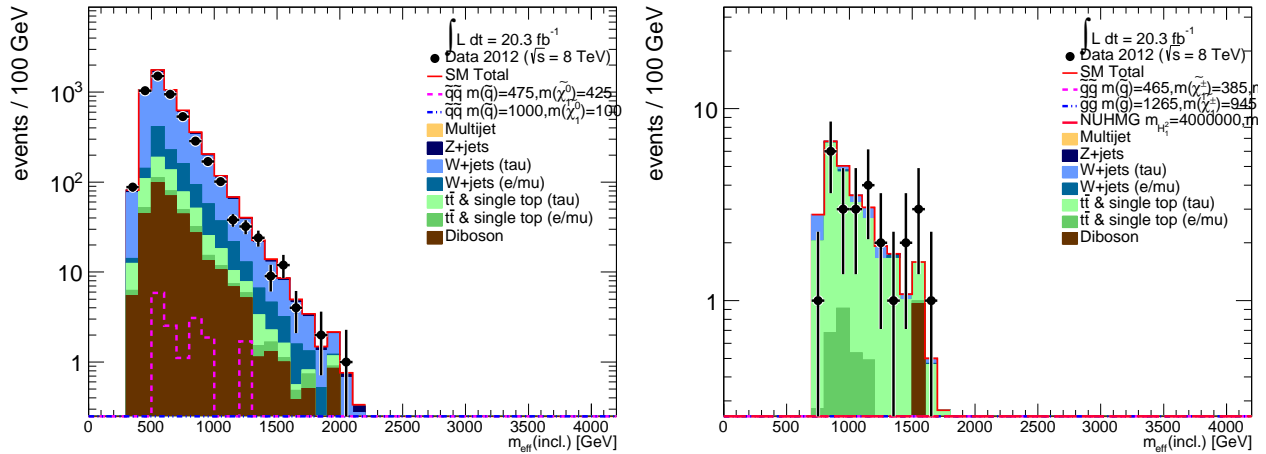


Figure 4.12: Data and expected MC background m_{eff} distribution normalised to luminosity before the last $m_{\text{eff}}(\text{incl.})$ cut, with the τ identified with the track counting algorithm. On the left the VRW2j1 is shown and on the right VRttbar6j1.

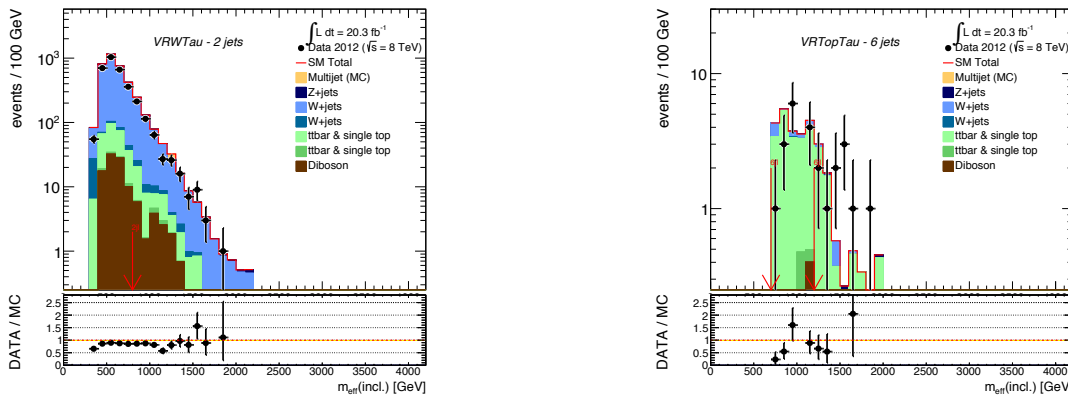


Figure 4.13: Data and expected MC background m_{eff} distribution normalised to luminosity before the last $m_{\text{eff}}(\text{incl})$ cut, with the τ identified with the BDT algorithm. On the left the VRW2j1 is shown and on the right VRttbar6j1.

Process	Region								
	2jl	2jt	3jm	4jm	4jt	5j	6jl	6jm	6jt
W	84	68	31	71	90	91	58	57	44
Z	4	29	68	8	0	0	0	0	0
Top	4	0	0	11	2	5	21	29	0
Diboson	8	3	0	10	3	13	21	14	53
signal	0	0	1	0	5	1	0	0	3

Table 4.3: The ratios of expected background and signal events over the total number of events in some VRW2j1 (in percent). The signal is estimated with mSUGRA point $m_0 = 800$ GeV and $m_{1/2} = 850$ GeV.

4.3.4 Comparison between track counting and BDT algorithms

The track counting and the BDT algorithm can be compared by examining the $m_{\text{eff}}(\text{incl.})$ distribution shown in Figures 4.12 and 4.13. In Figure 4.13 the τ identification is performed using the BDT 'loose' working point with the addition of the requirement on the $m_T(\tau, E_T^{\text{miss}})$. There is a good agreement between data and MC predictions in both regions and both algorithms give similar results. As explained before this comparison is shown just as a cross check as it became available in later stage of the analysis. It strengthens the confidence in the results obtained with the track counting algorithm.

4.3.5 Signal contamination

Up to now all the investigation towards designing VRs for τ s were concentrated on the background, but to be used in the final fit one should check that there is no contamination coming from signal events. To get the highest number of signal events with τ s in the final state a mSUGRA signal point has been chosen in the stau coannihilation region, ie. at low m_0 and high $m_{1/2}$ values. A point with $m_0 = 800$ GeV and $m_{1/2} = 850$ GeV is investigated in the following. The ratios of expected background and signal events over the total number of events in a given VR (in percent) are shown in Table 4.3 for VRW2j1 and in Table 4.4 for VRttbar6j1. The number of signal events entering the VRs is negligible in most of the regions. In some VRs there are a bit more signal events (up to 10% of all events), but it is expected as the event counts are very low in tight VRs, so some fluctuations are expected.

Process	Region								
	2jl	2jt	3jm	4jm	4jt	5j	6jl	6jm	6jt
W	18	24	0	18	0	29	4	2	0
Z	11	4	6	3	0	0	0	0	0
Top	67	69	88	74	90	62	93	94	98
Diboson	4	0	0	5	0	7	3	3	0
signal	0	3	6	0	10	2	0	1	2

Table 4.4: The ratios of expected background and signal events over the total number of events in some VRttbarTau (in percent). The signal is estimated with mSUGRA point $m_0=800$ GeV and $m_{1/2}=850$ GeV.

4.3.6 Agreement between the data and MC expectation in the VRs for τs

The easiest way to present the agreement between the data and the MC prediction in all the regions of the analysis is by looking at the difference between data and MC expectation divided by the uncertainty on the latter - denoted the pull value in the following. Here the emphasis is made on the two VRs for τs . In Figure 4.14 these are shown for two representative SRs, one for 2jl, and one for 6jl, and in the lower pad the pull values for VRs for τs are presented in red. All the uncertainties mentioned in the Section 3 are taken into account, with the addition of the uncertainty coming from the variation of the TES (explained in Section 4.1.5), after all the VR selection criteria. The agreement is good, despite the low number of events in the VRs with tight cuts (as can be seen also in Figure 4.12 on the right, after the $m_{\text{eff}}(\text{incl.})$ cut only few events remain). In 2jl for the τs originating from W decay, there is ~ 1000 events (~ 700 are expected on MC to come from τ), while the region for $t\bar{t}$ background is much less populated. The opposite is true for the 6jl VRs: here there is ~ 20 events in VRttbar, comparing to only few events in VRW. The systematic uncertainty coming only from the variation of TES is found to be of the order of 3 to 5 %, after all the VR selection criteria.

4.4 Tau veto in Signal regions

This Section illustrates the use of a veto on events containing τs in the 0-lepton analysis SR selection and its impact on the exclusion contours. As mentioned before, the addition of such a veto could be a possible improvement of the 0-lepton analysis. The $m_T(\tau, E_T^{\text{miss}})$ cut is not considered anymore for the τ selection.

4.4.1 Effect of the veto on the events containing tau leptons

First the effect of the addition of a veto on τs on the distribution of the $m_{\text{eff}}(\text{incl.})$ is investigated. In Figure 4.15 the nominal selection of the 0-lepton analysis for the SR2jl (on the left) is presented. In the middle plot there is the addition of the veto on the events containing τs identified by the track counting algorithm, and on the right plot, just for comparison, the same is shown but this time τs are identified with the BDT. Both algorithms give good agreement between the data and the SM prediction. In Figure 4.16 the same comparison is presented for the SR6jl.

In Figure 4.17 the same distribution of $m_{\text{eff}}(\text{incl.})$ is shown. In the lower pad of the Figure the comparison between the significances obtained for two points of the simplified model of squark pair production followed by the direct decay to quark and $\tilde{\chi}_1^0$ with the masses of $m(\tilde{q}) =$

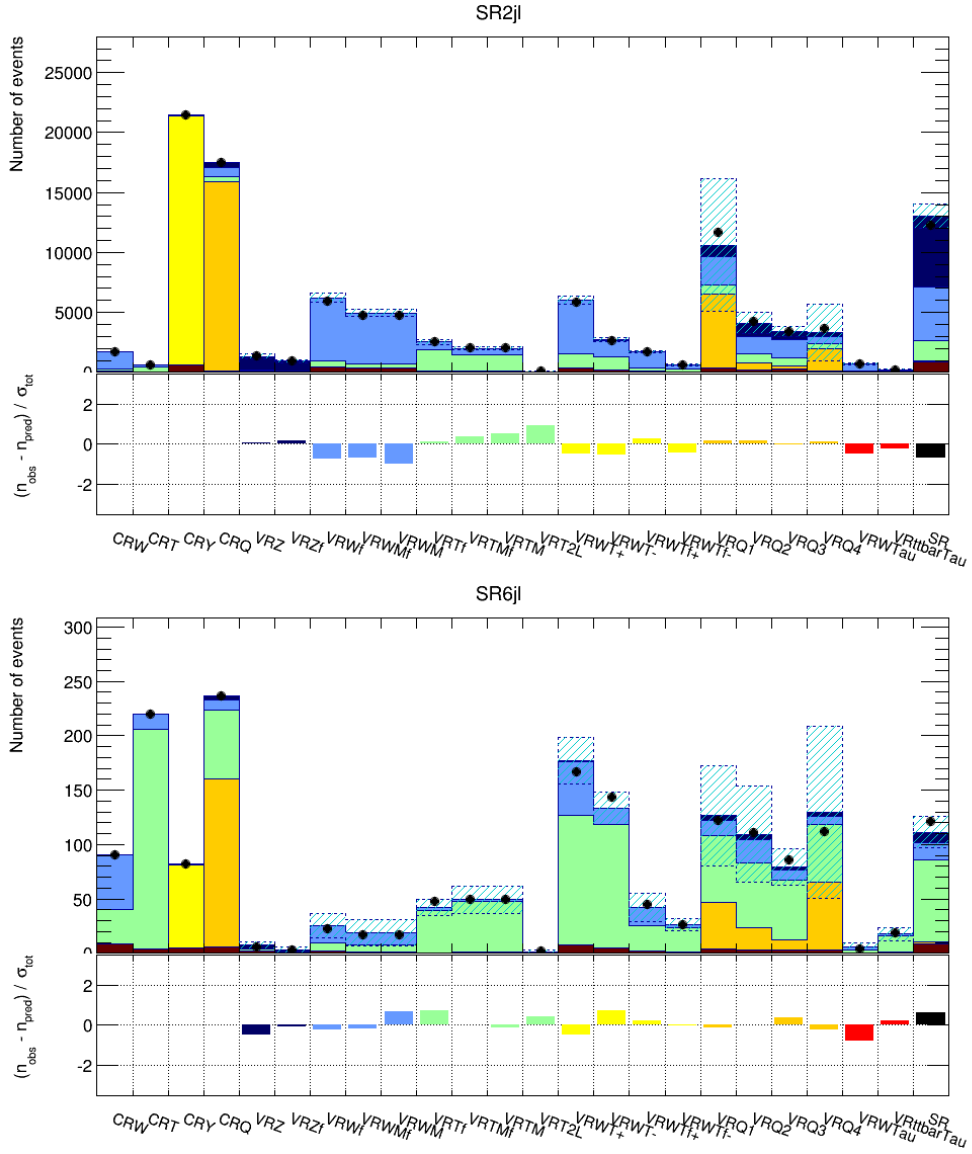


Figure 4.14: Plots showing the difference between data and MC expectation in all VRs of the 0-lepton analysis divided by the uncertainty on the latter (all the uncertainties mentioned in the Section 3 with the addition of the uncertainty coming from the variation of TES for the τ VRs). VRs corresponding to SR2jl and SR6jl are shown on the upper and lower plot respectively. VRs for the τ leptons (VRWTau and VRTtbarTau) are given in red.

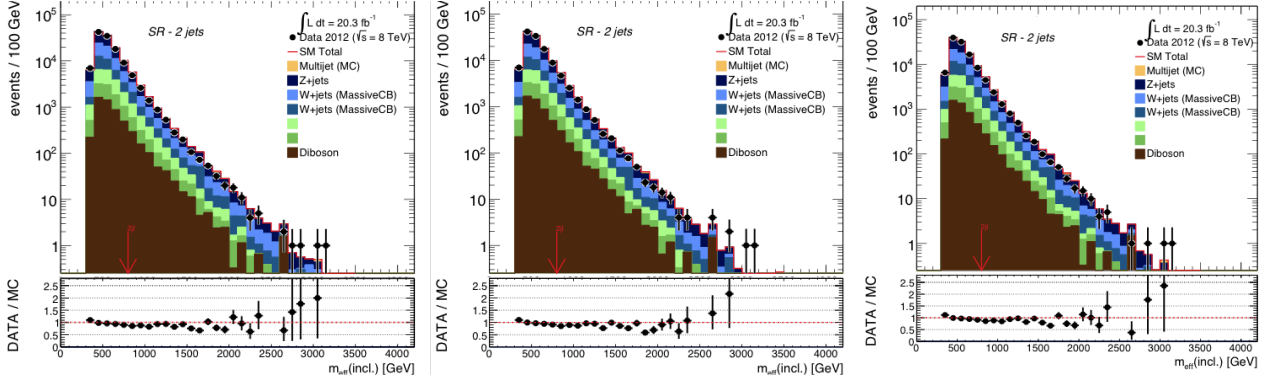


Figure 4.15: Data and expected MC background $m_{\text{eff}}(\text{incl.})$ distribution normalised to luminosity before the last $m_{\text{eff}}(\text{incl.})$ in SR2jl cut for nominal 0-lepton analysis selection (on the left), with the veto on the events containing τ s, selected by the track counting (in the middle) and the BDT algorithm (on the right).

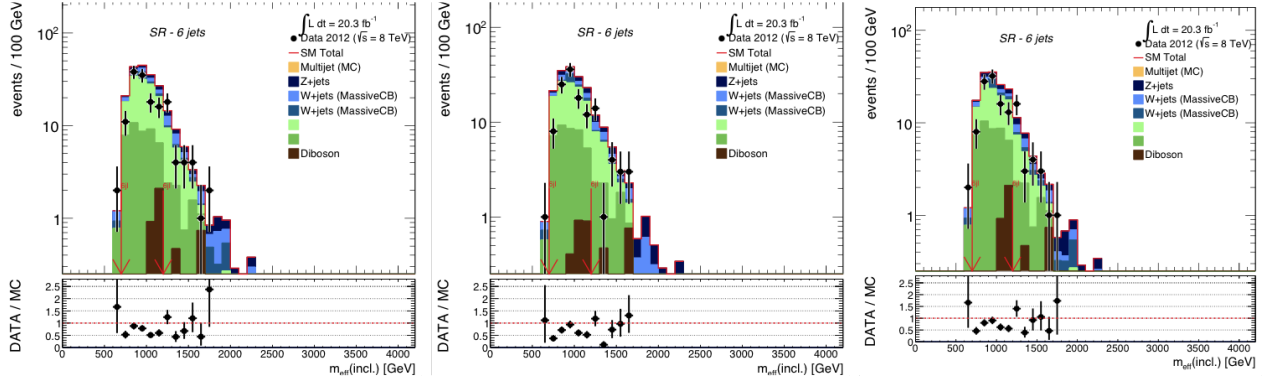


Figure 4.16: Data and expected MC background $m_{\text{eff}}(\text{incl.})$ distribution normalised to luminosity before the last $m_{\text{eff}}(\text{incl.})$ in SR6jl cut for nominal 0-lepton analysis selection (on the left), with the veto on the events containing τ s, selected by the track counting (in the middle) and the BDT algorithm (on the right).

850 GeV and $m(\tilde{\chi}_1^0) = 100$ GeV (dotted pink line), and $m(\tilde{q}) = 450$ GeV and $m(\tilde{\chi}_1^0) = 400$ GeV (dotted blue line) are shown. There are no τ s in the final states of this process. The significance is calculated using the following formula [135]:

$$z_0 = \sqrt{(2(s+b) \ln(1+s/b) - s)} \quad (4.4)$$

where s is the number of expected signal events, while b is the expected number of background events. The addition of the veto on events containing τ s increases the significance, especially for the point with large difference in mass between squark and neutralino (pink dotted line) for the $m_{\text{eff}}(\text{incl.})$ value of 1500 GeV, while the significance for the point with small mass splitting essentially stays the same.

Now let's consider the model of the gluino pairs production followed by either direct or the decay through intermediate chargino to quarks and $\tilde{\chi}_1^0$. These models are expected to have many jets in the final state, and therefore the most sensitive SRs are those with at least 6 jets. In Figure 4.18 the distribution of the $m_{\text{eff}}(\text{incl.})$ is shown for this SRs with the nominal selection criteria (on the left), and with the addition of the veto on the events containing τ s and b -tag jets (on the right). The gluino pairs production followed by the direct decay is shown by green solid line ($m(\tilde{g}) = 1162$ GeV, $m(\tilde{\chi}_1^0) = 337$ GeV), and the decay through intermediate chargino to quarks and $\tilde{\chi}_1^0$ is shown for two points corresponding to different gluino and neutralino masses in pink ($m(\tilde{g}) = 1200$ GeV, $m(\tilde{\chi}_1^\pm) = 760$ GeV, $m(\tilde{\chi}_1^0) = 60$ GeV) and blue ($m(\tilde{g}) = 1025$ GeV, $m(\tilde{\chi}_1^\pm) = 785$ GeV, $m(\tilde{\chi}_1^0) = 545$ GeV) dotted lines. As these SRs are dominated by the background coming from the top pair production, the addition of the veto on the events

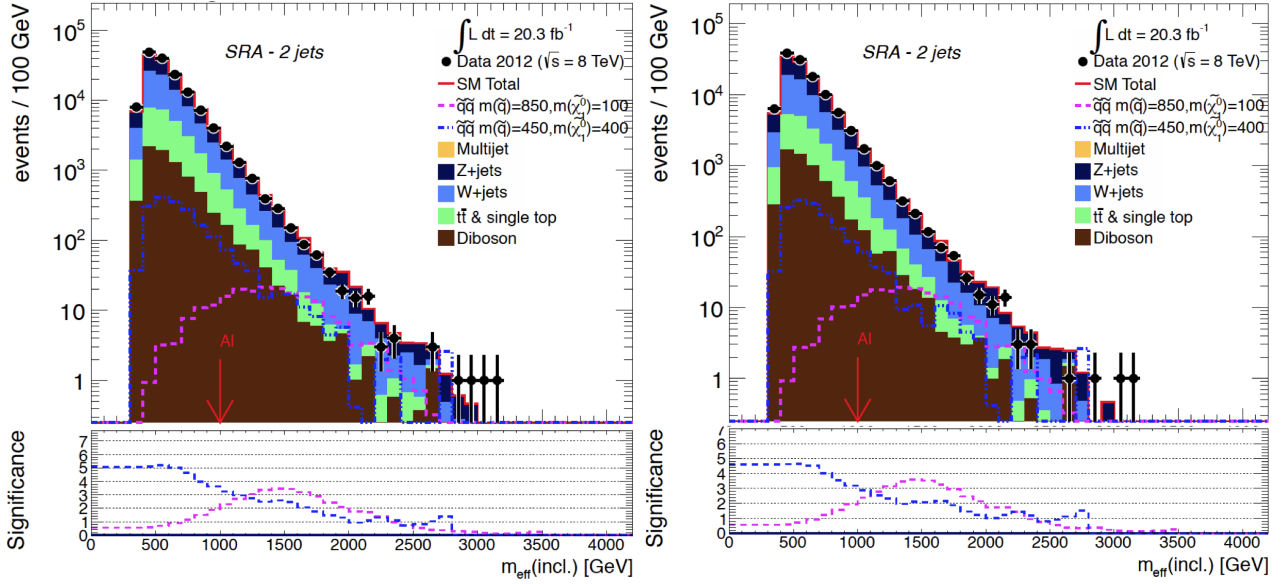


Figure 4.17: Data and expected MC background $m_{\text{eff}}(\text{incl.})$ distribution normalised to luminosity before the last $m_{\text{eff}}(\text{incl.})$ in SR2j1 cut for nominal 0-lepton analysis selection (on the left), with the veto on the events containing τ s selected by the track counting (on the right). On the lower pad the significance calculated for two points of the simplified model of squark pair production followed by direct decay to quark and neutralino is shown.

Uncertainty	Region						
	2jl	2jm	3jm	3jt	4jm	4jt	5j
TES down	2.4	4.4	4.1	0	0	0	0
TES up	3.3	3.6	2.9	0	2.7	0	3.3

Table 4.5: The systematic uncertainty coming from the TES calculated for several SR of the 0-lepton analysis. It is calculated as the difference between the number of events with varying TES up and down and the nominal number of events, divided by the nominal number of events in corresponding SR and is given in percent.

containing b -tagged jets was considered.

The addition of the veto on the events containing τ in the SRs help in suppressing the background coming from the W +jets and $t\bar{t}$ production, while keeping the possible signal, as can be seen from the increase in the significance. Although it is evident that not all the events with τ s are eliminated, still the suppression may be enough to bring an improvement to the 0-lepton analysis. This impact on the limits in sparticle masses set by this analysis will be estimated in the next Section.

In Table 4.5 the systematic uncertainty coming from the TES calculated for several SRs of the 0-lepton analysis is given. It is calculated as the difference between the number of events with varying TES up and down and the nominal number of events, divided by the nominal number of events in corresponding SR and is given in percent. The impact of this uncertainty is fairly small in most of the SRs. As the number of events with identified τ s in some SRs is small, sometimes it can occur that this uncertainty is zero.

4.4.2 Impact of tau veto on exclusion contours

In this Subsection, the impact of the veto on the events containing τ s will be assessed, this time on the exclusion contours of several simplified models.

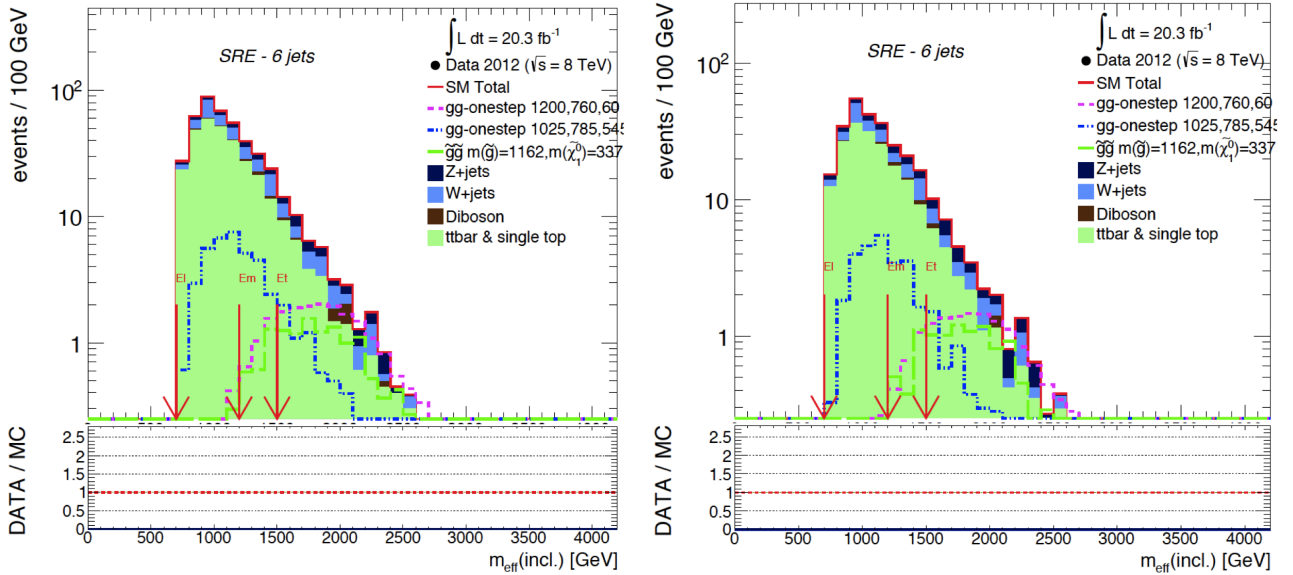


Figure 4.18: On the left default selection for the SR with at least 6 jets, on the right the same SR selection with the addition of a veto on the events containing τs (identified by the track counting algorithm) as well as on the events containing b -tagged jets.

4.4.2.1 Direct squark decay - no systematic uncertainty

First the case of the simplified model of squark pair production followed by the direct decay to quark and $\tilde{\chi}_1^0$ is considered. When the exclusion reach at 8 TeV for this model [1] is compared with the 0-lepton 7 TeV analysis [136], no sizable improvement is found. One explanation may be that τs dominate the background. To test this a comparison is made between the limits obtained without (the left plot of Figure 4.19) and with the addition of the veto on events containing τs (the right plot of the same Figure). Here the best possible scenario is assumed: no systematic uncertainties are added to the fit configuration. This is giving the best expected improvement using this veto. Two SRs with at least 2 jets are considered (here denoted by SRA, where A stands for 2 jets, as this notation was used for the conf note [1]), as well as one SR with at least 4 jets (here denoted by C, where C stands for 4 jets), as these are the SR that have the most sensitivity in this simplified model. The combined limit is the thin black line, while the thick black and the red line correspond to different tightness of the selection in SR with at least 2 jets, and the green line represents the exclusion reach for the SR with at least 4 jets. The improvement is mostly seen for the squark mass above 800 GeV and neutralino masses of around 200 GeV, driven by the SRA with the tighter $m_{\text{eff}}(\text{incl.})$ requirement (corresponding to SR2jt from Table 3.6). The exclusion reach is almost completely unchanged when squarks and neutralinos are nearly degenerate. Also it is having different effect depending on the SR. The SRC is showing improvement for the squark masses between 400 and 700 GeV, for a neutralino mass of almost 300 GeV. But as this SR is not the best expected SR, this effect is not present in the combined exclusion contour. For making the fair comparison, only the addition of the veto to the already existing SRs is considered. No reoptimisation of the analysis was done, so the possible improvement is underestimated. In general, it is seen that there is an increase in the combined exclusion reach with the addition of the veto on events containing τs , which motivates us to pursue it further. It would allow to push further the high squark mass limit for the massless neutralino.

4.4.2.2 Direct squark decay - systematic uncertainty included

Now the same model is considered but in a more realistic case, when all the systematic uncertainties are added to the fit setup with this time all the SRs considered. In Figure 4.20 the

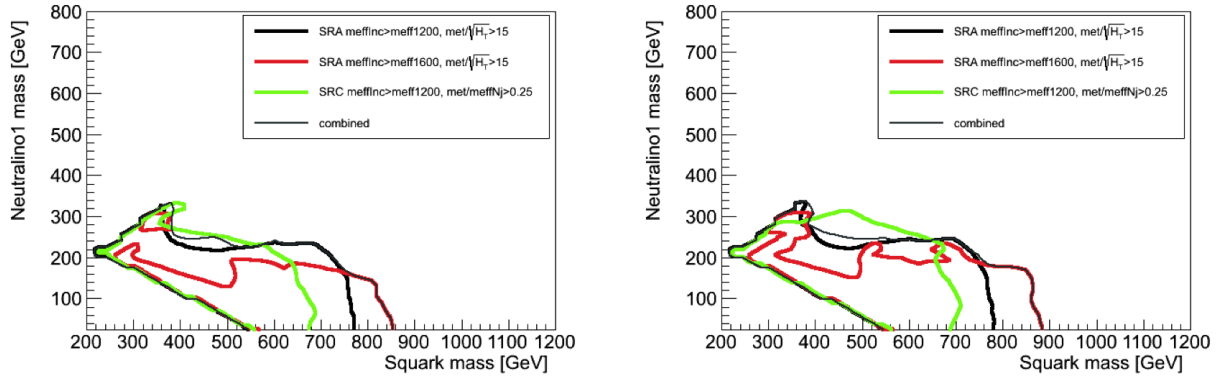


Figure 4.19: On the left default selection, on the right addition of a veto on the events containing τ s.

exclusion contours are shown in the squark - neutralino mass plane for the nominal 0-lepton analysis selection (4.20a), with the addition of a veto on the events containing τ (4.20b), and a veto on b -tagged jets (4.20c), and in 4.20d it is the combined veto on events that contain either τ or b -jet. Comparing the exclusion reach between the nominal 0-lepton selection and the selection that includes also veto on events containing τ s, the only visible change is for the squark mass of 700 - 800 GeV, for the $\tilde{\chi}_1^0$ mass of 300 - 400 GeV, the contour is much smoother. There is a slight improvement for $m(\tilde{q}) = 500$ GeV for $m(\tilde{\chi}_1^0) = 400$ GeV. The plots with the addition of the b -jet veto show almost no improvement. Thus the combined veto is mainly driven by the addition of the τ veto but its impact is almost negligible. This comes from the fact that the systematic uncertainties influence the exclusion contours, reducing the gain. Also one of the limiting factors is the efficiency of the τ selection - it is impossible to identify most of the τ s, and thus there are still many background events in our SRs coming from the processes that have τ s in the final state.

4.4.2.3 Onestep gluino decay - systematic uncertainty included

In Figure 4.21 one can see the impact of a combined τ and b -jet veto on the exclusion contours for the model of the gluino pairs production followed by the decay through intermediate chargino to quarks and $\tilde{\chi}_1^0$. The green dotted line represents the exclusion using nominal SRs, while the blue dotted line corresponds to the exclusion one can obtain by adding combined veto. All the systematic uncertainties are considered. The exclusion contour is made by taking into account the best expected SR. The improvement is present for the gluino masses between 1200 and 1300 GeV for x (the ratio of the mass splitting between chargino and neutralino, and the one of the gluino and neutralino, respectively) between 0.6 and 0.9. Also in some parts of the plane (for very low and very high values of x), the exclusion contour is getting worse. One can see that there is no sizable improvement by vetoing events containing τ s or b -jets.

4.5 Validation with the 13 TeV data

The VRs for τ s are part of this 0-lepton analysis strategy for the Run 2 of the LHC 3.5. They are designed to be close to those used for Run 1, with the same requirements on the presence of at least one τ in the event. Also the same separation between τ s coming from the production of W +jets and those from $t\bar{t}$ is retained, by requiring zero and at least one b -jet respectively. The τ is identified with the BDT algorithm. One of the main changes is the amount of the $m_{\text{eff}}(\text{incl.})$ in the events, which is higher in Run 2. In Figure 4.22 the data and expected MC background is presented for the VRWtau on the left, and for the VRttbarTau on the right,

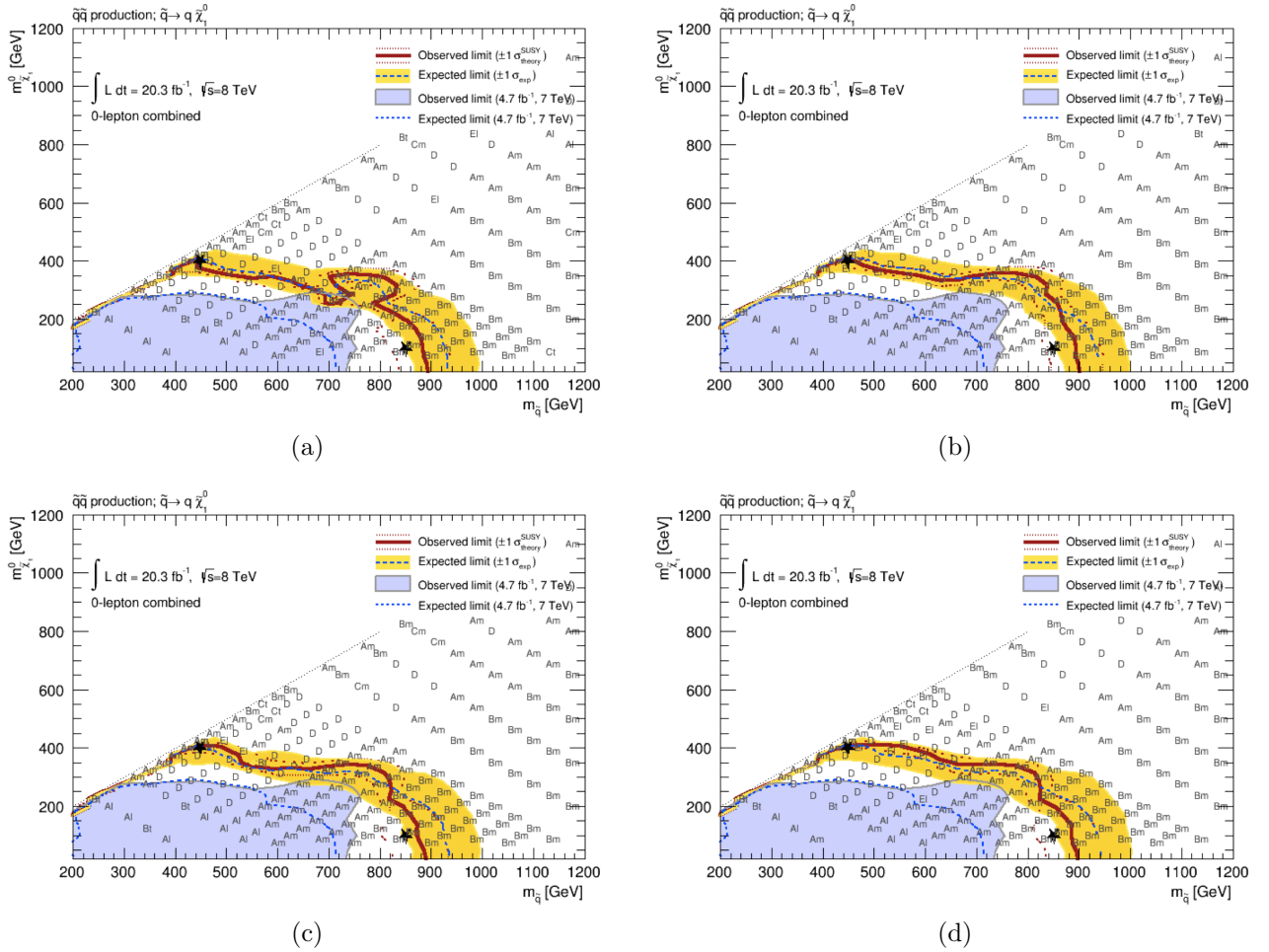


Figure 4.20: The 95% exclusion is shown for several selection criteria explored. In Figure (a) the nominal 0-lepton analysis selection is shown. It is to be compared with the same selection with the addition of the veto on events containing identified τ s (b), and the addition on the veto on the events with reconstructed b -jets (c). The 95% exclusion reach with the combined veto on the events containing either τ or a b -jet is shown in Figure (d). All the systematic uncertainties are taken into account.

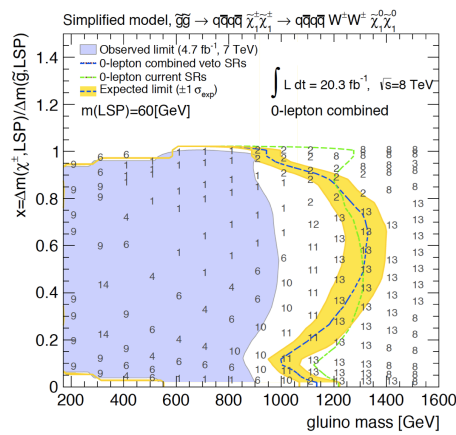


Figure 4.21: The exclusion reach for the model of gluino pair production followed by the decay through intermediate chargino to quarks and $\tilde{\chi}_1^0$ is shown. The green dotted line represents the exclusion using current SRs, while the blue dotted line corresponds to the exclusion one can obtain by adding combined veto on τ leptons and b -tagged jets.

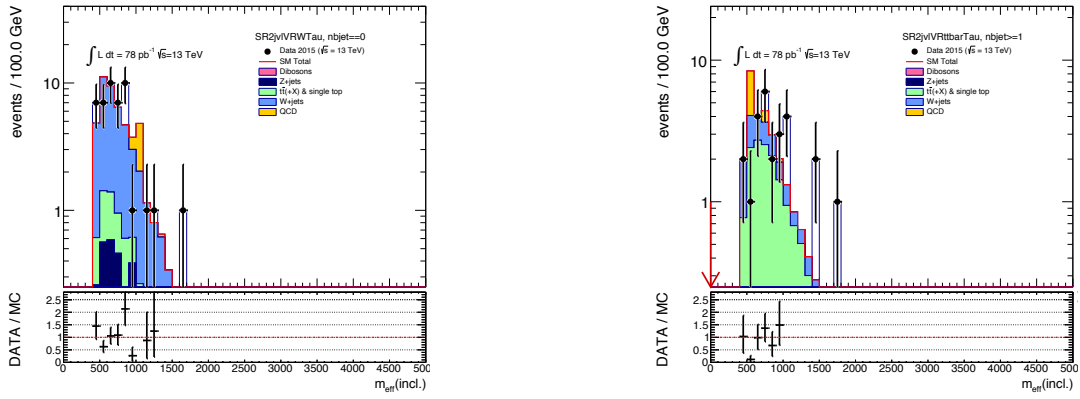


Figure 4.22: Data and expected MC background $m_{\text{eff}}(\text{incl.})$ distribution normalised to luminosity before the last $m_{\text{eff}}(\text{incl.})$ cut, with the τ identified with the BDT algorithm. On the left the VRWTau is shown and on the right VRttbarTau.

for the 13 TeV data. As the luminosity acquired for this plot is 78 pb^{-1} only the VR with the very loose selection have considerable number of events, thus here the very loose region with at least 2 jets is presented. The p_T of the first jet is required to be greater than 130 GeV, the second jet $p_T > 60$ GeV and $E_T^{\text{miss}} > 160$ GeV. The $m_T(\tau, E_T^{\text{miss}})$ is not used, but still there are not many fake τ s coming from the multijet events. The good agreement between the data and MC prediction is observed.

4.6 Conclusion

In this Chapter the impact of the background coming from τ s has been presented, and possible ways of reducing its effect are explored. In this thesis, two validation regions to test the modelling of τ s have been designed and added to the final fit for 8 TeV 0-lepton analysis. Good agreement between the observed number of events and the Monte Carlo predictions is present in these regions which gives us additional confidence in the results of the analysis. The addition of a veto on the events containing τ in signal regions has been considered. Although it is not found to bring considerable improvement in the exclusion reach of the analysis, this veto should be further pursued for the Run 2 analysis.

Chapter 5

pMSSM parameter space and ATLAS SUSY searches

The 0-lepton analysis as described in Chapter 3 is interpreted within the context of simplified models, or mSUGRA grids. To have a full overview of the constraints on wider SUSY models, the phenomenological MSSM (pMSSM) analysis within ATLAS was proposed by Rizzo et al. following their work [137, 138, 139, 140]. The pMSSM parameter space is designed to be both small enough to be explored, and large enough to allow many possible sparticle productions and decays. Thus it is very interesting to investigate it, as it is a theoretically well defined SUSY model. Also, while the mSUGRA and GMSB make assumptions on the unification of the breaking parameters at the high scale, the pMSSM is a low scale model with most of its parameters defined at the SUSY scale. As a byproduct, the exploration of the pMSSM permits to make a fair comparison with the simplified models. The pMSSM parameter space can be constrained with both indirect measurements and dedicated searches, and allows for the results of very different searches to be interpreted and compared. The idea is then to evaluate in a 19 parameters pMSSM, the impact of a combination of all ATLAS searches carried out with the data collected during LHC Run 1. The results therefore represent the legacy of the 7 and 8 TeV searches.

The pMSSM is used for the interpretation of the search results by several groups: for instance in [141, 142, 143, 144, 145, 146, 147, 148, 149, 150, 151, 152, 153, 154, 155] (this is not an exhaustive list). All those approaches are different either by the number of parameters they tackle (some focus on non universal Higgs models, other on the light neutralino sector...) or by the observables they use as inputs (some consider WMAP dark matter energy density, others do not consider the direct dark matter searches...) or by the kind of analysis they implement (frequentist, Bayesian or percentage of excluded models). The CMS also published several studies of the pMSSM [156, 157, 158, 159]. The ATLAS pMSSM analysis presented in this thesis and in Ref. [3, 160] differs from the previous ones by the huge number of pMSSM model points analysed, as this is the first time a study on that scale is carried out by an LHC experiment (in addition all relevant 8 TeV SUSY ATLAS analyses are considered comparing to a subset of the 7 and 8 TeV analyses considered by CMS).

Considering the complexity of such studies the three following chapters will be devoted to its description.

The first one (this Chapter) describes the 19 pMSSM parameters, the measurements that are a priori used to reduce the parameter space and the ATLAS searches that are considered. It also presents the pMSSM analysis strategy.

The second one (Chapter 6) describes the implementation and the validation of the 0-lepton analysis at the truth and at the reconstructed levels within different models. These have been necessary to give reliable results for the pMSSM analysis.

The third one (Chapter 7) describes the results on two aspects: the impact of the 0-lepton analysis on one side and the final ATLAS results on the pMSSM parameter space on the other side.

The work of this thesis has been to proceed with the 0-lepton analysis within the pMSSM study - from the selection of the model points with the truth code towards the interpretations of the results. It is mainly concentrated in Chapter 6, and the 0-lepton part of the Chapter 7.

In this Chapter, the pMSSM parameters are described first (Section 5.1). Then the indirect constraints are reviewed (Section 5.2), as well as their impact on the allowed model points (Section 5.3). The ATLAS searches that are considered to further constrain the model points are presented in the Section 5.4. Finally, the description of the strategy of the pMSSM analysis is also presented, how it is carried out and which criteria are applied to exclude model points (Section 5.5).

5.1 pMSSM parameter space

This Section describes what is understood under the denomination 19 parameters pMSSM in the following Chapters.

5.1.1 pMSSM parameters

The complete MSSM with its 124 parameters (described in Section 1.3) is too large to be fully explored. One possibility to proceed with it, is to impose some assumptions, as it is done in high-scale models, or in simplified models. Those are, in general, far too restraining, thus exploring a rather limited phenomenology. They also rely on many suppositions imposed for mere convenience. The need for assumptions is clearly recognised, but they should be as limited in number as possible. In this study this is done by imposing the exact R -parity conservation and the LSP is presupposed to be the lightest neutralino. Other assumptions that are imposed are motivated by the fact that no deviation with respect to SM have been observed:

- (i) The soft parameters (described in Section 1) are real, so that no new sources of CP violation exist beyond that present in the CKM matrix.
- (ii) Minimal Flavour Violation [161] is imposed at the electroweak scale.
- (iii) The first two generations of squarks and sleptons with the same quantum numbers are mass degenerate, and their Yukawa couplings are too small to affect sparticle production or precision observables assuring that all SUSY breaking terms are of the same order of magnitude.

This allows many possibilities at higher scales such as the unification of sparticle mass parameters. The SUSY breaking mechanism is also not constrained in any way. By imposing those assumptions the MSSM space is reduced to the 19-dimensional subspace considered here, which parameters are given in Table 5.1. It is impossible to use grid technique to explore it, therefore the parameters are sampled by randomly choosing values from a flat probability distribution across their allowed ranges (Section 5.1.2).

5.1.2 pMSSM parameters range

The model points considered in the following are sets of pMSSM parameters. To define the ranges in which they are sampled, it is assumed that sparticles that can be accessed at the LHC have masses below 4 TeV. Consequently, to give high density of model points below that limit,

Parameter	Min value	Max value	Definition
$m_{\tilde{L}_1} (= m_{\tilde{L}_2})$	90 GeV	4 TeV	Left slepton (first two gens) mass
$m_{\tilde{e}_1} (= m_{\tilde{e}_2})$	90 GeV	4 TeV	Right slepton (first two gens) mass
$m_{\tilde{L}_3}$	90 GeV	4 TeV	Left stau doublet mass
$m_{\tilde{e}_3}$	90 GeV	4 TeV	Right stau mass
$m_{\tilde{Q}_1} (= m_{\tilde{Q}_2})$	200 GeV	4 TeV	Left squark (first two gens) mass
$m_{\tilde{u}_1} (= m_{\tilde{u}_2})$	200 GeV	4 TeV	Right up-type squark (first two gens) mass
$m_{\tilde{d}_1} (= m_{\tilde{d}_2})$	200 GeV	4 TeV	Right down-type squark (first two gens) mass
$m_{\tilde{Q}_3}$	100 GeV	4 TeV	Left squark (3rd gen) mass
$m_{\tilde{u}_3}$	100 GeV	4 TeV	Right top squark mass
$m_{\tilde{d}_3}$	100 GeV	4 TeV	Right bottom squark mass
$ M_1 $	0 GeV	4 TeV	Bino mass parameter
$ M_2 $	70 GeV	4 TeV	Wino mass parameter
$ \mu $	80 GeV	4 TeV	Bilinear Higgs mass parameter
M_3	200 GeV	4 TeV	Gluino mass parameter
$ A_t $	0 GeV	8 TeV	Trilinear top coupling
$ A_b $	0 GeV	4 TeV	Trilinear bottom coupling
$ A_\tau $	0 GeV	4 TeV	Trilinear tau coupling
M_A	100 GeV	4 TeV	Pseudoscalar Higgs boson mass
$\tan \beta$	1	60	Ratio of the Higgs vacuum expectation values

Table 5.1: Scan ranges used for each of the 19 pMSSM parameters. Where the parameter is written with a modulus sign both positive and negative values are permitted.

the ranges of the relevant pMSSM parameters are restricted to be below 4 TeV. There is also a lower limit which is coming from pre-LHC searches for SUSY (Section 5.2). The ranges for M_1 , M_2 and μ are different (M_1 being lower than the others) in order to increase the number of model points in the Z/h -funnels (which satisfy the dark matter relic density upper bound). The ranges of all parameters are listed in Table 5.1.

The masses and branching ratios of each model point are then calculated. The mass of the top quark has been fixed to in all model points to 173.2 GeV. For the determination of the sparticles mass spectrum `SoftSUSY 3.4.0` [116] is used. The SM Higgs mass is recalculated with `FeynHiggs 2.10.0` [162, 163] for the inclusion of important three-loop corrections not present in `SoftSUSY`. For sparticle decay tables, a modified version of the program `SUSY-HIT 1.3` [115] is employed, updated to use `HDECAY 5.11` [164] for the Higgs decays. In some cases `SUSY-HIT` does not calculate some relevant decay modes (like three-body right-handed sfermion decays and three-body decays of neutralinos and charginos that have mass splittings with the LSP below the Z or W boson masses when other two-body decay modes are available) or predicts a value that differs significantly from the full matrix element prediction (for example the stop decays for any model point in which `SUSY-HIT` predicts a non-zero four-body decay rate for the light stop). These are recalculated with `MadGraph5_aMC@NLO 2.1.1` [165]. The accuracy of the spectrum generation has been cross checked with `SUSPECT` [166].

5.2 Experimental constraints

For a given model point, one can calculate the expected values of some of the observables (like the SUSY contribution to the anomalous magnetic moment of the muon, branching ratios of various rare decays ($\text{BR}(b \rightarrow s\gamma)$, $\text{BR}(B_s \rightarrow \mu^+\mu^-)$ and $\text{BR}(B^+ \rightarrow \tau^+\nu_\tau)$),...). They are determined with `micrOMEGAs 3.5.5` [167, 168], and are required to belong to the allowed ranges of the indirect constraints described in this Section. There are several experimental constraints that can be combined to constrain a priori the pMSSM parameter space. Those are coming from the electroweak precision measurements, flavour physics and pre-LHC searches carried out at LEP and at the Tevatron. Another constraint is the measurement of the mass of the Higgs boson, and it is the only ATLAS (and CMS) result [128] considered at the level of the generation of model points. The measurements of the dark matter relic density, and the results from the direct dark matter detection experiments are also taken into account, all of which will be detailed in this Section. In most cases the uncertainty is taken to be the union of the two standard deviation (2σ) intervals around the theoretical prediction and the experimental measurement. The summary of all experimental constraints applied is given in Table 5.2.

5.2.1 Electroweak precision data

Electroweak precision measurements constrain the pMSSM parameter space through the fitted value of ΔT [169] which is the parameter (as explained in Section 1.1.2) describing the radiative corrections to the total Z boson coupling strength, the effective weak mixing angle, and the W boson mass. It is required that $\Delta\rho = \alpha\Delta T$ (where $\alpha = 1/128$) is between -0.0005 and 0.0017 .

For the SUSY contribution to the anomalous magnetic moment of the muon, $\Delta(g-2)_\mu$, a larger range is allowed than for other constraints. This range is the union of the three sigma intervals around the SM value, $(0.0 \pm 5.9) \times 10^{-10}$ from Equation (18) of Ref. [170] and the experimental measurement, $(24.9 \pm 6.3) \times 10^{-10}$ from Equations (1) and (19) of Ref. [170]. Three sigma intervals are used to obtain a continuous range from the union.

5.2.2 Flavour physics

The branching ratio (BR in the following) of the decay $b \rightarrow s\gamma$ is constrained to be between 2.69×10^{-4} and 3.87×10^{-4} . This is the union of the two sigma intervals around theory and experiment from [171]. For $\text{BR}(B_s \rightarrow \mu^+\mu^-)$, the value calculated by `micrOMEGAs` is scaled by $1 / (1 - 0.088)$ as proposed in [172] for comparison with experiment. The scaled value is required to be between 1.6×10^{-9} and 4.2×10^{-9} corresponding to the two sigma interval from the combined LHCb and CMS result [173]. The two-sigma theoretical prediction for the SM $(3.20 - 4.12) \times 10^{-9}$ lies fully within this interval. Finally, $\text{BR}(B^+ \rightarrow \tau^+\nu_\tau)$ is calculated, using equations from [174], which includes $\tan\beta$ -enhanced corrections. The calculated value is required to be between 66×10^{-6} and 161×10^{-6} , taking the union of the two sigma intervals around theory and experiment from [175, 176, 177, 178] and the SM prediction [179].

5.2.3 Higgs and pre-LHC collider constraints

5.2.3.1 Higgs mass

The Higgs mass has been measured at both ATLAS and CMS experiments, and the combined value has been published in Ref. [128]. For this study the Higgs mass is constrained to lie within the [124-128] mass window, a standard theoretical uncertainty of 2 GeV on the `FeynHiggs` calculations being used.

5.2.3.2 Pre-LHC collider constraints

At LEP the measurement of the invisible width of the Z has been performed, and it is constrained to be less than 2 MeV [180]. Any model point with the additional contribution to the invisible width of the Z boson above this value is discarded. SUSY searches have been performed both at LEP and at the Tevatron. The main difference between the searches carried out by the experiments at those two colliders come from the type of colliding particles. The searches at LEP are almost independent of the model as it is e^+e^- collider, and the limits are up to the beam energy ~ 100 GeV [181]. The model points are discarded if any charged sparticle is lighter than 100 GeV. For charginos, the bound is increased to 103 GeV, provided that all sneutrinos are heavier than 160 GeV and the mass splitting between the chargino and the LSP is at least 2 GeV [181]. SUSY searches at hadron colliders are more complex due to the large backgrounds. The limits are therefore much more model dependent. Usually mSUGRA models were used, but when the results are translated in more general SUSY models the limits become much weaker. The results of the inclusive searches for squark and gluino production are interpreted in the mSUGRA framework, with $\tan \beta = 5$ (CDF [182]) or $\tan \beta = 3$ (D0 [183]), $A_0 = 0$ and $\mu < 0$, and set lower limits of about 310 GeV for all squark masses, or 390 GeV for the case $m_{\bar{q}} = m_{\tilde{g}}$. In this study the choice was made to require the first and second generation squarks to be heavier than 200 GeV, and M_3 (gluino mass parameter) is also set to values higher than 200 GeV making the gluino mass also higher.

5.2.4 Cosmological constraints

Two important pMSSM assumptions are needed to be recalled here: since R -parity is exactly conserved, the LSP is stable therefore producing a non-zero cosmological abundance. In addition the LSP is here presumed to be the lightest neutralino, but is not required to saturate the measured cosmological relic density: only an upper limit is requested. Finally it is also assumed that the LSP were created thermally in the early universe (Section 1.5) and that it is not diluted for instance by late time entropy production. Cosmological probes (CMB, LSS, SN, BAO)¹ give a measurement of the cold dark matter density of the universe within the Λ CDM scenario [32]. The latest Planck measurement $+2\sigma$ is used here leading to $\Omega_{\text{CDM}}h^2 \leq 0.1208$ from the $\Omega_{\text{CDM}}h^2 = 0.1188 \pm 0.0010$ value of Table 4 of Ref. [25]. No theoretical error is considered, in other works like Ref. [145], it is estimated to be 0.012.

5.2.5 Direct detection of dark matter

Direct searches for dark matter aim at testing that our own galactic halo is filled with particular dark matter particles. They observe the nucleon recoils due to an elastic scattering of dark matter particles on the nuclei of a target. Dependent on whether they look for an axial or a scalar neutralino - quark coupling, they set limits on the spin dependent (resp. spin independent) neutralino-nucleus cross-section as a function of the neutralino mass.

The limits used in this analysis correspond to the spin independent LUX limits [184], the proton-spin dependent COUPP results [185] and the neutron-spin dependent XENON100 measurements [186]. The calculated value from microOMEGAs is scaled down by the ratio of the expected relic density from the LSP to the observed $\Omega_{\text{CDM}}h^2$ value [25] and by a factor four to account for the nucleon form factor uncertainties [187].

¹The Planck results published are a combination of all available cosmological data - the Cosmological Microwave Background, the Large Scale Structures, the SuperNovae, the Baryonic Acoustic Oscillations

Observables	Minimum value	Maximum value	Ref.
$\Delta\rho$	-0.0005	0.0017	[169]
$\Delta(g-2)_\mu$	-17.7×10^{-10}	43.8×10^{-10}	[170]
$\text{BR}(b \rightarrow s\gamma)$	2.69×10^{-4}	3.87×10^{-4}	[171]
$\text{BR}(B_s \rightarrow \mu^+\mu^-)$	1.6×10^{-9}	4.2×10^{-9}	[173]
$\text{BR}(B^+ \rightarrow \tau^+\nu_\tau)$	66×10^{-6}	161×10^{-6}	
$\Omega_{\tilde{\chi}_1^0} h^2$	—	0.1208	[25]
$R_\Omega \times \sigma_{N-\tilde{\chi}_1^0}^{\text{SI}}$	—	$4 \times f(\tilde{\chi}_1^0)$ from LUX	[184]
$R_\Omega \times \sigma_{p-\tilde{\chi}_1^0}^{\text{SD}}$	—	$4 \times f(\tilde{\chi}_1^0)$ from COUPP	[185]
$R_\Omega \times \sigma_{n-\tilde{\chi}_1^0}^{\text{SD}}$	—	$4 \times f(\tilde{\chi}_1^0)$ from XENON100	[186]
$\Gamma_{\text{invisible(SUSY)}}(Z)$	—	2 MeV	[180]
Masses of charged sparticles	100 GeV	—	[181]
$m(\tilde{\chi}_1^\pm)$	103 GeV	—	[181]
$m(\tilde{u}_{1,2}, \tilde{d}_{1,2}, \tilde{c}_{1,2}, \tilde{s}_{1,2})$	200 GeV	—	[182, 183]
$m(\tilde{g})$	200 GeV	—	[182, 183]
$m(h)$	124 GeV	128 GeV	[128]

Table 5.2: Experimental constraints used to accept pMSSM model points from considerations of precision electroweak and flavour results, dark matter relic density and direct detection, and other collider measurements. A long dash (—) indicates that no requirement is made. Further details may be found in the text.

LSP type	Definition	Sampled	Simulated		Weight
			Number	Fraction	
‘Bino-like’	$N_{11}^2 > \max(N_{12}^2, N_{13}^2 + N_{14}^2)$	480×10^6	103,410	35%	1/24
‘Wino-like’	$N_{12}^2 > \max(N_{11}^2, N_{13}^2 + N_{14}^2)$	} 20×10^6 {	80,233	26%	1
‘Higgsino-like’	$(N_{13}^2 + N_{14}^2) > \max(N_{11}^2, N_{12}^2)$		126,684	39%	1
Total		500×10^6	310,327		

Table 5.3: Categorisation of the 310,327 model points by the type of the LSP (assumed to be the $\tilde{\chi}_1^0$) according to the neutralino mixing matrix parameters N_{ij} , where the first index indicates the neutralino mass eigenstate and the second indicates its nature in the lexicographical order ($\tilde{B}, \tilde{W}, \tilde{H}_1, \tilde{H}_2$). For example, $N_{1,2}$ is the amplitude for the LSP to be \tilde{W} (Section 1.3.4.1). The final two columns indicate the fraction of model points in that category that are sampled, and their weighted fraction after sampling.

5.3 Resulting parameter space

The pMSSM parameter space, before applying any of the ATLAS searches, is already sculpted by the theoretical choices (Section 5.1) and the experimental constraints (Section 5.2). This Section describes the main impacts of those choices on the parameters. The bino-, wino-, and higgsino-like LSP (Section 1.3.4.1) are discussed separately as the related parameters show different sensitivity to constraints.

5.3.1 Different model sets corresponding to the LSP type

In total 500 million model points in the pMSSM parameter space are sampled. As explained in Section 5.1.1 the LSP is required to be the lightest neutralino and it can be predominantly bino (\tilde{B}), wino (\tilde{W}) or higgsino (\tilde{H}), according to the neutralino mixing matrix parameters N_{ij} , where the first index indicates the neutralino mass eigenstate. It is chosen to define the neutralino as bino-like if $N_{11}^2 > \max(N_{12}^2, N_{13}^2 + N_{14}^2)$, wino-like if $N_{12}^2 > \max(N_{11}^2, N_{13}^2 + N_{14}^2)$ and higgsino-like in case $(N_{13}^2 + N_{14}^2) > \max(N_{11}^2, N_{12}^2)$ (second column of Table 5.3). In order to be able to explore the phenomenology of the model points with bino-, wino-, and higgsino-like LSP separately, the choice was made to oversample the model points with bino-like LSP so to get roughly the same number of model points in each set after applying all the constraints. After requiring that the LSP is the lightest neutralino and that the experimental constraints (described in Section 5.2) are satisfied, there are 310,327 surviving model points. The numbers of model points in each model set are comparable: bino-like makes 35%, wino-like 26% and higgsino-like 39% out of all model points, as shown in Table 5.3. The 90.4% of model points have a bino, wino or higgsino fraction of the LSP of more than 80%, so there are relatively low number of model points with the LSP being mixed.

In Figure 5.1 the distributions of the LSP mass (on the left) and the gluino mass (on the right) are shown. The model points with the bino-like LSP are shown in dotted red line, while model points with wino- and higgsino-like LSPs are shown with dashed blue and solid green line respectively. There is a clear difference between the mass distributions depending of the LSP type: the model points with bino-like LSP are present for the LSP masses below 100 GeV corresponding to Z and SM-like Higgs funnels (h -funnel in the following). This difference in the neutralino mass distribution influence the gluino mass distribution, giving higher number of model points with lower gluino mass for the models with bino-like LSP compared to the wino- and higgsino-like LSPs.

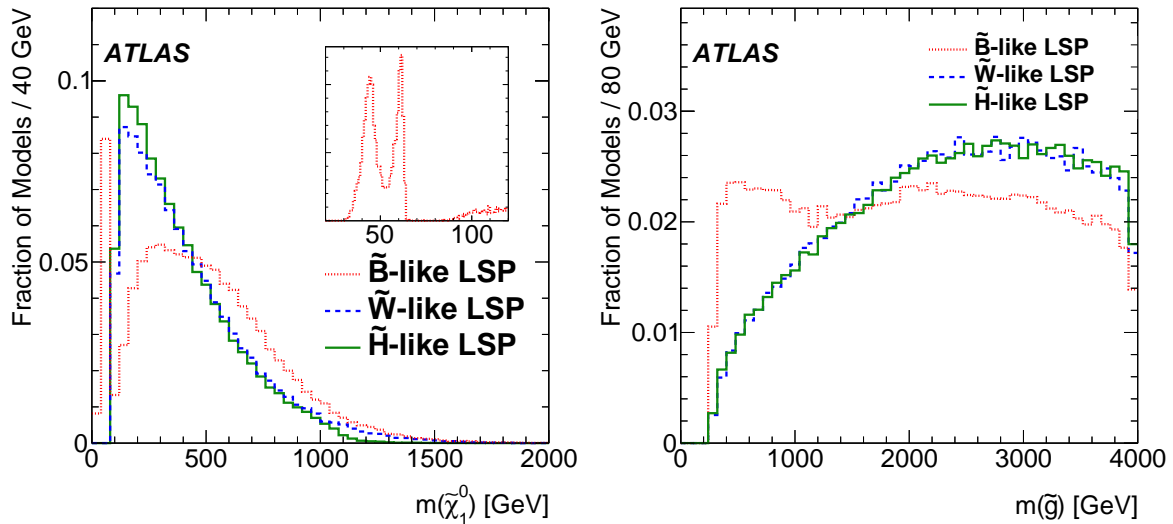


Figure 5.1: Distributions of the LSP and gluino masses, shown separately for model point with a bino-(dotted red), wino-(dashed blue) or higgsino-like (solid green) LSP. The constraints listed in Table 5.2 have been applied to choose the model points entering the plots, but not the constraints from the ATLAS searches. The distributions have been normalised to unit area. The inset in the plot on the left shows in more details the region of low neutralino mass for the bino-like LSPs, pointing to the Z and SM-like Higgs funnel (h -funnel in the following).

The nature of the NLSP also significantly influences the phenomenology of the model points. Table 5.4 shows how often different NLSP types occur (given in percent) corresponding to the LSP types. When the LSP is dominantly wino or higgsino-like, the NLSP is almost always chargino. It is true in almost 100% cases when the LSP is wino-like, while for the higgsino-like LSP, it is true in 90% of the model points, other 10% NLSP being $\tilde{\chi}_2^0$ (but the mass difference between $\tilde{\chi}_2^0$ and chargino is ~ 0.5 GeV). Thus when the LSP is wino- and higgsino-like, the co-annihilation between the $\tilde{\chi}_1^\pm$ and $\tilde{\chi}_1^0$ gives acceptable dark matter relic density. This is not the case for the models where the LSP is bino-like and there are much more possibilities for NLSP types who can act as co-annihilators (Section 1.5), like squarks, staus and selectrons.

In Figure 5.2 the mass splitting between LSP and NLSP is shown for model points with the bino-like LSP. It can be seen that it is frequently less than 100 GeV. This small difference

NLSP Nature	Bino	Wino	Higgsino
$\tilde{\chi}_1^+$	31.893%	99.981%	89.034%
\tilde{g}	12.941%	0	0.025%
$\tilde{\chi}_2^0$	11.698%	0.001%	10.650%
\tilde{u}_L	8.910%	0	0.016%
\tilde{b}_1	7.778%	0.001%	0.017%
\tilde{d}_R	7.056%	0	0.023%
\tilde{u}_R	7.046%	0	0.019%
\tilde{t}_1	4.380%	0.001%	0.013%
\tilde{e}_R	2.624%	0.001%	0.052%
$\tilde{\tau}_1$	2.398%	0.002%	0.050%
$\tilde{\nu}_{eL}$	1.758%	0.007%	0.047%
$\tilde{\nu}_{\tau L}$	1.518%	0.004%	0.054%

Table 5.4: Percentage occurrence of NLSP sparticle types for the model sets described above.

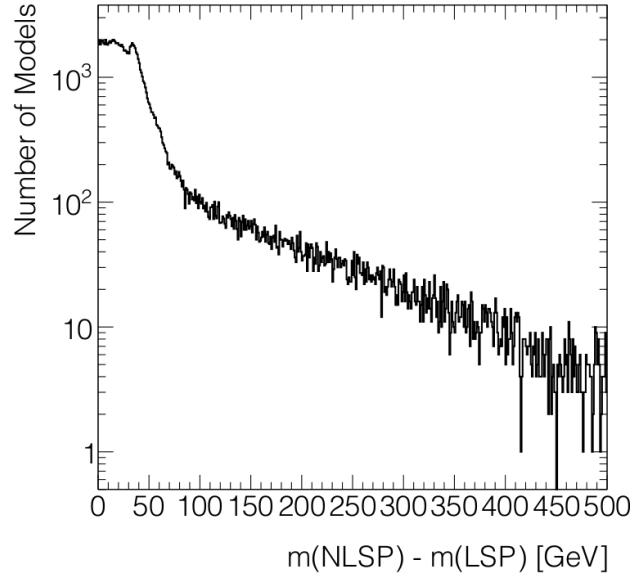


Figure 5.2: Difference between the LSP ($\tilde{\chi}_1^0$) mass and the NLSP mass for the model points where the LSP is bino-like.

between LSP and NLSP masses is required for the NLSP to be an effective co-annihilator. This small mass difference causes very soft objects being produced, making it even more challenging to tackle with the ATLAS searches.

5.3.2 Examples of the intertwining between parameters and observables

Some of the observables have a clear dependence on the MSSM parameters, for example, the rare B decays are related to the MSSM parameters through the following equations:

$$BR(B_s \rightarrow \mu\mu) \sim \frac{\tan^6 \beta}{m_A^4} \quad (5.1)$$

$$BR(B_u \rightarrow \tau\nu_\tau) \sim \left[1 - \frac{m_B^2}{m_A^2} \tan^2 \beta\right]^2 \quad (5.2)$$

$$BR(b \rightarrow s\gamma) \sim 1 + A \tan \beta + B \frac{\tan \beta}{m_A^2} \quad (5.3)$$

where parameters A and B depend on other MSSM parameters [188].

In Figure 5.3 the dependence of the value of the $BR(B_s \rightarrow \mu\mu)$ on the $\tan \beta$ is shown for two LSP types: in 5.3a the LSP is dominantly higgsino, while in 5.3b it is a bino-higgsino admixture. The plots are made using SFitter [189], and the points represented in the plots correspond to those of the last two columns of Table 4 of Ref. [145], and are used only for illustration. The values of $BR(B_s \rightarrow \mu\mu)$ are calculated for three values of m_A : $m_A = 333$ GeV (in blue), $m_A = 666$ GeV (in green) and $m_A = 1000$ GeV (in black). These illustrate Eq. 5.1, where the $\tan^6 \beta$ behaviour is recovered for high $\tan \beta$ values. As the $BR(B_s \rightarrow \mu\mu)$ is required to be between 1.6×10^{-9} and 4.2×10^{-9} , it is much easier to respect it for the model points with low $\tan \beta$ values, but it also depends on other pMSSM parameters.

In Figure 5.4 the dependence of the value of the $BR(b \rightarrow s\gamma)$ on $\tan \beta$ is shown for the LSP being higgsino-like. These illustrate Eq. 5.2. The values of $BR(b \rightarrow s\gamma)$ are very flat as a function of $\tan \beta$, so they do not put any strong preference for the value of this parameter, but the expected mean value may help selecting m_A in agreement with the observation.

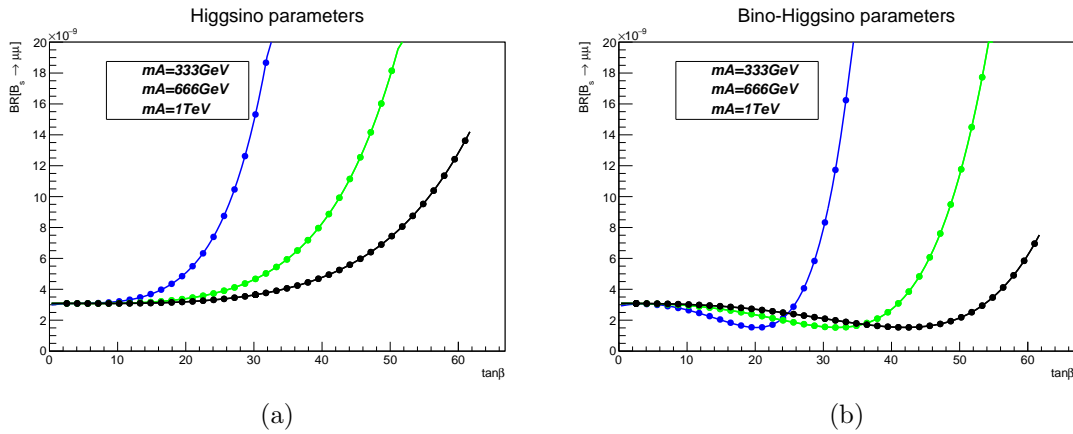


Figure 5.3: The value of $BR(B_s \rightarrow \mu\mu)$ as a function $\tan\beta$ for the LSP being (a) dominantly higgsino and (b) bino-higgsino admixture.

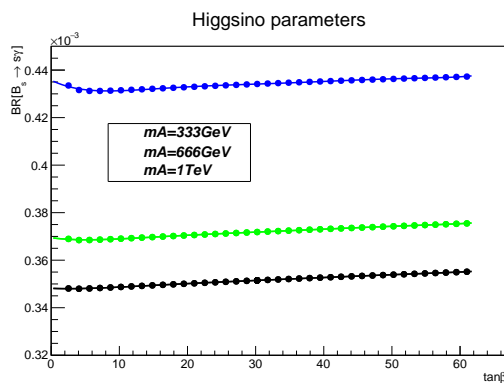


Figure 5.4: The value of $BR(b \rightarrow s\gamma)$ as a function of the $\tan\beta$ for the LSP being higgsino-like.

The dependance of $\Delta(g-2)_\mu$ is exemplified as a function of M_1 , (5.5a) M_2 (5.5b) and $\tan\beta$ (5.5c) (see caption for details). The other parameters are set to the ones of the bino-higgsino point. This Figure shows that the correlations between this observable and the pMSSM parameters are very complex. Still the value of $\Delta(g-2)_\mu$ is chosen to be within -17.7×10^{-10} and 43.8×10^{-10} , therefore having almost no impact on the parameters. In addition the expected values of this observable for the pMSSM model points are mostly distributed around zero, and far from the central value of the experimental measurement, as illustrated in Figure 5.6, where the distribution of the pMSSM model points is shown in the plane of the mass of the lightest left- or right-handed smuon versus $\Delta(g-2)_\mu$ and compared with the 1σ measurement (although also charginos can contribute to the value of $\Delta(g-2)_\mu$ [190]). If this experimental measurement is to be more precise, it would place a strong limit on the allowed pMSSM model points before applying any constraints coming from the direct searches for SUSY at colliders.

As for the Higgs mass measurement, the SM-like Higgs mass and properties are dominantly controlled by just a few weak-scale MSSM parameters: at tree level, m_A and $\tan\beta$, with the addition of the stop masses $m_{\tilde{t}_{1,2}}$ and the stop mixing parameter $X_t \equiv A_t - \mu \cot\beta$ at the higher scales [4]. One-loop corrections from stops are responsible for lifting the bound on the Higgs mass to 130 GeV. Other parameters of the MSSM contribute radiative corrections to the Higgs mass, but in general are highly subdominant to the stop sector. Even with large loop effects, 125 GeV is a relatively large Higgs mass for the MSSM. Thus it has some consequences on the MSSM parameter space. It implies either the existence of extremely heavy stops ($\gtrsim 10$ TeV), or near-maximal stop mixing, so those parameters can be constrained by the

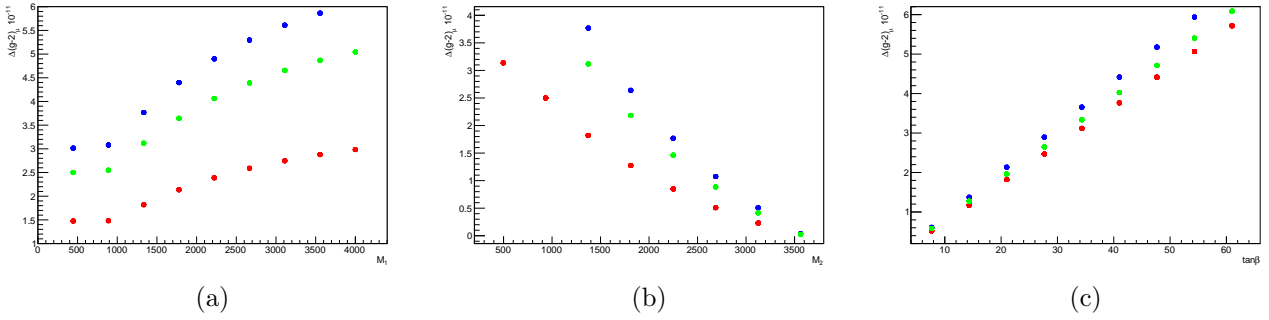


Figure 5.5: The value of $\Delta(g-2)_\mu$ as a function of
 (a) M_1 where $M_2 = 222$ GeV, $m_A = 500$ GeV, and $\tan\beta = 41$ (in blue), $M_2 = 1373$ GeV, $m_A = 500$ GeV and $\tan\beta = 41$ (in red) and $M_2 = 1373$ GeV, $m_A = 500$ GeV and $\tan\beta = 34$ GeV (in green).
 (b) M_2 where $M_1 = 1333$ GeV and $m_A = 500$ GeV and $\tan\beta$ is varied: $\tan\beta = 41$ (in blue), $\tan\beta = 21$ (in red) and $\tan\beta = 34$ (in green),
 (c) $\tan\beta$ where $M_1 = 1333$ GeV, $M_2 = 1373$ GeV and $m_A = 500$ GeV (in red) $M_1 = 1333$ GeV, $M_2 = 498$ GeV and $m_A = 1500$ GeV (in blue) and $M_1 = 498$ GeV, $M_2 = 1373$ GeV and $m_A = 2000$ GeV (in green).

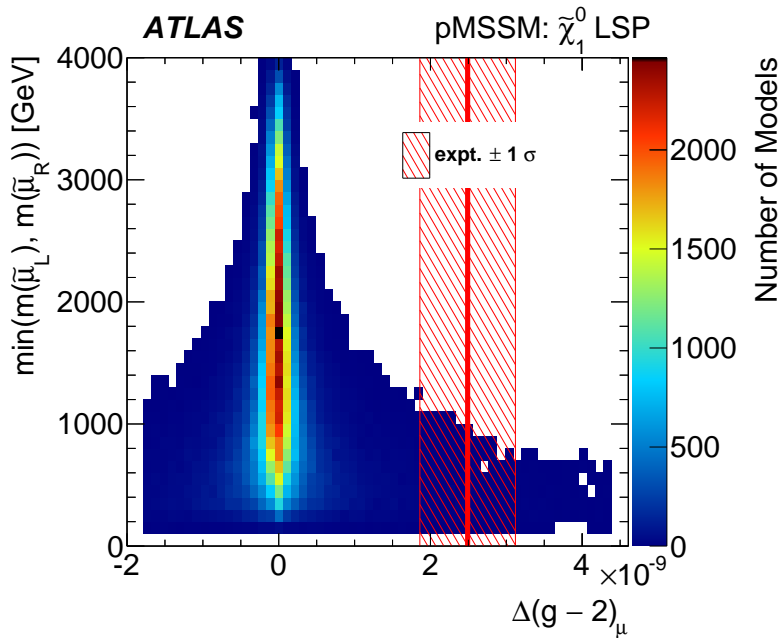


Figure 5.6: Distribution of model points in the plane of the mass of the lightest left- or right-handed smuon versus $\Delta(g-2)_\mu$. The experimental measurement is overlaid as the hatched band [170].

Higgs mass measurement.

$$m_h^2 = m_Z^2 \cos 2\beta + \frac{3m_t^4}{4\pi^2 v^2} \left(\log \left(\frac{m_s^2}{m_t^2} \right) + \frac{X_t}{m_s^2} \left(1 - \frac{X_t^2}{12m_s^2} \right) \right) \quad (5.4)$$

The relationship between observables and parameters has been exemplified in this section. As far as the 19 parameters pMSSM is concerned, the main constraints for the selection of model points before ATLAS searches come from the Higgs mass and the dark matter relic density measurements, as will be shown in next Section 5.3.3. The dark matter energy density as measured by the Planck Collaboration has a very important influence on the allowed pMSSM parameter space, and the size of that influence would be even bigger if it is not used only as upper limit (see Ref. [145]). Many pMSSM model points don't saturate the measured $\Omega_{\text{CDM}} h^2$ value, and one would need another theory to explain the missing dark matter component.

5.3.3 Effects of indirect constraint on pMSSM parameters

The 19 pMSSM parameters are scanned rather flatly and most of them remain quite homogeneous even after applying the indirect constraints as it can be seen in Figure 5.7, for bino- 5.7a, wino- 5.7b and higgsino-like 5.7c LSP. In this Figure, all other dimensions are projected to the A_b - A_τ plane, and as they are so uniform, one can conclude that these parameters are insensitive to indirect constraints and to the nature of the LSP. The z-axis shows the number of model points in each bin after the indirect constraints are satisfied. Still some 2D parameters' plots exhibit patterns linked to the impact of the observables.

In Figure 5.8 the $\tan\beta$ - m_A parameter planes are shown. The number of model points for high $\tan\beta$ and low m_A is small as a consequence of the B physics observables, especially $\text{BR}(B_s \rightarrow \mu\mu)$ measurement. As these observables depend also on other parameters (like μ , M_3 , A_t and squark mass parameters), it is not always evident which model points are allowed and which are not in the agreement with the B-physics observables.

The projection on other parameters planes may exhibit some typical shapes and be quite different depending on the LSP type, as the values of some parameters are very connected with the corresponding LSP type. For example, in Figure 5.9 the M_1 - M_2 parameter planes are shown, and they depend on the LSP type as M_1 is the bino mass parameter, and M_2 is the wino mass parameter.

The M_1 parameter drives the mass of the neutralino in the bino case (as can be seen in Figure 5.10a it is directly proportional to it). The choice of a neutralino mass below 1 TeV therefore forces M_1 to be below ~ 1 TeV. In addition for low value of the neutralino mass, the annihilation DM channels are mainly driven by the SM-like Higgs and Z funnel, therefore explaining the bump of model points in the low region of M_1 values. The explanation are the same for the wino-like LSP and $M_2 \lesssim 1$ TeV in Figure 5.9b.

The A_t values of the model points considered in this analysis are mainly concentrated around 3 TeV independently of the neutralino nature (as can be seen in Figure 5.10). This is linked to the Higgs mass through equation 5.4 and is exemplified in Figure 5.11 where are shown the relative number of model points in the $m(h) - A_t$ plane for the bino-like LSP (Figure 5.11a), wino (Figure 5.11b) and higgsino-like LSP (Figure 5.11c).

This is different in the case of the wino since the LSP mass is mainly driven by the M_2 parameter as it is seen in Figure 5.12b for which the M_2 values are lower than about 1.5 TeV. The same argument applies for the $|\mu|$ parameter in the higgsino case (Figure 5.13c). The lower bound on M_2 and μ are a consequence of the charginos mass lower bound [191].

The parameters that are mainly pre-constrained are A_t , μ , and for the wino-like LSP M_2 , and this is the consequence of the SM-like Higgs measurements, and also the allowed dark matter annihilation channels. The limits coming from the direct searches for the dark matter have

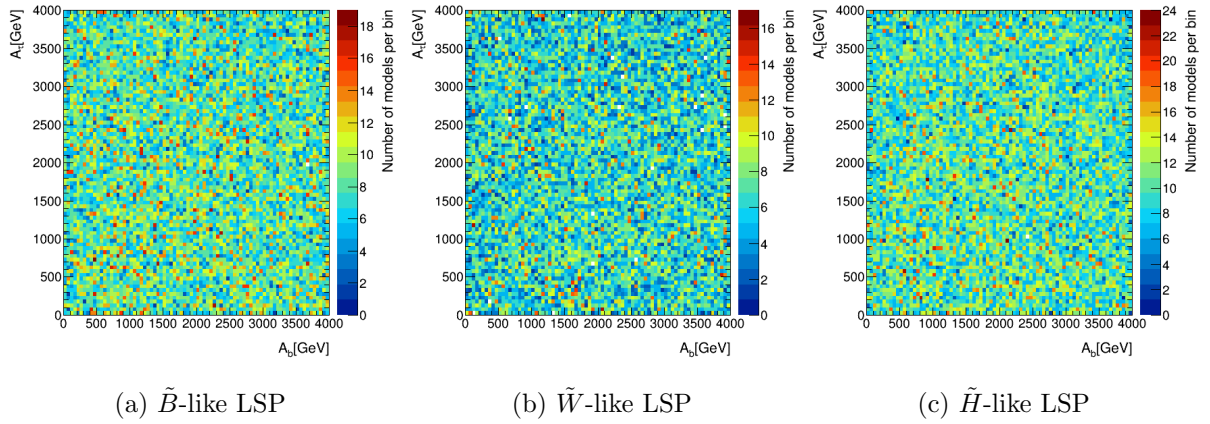


Figure 5.7: The A_b - A_τ parameter planes for (a) bino-like LSP, (b) wino-like LSP and (c) higgsino-like LSP. The z -axis shows the number of model points in each bin after the indirect constraints are satisfied.

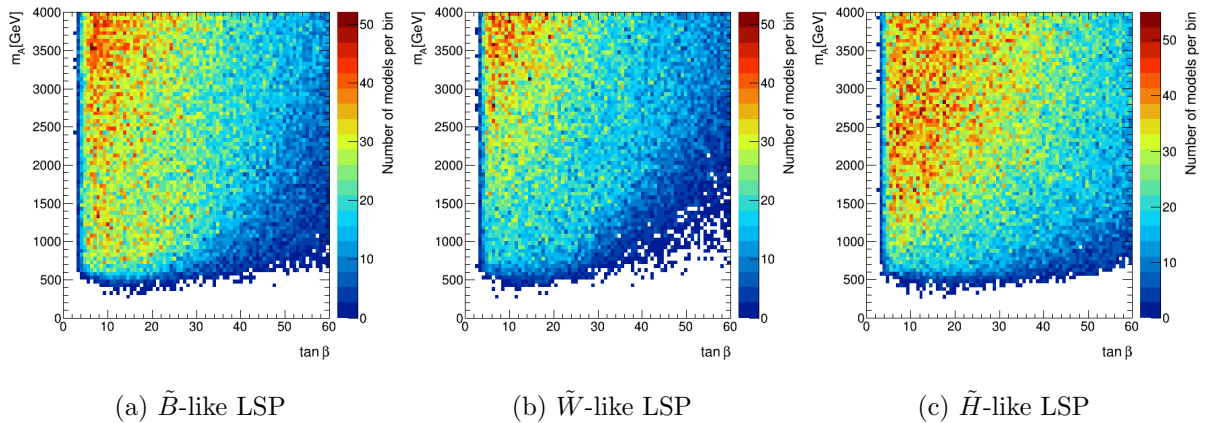


Figure 5.8: The $\tan \beta$ - m_A parameter planes for (a) bino-like LSP, (b) wino-like LSP and (c) higgsino-like LSP. The z -axis shows the number of model points in each bin after the indirect constraints are satisfied.

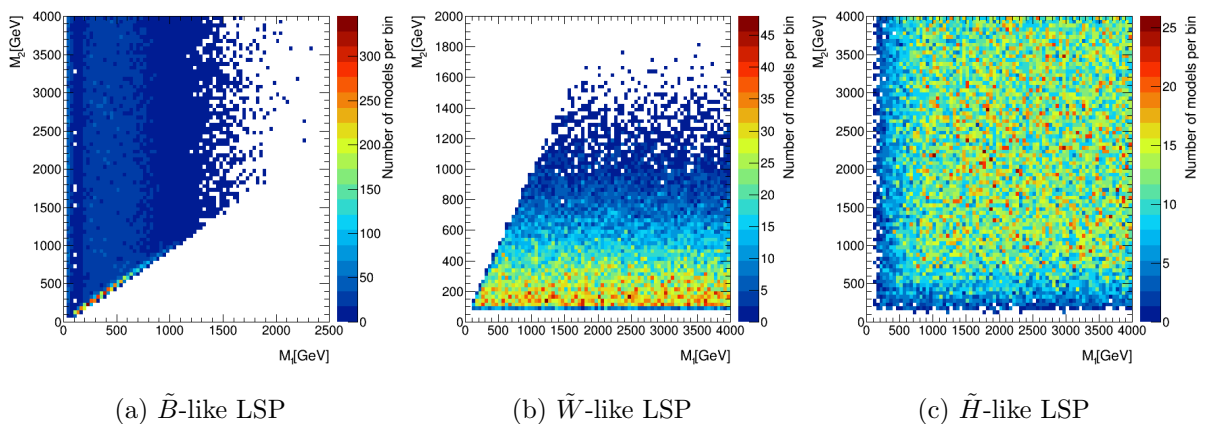


Figure 5.9: The M_1 - M_2 parameter planes for (a) bino-like LSP, (b) wino-like LSP and (c) higgsino-like LSP. The z -axis shows the number of model points in each bin after the indirect constraints are satisfied.

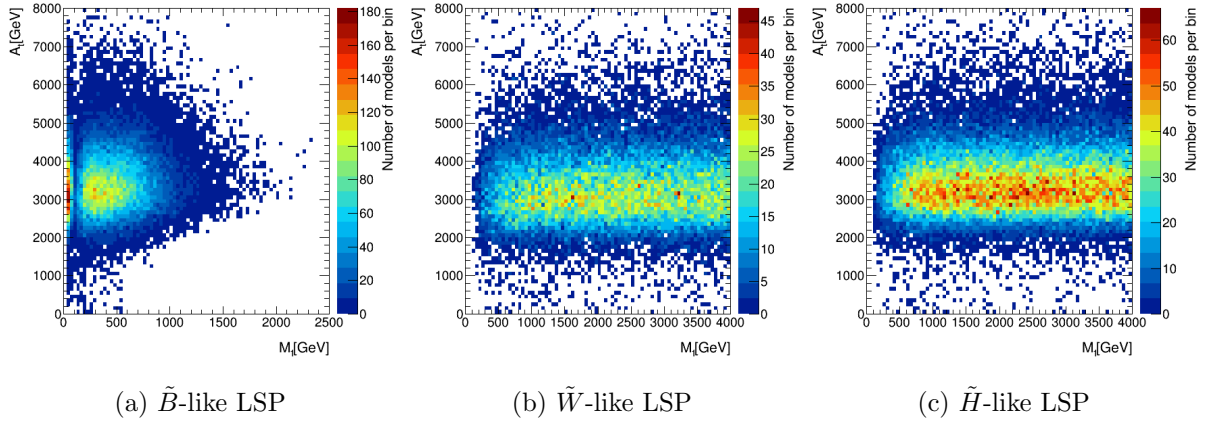


Figure 5.10: The M_1 - A_t parameter planes for (a) bino-like LSP, (b) wino-like LSP and (c) higgsino-like LSP. The z-axis shows the number of model points in each bin after the indirect constraints are satisfied.

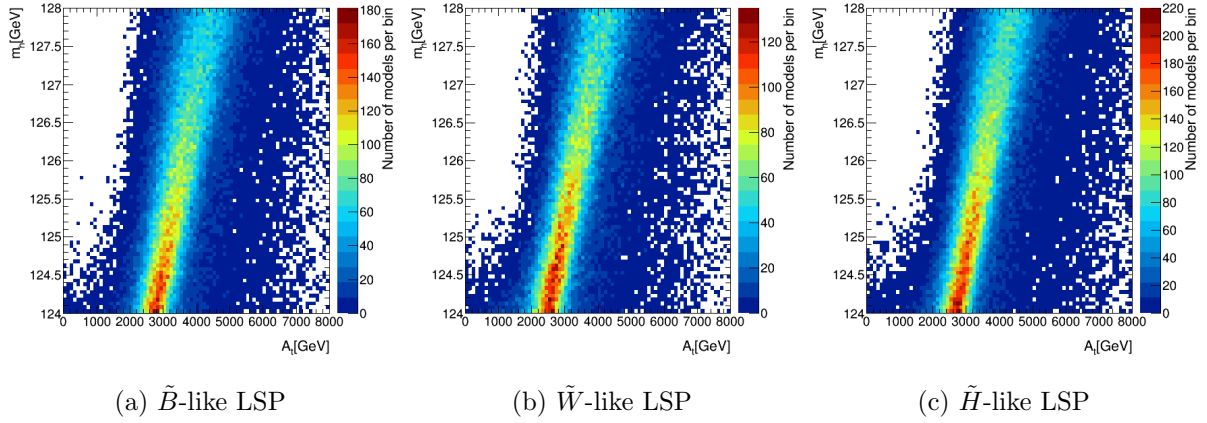


Figure 5.11: The m_h - A_t plane for the different LSP types.

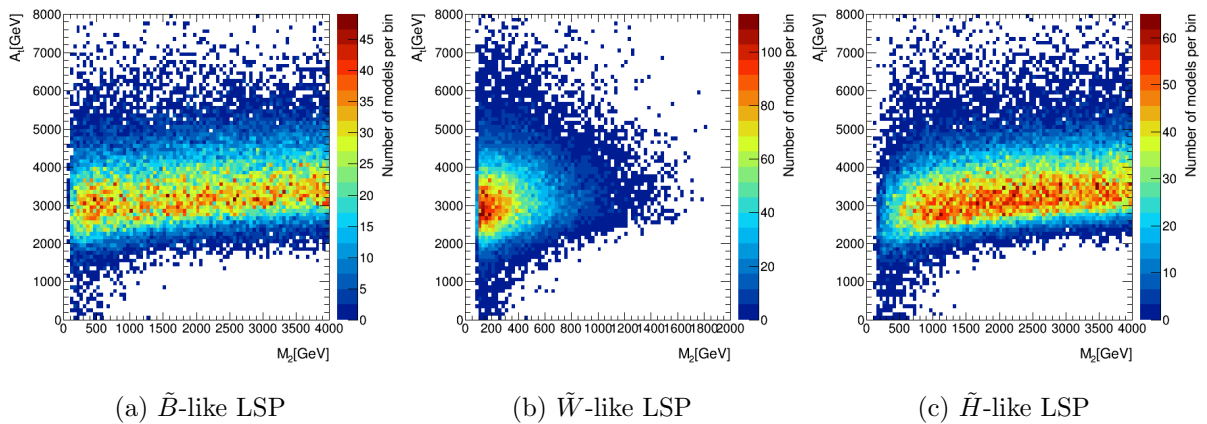


Figure 5.12: The M_2 - A_t parameter planes for (a) bino-like LSP, (b) wino-like LSP and (c) higgsino-like LSP. The z-axis shows the number of model points in each bin after the indirect constraints are satisfied.

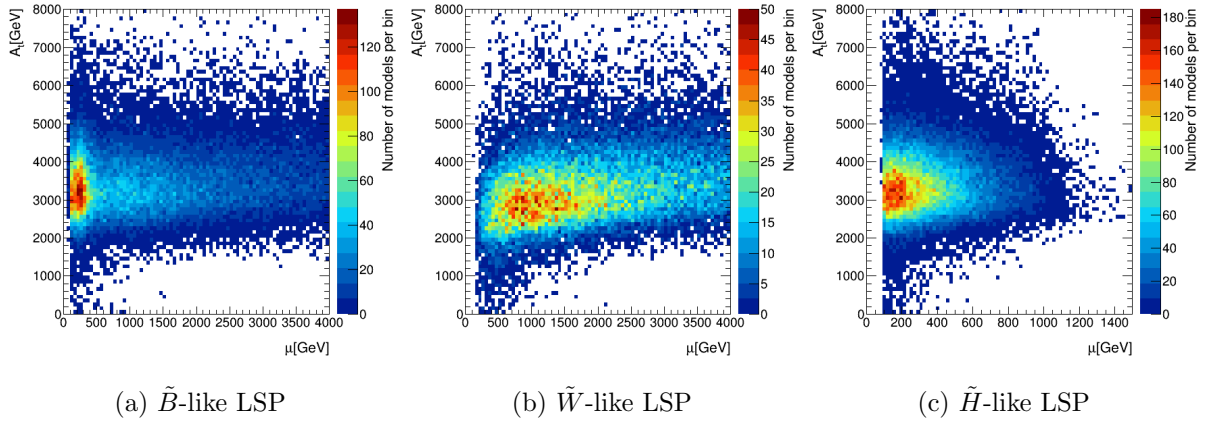


Figure 5.13: The μ - A_t parameter planes for (a) bino-like LSP, (b) wino-like LSP and (c) higgsino-like LSP. The z-axis shows the number of model points in each bin after the indirect constraints are satisfied.

almost no influence on the allowed pMSSM parameter space. Of all the b-physics observables, the $BR(B_s \rightarrow \mu\mu)$ has the largest impact.

5.4 ATLAS SUSY searches

A total of 22 distinct ATLAS searches are considered, spanning a wide range of search strategies and final states, as listed in Table 5.5. Each analysis has several signal regions — for instance as discussed in Section 3 the 0-lepton analysis has 15 signal regions and most of them are considered for this full pMSSM analysis. However, in some cases, for practical reasons it was necessary to leave out some specialised signal regions or more complex combined fits. This leads to a slight underestimate of the full reach of the search. In total almost 200 distinct signal regions are considered.

The analyses are classified into the four broad categories shown in Table 5.5. ‘Inclusive’ searches are those primarily targeting decays, including cascade decays, initiated by production of squarks of the first two generations or gluinos. ‘Third generation’ searches are those targeting particularly the production of top and bottom squarks. ‘Electroweak’ searches include those for direct production of electroweakinos and sleptons. Since each search involves multiple signal regions, and since different SUSY production and decay processes can contribute to each of those, this categorisation can only be considered to be a rough guide when interpreting the type of particles to which the analysis might show sensitivity. ‘Other’ searches are the searches for heavy, long-lived particles which are only considered for a small subset of model points and the search for heavy Higgs bosons. The details of the analyses can be found in the corresponding papers (listed in Table 5.5) and a brief summary for each is given below.

In what follows the term ‘lepton’ is used to refer specifically to the charged leptons e^\pm and μ^\pm of the first two generations. Where τ leptons are also included – for the 3-leptons and 4-leptons electroweak searches – this is indicated explicitly.

5.4.1 Inclusive searches

The inclusive searches are designed to be sensitive to prompt decays of squarks, particularly those of the first two generations, and gluinos. Strongly interacting sparticles may decay directly to the LSP, via the decay $\tilde{q} \rightarrow q + \tilde{\chi}_1^0$ for the squark and via $\tilde{g} \rightarrow q + \bar{q} + \tilde{\chi}_1^0$ for the gluino. Alternatively, cascade decays may also occur involving one or more additional sparticles yielding

Analysis	Ref.	Category
0-lepton	[134]	Inclusive
0-lepton + 7–10 jets + E_T^{miss}	[192]	
1-lepton + jets + E_T^{miss}	[193]	
Taus + jets + E_T^{miss}	[194]	
SS/3-leptons + jets + E_T^{miss}	[195]	
0/1-lepton + 3 <i>b</i> -jets + E_T^{miss}	[196]	
Monojet	[197]	
<hr/>		
0-lepton stop	[198]	Third generation
1-lepton stop	[199]	
2-leptons stop	[200]	
Monojet stop	[201]	
Stop with Z boson	[202]	
2 <i>b</i> -jets + E_T^{miss}	[203]	
<i>tb</i> + E_T^{miss} , stop	[204]	
<hr/>		
ℓh	[205]	Electroweak
2-leptons	[206]	
2-taus	[207]	
3-leptons	[208]	
4-leptons	[209]	
Disappearing Track	[210]	
<hr/>		
Long-lived particles	[211, 212]	Other
$H/A \rightarrow \tau^+\tau^-$	[213]	

Table 5.5: The 22 different ATLAS searches considered in this study. The term ‘lepton’ (ℓ) refers specifically to e^\pm and μ^\pm states, except in the cases of the electroweak 3-leptons and 4-leptons analyses where τ s are also included.

final states with further jets, large E_T^{miss} and possibly leptons (ℓ). The ATLAS searches targeting these final states are classified according to the different dominant signal signatures, as follows.

The 0-lepton analysis [134] is already explained in Chapter 3.

The 0-lepton + 7–10 jets + E_T^{miss} analysis [192] was designed to target, amongst others, models where each gluino of a produced pair decays through a (possibly virtual) top squark to $t + \bar{t} + \tilde{\chi}_1^0$. The four top quarks produced generally lead to large jet multiplicities in the final state. This search also has sensitivity to other models in which cascade decays generate large numbers of jets. It has a looser requirement on the E_T^{miss} because of the many possible intermediate stages of the cascade decay.

The 1-lepton + jets + E_T^{miss} analysis [193] explicitly requires one isolated lepton, several jets and high E_T^{miss} in its selection. This search has two channels – one including relatively high p_T leptons (sensitive to SUSY scenarios with larger mass splittings between the produced sparticle and the LSP) and another using low p_T leptons (lower mass splittings). Overall, it is sensitive to long decay chains where leptons can be produced through the cascade decay of squarks and gluinos.

The Taus + jets + E_T^{miss} search [194] targets final states arising from cascades producing hadronically decaying τ leptons – with signal regions requiring either one or two τ leptons; including large E_T^{miss} , jets and either exactly zero or one additional light lepton. This search can be sensitive to long decay chains in models with light staus.

Cascade decays of squark and gluino pairs can also lead to final states with multiple leptons, or with leptons of the same electric charge, known as same-sign (SS) leptons. Those final states are addressed by the SS/3-leptons + jets + E_T^{miss} analysis [195] requiring multiple jets in the final state, and either two SS leptons (with or without b -jets in the final state) or at least three leptons.

For models where many jets originate from b -quarks, the 0/1-lepton + 3 **b** -jets + E_T^{miss} analysis [196] has been specially designed, again with the requirement of large E_T^{miss} , with the definition of two channels: one with no isolated leptons, and another with at least one isolated lepton.

The Monojet analysis [197] selects events where the leading jet p_T is as large as 50% of the E_T^{miss} , and there is large E_T^{miss} and no leptons. The single jet can originate from initial-state QCD radiation (ISR), providing sensitivity to collisions in which no decay products from sparticle decays are observed. This can occur either for direct pair production of invisible LSPs, or of more relevance, if the produced sparticles are only a little heavier than the LSP, and their decays therefore produce SM particles of too low energy to be detected in the other searches.

5.4.2 Third generation searches

This set of analyses is focused on searches for direct production of third generation squarks. Their masses are generally needed to be at the TeV scale or below if scalar particles are to be protected from large unnatural quantum corrections. The decay of \tilde{t} and \tilde{b} quarks also leads to distinctive experimental signatures, typically involving the production of t or b quarks in association with large E_T^{miss} .

The 0-lepton stop search [198] is optimised for the direct production of top squarks decaying directly to a top quark and neutralino, leading to an all hadronic final state with at least two b -jets and large E_T^{miss} . Most of the signal regions rely on the variables related to reconstructed top quarks present in the final state and lepton vetoes, but there are also signal regions targeting the top squark decaying to a bottom quark and a chargino.

Its complement is the 1-lepton stop search [199], with all of its signal regions characterised by exactly one isolated lepton, at least two jets and large E_T^{miss} . The presence of the b -jet is used in both signal regions targeting $\tilde{t}_1 \rightarrow b\tilde{\chi}_1^\pm$ and those designed for $\tilde{t}_1 \rightarrow t\tilde{\chi}_1^0$, while the latter

also use variables related to reconstructed top quarks.

The 2-leptons stop search [200] is designed for final states containing two isolated leptons and large E_T^{miss} , primarily targeting top squarks decaying through an intermediate chargino.

The Monojet stop analysis [201] looks for final states characterised by large E_T^{miss} , at least one high p_T jet (vetoing events with more than 3 jets), and no leptons. Signal regions of this search were designed in the context of a search for top squarks, each decaying into an undetected charm quark and a neutralino.

The search for top squarks with a Z boson in the final state [202] is motivated by the decay of $\tilde{t}_2 \rightarrow \tilde{t}_1 Z$, which produces many leptons in the final state. It is required that leptons form a pair with a mass consistent with the Z boson, at least one b -jet and large E_T^{miss} .

The $2b$ -jets + E_T^{miss} analysis [203] searches for SUSY scenarios that produce events that contain exactly two b -jets, significant E_T^{miss} and no isolated leptons, for example those coming from decays of bottom squarks to b -quark and the LSP and from top squark to b -quark and chargino.

The $tb + E_T^{\text{miss}}$, stop analysis [204] was designed for a mixed scenario: direct production of pairs of top or bottom squarks with 50% branching ratio to neutralinos and charginos, yielding final states consisting of a top quark, bottom quark and large E_T^{miss} .

5.4.3 Electroweak searches

This section details the analyses considered for the pMSSM analysis which target sparticles produced via electroweak interactions. This entails the production of pairs of sleptons or electroweakinos which typically decay into final states containing several high p_T leptons and E_T^{miss} .

The ℓh search [205] is designed to tackle the direct pair production of a chargino and a neutralino, which decay to final states with large E_T^{miss} , an isolated lepton, and a Higgs boson which is identified by requiring either two b -jets, or two photons, or a second lepton with the same electric charge (targeting $h \rightarrow WW$ decays).

The 2-leptons analysis [206] targets electroweak production of charginos and/or neutralinos, or sleptons in events with at least two leptons, E_T^{miss} and for some signal regions two or more jets in the final state.

A search targeting a similar production process is the 2-taus analysis [207] searching for SUSY in events with at least two hadronically decaying τ leptons, large E_T^{miss} and jet vetoes.

The 3-leptons analysis [208] is a search for the direct production of charginos and neutralinos in final states with three leptons — which here may include up to two hadronically-decaying τ leptons — and large E_T^{miss} , that can come through the decays via sneutrinos, sleptons or W , Z or Higgs bosons.

The 4-leptons analysis [209] looks for SUSY in events with four or more leptons including hadronically decaying τ leptons, though at least two of the leptons are required to be electrons or muons. Such high lepton multiplicity final states can occur if a degenerate $\tilde{\chi}_2^0 \tilde{\chi}_3^0$ pair is produced which decay via sleptons or staus to $\tilde{\chi}_1^0$ and many leptons. The decay to a Z boson and $\tilde{\chi}_1^0$ is also considered by the analysis.

5.4.4 Other searches

The Long-lived particles searches [211, 212] are designed to detect heavy long-lived particles by measuring their speed β from the time-of flight to the calorimeters and muon detectors and $\beta\gamma$ (where γ is the relativistic Lorentz factor) from the specific ionisation energy loss in the pixel detector. In the pMSSM analysis, only the search for direct production of pairs of long-lived top or bottom squarks, gluinos, staus or charginos are considered. The search using 7 TeV

data from 2011 [211] considered sparticles as light as 200 GeV, while in most cases the later analysis [212] only considered sparticles above 400 GeV. Both searches are therefore included for maximal sensitivity.

The $H/A \rightarrow \tau^+\tau^-$ search [213] is designed to detect the heavy, neutral Higgs bosons predicted in the MSSM if they decay to τ -pairs.

5.5 Analysis strategy

In this Section, the strategy of the pMSSM analysis is described. The criteria for excluding pMSSM model points (that satisfied all constraints from Section 5.2) are detailed:

- First a selection based only on the expected cross-section is performed on the 300,000 model points (see Subsection 5.5.1).
- Then the remaining 280 000 model points are generated at the truth level and are classified as not excluded (Cat.1), in between (Cat.2) and excluded (Cat.3) (see Subsection 5.5.2).
- The 45 000 model points (all model points being classified as Cat 2. and also a fraction of Cat 3. model points) are then fully reconstructed and the CLs are calculated for each ATLAS search that have been previously identified to be sensitive (see Subsection 5.5.3).

5.5.1 Cross-section calculations

The production cross-section of each model point is calculated with a slightly modified version of Prospino 2.1 [39, 40, 41, 42, 43]. The sbottom pair production cross-section is excluded from the sum of light-flavour squark pair production as it is calculated separately. Furthermore, the NLO cross-section for a given process is only calculated if the LO cross-section is above 0.25fb except for processes involving just light-flavour squarks and gluinos. This was done in order to reduce the CPU consumption. Note that neither the NLL corrections [118, 119, 120, 121, 122], nor the enveloping of PDFs and factorisation and normalisation scales as described in Ref. [214] are applied, again in order to reduce CPU consumption. The default CTEQ6.6M PDF set is used in this calculation. The effect of neglecting the NLL corrections is cross-checked on the model points that were on the fringe of the exclusion and is found not to affect the exclusion.

The production processes are split into three groups: strong (involving squarks and/or gluinos), electroweak (electroweakinos and sleptons) and mix production (associated production of squark/gluino and electroweakino), and the cross-sections are evaluated for each group. Although the slepton pair production is a subset of electroweak production, it was added as a separate group as the acceptance for slepton pairs in some cases can be much higher than for electroweakino production. If the production cross-section is above the limit determined for each group separately the model point is considered as potentially observable at the LHC. The minimal values for each process are listed in Table 5.6. The model points with a cross-section below this limit are considered as not excludable by ATLAS. The model points with the $\tilde{\chi}_1^0$ mass above 1 TeV are also marked as not observable at the LHC. These decisions are supported by Figure 5.14 where the strong production cross-section (on the left) and the $\tilde{\chi}_1^0$ mass (on the right) are shown, and they are below the limits from the Table 5.6.

5.5.2 Model points at the truth level

The model points are then generated at the truth level using MadGraph 1.5.12 [215] with the CTEQ 6L1 PDF set [98] and Pythia 6.427 [106] with the AUET2B tune. For each model point

Production mode	Minimum cross section [fb]	Fraction of models generated		
		Bino LSP	Wino LSP	Higgsino LSP
Strong	0.25	82.5%	74.9%	76.7%
Mixed	0.25	52.6%	42.1%	13.9%
Electroweak	7.5	38.3%	72.5%	75.0%
Slepton pair	0.75	9.6%	7.9%	9.5%

Table 5.6: Minimum cross-sections required to do particle-level event generation for the four different production modes and the fraction of the model points above this cross-section for each LSP type.

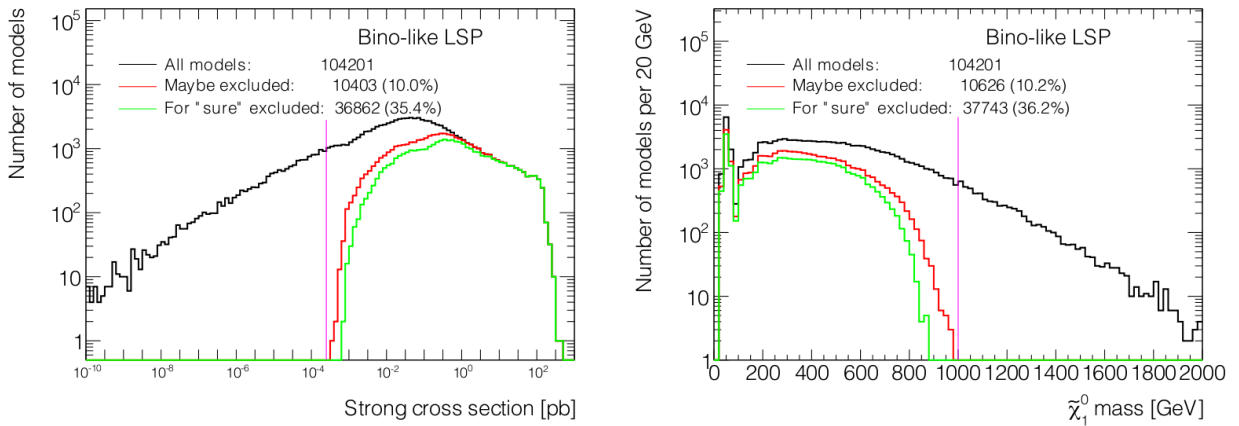


Figure 5.14: Production cross-section (on the left) and LSP mass (on the right) for strong production for a bino-like LSP. The green line shows the models that are evaluated to almost certainly be excluded (Cat. 3) and the red line shows the models that potentially could be excluded (Cat. 2 and low-acceptance models as defined in Section 6.1.2.5). The vertical purple line indicates the minimum cross-section/maximum LSP mass required for events to be generated.

the number of events corresponding to 200fb^{-1} is generated for relevant production cross-section (but with a minimum of 10,000 events and a maximum of 300,000 events).

The initial pair of sparticles and up to one additional parton are generated with `MadGraph`, and all sparticle decays and parton showering are handled by `Pythia`. Those should have been merged using the MLM jet matching procedure [97] to ensure a smooth transition between `MadGraph` and `Pythia`. The matching is configured to use a `MadGraph` k_T measure of 20 GeV, and a 25 GeV jet cut-off in `Pythia`. Unfortunately the matching was disabled in `MadGraph` for the first generation of model points. In addition, the cut-off chosen is lower than what is normally recommended for SUSY production, namely 1/4 the main sparticle scale. This results in the generation of a softer initial state jet spectrum and higher final state jet multiplicity. This effect will be studied in Section 6.1.3.3. Following these studies, one third of the model points has been resimulated.

5.5.3 Model points at the reconstructed level

The model points at the reconstructed level are generated with the same `MadGraph 1.5.12+Pythia 6.427` setup as is done for the truth level evaluation described in Section 5.5.2. The same problem with jet matching of the generation at the truth level is also present for the generation of events at the reconstructed level. The simulation of the events is done with `AtI Fast-II` [66] with pile-up and simulation parameters.

The generation of events at the reconstructed level starts from the different seeds, as the EVNT files of the truth generation were not kept. This leads to different events generated at the truth and at the reconstructed level. For the events generated at the reconstructed level, there is also the information about the truth level events, thus making them more easily comparable.

5.5.4 Categorisation of model points

Each ATLAS search from Table 5.5 has designed its truth code - an implemented of the analysis selection criteria in a simplified code that runs on the samples generated at the truth level. Once the 280 000 pMSSM model points are generated at the truth level, the truth code is run over them to obtain the truth yields (n_{truth}), normalised to the luminosity, for each SR of each ATLAS search. In principle they are supposed to be compared with the observed model independent upper limit calculated using MC pseudo experiments (UL, Section 3) coming from the best expected SR. Since the best expected SR is not determined, and the event yields are compared to the observed UL of all SRs of all analyses. This will be revisited in Section 6.2.2.

Deducing a limit at the reconstructed level from this comparison is not straightforward since the truth code is a simplified version of the full analysis code and since the impact of the detector has not been considered: for this purpose one has defined a safety margin that covers the discrepancy between the analysis at the truth and at the reconstructed level. For each SR a comparison of the event yields obtained at the truth and at the reconstructed level has been beforehand performed from which were deduced two numbers r_1 and r_3 corresponding to the minimal and maximal values of the distribution of the ratio between the yields obtained at the truth and at the reconstructed level (see Section 6.1 for a full description how these numbers are estimated for the 0-lepton SRs). A given model point can therefore be classified in one of the three categories (for one SR, and one search):

- $n_{\text{truth}} < r_1 \times \text{UL}$: The SR doesn't have any sensitivity for this model point - it is marked as not excludable by that SR and is classified as Cat. 1.
- $n_{\text{truth}} > r_3 \times \text{UL}$: The model point is considered to be excluded at the truth level, as the number of expected events is sufficiently high to be well above the UL and is Cat. 3.

- $r_1 \times \text{UL} < n_{\text{truth}} < r_3 \times \text{UL}$: The model points that are neither Cat. 1 nor Cat. 3 are classified as Cat. 2. The SR shows sensitivity to the model point but it is too close to the UL for decision to be made with the analysis at the truth level.

When multiple SRs and searches are considered for a model point to be in Cat. 1 it is required for it to be in Cat. 1 for all SR of all analyses. To be in Cat. 3 it is sufficient to be there for at least one SR of at least one analysis. All the other model points are classified as Cat. 2.

For the model points in Cat. 2 at least one SR shows good sensitivity, but the estimate at the truth level is not precise enough to conclude. To make the final decision if the model point is excluded or not, it is necessary to simulate it at the reconstructed level and analyse it with the full analysis code. This final step is also indispensable in order to check the analyses implemented at the truth level. The evaluation of r_1 and r_3 values is difficult and depend on each analysis: the scope of the next Chapter is to estimate them for the 0-lepton analysis.

5.6 Conclusion

In this Chapter the pMSSM parameters used in the analysis were reviewed. The link between the observables (external constraints) and those parameters have been exemplified. Then all the ATLAS searches that will be considered later on have been detailed, and finally the analysis strategy has been described and is represented in Figure 5.15. The next Chapter will focus on the validation of the 0-lepton inputs in the final pMSSM-19 ATLAS analysis.

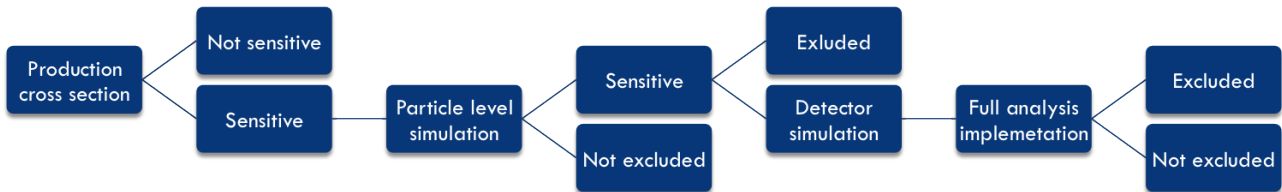


Figure 5.15: Analysis strategy

Chapter 6

Implementation and validation of the 0-lepton analysis for the pMSSM analysis

This Chapter focuses on the procedure for the exclusions of the pMSSM model points by the 0-lepton analysis. The implementation of the 0-lepton analysis at the truth level is the first step towards the interpretation of the exclusion limits. The implementation should be verified, and the values of r_1 and r_3 should be derived. Those are checked by making a comparison between the expected yields in the signal regions obtained at the truth and at the reconstructed level.

As a matter of fact, the choice of the pMSSM model points to be reconstructed has been performed in several steps. To initiate the process a first estimation of the r_1 and r_3 values has been made on simplified models. Several of them were investigated to better reproduce the wide range of final states present in the pMSSM model points. Once the production of the reconstructed samples of the pMSSM model points has started those r_1 and r_3 values were checked and refined.

Due to the large number of pMSSM model points needed to be processed for the 0-lepton analysis, and considering the fact that one has to deal with 13 signal regions, the work presented in this Chapter relies on a wide hand-made careful book-keeping of all the results at the different stages of the analysis.

In Section 6.1 the description of the 0-lepton analysis implementation at the truth level is presented. Then the comparison between the analysis at the truth and at the reconstructed level is performed (for both the simplified models and pMSSM model points). Various ways to get a better agreement are investigated. In Section 6.2 a comparison is made between the CLs values and the yields calculated at the truth and at the reconstructed level. This led to the derivation of a procedure to predict the CLs values based on the yields calculated at the truth level using a fit, which are later used for the exclusion of the pMSSM model points. In Section 6.3 the final classification of the pMSSM model points at the truth level is presented.

6.1 Implementation of the 0-lepton analysis at the truth level

6.1.1 Truth code

The benefits of having the full analysis implemented at the truth level are clear: it is much faster to run and the generation of the truth based samples is much less resource consuming. That makes the truth code very useful for quick studies. It permits to assure that the production

of the fully reconstructed samples is justified and that one does not reconstruct model points that are almost certainly excluded or that would never be excluded with the currently available luminosity (20.3 fb^{-1} at 8 TeV). The precision of the truth code compared to the code at the reconstructed level determines if and how widely it can be used: the better is the agreement between them, the more widely the truth code can be relied upon.

The 0-lepton analysis has been shown to be the most powerful ATLAS SUSY search for strong production in previous pMSSM analyses [216]. It is therefore very important to evaluate the 0-lepton analysis effect, first at the truth level. One of the initial steps of this thesis work has been to translate the full analysis code into a code at the truth level (the version for the pMSSM analysis is `ZeroLeptonTruth-00-00-05`).

The main changes compared to the full analysis are in the applied selection criteria and in the objects it uses. Related to the selection criteria: there are no data quality and trigger related cuts, also there is no event cleaning (cuts 1, 2 and 4-8 from Tables 3.5 and 3.6). Regarding the objects, the differences are on the identification of the objects. Jets are reconstructed with the same anti- k_T algorithm with $\Delta R = 0.4$ from visible stable particles, i.e. excluding neutrinos, muons, neutralinos. . . The identical criteria on the p_T and η as in the analysis at the reconstructed level is applied (baseline jet $p_T > 20 \text{ GeV}$ and $|\eta| < 2.8$). Electrons and muons from the decays of W or Z -bosons, τ leptons or from the decays of the possibly produced sparticles, are selected. No identification efficiency is simulated. They are also required to have $p_T > 10 \text{ GeV}$ and $|\eta| < 2.47$ (for electrons) and $|\eta| < 2.5$ (for muons). In the definition of E_T^{miss} all particles not-interacting with the calorimeters are taken into account. As explained in Section 3.3.3, two SRs of the 0-lepton analysis require reconstructed W -bosons in the final state. Those are reconstructed from the jet pairs compatible with the W -boson mass. The possible limitations with their implementation at the truth level is that the effects of jet merging are not reproducible at the truth level.

As explained before (Section 3.1.2), the main objects of the 0-lepton analysis are jets and E_T^{miss} . Those are usually well reproduced with the truth codes (for example this is not the case for τ leptons as their identification efficiency is low), so it is expected that there is a good agreement between the analysis at the truth and at the reconstructed level. Nevertheless, it has to be checked. For this purpose two approaches can be considered that are explored in the following: a comparison of the number of events passing the cuts at different levels of selection and a study of the most important variables distributions. Instead of comparing the number of events after different levels of selection, it is more instructive to compare the acceptances of the selection. The acceptance is defined as the ratio between the events passing all the selection criteria of one SR (n) and the total number of generated events (n_{gen}):

$$a = \frac{n}{n_{\text{gen}}}. \quad (6.1)$$

It is defined at both the truth (a_{truth}) and the reconstructed level (a_{reco}). The agreement between the acceptances depends strongly on their values. It is expected that relatively small values of acceptances are strongly influenced by statistical fluctuations. Another important quantity is the efficiency ($\epsilon_{\text{T/R}}$) of the selection, defined as the ratio between the event yields in SRs considered calculated at the truth level (n_{truth}) and the yields calculated at the reconstruction level (n_{reco})

$$\epsilon_{\text{T/R}} = \frac{n_{\text{truth}}}{n_{\text{reco}}} = \frac{a_{\text{truth}}}{a_{\text{reco}}}. \quad (6.2)$$

For the 0-lepton analysis its mean value is very close to one. For some studies, the variable:

$$r = \frac{n_{\text{truth}}}{\text{UL}} \quad (6.3)$$

proves to be useful. The UL denotes the observed model independent UL calculated using MC pseudo experiments, otherwise explicitly stated. This variable is calculated for every SR

and is used to classify model points: if its value is greater than one - meaning that the yields calculated at truth level are greater than the UL - the model point is considered excluded (on the basis of the UL), and not-excluded otherwise.

6.1.2 Comparison of the analysis at the truth and at the reconstructed level - simplified models

As a first step, the acceptances are studied for the simplified models (presented before in Section 3). These are used to derive the preliminary values of r_1 and r_3 needed to categorise the pMSSM model points at the truth level. The limitation of the simplified models with direct decays lies in the fact that there are no light leptons in the final state, therefore not fully suitable to generalise the results obtained within those simplified models to the pMSSM model points. Therefore simplified models assuming squark pair production followed by the decay through intermediate chargino, were also studied. These simplified models are generated such that the light leptons coming from the decays of W -bosons can be present in the final state.

6.1.2.1 Simplified model of gluino pair production followed by direct decay

In Figure 6.1 the yields calculated at the truth level (n_{truth}) divided by the UL (r) as a function of $\epsilon_{T/R}$ for all 0-lepton SRs is shown. The simplified model assuming gluino pair production followed by the direct decay into quark pair and a neutralino is considered. Points that are excluded are represented in dark blue, and the others are shown in pink. The points represented in green denote the model points whose acceptance is lower than a limit set for each SR (explained later in Section 6.1.2.5).

It can be seen that the ratio is very close to one, thus the mean efficiency is set to exactly one in the following, and the possible deviations are taken into account by the r_1 and r_3 values. This simplified model does not produce leptons in the final state, thus being far from the general case which can be considered (where there are many production processes and decay patterns available). The spread observed on $\epsilon_{T/R}$ is the most striking when considering the SR2jl which is the region with the loosest selection (the value of the UL is 1223), and SR4jt (the UL equals to 3.1), where only few events are expected. Statistical effects are responsible for this enlargement in spread in SR4jt. While the spread in SR2jl is coming from the points that have small mass splitting between sparticles. The largest spread is found for the SR2jW and SR4jW, which is understood as there were no dedicated studies conducted in order to understand the effects of jet merging at the truth level. Those SRs cannot be relied upon and are discarded in what follows. Results are quite similar for the simplified models assuming squark pair production or squark-gluino production followed by direct decays, so they are not shown. Two vertical and horizontal lines are also shown: both mark the r_1 and r_3 values estimated using another simplified model (different in each SR) and will be discussed in Section 6.1.2.2).

6.1.2.2 Simplified model of squark pair production followed by onestep decay

In Figure 6.2 the yields calculated at the truth level divided by the observed UL (r) as a function of $\epsilon_{T/R}$ for SR2jl and SR4jt are shown. Only these two SRs are shown, as they are expected to show the largest variations. This time it is presented for the simplified model of the production of squark pairs that decay through intermediate chargino. It is seen that the value of $\epsilon_{T/R}$ is a bit smaller, and lower than one and its spread is wider than in the previous Section. The likely reason for this is the presence of the light leptons in the final states expected to come from the W -boson decay. From here the conclusion is reached that the veto on events with light leptons makes a difference, and that one should try to find a SUSY model that reflects the best all the possible production and decay processes. One candidate for this would be the mSUGRA

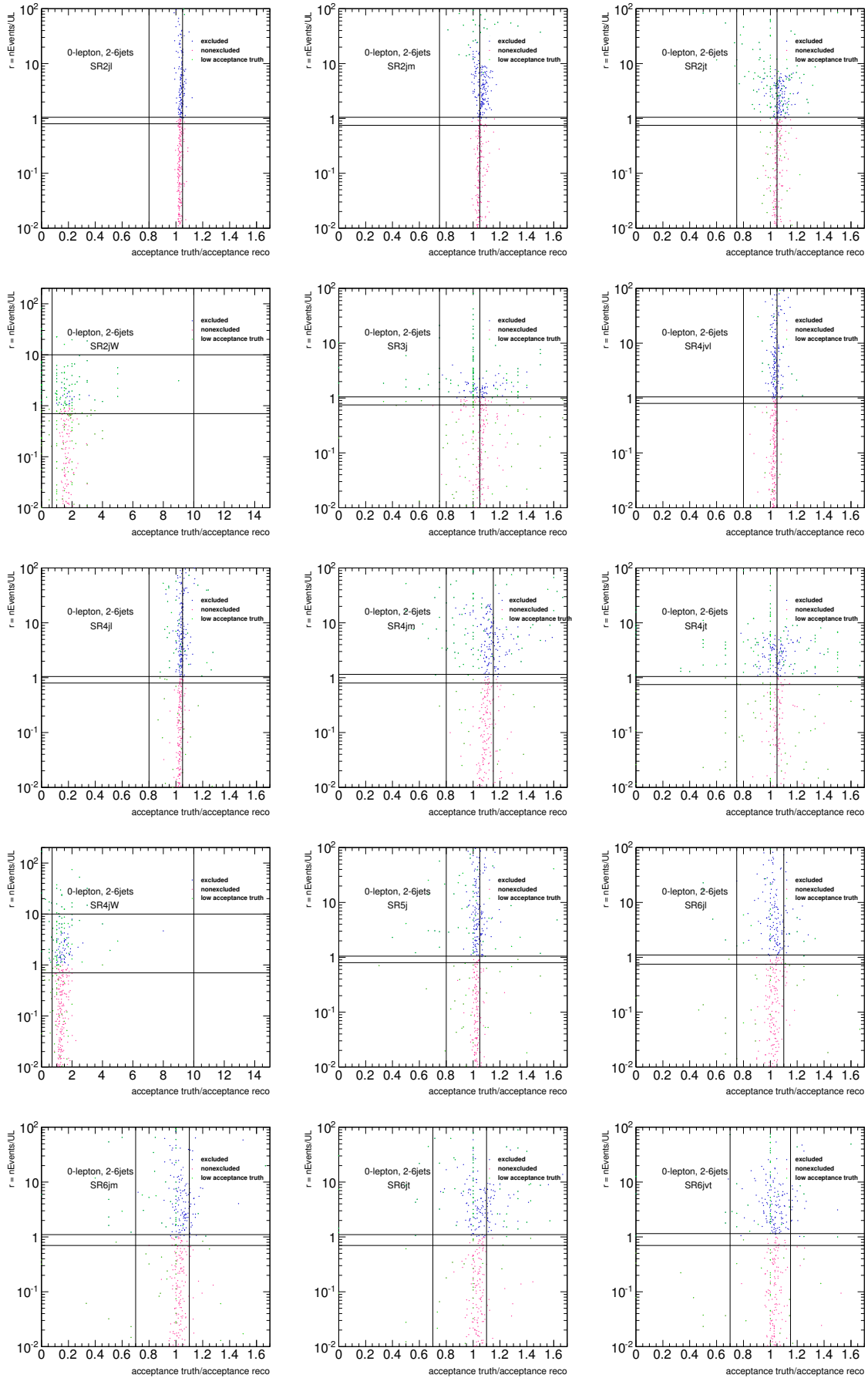


Figure 6.1: The number of the events selected at the truth level divided by the observed UL as a function of $\epsilon_{T/R}$ for all 0-lepton SRs for the simplified model assuming gluino pair production followed by the direct decay. Points that are excluded are represented in dark blue, and the others in pink. The points represented in green denote the model points whose acceptance is lower than a limit set for each SR (explained in Section 6.1.2.5). Two vertical and horizontal lines are shown: both mark the r_1 and r_3 values, different in each SR (this is discussed in Section 6.1.2.5).

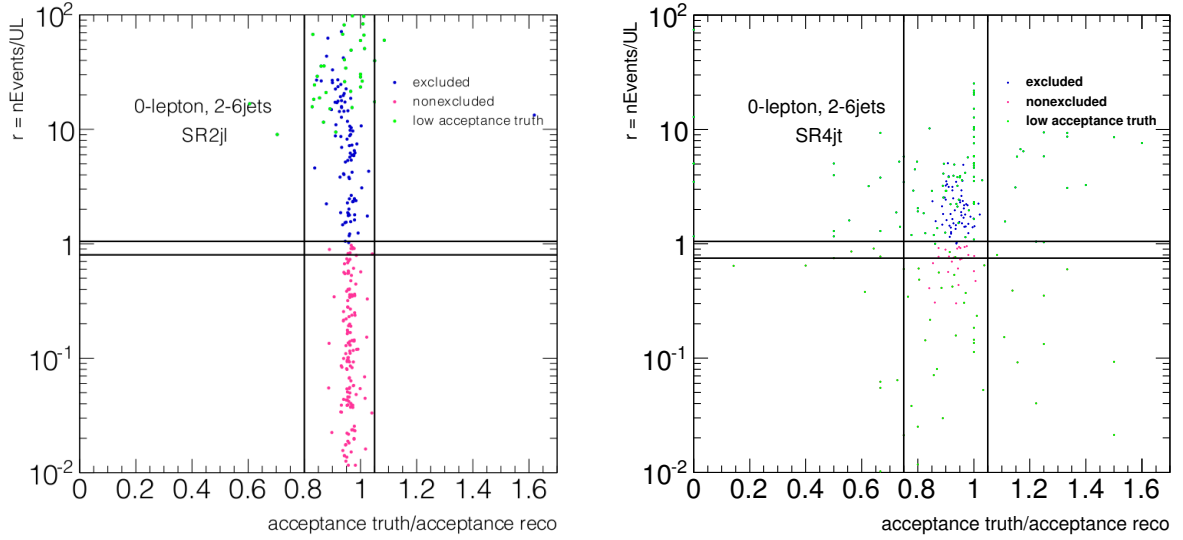


Figure 6.2: The yields calculated at the truth level divided by the observed UL as a function of $\epsilon_{T/R}$ for 0-lepton SR2jl and SR4jt for the simplified model assuming squark pair production followed by the onestep decay. Points that are excluded are represented in dark blue, and the others in pink. The points represented in green denote the model points whose acceptance is lower than a limit set for each SR (explained in Section 6.1.2.5). Two vertical and horizontal lines are shown: both mark the r_1 and r_3 values, different in each SR (how are they derived is described in Section 6.1.2.5).

model. Unfortunately, this model was produced with **Herwig**, while pMSSM model points were produced with **MadGraph**, and this was expected to introduce additional discrepancies. To be consistent, the studies are done only on the simplified models produced with **MadGraph**.

The dependence between the acceptances calculated at the truth level and $\epsilon_{T/R}$ is shown in Figure 6.3 for all 0-lepton SRs. Points that are excluded are represented in dark blue, and the others in pink. It is seen that the spread is getting broader as the acceptances are getting smaller. From these plots, the value of the minimal acceptance beyond which the agreement is getting worse, can be derived. The model points with extremely small truth acceptances will be treated differently (as explained in Section 6.1.2.5).

6.1.2.3 Lepton efficiencies

Since a slight shift has been observed in the mean value of $\epsilon_{T/R}$ calculated for the simplified models considered in Section 6.1.2.1 and 6.1.2.2, and attributed to the impact of the veto on the events with light leptons, one could consider introducing more realistic reconstruction and identification efficiencies and energy measurements. The addition of a 95% efficiency factor (a typical value of the identification efficiency for an isolated lepton in considered p_T range) on the lepton identification at the truth level has been investigated. The results are shown in Figure 6.4 for the simplified model of the squark pair production followed by the decay through intermediate chargino, where the points in blue correspond to the standard analysis, while the points in violet are obtained when the lepton identification efficiency factor is applied. Although the effect is sizable, using this factor doesn't help reducing the discrepancy. In addition, the spread present for the points with low acceptances is not getting smaller either.

The smearing of electrons and muons using specially designed functions (depending on η and the average number of interactions per event - μ) has also been considered [217]. Those smearing functions are derived for the loose and tight definition of leptons, while the 0-lepton analysis uses medium leptons in the definition of its SRs. Even after investigating the effect

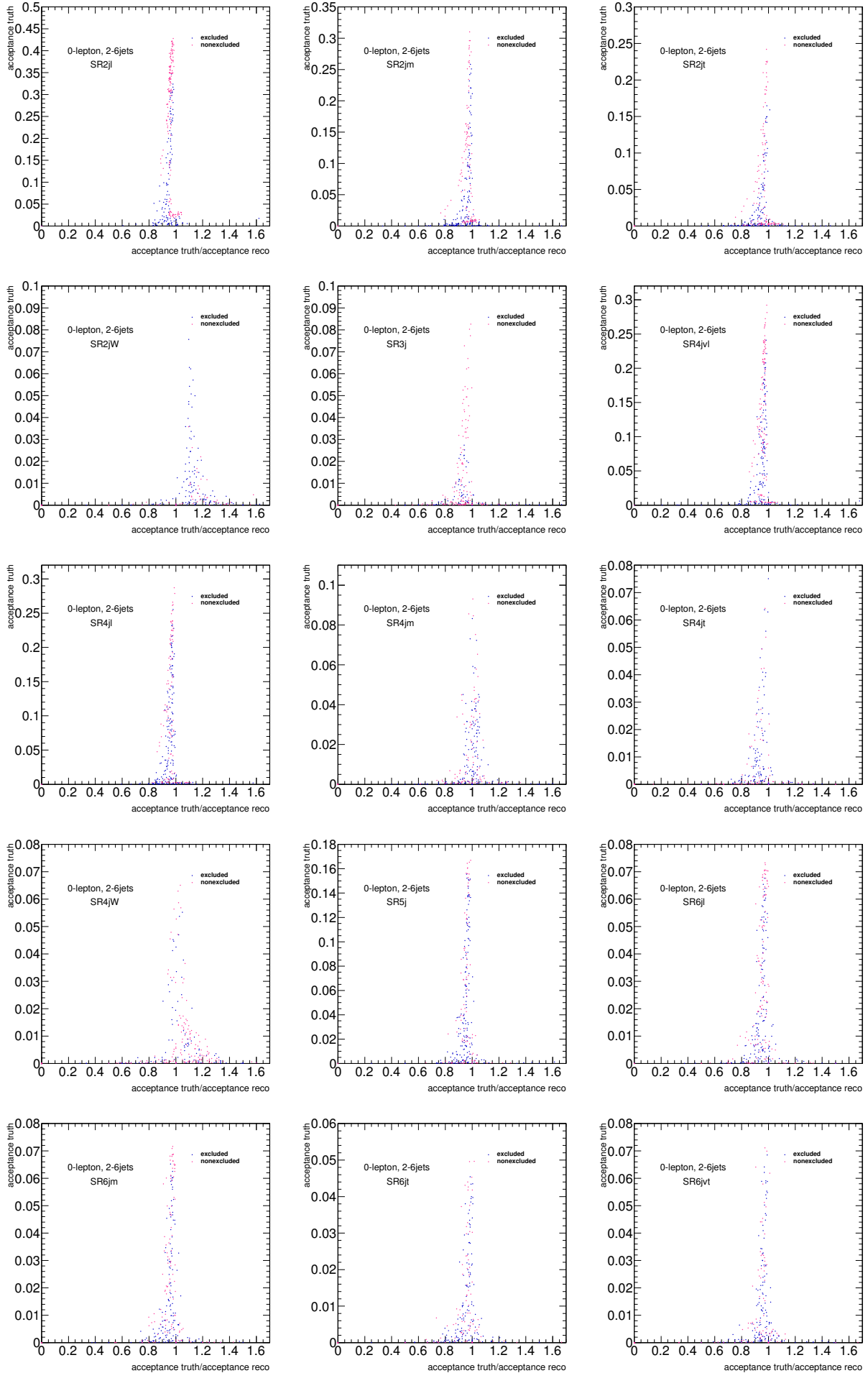


Figure 6.3: The acceptance calculated at the truth level as a function of $\epsilon_{T/R}$ for all 0-lepton SRs. Points that are excluded are represented in dark blue, and the others in pink.

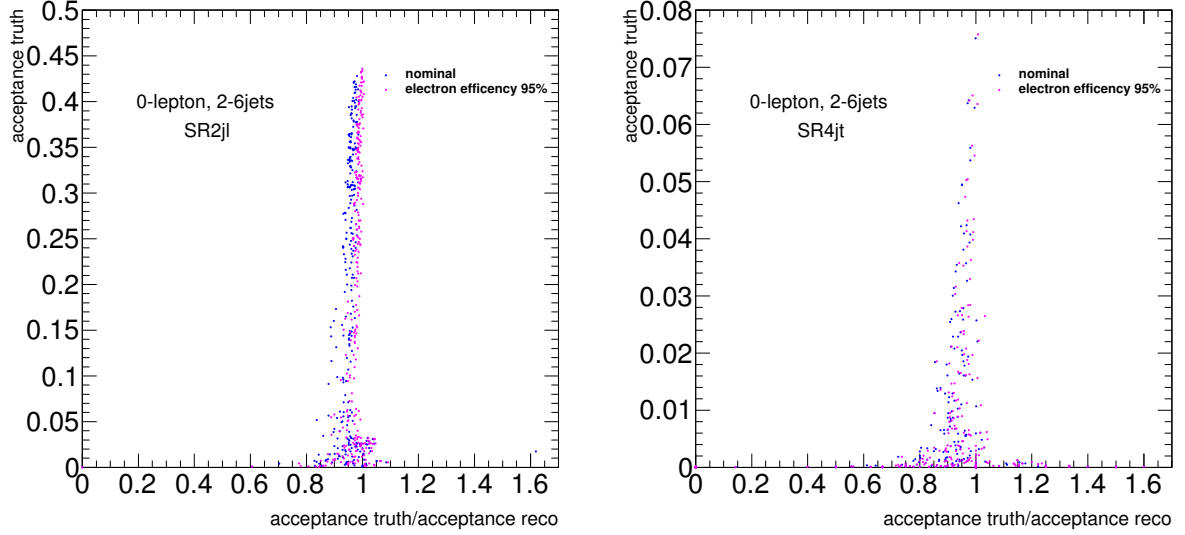


Figure 6.4: The acceptance evaluated on the truth level as a function of $\epsilon_{T/R}$ for all 0-lepton SRs with lepton identification efficiency factor of 95% applied. The points in blue are with nominal lepton identification efficiency, while the points in violet are with the lepton identification efficiency factor of 95% applied.

of the smearing, the results do not change. Electrons and muons are left unmodified in the following.

6.1.2.4 Jet smearing

The most important objects in the SR selection for the 0-lepton analysis are jets and E_T^{miss} , so it was expected that a better modeling of those objects could also help improving the agreement between the analysis at the truth and at the reconstructed level: a smearing of the jets at the truth level was therefore applied (which also leads to a change of E_T^{miss} as they are very tightly connected) [217]. The smearing function is parametrised by the jet p_T , η and the average number of interactions per event. It is defined only for jets with p_T between 10 and 1500 GeV, and $|\eta| < 3.6$, jets that are outside these limits are not smeared. After changing the values of the jet p_T , the calculation of the E_T^{miss} is affected. It is then recalculated starting from the unsmeared E_T^{miss} by first subtracting the unsmeared jet p_T , and then adding the new smeared jets. In Figure 6.5 the difference between nominal setup (blue points), and the one with the jet smearing applied (orange points) is shown. The simplified model considered is the squark pair production followed by the onestep decay through intermediate chargino. Unfortunately this only deteriorates the agreement so it is not considered further.

6.1.2.5 Derivation of the r_1 and r_3 values from simplified models

In each SR the distribution of $\epsilon_{T/R}$ gets wider as the acceptance calculated at the truth level gets smaller. In order to capture all those possible disagreements and if one wanted to be conservative, the r_1^{SM} and r_3^{SM} values (SM denotes values derived using simplified models) would have been very far apart one from the other. This would categorise many pMSSM model points as possibly excluded (Cat. 2) that would needed to be reconstructed and their categorisation checked. This would have led to an unacceptably high resource consumption, so alternatives have been explored.

For example using a limit on the minimal acceptance (a_{min}) would restrict the $[r_1, r_3]$ range. The model points that are above the acceptance limit would be normally categorised as Cat. 1, Cat. 2 and Cat. 3. The model points below this limit are classified as Cat. 1 if $n_{\text{truth}} < r_1 \times \text{UL}$

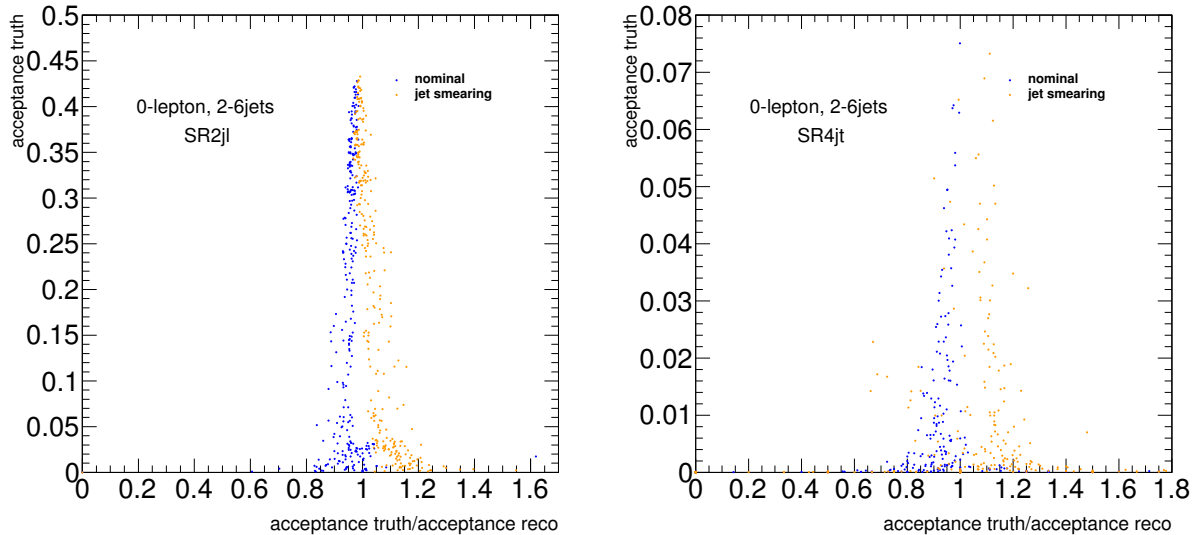


Figure 6.5: The acceptance evaluated at the truth level as a function of $\epsilon_{T/R}$ for 0-lepton SR2jl and SR4jt with jet smearing applied. The points in blue are without jet smearing, and the points in orange are with the jet (and E_T^{miss}) smearing applied.

as for the higher acceptance case and the others are assigned to Cat. 2 and are consequently fully reconstructed. This approach is considered conservative, as no pMSSM model points are excluded using the analysis at the truth level if they have very low acceptances. The minimal acceptance limits for each SR are given in Table 6.1.

The truth level implementation of the 0-lepton analysis performed in this Section leads to the definition of the r_1^{SM} and r_3^{SM} values taken as a starting point in the categorisation of the pMSSM model points. Those values are given in Table 6.1 for each SR.

6.1.3 Comparison of the analysis at the truth and at the reconstructed level - pMSSM

From the preliminary r_1^{SM} and r_3^{SM} values derived in the previous Section, a categorisation of the pMSSM model points is performed and it is decided which pMSSM model points are to be reconstructed. In the first round of reconstruction, from the 280,000 pMSSM model points simulated at the truth level, only 20% of the pMSSM model points classified as Cat. 2 for the 0-lepton analysis are reconstructed, as well as a few percent of the model points classified as Cat. 3 (around 5,000 model points in total). They have been passed through the full 0-lepton analysis using the same version of the codes as for the 0-lepton paper [2] `ZeroLeptonFactory-00-00-53` and `ZeroLeptonFitter-00-00-25-06` to calculate the yields and the CLs values. From those new model points the values of r_1^{SM} and r_3^{SM} are revisited and new values are derived: r_1^{pMSSM} and r_3^{pMSSM} . The results are presented in this Section, first by comparing the yields at the truth and at the reconstructed level, and then by performing a comparison of the distributions of several kinematical variables.

For all the pMSSM model points presented in this Section only the strong production processes are considered, as the 0-lepton analysis is designed and thus most sensitive for this production type. The r_1 and r_3 values derived for the strong production are nevertheless applied also for the mix and electroweak production of sparticles.

	Description	Channel												
		2j			3j	4j				5j	6j			
		2jl	2jm	2jt		4jl-	4jl	4jm	4jt		6jl	6jm	6jt	6jt+
1	mean efficiency	1.0												
2	UL (toys)	1223	86	38	8.2	273	91	10	3.1	35	39	25	6.6	7.9
3	UL (asymptotic)	1259	81	37	8.1	268	87	9.2	2.5	32	37	22	6.1	7.3
4	UL (toys)	1400	86	38	8.2	310	91	10	3.1	35	39	25	6.6	7.9
5	r_1^{SM}	0.80	0.75	0.75	0.75	0.80	0.80	0.80	0.75	0.80	0.75	0.70	0.70	0.70
6	r_3^{SM}	1.05	1.05	1.05	1.05	1.05	1.05	1.15	1.05	1.05	1.10	1.10	1.10	1.15
7	a_{min}	0.01	0.005	0.005	0.002	0.005	0.005	0.002	0.004	0.005	0.002	0.002	0.002	0.002
8	r_1^{pMSSM}	0.80	0.75	0.75	0.60	0.80	0.80	0.80	0.75	0.80	0.75	0.70	0.70	0.70
9	r_3^{pMSSM}	1.05	1.10	1.10	1.40	1.05	1.05	1.15+1 σ	1.05+2 σ	1.05	1.10	1.10	1.40	1.50

Table 6.1: The criteria used for the selection of the pMSSM model points for the reconstruction. The UL are 95% CL model independent upper limits on the observed number of signal events evaluated using MC pseudo experiments (toys), and using asymptotic formula from [134], as well as their values considered in the pMSSM study (see Section 6.2.1). The r_1 and r_3 values derived using simplified models (r_1^{SM} and r_3^{SM}), and corrected ones determined with reconstructed pMSSM model points (r_1^{pMSSM} and r_3^{pMSSM}), and the values of minimal acceptance (a_{min}), are also presented.

6.1.3.1 Comparison of the yields

In Figure 6.6 the yields calculated at the truth level as a function of those determined at the reconstructed level in each SR of the 0-lepton analysis are shown. The pMSSM model points belonging to all the categories are presented. In the plots are indicated the UL corresponding to that SR (horizontal line), also two vertical lines indicating the $r_1^{\text{SM}} \times \text{UL}$ and $r_3^{\text{SM}} \times \text{UL}$ are shown. Those lines delimit the categories of model points. Two purple diagonal lines illustrate the expected spread for the given SR, obtained by multiplying the yields at the truth level by r_1^{SM} and r_3^{SM} values. In general a good agreement is observed in all SRs and the mean efficiency is close to one. By looking at these plots, one wants to make sure that there are no model points that have a yield at the truth level above $r_3^{\text{SM}} \times \text{UL}$ (excluded by the analysis at the truth level), but have a yield at the reconstructed level below UL (thus not excluded at the reconstructed level), which would appear in the lower-right hand side rectangle. In some SRs this is indeed the case, while in other ones some adjustments were needed. The values of the r_1^{SM} and r_3^{SM} are modified accordingly - the final values for the pMSSM model points - r_1^{pMSSM} and r_3^{pMSSM} . In SR2jm and SR2jt r_3 is changed to 1.10, in SR3jt to 1.40. In SR6jt it is changed to 1.40 and in SR6jvt to 1.50, as quoted in Table 6.1. Relatively small yields are expected in SR4jm and SR4jt which results in considerable differences between the yields calculated at the truth and at the reconstructed level. As this is largely a statistical effect, in those SRs the r_3 value is not changed, instead the yields are reduced by 1 σ and 2 σ statistical uncertainty respectively, before being compared to $r_3^{\text{pMSSM}} \times \text{UL}$.

The pMSSM model points that have worse agreement between the results at the truth and at the reconstructed level are usually those that have small mass difference between the NLSP and the LSP, so called model points with a compressed spectra.

6.1.3.2 Comparison of shapes

A complementary way of assessing the agreement between the analysis at the truth and at the reconstructed level is to compare the main distributions of the kinematic variables used in the analysis. The main variables used in the 0-lepton analysis are the number of jets, their p_{T} , $E_{\text{T}}^{\text{miss}}$ and m_{eff} . If there is a good agreement between the distributions of these variables at the preselection level (after applying cuts 3, 9, 10, 11 and 12 of Tables 3.5 and 3.6) it is expected

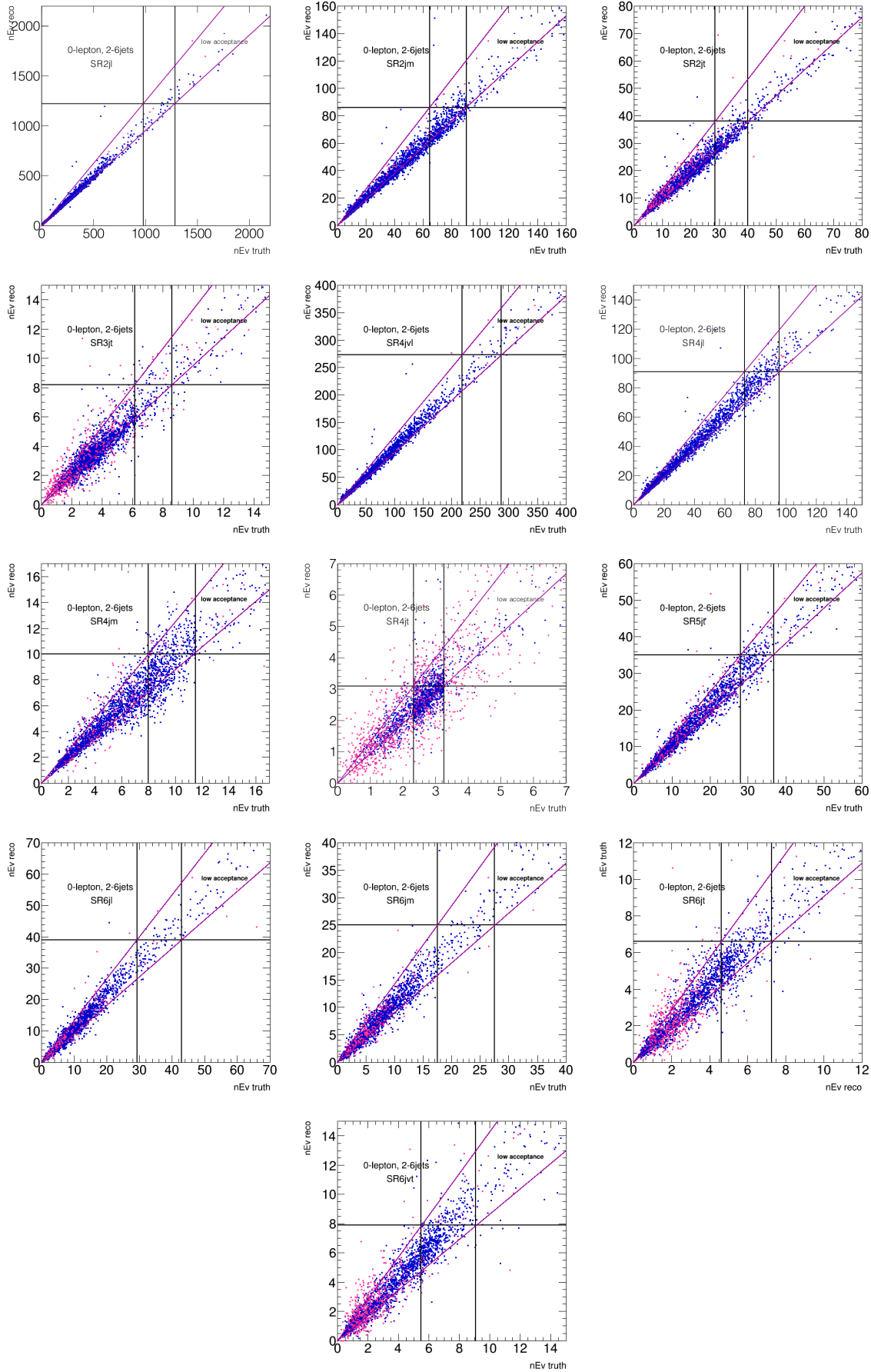


Figure 6.6: The expected yields at the truth level as a function of the yields at the reconstructed level for all 0-lepton SRs. The pMSSM model points belonging to all the categories are presented. The points in blue are above the minimal value of the acceptance at the truth level, while the points in pink are below that value. Horizontal line represents value of the observed UL for a given SR, while two vertical lines correspond to $r_1^{\text{SM}} \times \text{UL}$ and $r_3^{\text{SM}} \times \text{UL}$. Two purple diagonal lines limit the expected spread for given SR.

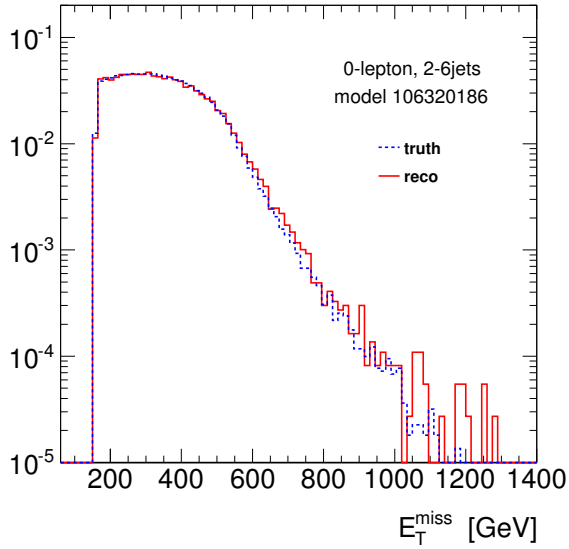
that the results are similar after applying all the analysis selection criteria. These distributions are shown on Figure 6.7 for one pMSSM model point. The dotted blue line (resp. solid red line) represents the results obtained with the analysis at the truth level (resp. at the reconstructed level). The fact that both distributions are very similar is another confirmation that the results of the analysis at the reconstructed level are quite well reproduced by the analysis at the truth level. The difference in the N_{jet} distributions (6.7c) exhibits a somewhat smaller number of jets at the truth level, possibly comes from the fact that one considers the electron and muon identification efficiency as being 100%, so the number of light leptons is higher at the truth level, when the overlap removal with the jets is performed, some of the jets could be classified as light leptons which would result in a smaller number of jets at the truth level.

The pMSSM model point that has been chosen for this comparison is expected to be excluded with all 0-lepton SRs - it is one of the model points targeted by this analysis - and this is why it is important to have a reliable analysis at the truth level especially in this case. Its particle spectrum and decays are shown in Figure 6.8. Several pMSSM model points have been looked at and exhibit similar features as the one chosen here. The dominant production process for this model point is strong production, but there are also model points where this is not the case, where either electroweak or mix production dominate. Those model points were also tested and have the same features thus the 0-lepton can be used even in the case of other production processes.

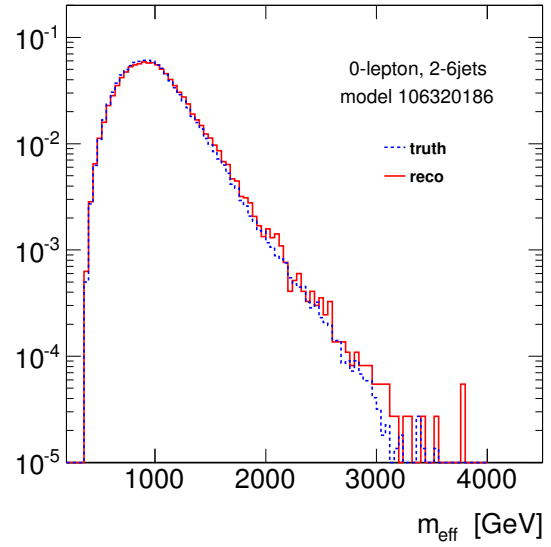
6.1.3.3 Jet matching

As mentioned in Section 5.5.2 the first round of pMSSM model points was generated with the jet matching disabled in MadGraph. All pMSSM model points being classified as Cat. 2, model points with low acceptances and a fraction of Cat. 3 have therefore been regenerated with the correct jet matching applied at the truth level to first study the effect. In Figure 6.9 the ratio between the acceptance calculated for the model point with jet matching configured correctly and the one with a misconfigured jet matching is shown for three SRs of the 0-lepton analysis. All the resimulated model points are presented in these plots, except for the model points with low acceptance. The model points with low acceptances introduce even more spread, but anyway they are not excluded by the results of the truth level analyses. These SRs (6.9a SR2jl, 6.9b SR4jl and 6.9c SR6jm) are chosen to illustrate potential dependence on the requirement on the minimal number of jets. It is seen that the ratio is closest to one in the SR2jl (Figure 6.9a), and that the spread is narrow, while as the minimal number of jets increases, the ratio shifts to lower values, and also gets wider. One can try to derive a correction factor that can be applied to the acceptances calculated with the misconfigured jet matching to bring them into agreement with the ones calculated with the correct jet matching, but this is difficult as there is a lot of spread, although the mean value (especially in SRs with small minimal number of jets) is close to one. When one considers this, the most important is if the model points stay in the same category when the jet matching is or not properly applied. Unfortunately, as the 0-lepton analysis has very tight requirements on r_1^{pMSSM} and r_3^{pMSSM} , the jet matching has an effect on its categorisation, and although the number of model points in each category stays the same, many model points do change category. When this effect had been assessed, it was decided that about one third of the model points were needed to be resimulated at the truth level in order for their categorisation to be properly determined. The effect was also studied for the reconstructed pMSSM model points, and here also differences were observed and consequently part of them were resimulated.

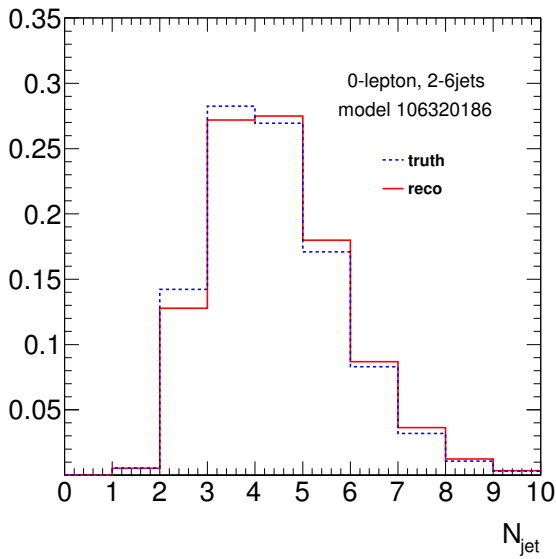
In this Section the categorisation of pMSSM model points is tested using the reconstructed samples, and the adjusted r_1^{pMSSM} and r_3^{pMSSM} values are derived from them. The final values are presented in Table 6.1. Also the effect of the jet matching misconfiguration is assessed, which



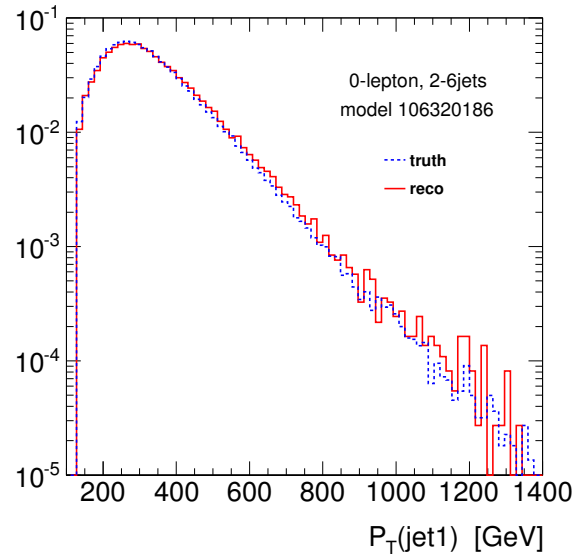
(a)



(b)



(c)



(d)

Figure 6.7: The distributions of (a) E_T^{miss} , (b) m_{eff} , (c) number of jets and (d) leading jet p_T at the preselection level for the model 106320186 (should be excluded by all 0-lepton SRs). The arrows denote the decays (the ticker is the arrow, the higher is the branching ratio).

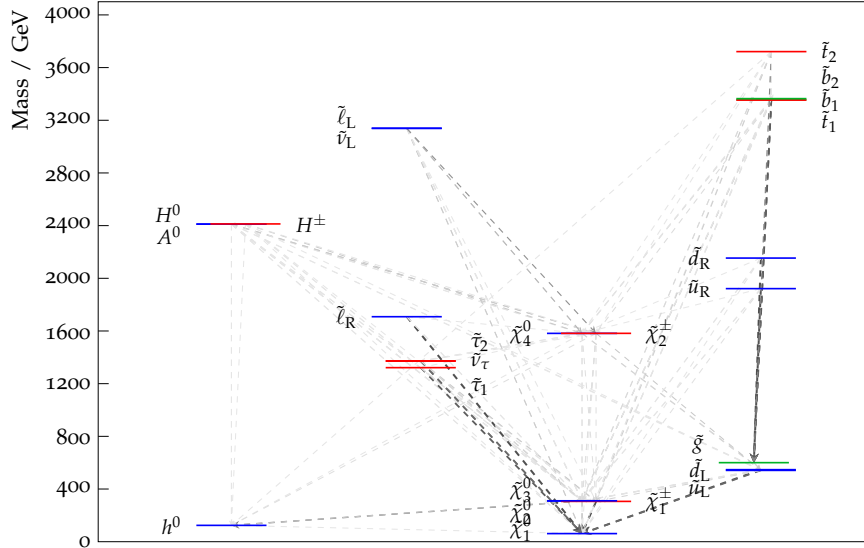
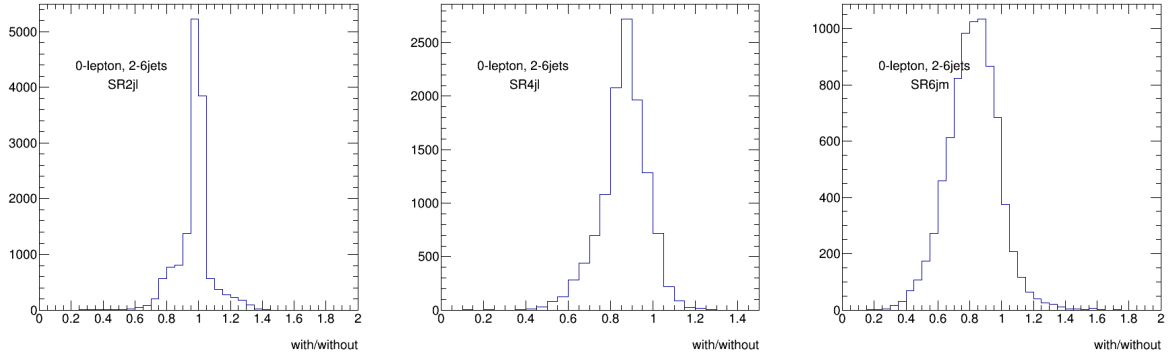


Figure 6.8: The particle spectrum and decays of the model point 106320186 (should be excluded by all 0-lepton SRs) used to produce Figure 6.7.



(a) SR2jl

(b) SR4jl

(c) SR6jm

Figure 6.9: The ratio between the acceptances calculated at the truth level for the model points with the jet matching configured correctly (denoted by 'with') and the ones with a misconfigured jet matching (denoted by 'without') is shown for three SRs of the 0-lepton analysis ((a) SR2jl, (b) SR4jl and (c) SR6jm).

led to the regeneration of part of the model points at the truth level and at the reconstructed level.

6.2 CLs - yields discussion

In Section 6.1 the categorisation of the pMSSM model points is based on the yields calculated at the truth level, and compared to the best observed UL. These were derived from a fit that has no signal contamination - on the other hand, actual exclusions of model points are based on CLs that takes into account uncertainties on the signal and signal contributions to CRs. In this Section, the interplay between classification and exclusion of model points is studied.

6.2.1 Comparison between the yields and CLs values - pMSSM model points

In order to make sure that the procedure of the categorisation and the exclusion of a model point is fully controlled, a comparison has been made between the CLs and the (truth and reconstructed) yields.

Since the UL are calculated without taking into account the systematics on the signal (Section 3.4.2), the first step has been to compare the CLs calculated in the same condition and the yields calculated at the reconstructed level. This is shown in Figure 6.10 for 2 SRs (SR2jl and SR4jt) where the UL calculated on the basis on the MC pseudo experiments is shown in full line, and the UL corresponding to the asymptotic formula is in dotted line. A zoom of the left-hand plot is given on the right. As stated in Section 5.5.4 the UL computed on the toys has been used as a baseline. There is a good agreement between the model points that would have been excluded from the CLs (no systematics) information and the ones excluded from the reconstructed yields. Still, some model points that appear on the right upper box of the plots would not have been properly excluded for SR2jl. To go further, an estimation of the impact of the systematics of the signal has been assessed and the same plot is shown in Figure 6.12, where this time the CLs are properly estimated plugging the signal systematics. The number of model points wrongly excluded by the reconstructed yields is even larger in SR2jl. From those comparisons that have been performed SR by SR (only two of them are shown here), a change of the UL for some SR has been made: for SR2jl it has been changed to 1400 events and for SR4jl- it has been pushed to 310 events. Those changes ensure that the model points that were on the fringe of Cat. 3 are now reconstructed.

However the exclusions of the model points at the truth level makes use of those UL, one therefore has to check that the CLs (calculated with the uncertainties of the signal this time) and the yields calculated at the truth level are consistent. This is done in Figure 6.11 for the same two SRs before considering the change of the UL described above. It is seen that some pMSSM model points get excluded with the observed UL at the truth level (the truth yields being higher than $r_3 \times \text{UL}$) but are not excluded by the CLs ($\text{CLs} > 0.05$) - those model points show up on the upper right corner of the plots. This study led to the conclusion that one should not based the actual exclusion of a model point on the yield calculated at the truth level versus the UL, and that a better estimator was needed.

Moreover, the classification uses the best observed UL amongst all SR while the exclusion should select the CLs from the best expected SR. Estimating the effect on a fraction of Cat. 3 model points that were fully reconstructed, it was found that $\simeq 10\%$ of the model points in this category were not excluded. Being able to estimate the CLs from the yields at the truth level would solve the problem and give a mean to select the best expected SR. This is described in the next Section.

6.2.2 Predicting CLs value based on the yield at the truth level

There are around 27,000 reconstructed pMSSM model points to which the 0-lepton analysis shows sensitivity (Section 6.3). For all those model points the CLs values have been computed for each of the 13 SRs with all the systematics uncertainties considered. This large statistics does allow us to fit for the correlation between the CLs values and the yields calculated both at the truth and at the reconstructed level. This correlation in SR2jt is shown in the Figure 6.13. A larger spread is seen when comparing the CLs values and the yields calculated at the truth level (Figure 6.13, right), nevertheless the correlation is still good enough to let us determine the CLs values based on the truth yields. The expected and the observed CLs values are fitted with one-sided Gaussian function, and the fit does describe well the correlation. This allows the

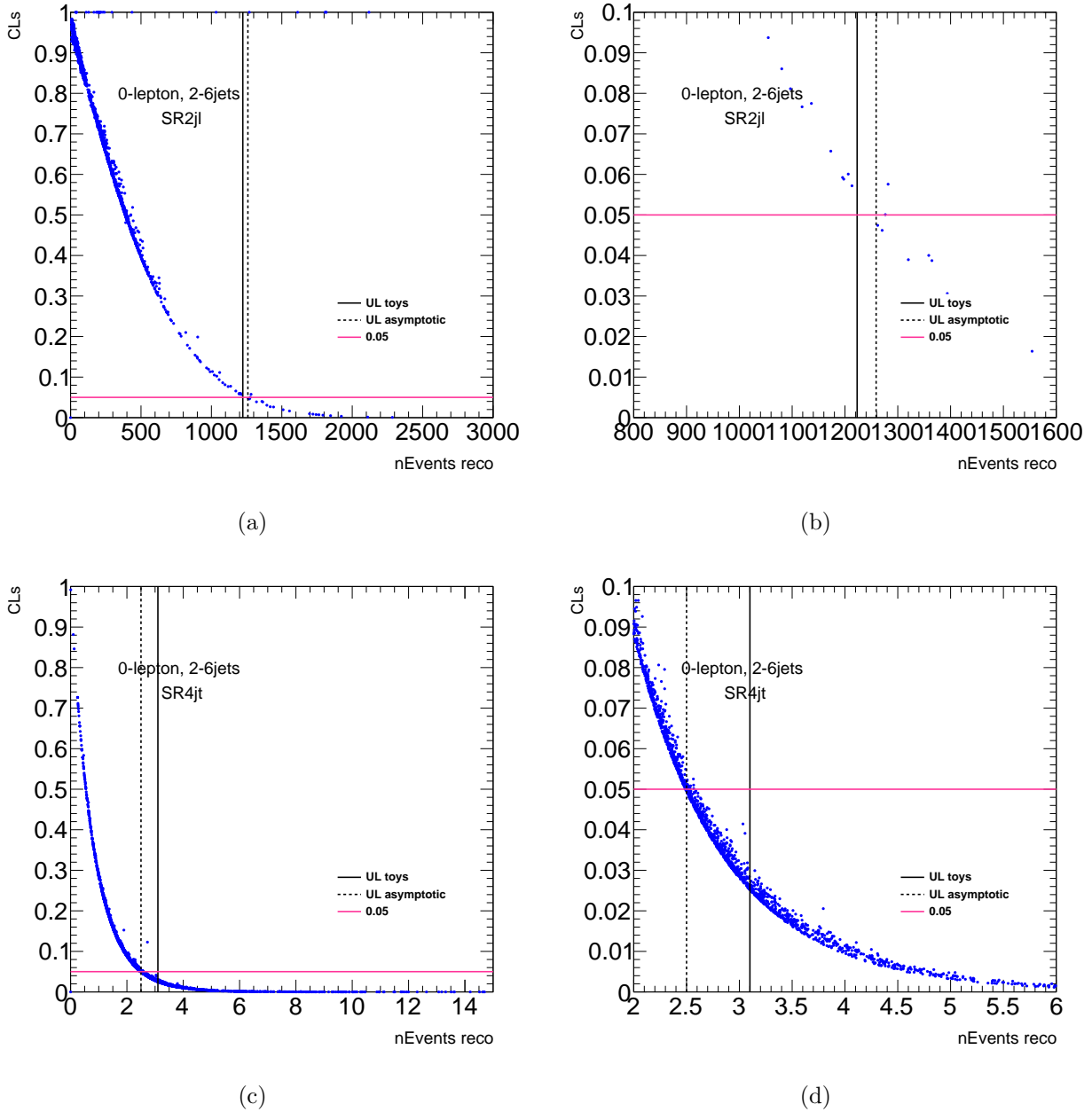


Figure 6.10: The CLs values calculated without the uncertainties on the signal as a function of the expected yields calculated at the reconstructed level. The plots on the right are just the enlarged interesting part of the plots of the left. The full line corresponds the UL calculated using the MC pseudo experiments, while the dotted line corresponds to the UL calculated using the asymptotic formula.

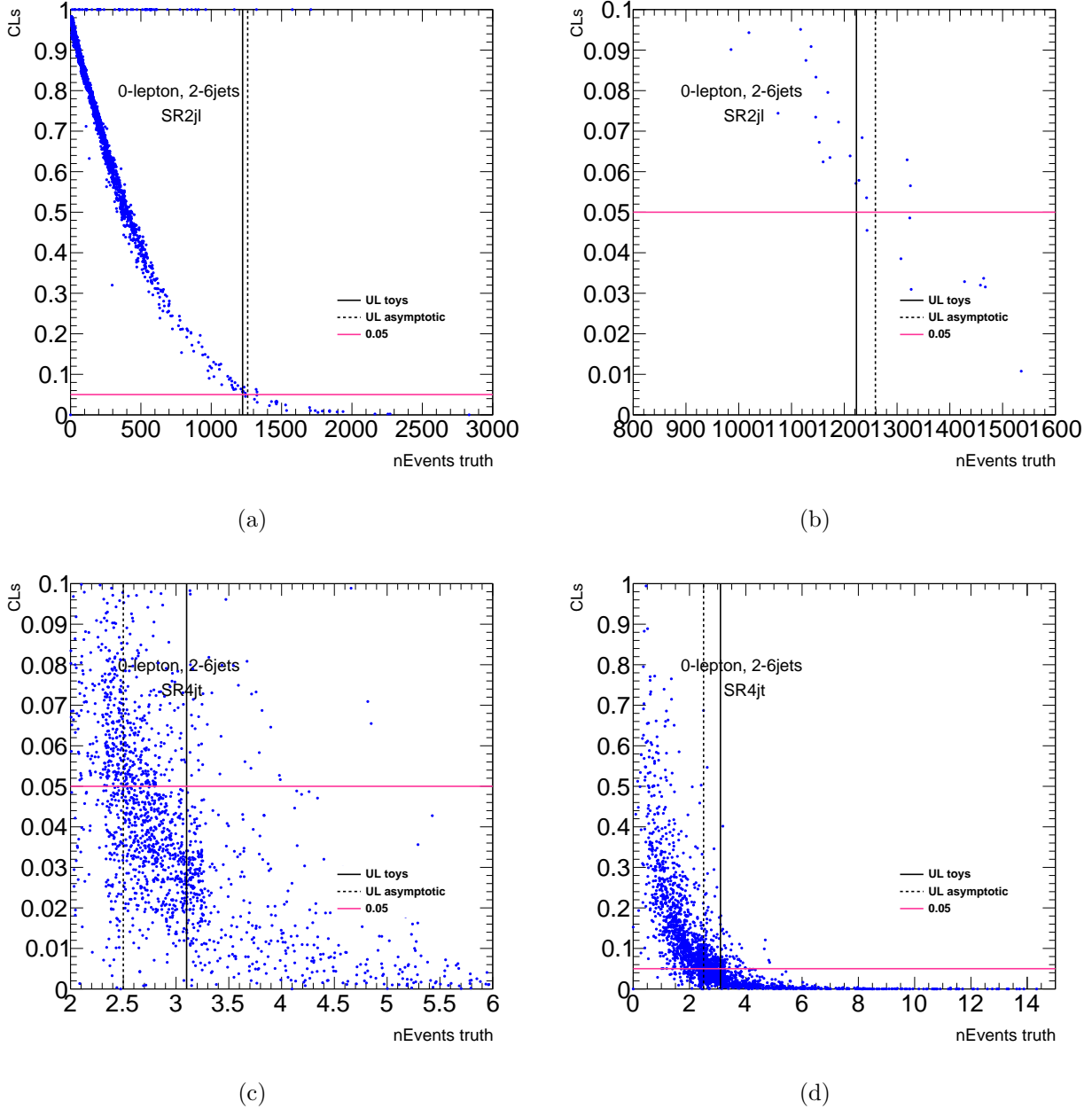


Figure 6.11: The CLs values with all the uncertainties on the signal as a function of the expected yields estimated at the truth level for SR2jl and SR4jt. The plots on the right are just the enlarged interesting part of the plots of the lefthand side. The full line corresponds to the UL calculated using the MC pseudo experiments, while the dotted line corresponds to the UL calculated using the asymptotic formula.

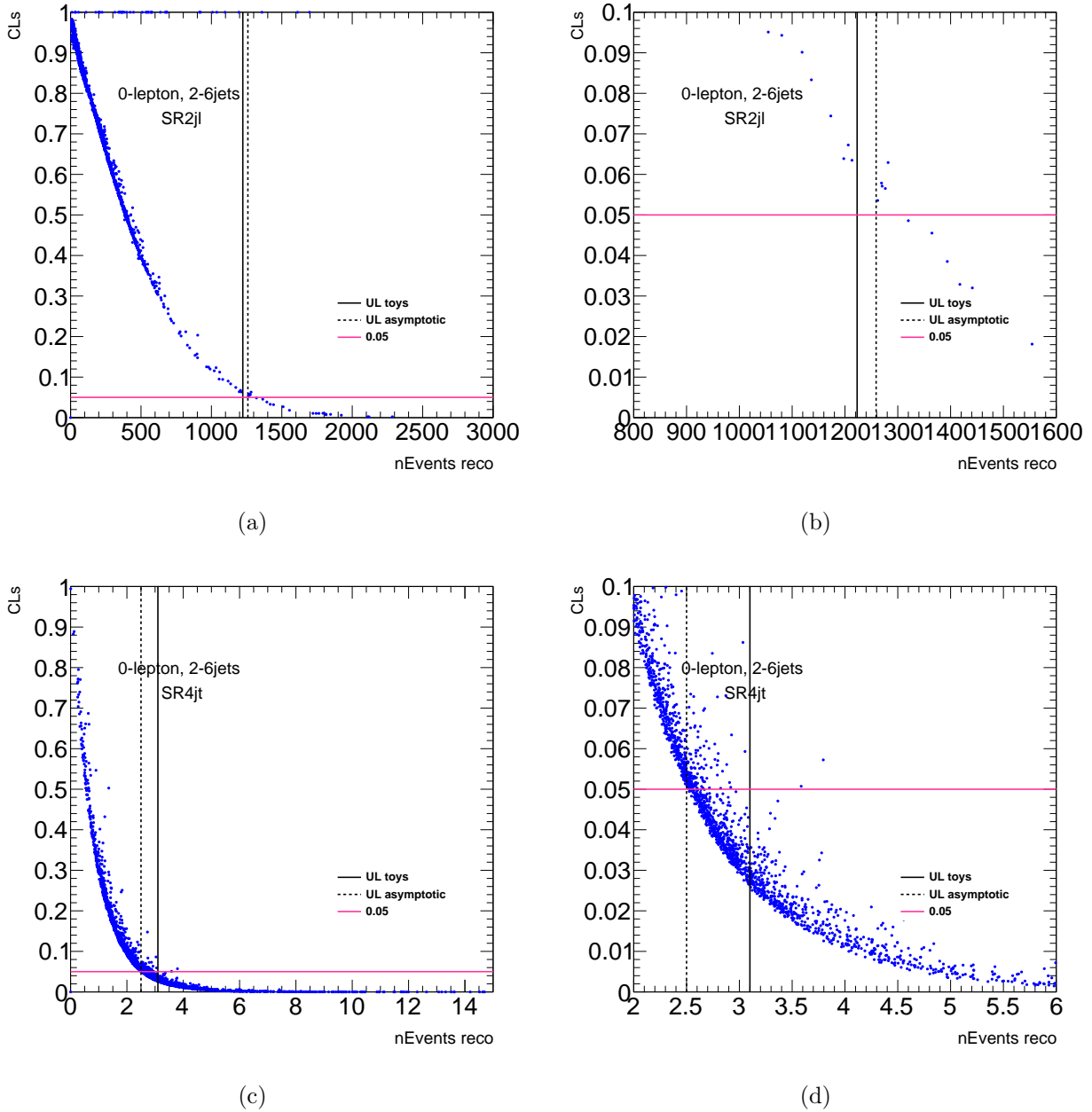


Figure 6.12: The CLs values calculated with all the uncertainties on the signal as a function of the expected yields calculated at the reconstructed level. The plots on the right are just the enlarged interesting part of the plots of the left. The full line corresponds the UL calculated using the MC pseudo experiments, while the dotted line corresponds to the UL calculated using the asymptotic formula.

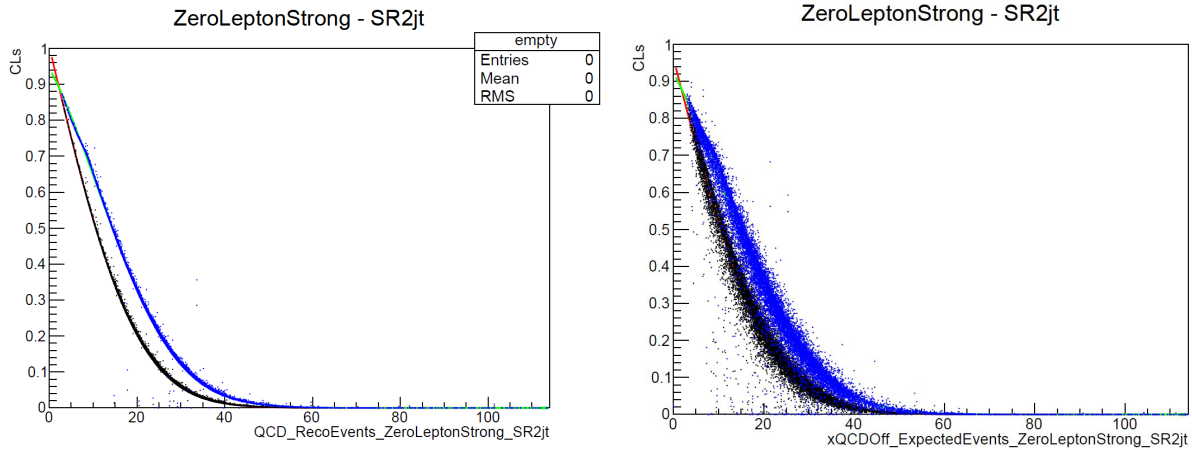


Figure 6.13: The CLs values calculated at the reconstructed level as a function of the yields calculated at the reconstructed (left), and at the truth level (right). Expected CLs values are shown in black, while observed values are shown in blue. Fitted one-sided Gaussian is shown in red for expected CLs, and in green for the observed CLs.

prediction of the CLs value for all the pMSSM model points only on the basis of the information at the truth level.

After all these considerations it is decided that for the 0-lepton analysis the described fit and the yields calculated at the truth level can be used to predict the CLs values.

6.3 Categorisation of pMSSM model points for the 0-lepton analysis

In this Section, first a short summary of the exclusion procedure is presented just as a reminder. Then the results of this classification are discussed.

6.3.1 Exclusion procedure

The exclusion of the pMSSM model points proceeds as follows:

- the yields are calculated using the analysis at the truth level
- they are subsequently used to determine a preliminary categorisation of the pMSSM model points based on the r_1^{pMSSM} and r_3^{pMSSM} values
- for the model points that are possibly excluded (Cat. 2) the full reconstruction is performed and the full analysis is run to determine the CLs values
- finally the pMSSM model points are deemed excluded or not excluded based on the CLs values calculated using reconstructed model points when available, and on the truth based CLs otherwise estimate

6.3.2 Results of the categorisation

The derivation of r_1^{pMSSM} and r_3^{pMSSM} values leads to the categorisation of the pMSSM model points presented in Table 6.2 for the strong production. Each row corresponds to one of the ATLAS searches, except that there are two rows that correspond to the 0-lepton analysis: one marked 0-lepton and a special one for the model points with low acceptances. As expected the highest number of model points is in the Cat. 2 and 3 for the 0-lepton analysis. From here one

can already see that it is the most constraining analysis for the strong production. It is also important to note the number of model points in the Cat. 2, as those are the ones that are to be reconstructed and further analysed. Thus it is essential to keep this number in manageable limits of the resource and time consumption, which was the goal of the studies presented in this Chapter.

Although it is not designed for the mix production, the 0-lepton analysis gives additional constraints in that case, as can be seen in Table 6.3. Only few model points that are marked as Cat. 2 for the mix production are really reconstructed as most of them are excluded through strong production at the truth level. A similar table for the electroweak production is not shown, as the 0-lepton analysis is not effective in that case.

Not all the model points that are in Cat. 2 of one analysis are reconstructed, as they can be also in Cat. 3 of some other analysis. In Table 6.4 the number of the reconstructed model points and events is presented for each analysis. The 0-lepton analysis shows sensitivity to more than 60% of them (20,000 model points) for a total of more than 350,000 events. They are passed through the `ZeroLeptonFactory` code for the calculation of the yields at the reconstructed level, and also the CLs values are calculated using `ZeroLeptonFitter`. This number of model points processed by the 0-lepton analysis is several order of magnitude higher compared to the nearest analysis by the number of model points. The effect of this will be made apparent in the next Chapter when the comparison between the exclusion reaches of the analyses is performed.

Analysis	Bino LSP			Wino LSP			Higgsino LSP		
	Cat.1	Cat.2	Cat.3	Cat.1	Cat.2	Cat.3	Cat.1	Cat.2	Cat.3
0-lepton	24250	7019	34773	27466	5726	22884	43599	10103	39915
0-lepton(low acc.)	35538	758	1863	23604	330	229	32202	638	312
0 ℓ , 7-10 jets	97693	2569	3939	73226	2602	4411	115308	3779	7682
1 ℓ , 2-6 jets	97928	4320	1953	72444	5924	1871	114314	7887	4568
1-2 τ , jets	101649	2332	220	76056	3638	545	120101	5981	687
2 ℓ SS/3 ℓ	102347	1231	623	78286	1626	327	123457	2287	1025
3 b -jet	95040	5127	4034	71085	4883	4271	109511	6728	10530
Exotics mono-jet	70789	18782	14630	64303	10831	5105	97935	19874	8960
0 ℓ , stop	91801	9401	2999	70824	6528	2887	109560	10719	6490
1 ℓ , stop	100104	2331	1766	74426	3295	2518	115646	4910	6213
2 ℓ , stop	103190	656	355	79541	432	266	126176	462	131
Monojet stop	83989	9902	10310	74180	4372	1687	115578	7680	3511
Stop with Z boson	102999	395	807	79883	170	186	125782	535	452
Two b -jet	98992	2525	2684	77596	1268	1375	120387	2561	3821
tb+MET,stop	100658	2659	884	75851	3241	1147	117350	6039	3380
ℓh , electroweak	18945	33	0	20674	56	0	29936	24	0
2 ℓ , electroweak	104008	109	84	80151	61	27	126716	43	10
2 τ , electroweak	103934	267	0	80084	155	0	126646	123	0
3 ℓ , electroweak	103658	220	323	79631	302	306	126204	283	282
4 ℓ	102805	868	528	79621	315	303	125824	542	403
Disappearing Track	104063	0	138	68461	0	11778	126722	0	47
Overall	23952	10064	36862	27098	8576	24992	42509	14057	41726
Overall (low acc.)	32984	326	13	19380	186	7	28010	440	27

Table 6.2: Categorisation of pMSSM model points for each analysis based on truth-level evaluation of strong production.

Analysis	Bino LSP			Wino LSP			Higgsino LSP		
	Cat.1	Cat.2	Cat.3	Cat.1	Cat.2	Cat.3	Cat.1	Cat.2	Cat.3
0-lepton	49354	247	127	46439	1366	1507	109121	67	20
0-lepton(low acc.)	54442	18	13	30866	27	34	17556	5	0
0 ℓ , 7-10 jets	104200	1	0	80238	1	0	126764	4	1
1 ℓ , 2-6 jets	104168	33	0	80220	18	1	126751	18	0
1-2 τ , jets	104179	22	0	80232	7	0	126756	12	1
2 ℓ SS/3 ℓ	104183	18	0	80228	11	0	126765	4	0
3 b -jet	104194	7	0	80238	1	0	126748	20	1
Exotics mono-jet	103746	447	8	76570	3348	321	126764	5	0
0 ℓ , stop	104184	17	0	80150	88	1	126750	19	0
1 ℓ , stop	104195	6	0	80238	1	0	126765	4	0
2 ℓ , stop	104193	6	2	80233	3	3	126764	5	0
Monojet stop	104153	46	2	79326	879	34	126769	0	0
Two b -jet	104189	6	6	80153	59	27	126769	0	0
tb+MET,stop	104198	3	0	80214	24	1	126768	1	0
ℓh , electroweak	49373	0	0	46629	0	0	109314	0	0
2 ℓ , electroweak	104186	13	2	80235	3	1	126766	3	0
2 τ , electroweak	104199	2	0	80237	2	0	126768	1	0
3 ℓ , electroweak	104185	6	10	80220	14	5	126765	2	2
4 ℓ	104169	26	6	80166	46	27	126717	38	14
Disappearing Track	104125	0	76	74939	0	5300	126769	0	0
Overall	49354	489	221	46439	382	5382	109121	155	35
Overall (low acc.)	54133	4	0	28035	1	0	17454	4	0

Table 6.3: Categorisation of pMSSM model points for each analysis based on truth-level evaluation of the mix production.

6.4 Conclusion

In this Chapter the characteristics of the 0-lepton analysis implementation for the pMSSM interpretation are presented. First a preliminary categorisation of model points is performed based on simplified models studies, that is later revisited using the reconstructed pMSSM model points. Finally the criteria are determined for the classification of the pMSSM model points. Several ways are explored to reach a reliable exclusion of the model points based on the comparison between CLs values and the yields calculated at the truth and at the reconstructed level. As a result of this complete analysis, one can have full confidence in the constraints imposed by the 0-lepton analysis in the pMSSM parameter space that are presented in the next Chapter.

Analysis	Cat.2		Cat.3		All	
	Models	Events	Models	Events	Models	Events
0-lepton	17519	243400k	2286	50360k	19805	293760k
0-lepton(low acc.)	1172	31580k	350	24035k	1522	55615k
0 ℓ , 7-10 jets	112	780k	129	1260k	241	2040k
1 ℓ , 2-6 jets	527	5020k	144	2965k	671	7985k
1-2 τ , jets	207	1890k	23	240k	230	2130k
2 ℓ SS/3 ℓ	125	1365k	31	475k	156	1840k
3 b -jet	4530	34765k	394	6415k	4924	41180k
Exotics mono-jet	1880	53995k	0	0k	1880	53995k
0 ℓ , stop	4909	67665k	427	10980k	5336	78645k
1 ℓ , stop	770	13190k	196	3030k	966	16220k
2 ℓ , stop	39	645k	72	785k	111	1430k
Monojet stop	674	63170k	534	21430k	1208	84600k
Stop with Z boson	36	730k	13	225k	49	955k
Two b -jet	1418	29810k	95	4850k	1513	34660k
tb+MET,stop	77	855k	0	0k	77	855k
ℓh , electroweak	91	1485k	0	0k	91	1485k
2 ℓ , electroweak	5432	63025k	178	2110k	5610	65135k
2 τ , electroweak	324	3090k	2	15k	326	3105k
3 ℓ , electroweak	1182	22680k	81	1545k	1263	24225k
4 ℓ	1018	13035k	75	1245k	1093	14280k
Total	32028	419235k	2856	77110k	34884	496345k

Table 6.4: Number of the reconstructed pMSSM model points and events. The total number of model points is less than the sum as a model point can be marked for simulation by more than one analysis and in more than one category.

Chapter 7

pMSSM interpretation

Since the truth code and the exclusion strategy have been proved to be reliable in the previous Chapter, they are used to derive limits within the pMSSM model presented in this Chapter. As explained in Section 5.4 22 analyses are considered for the pMSSM interpretation, and all of them are expected to contribute to the final results. In this Chapter the results for the strongly produced sparticles ($\tilde{g}, \tilde{q}, \dots$) are presented, as these are targeted by the 0-lepton analysis. The results of the pMSSM analysis are also interpreted as limits on sleptons, third generation squarks and electroweakinos, but they are not shown here. After assessing the impact of all the searches, the focus is put on the individual exclusion obtained by the 0-lepton analysis.

First the exclusion in the sparticles mass planes are shown - this is a usual way of presenting the results as they are the primary quantities to be observed and measured. This also enables a comparison with the limits set on the sparticle masses in simplified models. Later the exclusion in the parameters planes are explored - those are important as they tell us the limits on a more fundamental level.

In this study several approaches towards the presentation of the results as 2D maps of the parameter of interest are pursued: the fraction of excluded model points, the maximal and the minimal values of CLs. These methods are complementary as each of them contains different informations, and they also answer distinct questions. With maximal CLs values one identifies the parts of the plane that are excluded, while with the minimal CLs value, the less excluded values of the parameters are determined.

First the results of all ATLAS searches are presented in Section 7.1, interpreted in the sparticle mass planes and the complementarity of the searches is explored. In Section 7.2 the emphasis is put on the 0-lepton analysis, with the exclusion reach obtained using only this analysis, and also showing the contribution of each of its signal regions. Up to this point, all the results are interpreted in the sparticles masses planes, and in Section 7.3, the focus is shifted to the exclusion as a function of the pMSSM parameters. In Section 7.4 the attention is put on the dark matter. The impact of ATLAS searches is explored. Two hypothesis on the relic density components are considered: when other dark matter candidate can contribute, and when the neutralino by itself saturates dark matter relic density.

7.1 ATLAS SUSY limits

This Section details the results of the interpretation of all the ATLAS searches considered in this study (Table 5.5). The results are shown as the fraction of excluded model points (number of model points excluded divided by the number of model points that survive the pre-LHC constraints in each bin). The exclusions are the results of the combination of the choice of the parameter ranges (Table 5.1), the indirect constraints (Table 5.2) and the ATLAS searches (Table 5.5). The effects of the LSP composition are also explored. The limits are set and

discussed in the sparticles mass planes, as this is the most intuitive way of assessing the results. Different searches are designed for different final states and production modes, so they are expected to be complementary and this is also explored in this Section.

The results of this Section are published in Ref. [3], although sometimes the plots presented in this thesis need to have different ranges (to enable an easier comparison with the plots for the 0-lepton analysis shown later in Section 7.2).

7.1.1 ATLAS searches exclusion

In Table 7.1 the fraction of model points excluded by each individual analysis is shown for each LSP type. It is similar to Table 6.2 but now all production modes are included, and the results presented here are obtained taking into account both the truth and the reconstructed level analysis. This table should be treated with care as the fraction of excluded model points strongly depends on the scan of the parameter space. Still, the 0-lepton analysis excludes the highest fraction of generated model points, more than 30%.

The exclusion of some analyses depends strongly on the LSP type. For example, the Disappearing Track analysis excludes a very high fraction of model points when the LSP is wino-like (almost 30%). For those model points the chargino is the NLSP and the mass difference with the LSP can be very small. Since this analysis searches for long-lived charginos, it perfectly targets the corresponding model points.

Another example is the search for monojet like signatures - both inclusive and stop - that are more effective for the model points when the LSP is bino-like. Those model points have a small mass splitting between the LSP and the NLSP, thus producing soft decay products almost impossible to observe. One possible way to capture them is by requiring a single hard jet that is coming from ISR. These searches are designed with loose E_T^{miss} requirements.

Analysis	Combined	Bino	Wino	Higgsino
0-lepton	32.1%	35.8%	29.7%	33.5%
0-lepton + 7–10 jets + E_T^{miss}	7.8%	5.5%	7.6%	8.0%
0/1-lepton + 3 b -jets + E_T^{miss}	8.8%	5.4%	7.1%	10.1%
1-lepton + jets + E_T^{miss}	8.0%	5.4%	7.5%	8.4%
Monojet	9.9%	16.7%	9.1%	10.1%
SS/3-leptons + jets + E_T^{miss}	2.4%	1.6%	2.4%	2.5%
Taus + jets + E_T^{miss}	3.0%	1.3%	2.9%	3.1%
0-lepton stop	9.4%	7.8%	8.2%	10.2%
1-lepton stop	6.2%	2.9%	5.4%	6.8%
2 b -jets + E_T^{miss}	3.1%	3.3%	2.3%	3.6%
2-leptons stop	0.8%	1.1%	0.8%	0.7%
Monojet stop	3.5%	11.3%	2.8%	3.6%
Stop with Z boson	0.4%	1.0%	0.4%	0.5%
$tb + E_T^{\text{miss}}$, stop	4.2%	1.9%	3.1%	5.0%
ℓh , electroweak	0	0	0	0
2-leptons, electroweak	1.3%	2.2%	0.7%	1.6%
2-taus, electroweak	0.2%	0.3%	0.2%	0.2%
3-leptons, electroweak	0.8%	3.8%	1.1%	0.6%
4-leptons	0.5%	1.1%	0.6%	0.5%
Disappearing Track	11.4%	0.4%	29.9%	0.1%
Long-lived particles	0.1%	0.1%	0.0%	0.1%
$H/A \rightarrow \tau^+ \tau^-$	1.8%	2.2%	0.9%	2.4%
Total	40.9%	40.2%	45.4%	38.1%

Table 7.1: Fraction of model points excluded by each individual analysis based on the best expected analysis.

7.1.2 Sparticle masses

The results of the pMSSM analysis in this Section are presented as 2D mass plots where the fraction of excluded model points in each bin is shown on the z-axis. There is no requirement on the minimal number of model points in each bin. The comparison with respect to the simplified model is difficult to assess since the limits are not comparable (the simplified model limit is derived from one search results, while the pMSSM model points are excluded taking into account 22 searches). This point is discussed in Section 7.2.

7.1.2.1 Gluino - neutralino mass plane

In Figure 7.1 the fraction of excluded model points is shown in the \tilde{g} - $\tilde{\chi}_1^0$ mass plane, for all LSP types (7.1a), and when the LSP is bino (7.1b), wino (7.1c) and higgsino-like (7.1d). The white bins for neutralino masses below ~ 100 GeV when the LSP is wino or higgsino-like, come from the lower values of the M_2 and μ parameters considered in the scan (70 and 80 GeV, respectively). The exclusion is evaluated taking into account all ATLAS searches. The simplified model limit overlaid comes from the 0-lepton analysis, that assumes \tilde{g} pair production followed by the direct decay to a pair of quarks and a $\tilde{\chi}_1^0$ (Section 3.4.3.3). Near the diagonal, model points are excluded by the Monojet analysis. In this region where there is a small mass splitting between \tilde{g} and $\tilde{\chi}_1^0$, the 0-lepton analysis is not very performant as the minimal number of jets it requires is two. In the plot where the LSP is wino-like, there is a strip of excluded model point when $m(\tilde{\chi}_1^0)$ is below 200 GeV extending to large gluino masses, that is not present for other LSP types, and the exclusion in this region comes from the Disappearing Track analysis.

This search is effective when the mass splitting between the chargino and the $\tilde{\chi}_1^0$ is of the order of 200 MeV. The disagreement between the exclusion in pMSSM framework and in the simplified model present for small neutralino masses and gluino masses between 1200 and 1400 GeV, comes from the downward fluctuation in data in SR4jt which is the best expected SR in that part of the mass plane for the simplified model, while in the pMSSM a vast majority of the model points in that region have SR6jvt as the best expected SR.

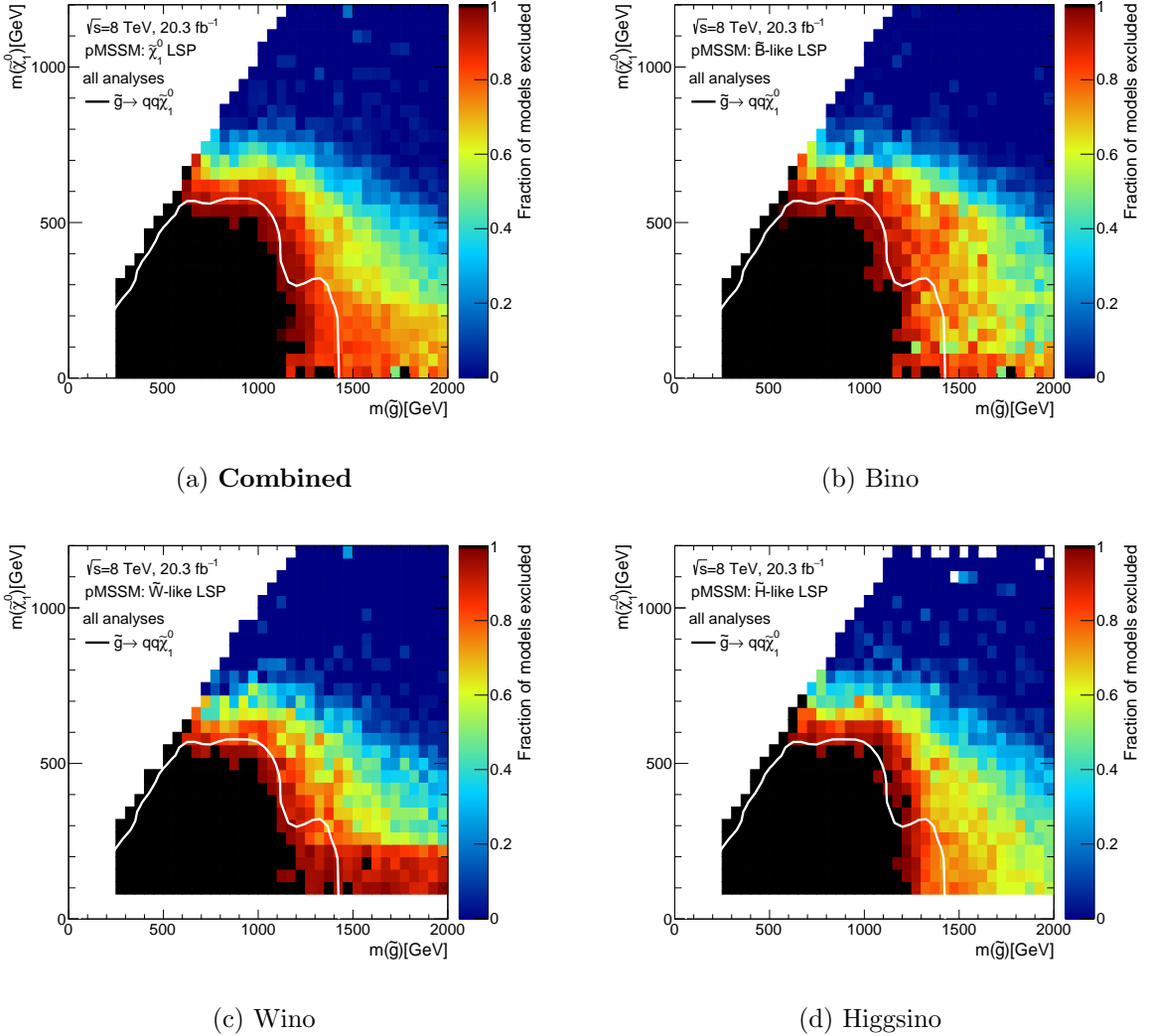


Figure 7.1: Fraction of pMSSM model points excluded in the $\tilde{g}-\tilde{\chi}_1^0$ mass plane by taking into account all the ATLAS searches. The full model set is presented in (a), while the model points when the LSP is bino (b), wino (c) and higgsino-like (d) are shown also separately. The colour code indicates the fraction of model points excluded in each mass bin. The solid white line is the observed simplified model limit from the 0-lepton search [134] at 95% CLs, which assumes direct production of gluino pairs and decoupled squarks, with gluino decaying to quarks and a neutralino, $\tilde{g} \rightarrow q\bar{q}\tilde{\chi}_1^0$.

7.1.2.2 Lightest squark - gluino mass plane

In Figure 7.2 the exclusion in the lightest 1st/2nd generation $\tilde{q}-\tilde{g}$ mass plane is shown. All the LSP types are treated separately and also combined. The simplified model limit overlaid is derived by the 0-lepton analysis and assumes strong associated production of gluinos and degenerate first- and second-generation squarks, with direct decays to quarks and massless neutralinos. Constraints on the \tilde{q} masses weaken as the \tilde{g} mass increases due to the suppression

both of the direct squark-pair production via a t -channel gluino exchange and of associated squark-gluino production. There is a difference in the observed exclusion depending on the LSP type - notably when the LSP is bino-like the model points need to have a small mass difference between the squark and the LSP in order to satisfy the dark matter relic density (as can be seen in Figure 5.2). This small mass difference leads to compressed mass spectra, thus those model points are difficult to observe.

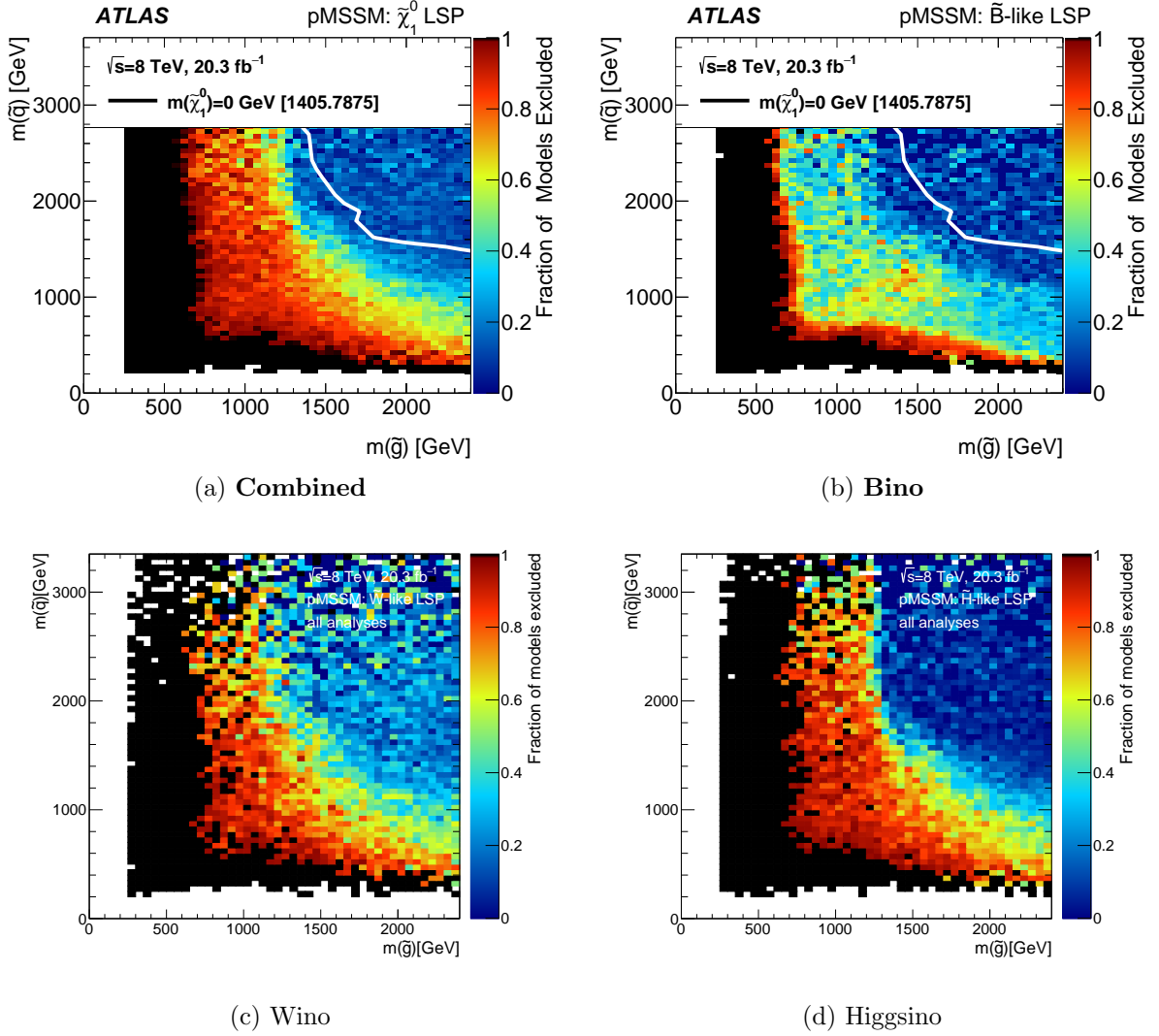


Figure 7.2: Fraction of the model points excluded in the \tilde{g} - \tilde{q} mass plane by taking into account all the ATLAS searches. The simplified model limit is from [134] which assumes strong associated production of gluinos and degenerate first- and second-generation squarks, with direct decays to quarks and massless neutralinos.

7.1.2.3 Lightest squark - neutralino mass planes

In Figure 7.3 the pMSSM space is projected onto the lightest 1st/2nd generation squark - neutralino mass plane. There is a good sensitivity for low squark masses. Both simplified model limits overlaid are from the 0-lepton analysis and the solid line assumes that all eight squarks are degenerate, while the dashed line corresponds to the case where the two squarks are degenerate (this is achieved by dividing the production cross-section by four), as explained in Chapter 3. The highest fraction of model points is excluded for the model points where the LSP is bino-like. One can see that the higher fraction of model points excluded for the

neutralino masses less than 200 GeV for all the squark masses, comes from the model points where the LSP is wino-like. This is not the effect of the searches that are looking for squark decay products, but it is the consequence of the exclusion by the Disappearing Track analysis, as explained before.

When comparing the exclusion with the limits set within the simplified models, one can observe that a better correspondence is obtained with the simplified model that assumes only two degenerate squarks. This is simply a consequence of the fact that the pMSSM does not make any assumption on the equality between squarks masses.

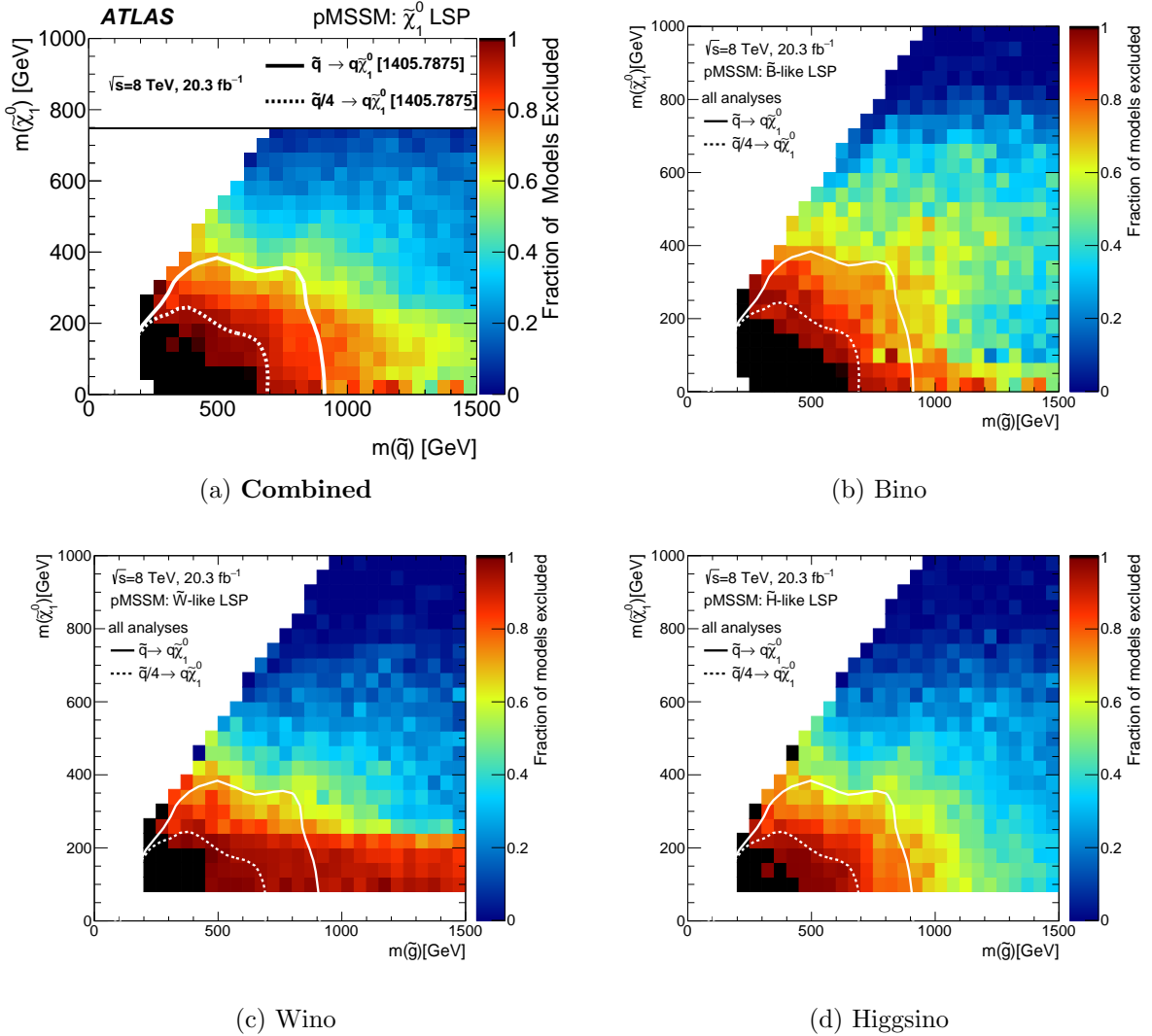


Figure 7.3: The fraction of the model points excluded in the $\tilde{q}\tilde{\chi}_1^0$ mass plane by taking into account all the ATLAS searches. The simplified model limit has been taken from Ref. [134] and is made under the assumption of directly produced first/second generation squark pairs, with squarks decaying to a squark and a neutralino, $\tilde{q} \rightarrow q\tilde{\chi}_1^0$. The solid line corresponds to the case where all eight squarks have been assumed to be degenerate whereas the dashed line assumes there are four non-degenerate squarks.

In Figure 7.4 the exclusion of the model points is explored depending on the squark nature. First one should recall that the production of down squarks is suppressed compared to the production of the up squarks, as in the proton there are less valence down quarks. This does not affect much the exclusion contours. Other more important effect comes from the fact that squarks can be left or right. The left squarks (up and down) are degenerate in mass up

to electroweak symmetry breaking effects. That means that their production cross-section is effectively doubled, resulting in the apparent increase in the search sensitivity. Thus when the limits are projected on the mass planes of the left squarks and neutralinos, they show a higher fraction of excluded model points. One more effect enhances the sensitivity to the left squarks compared to the right squarks: right squarks do not have weak couplings, and also have small Yukawa couplings, which means that the decays to wino- and higgsino-like LSPs are suppressed. They instead generally cascade decay to final states with small E_T^{miss} and high number of decay products but which have low p_T .

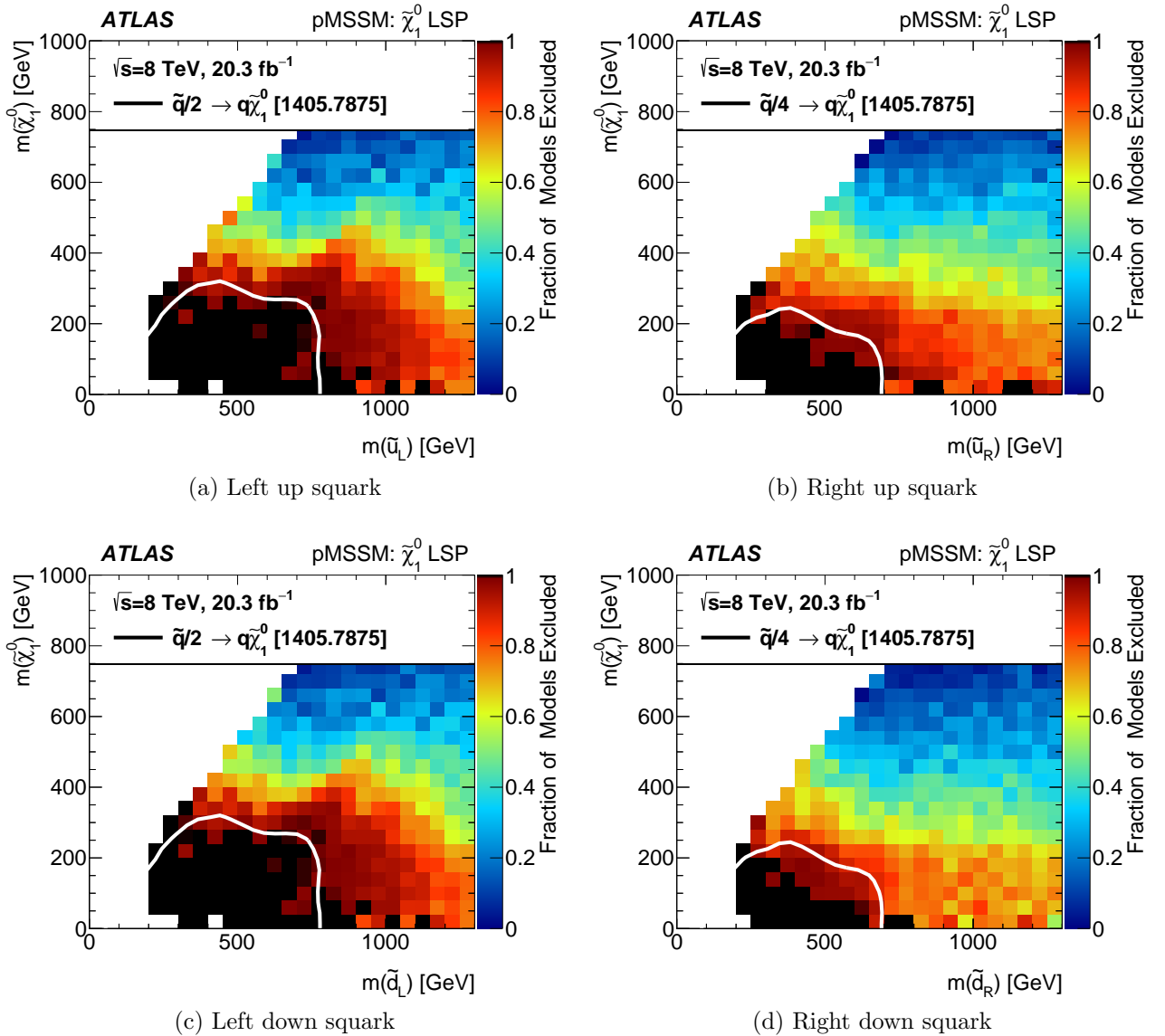


Figure 7.4: Fraction of the pMSSM model points excluded in the planes of the masses of the left-handed and right-handed squarks (of the first two generations) versus the neutralino mass. Both simplified-model limit contours are taken from the 0-lepton analysis (Figure 10(c) of Ref. [134]); however, for the left (right) handed squarks the assumption of four (two) degenerate squarks is emulated by dividing the cross-section for production of the eight degenerate squark states by a factor of two (four).

7.2 0-lepton limits

As shown in the last Section, the 0-lepton analysis excludes the largest fraction of pMSSM model points, thus it is interesting to look at the exclusion made by this analysis alone. In that way one identifies the strong and weak points of the SR selection, by studying the parts of the plane that are covered (or missed). Also analysing the exclusions set by the individual SRs, should enable one to better optimise this search in the future.

The 0-lepton analysis exclusion is fully based on the CLs values, thus it is statistically better founded. The exclusion performed for other analyses, at least partly, rely on the exclusion based on the best observed ULs. Therefore it is possible to consider also the maximal CLs value found for all the model points belonging to each bin in the various mass and parameters planes. The region where the maximal CLs is below 0.05 (the darkest blue bin of the plot directly gives the exclusion limit) is excluded for any value of the other parameters. This gives the same information as the fraction of excluded model points, but it is the only way to have a statistically well defined exclusion reach since one can rely on CLs values estimated for each pMSSM model point. This is also the only way one can make a proper comparison between the exclusion of the pMSSM model points and that of the simplified models, for the strong production at least.

7.2.1 Sparticle masses

First the obtained exclusions will be presented for part of the sparticle mass planes shown in the previous Section. In the previous Section, the exclusion obtained with all the searches is compared with the limits derived with the simplified models assumptions. However, the simplified model limits are derived in the context of the 0-lepton search, so a fair comparison is explored in this Section, as they are compared only with the pMSSM model points excluded with this search alone.

7.2.1.1 Gluino - neutralino mass plane

In Figure 7.6 the exclusion reach of the 0-lepton analysis is shown for the full model set in the gluino - neutralino mass plane. Two different statistical treatments are shown: in 7.6a the fraction of excluded model points in each bin is on the Z-axis, while in 7.6b the maximal CLs value (CL_s^{max}) of all models are used.

The limits obtained with the fraction of excluded models (Fig. 7.6a) are very similar to those achieved when using all the ATLAS searches. The decisive effect of this analysis is clear. The 0-lepton search (and also other analyses) are capable of excluding model points across the whole range of gluino mass - up to 4 TeV. This is clearly not coming from the sensitivity of the searches to such high mass gluinos, instead they are excluded because of the other sparticles with lower masses.

The CL_s^{max} figure can be read as follows: the darker blue bins are those for which all the model points are excluded at 95%CL or more. The corresponding area is exactly the same as the 100% bin of the fraction of excluded model plot, which is difficult to pin-point due to the Z-axis scale that has been smoothed. To assess the exclusion reach with a statistically well defined criterium, one therefore needs Fig. 7.6b, which has been added (as well as the same plane for each LSP type) in the auxiliary material of Ref. [3]. In this Figure, one can observe that there remains non excluded model points with maximal CLs values > 0.05 even for gluino masses around 700 GeV. Those are coming from the model points when the LSP is wino-like. They have many leptons in the final state.

In addition, Fig. 7.6b allows for a full comparison of the limits obtained within the pMSSM and the simplified models for two reasons: first, they are based on the same statistical tools,

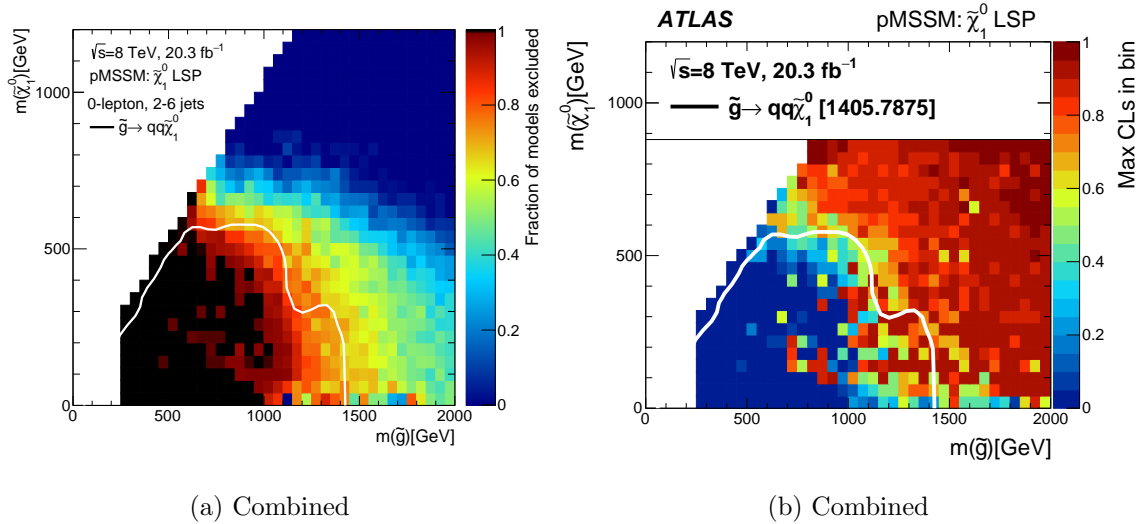


Figure 7.6: Figure (a): Fraction of pMSSM model points excluded in the $\tilde{g}-\tilde{\chi}_1^0$ mass plane considering only 0-lepton analysis. Figure (b): The maximal value of the CLs in each bin for the $\tilde{g}-\tilde{\chi}_1^0$ mass plane considering only 0-lepton analysis. The solid white line is the observed simplified model limit from the 0-lepton search [134] at 95% CLs, which assumes direct production of gluino pairs and decoupled squarks, with the gluino decaying to quarks and a neutralino, $\tilde{g} \rightarrow q\bar{q}\tilde{\chi}_1^0$.

second they have been made for the same (0-lepton) analysis. This is the first time a full comparison of this kind has been performed within the ATLAS collaboration. As expected, the simplified model limits overestimate the exclusion power. Even if the simplified models are very easy to study and therefore convenient for quick interpretations, deciding a definite limit on the sparticle masses based on their study would probably require to combine the results of several of them with a relative weight in order to fake a "pMSSM like" final states composition.

7.2.1.2 Squark - neutralino mass plane

In Figure 7.7 the exclusion reach is shown in the mass plane of the lightest 1st/2nd generation squark - neutralino, in 7.7a for all LSP types, in 7.7b when the LSP is bino-like, in 7.7c wino-like and in 7.7d it is higgsino-like. When the LSP is bino-like, around 100 GeV, one can see the effect of Z and SM-like Higgs funnels. The first comment is that, as for the previous Section, this plot is very close to the full ATLAS analysis one, although the exclusion by the all ATLAS searches adds sensitivity for neutralino masses below 200 GeV, coming from the Disappearing Track analysis when the LSP is wino-like. Still, there are some interesting features that show up when looking at the different LSP types, that cannot be identified by only considering the exclusion for the full model set. For example in the 7.7b one can observe the strip for neutralino masses between 200 and 600 GeV, independent of the lightest squark mass. The limits on the both squark and neutralino masses are weakest when the LSP is wino-like.

7.2.2 0-lepton signal regions

In Figure 7.8 the limits are given in the $\tilde{g}-\tilde{\chi}_1^0$ mass plane for all the SRs of the 0-lepton analysis. This is interesting as it allows for a comparison of the effectiveness of all SRs in different parts of the plane. In Figures 7.8a, 7.8e, 7.8f, 7.8j the 'loose' selections are applied, and in that case quite low \tilde{g} masses are excluded. For regions with 'tight' selections (Figures 7.8c 7.8c 7.8d 7.8i 7.8l 7.8m) the excluded \tilde{g} masses are pushed to higher values. Re-

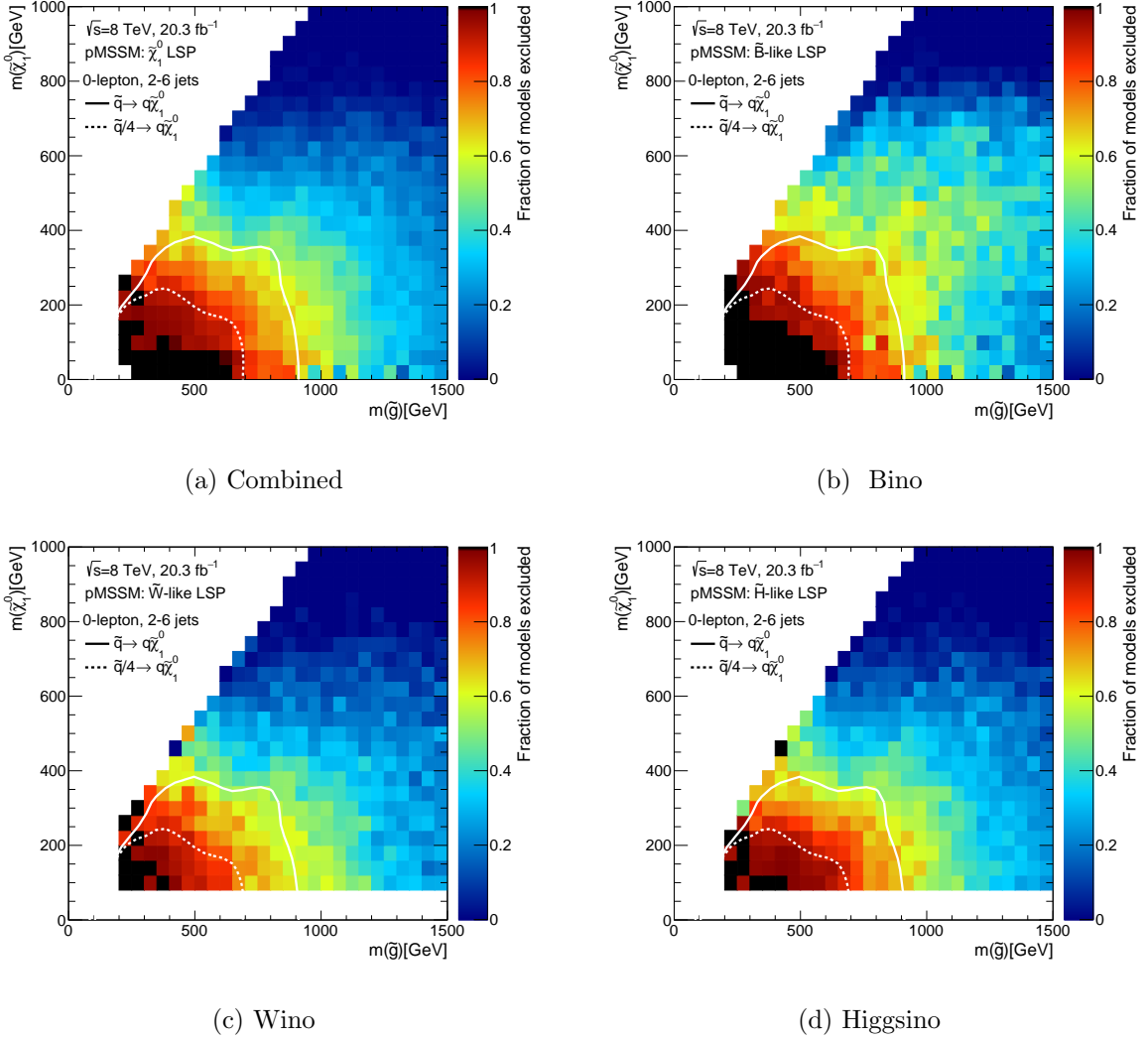


Figure 7.7: Fraction of pMSSM model points excluded in the lightest 1st/2nd \tilde{q} - $\tilde{\chi}_1^0$ mass plane considering only the 0-lepton analysis: in 7.7a for all LSP types, in 7.7b when the LSP is bino-like, in 7.7c wino-like and in 7.7d it is higgsino-like. The solid white line is the observed simplified model limit from the 0-lepton search [134] at 95% CLs, which assumes direct production of gluino pairs and decoupled squarks, with the gluino decaying to quarks and a neutralino, $\tilde{g} \rightarrow q\bar{q}\tilde{\chi}_1^0$.

regardless of the tightness of selection, there is no change in the excluded $\tilde{\chi}_1^0$ masses, except maybe for SR2jm (7.8b) and SR4jm (7.8g) that are effective for a bit higher $\tilde{\chi}_1^0$ masses, up to 700-800 GeV. There are just two SRs that show useful for excluding the model points with compressed spectra, and as expected those are the SRs that require a small number of jets (in the 0-lepton analysis the minimum is two jets). When pair of \tilde{g} are produced, they decay to final states with a minimum of four jets, thus the exclusion of the SRs with small number of jets is possibly driven by some other sparticles being light. It is also possible that there are small mass splittings between the \tilde{g} and the particle it decays to, thus producing soft jets, that remain undetected by this analysis.

7.3 SUSY parameter space - 0-lepton limits

This Section explores the effect of the 0-lepton search on the pMSSM parameter space. While previous Sections dealt with the sparticle masses, that are somewhat easier to understand, this one handles directly pMSSM parameters, which relation with the observable quantities is not always straightforward.

7.3.1 Fraction of excluded model points

In Figure 7.9 the fraction of excluded pMSSM model points is shown for the $M_3 - M_2$ parameter planes. In Figure 7.9a the model points when the LSP is bino-like are presented, in Figure 7.9b it is wino-like, while in Figure 7.9c it is higgsino-like. There is much similarity between Figure 7.9b and 7.6, that present the fraction of excluded model points in the gluino-neutralino mass plane, as the M_2 parameter controls the neutralino mass when the LSP is wino-like, while gluino mass is proportional to M_3 . The $M_3 - M_2$ parameter planes when the LSP is bino-like - Figure 7.9a and when it is higgsino-like - Figure 7.9c, illustrate that the exclusion for those LSP types is independent of the M_2 parameter, as expected. In Figure 7.9a, one can see there is a higher fraction of excluded model points for low M_2 values, which means that higher gluino masses are excluded. Figure 7.9c shows a much smoother transition to higher M_3 values, while Figure 7.9a has a sharper cut-off around 500 GeV. The plots are very similar when the LSP is bino-like and one considers the $M_3 - M_1$ parameter plane, and also when the LSP is higgsino-like in the $M_3 - \mu$ parameter plane (as M_1 controls the LSP mass when it is bino-like, and μ when the it is higgsino like).

There is no indication of favouring or disfavouring $M_1 - M_2 - M_3$ relations similar to those of models with unification of soft SUSY breaking terms at the high scale.

7.3.2 CLs max

This Section aims at presenting and discussing the exclusion of the pMSSM model points by displaying the maximal CLs value found for all the model points belonging to each bin of the parameter plane on the z-axis. As outlined in Section 3, the point of the parameter space is considered excluded if its maximal CLs value is below 0.05, thus the darkest blue bins represent the parts of the plane where all the model points are excluded.

In Figure 7.10 the $M_3 - \mu$ plane is shown. In Figure 7.10a one observes that the model points that have the M_3 parameter below 500 GeV are excluded independently of the value of μ for the bino-like LSP. There is a high concentration of model points with the CLs values higher than 0.8 for $M_3 \sim 700$ GeV, for $\mu > 700$ GeV. The apparent lower values of the maximal CLs above 700 GeV are only a consequence of the fact that model points with neutralino mass above 1 TeV do not have CLs values calculated, so are an artifact of the selection of model points in this scan. For μ values below 500 GeV the model points are excluded up to 1 TeV values of the

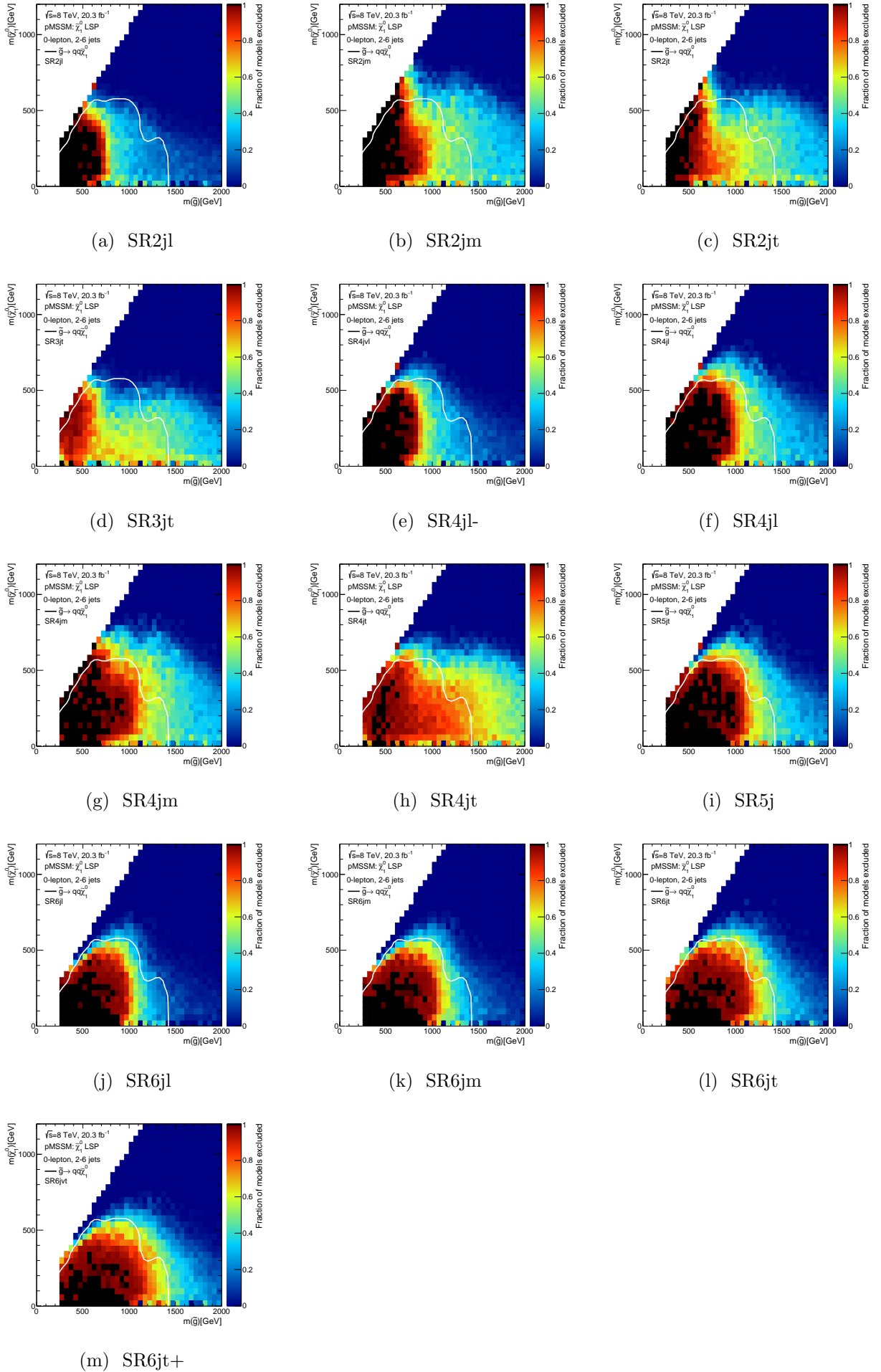


Figure 7.8: Exclusion in the $m(\tilde{g})$ - $m(\tilde{\chi})$ plane for pMSSM model points for each 0-lepton SR individually. On the z-axis the ratio between the number of excluded model points and the number of generated model points is shown.

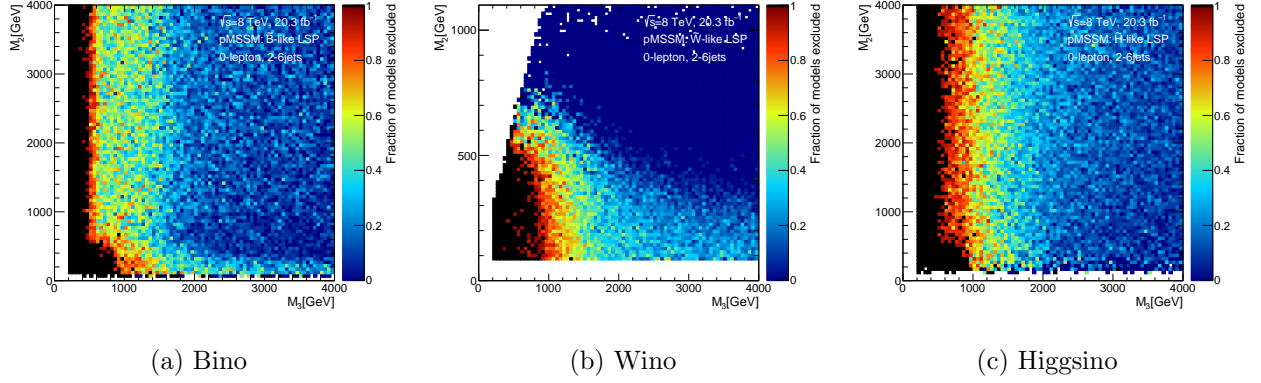


Figure 7.9: The fraction of excluded model points using only the 0-lepton analysis is shown in each bin in the $M_3 - M_2$ parameter plane. The model points when the LSP is bino (a), wino (b) and higgsino-like (c) are shown separately.

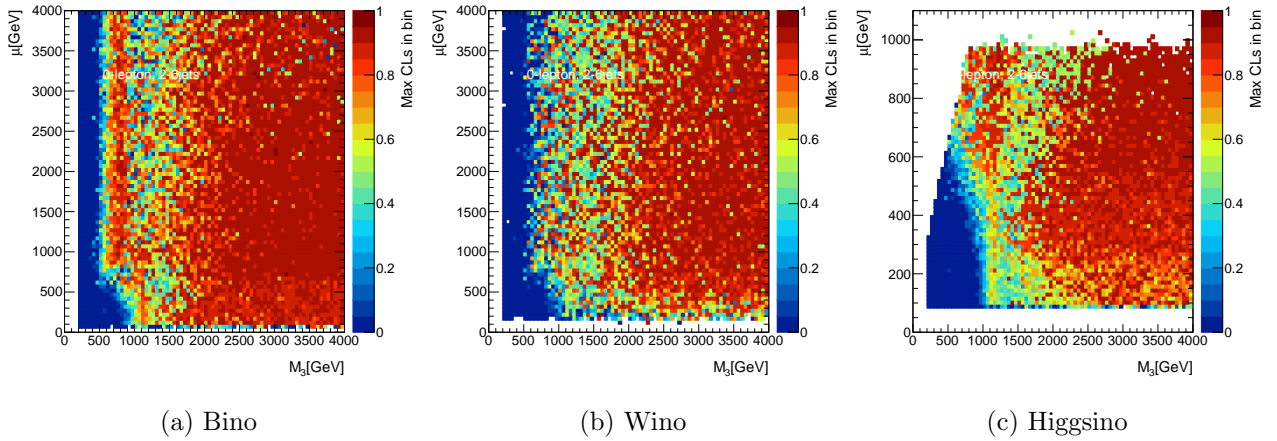


Figure 7.10: The maximal CLs value of the 0-lepton analysis is shown in each bin in the $M_3 - \mu$ parameter plane. The model points when the LSP is bino (a), wino (b) and higgsino-like (c) are shown separately. The z-axis is directly giving the 95% CL exclusions.

M_3 parameter, which is a direct consequence of the limit on the gluino mass. For M_3 values higher than 1 TeV, there is again a gradual transition towards high CLs values. In Figure 7.10b again the whole μ range is excluded when M_3 is below 500 GeV. As explained before this is expected as the exclusion of the model points when the LSP is bino and wino-like do not depend on μ - the higgsino mass parameter. The Figure 7.10c is very similar to Figure 7.1 as the M_3 parameter controls gluino mass, while μ governs the neutralino mass when the LSP is higgsino-like. This Figure shows a very high number of bins with the maximal CLs around 0.5 present for relatively high values of M_3 parameter (up to 2 TeV, in the whole range of μ). Similar planes to this one are $M_3 - M_1$ when the LSP is bino-like, and $M_3 - M_2$ when the LSP is wino-like. They also exhibit much higher maximal CLs values when M_3 is below 2 TeV, and for the whole M_1 range (when the LSP is bino-like), and for the whole M_2 range (for wino-like LSP) - almost all \sim one, especially when the LSP is wino-like.

The $M_3 - A_t$ parameter plane is strongly influenced by the SM-Higgs mass constraint (Section 5.2). This plane exhibits the same features for all the LSP types, except maybe for the case when the LSP is bino-like - Figure 7.11a which shows a somewhat higher concentration of the model points with high CLs values when the value of the M_3 parameter is around 700-800 GeV. Despite that small difference in the pattern of the CLs, all the model points are excluded for

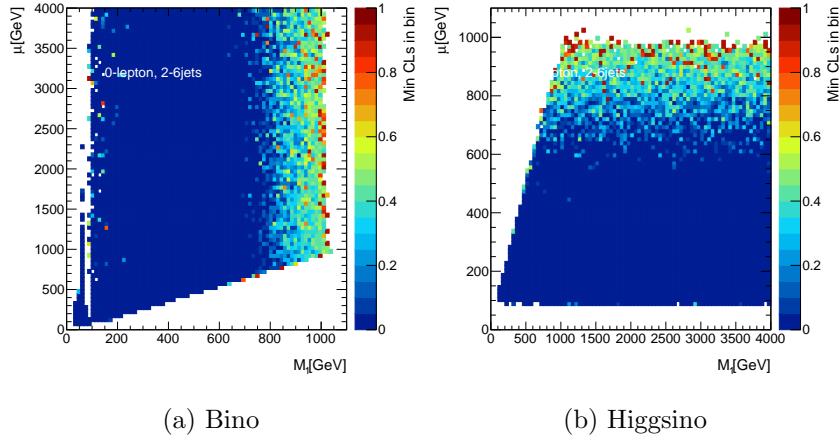


Figure 7.12: The minimal CLs value of the 0-lepton analysis is shown in each bin. In (a) it is the $M_1 - \mu$ parameter plane with the model points when the LSP is bino-like, while in (b) the model points when the LSP is higgsino-like are depicted in the $M_1 - \mu$ parameter plane.

In Figure 7.12a the value of μ is presented as a function of M_1 - for pMSSM model points when the LSP is bino-like. The areas where the exclusion power is reduced correspond to M_1 above 700-800 GeV, independently of the μ parameter. A parallel statement is true for the higgsino-like case, 7.12b, where the reduction of the exclusion power is present for μ values above 800 GeV, independently of M_1 . This points to large LSP masses, pushing the entire spectrum to large masses.

In Figure 7.13 several different parameter planes are shown. In Figure 7.13a $M_3 - M_1$ parameter plane is presented for the pMSSM model points when the LSP is bino-like, in Figure 7.13b $M_3 - M_2$ for the model points when the LSP is wino-like, while in Figure 7.13c $M_3 - \mu$ plane for the model points when the LSP is higgsino-like. All these planes are responsible for the gluino mass for different LSP types, and for each similar conclusion can be reached: the less excluded values of the parameters are pushed to high values - $M_3 > 2$ TeV and M_1 , M_2 and μ higher than 800 GeV (depending on the LSP type considered). This comes from the fact that the gluino production plays dominant role and as the cross-section for it decreases with the gluino mass, so does the sensitivity of ATLAS searches. All this translates to high gluino masses being favoured by the ATLAS searches carried up until now.

In Figure 7.14 $M_1 - M_2$ parameter plane is shown, the model points when the LSP is bino-7.14a, wino 7.14b and higgsino-like 7.14c. In Figure-7.14a, one can see that less excluded values of the M_1 parameter are above 800 GeV, independently of the values of M_2 . For the model points when the LSP is wino-like (Figure-7.14b) the less excluded M_2 values are above 700-800 GeV, for the whole range of M_1 parameter. This parameter plane does not tell anything when the LSP is higgsino-like, as in almost all bins there is at least one model point with the CLs below 0.05.

7.3.4 Distinction between $\mu > 0$ and $\mu < 0$

This Section explores the effect of the sign of the μ parameter on the exclusion of the pMSSM model points. First one should recall that the $\text{BR}(b \rightarrow s\gamma)$ prefers positive μ values [219]. Also the $\Delta(g-2)_\mu$ favours positive μ values [220]. This is the consequence of the possible cancellation in the off-diagonal entries of the third generation scalar mass matrices. Up to now the plots were showing $|\mu|$. In Figure 7.15a, one can see that for negative μ values, there are less model points sampled for m_A values below around 700 GeV, while for positive μ values the lower value of m_A is as low as 500 GeV. In Figure 7.15b, also there is smaller number of model

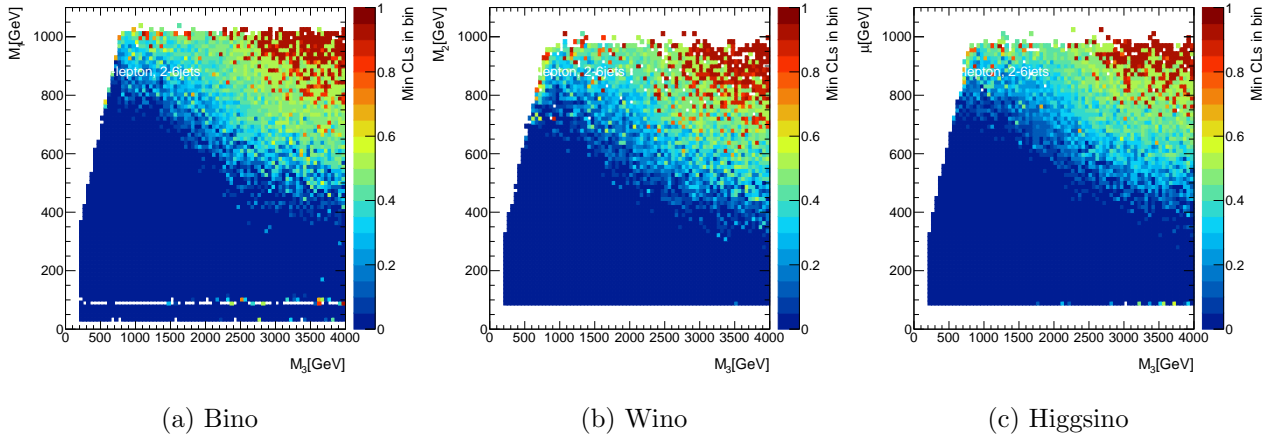


Figure 7.13: The minimal CLs value of the 0-lepton analysis is shown in each bin. In (a) the model points when the LSP is bino-like are depicted in $M_3 - M_1$ parameter plane, in (b) it is the considered plane is $M_3 - M_2$ and the model points have the LSP that is wino like. In Figure (c) shows the model points when the LSP is higgsino-like in $M_3 - \mu$ parameter plane.

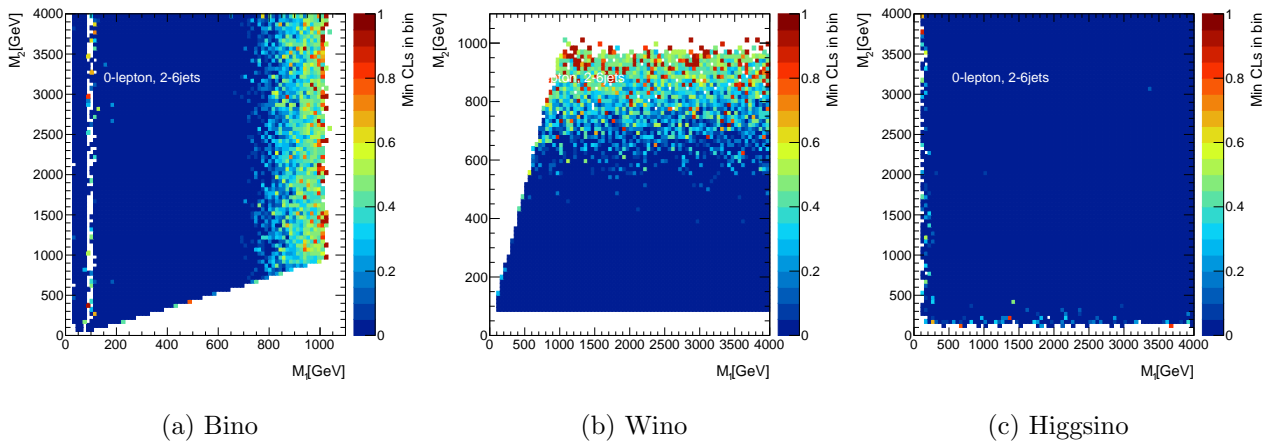


Figure 7.14: The minimal CLs value of the 0-lepton analysis is shown in each bin in the $M_1 - M_2$ parameter plane. The model points when the LSP is bino (a), wino (b) and higgsino-like (c) are shown separately.

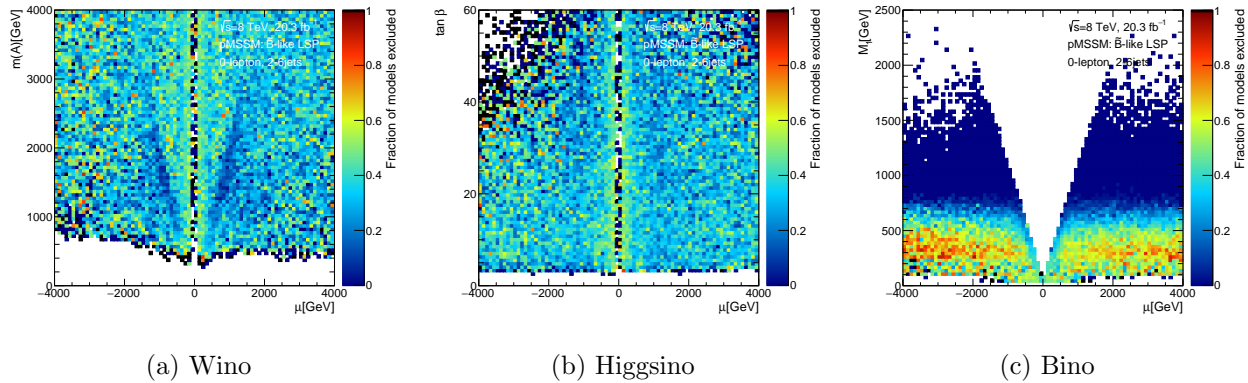


Figure 7.15: The fraction of model points excluded by the 0-lepton analysis is shown in each bin in the $\mu - M_1$ parameter plane in (c), the $\mu - m_A$ plane is presented in (a), while the $\mu - \tan\beta$ parameter plane is on (b).

points sampled for high $\tan\beta$ values (above 50), when μ values are between -4 and -3 TeV. This confirms the expectation that positive μ values are preferred by the imposed indirect constraints. Still, ATLAS searches also show trend to exclude more model points for negative μ values as can be seen in Figure 7.15c, where the the $\mu - M_1$ parameter plane considering the sign of μ . There is a slightly higher fraction of excluded model points for the negative values of μ .

In general, model points with negative μ values are less frequent in the model set, which is the consequence of the indirect constraints. This is even more pronounced after the effect of the ATLAS searches, which also favour positive μ values.

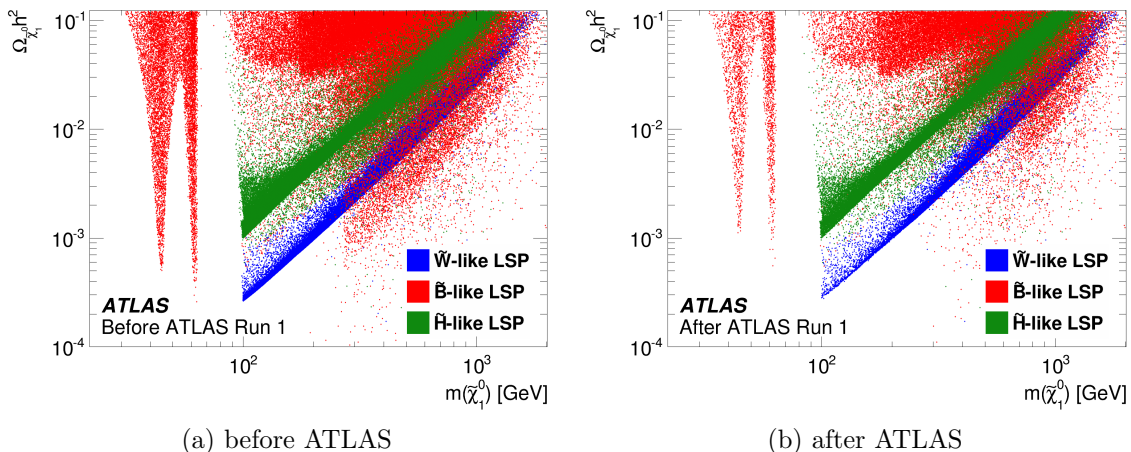
7.4 Dark matter

As explained before (Section 5.2) in all the results presented so far the LSP was not required to saturate the observed dark matter energy density. After considering the exclusion by the ATLAS searches, one can look at the neutralino nature within the remaining model points, and its annihilation channels. Another interesting thing is to see is if the results change when one considers only the model points that saturate the dark matter relic density.

7.4.1 Non-saturated dark matter

The constraint on the upper limit on the neutralino relic density is a very strong constraint. In Figure 7.16a the density of pMSSM model points in the neutralino relic density ($\Omega_{\tilde{\chi}_1^0} h^2$) - neutralino mass plane is shown before applying the constraint coming from the ATLAS searches. The full model set is presented: the model points when the LSP is bino-like are shown in red, those when it is wino or higgsino-like are illustrated in blue and green respectively. The sharp cut-offs for the neutralino mass come from the imposed constraints on the masses of the charged sparticles and also squarks. For the neutralino masses less than 100 GeV, Z and SM-like Higgs funnels are easily identifiable. There are few model points with a wino or higgsino-like LSP in the low mass as for those model points the NLSP is a chargino almost degenerate with the neutralino, which would have been observed at LEP [181]. Their thermally averaged annihilation cross-section is proportional to the inverse square of the neutralino mass:

$$\Omega_{\tilde{\chi}_1^0} h^2 \propto m^2(\tilde{\chi}_1^0) \quad (7.1)$$



(a) before ATLAS

(b) after ATLAS

Figure 7.16: The density of pMSSM model points projected onto the plane of dark matter relic density versus the neutralino mass, (a) before and (b) after the constraints from the ATLAS searches. The model points when the LSP is bino-like are shown in red, when it is wino-like are in blue and higgsino-like in green.

which is clearly identifiable in the plots for the model points when the LSP is wino- and higgsino-like.

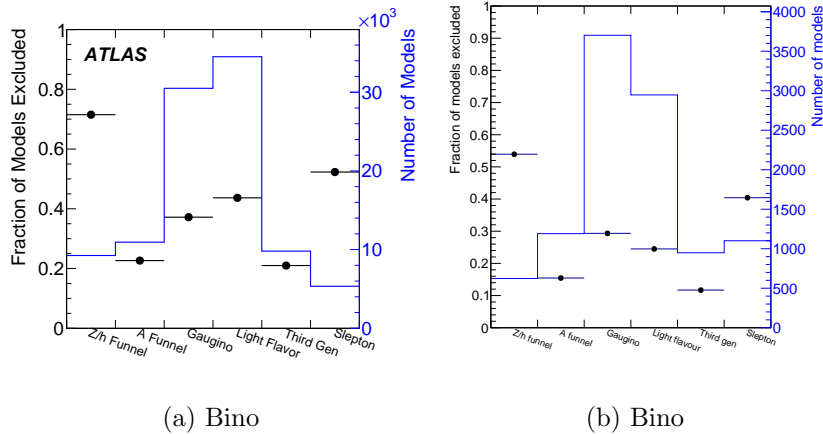
In Figure 7.16b the density of pMSSM model points in the neutralino relic density ($\Omega_{\tilde{\chi}_1^0} h^2$) - neutralino mass plane is shown after considering the exclusion coming from the ATLAS searches. They show sensitivity across a wide range of neutralino masses (up to 800 GeV) and also across the whole range of expected neutralino relic densities. In the Z - and SM-like Higgs funnels, about one third of the model points are excluded. For the model points when the LSP is wino-like the good sensitivity of the Disappearing Track analysis excludes around 80% of the model points with a neutralino mass below 220 GeV.

Nevertheless, all the LSP types are still possible after considering the results of the ATLAS searches, and there is no evidence for choosing one LSP type rather than another. In Figure 7.17a the fraction of the excluded pMSSM model points is shown for the different annihilation and co-annihilation mechanisms for the bino-like LSP (as black points) and the number of model points generated (in blue). The gaugino annihilation encompasses the NLSP being $\tilde{\chi}_2^0$ and chargino, while light flavour denotes squarks of the first two generations and gluinos. As one can see, all the annihilation and co-annihilation channels are still represented and the results of the pMSSM analysis cannot help distinguishing between any of them.

7.4.2 Saturated dark matter

One can also explore the possibility that all the dark matter relic density comes from the lightest neutralino. $\Omega_{\text{CDM}} h^2$ is therefore restricted to the range allowed by taking into account the experimental (0.0010) and also the theoretical uncertainty (0.012 from Table 5.2) of $\Omega_{\text{CDM}} h^2$. This reduces the number of allowed model points substantially. The largest fraction of pMSSM model points within this scan found to fulfill this requirement has a bino-like LSP. One should recall that the model points when the LSP is bino-like are oversampled for this study.

Still one can look at the minimal CLs value in each bin the $M_1 - M_2$ parameter plane that is shown in Figure 7.18a when the LSP is bino-like. It is difficult to derive any conclusion by comparing this plot with Figure 7.14a since one cannot disentangle two effects: the fact that the number of excluded model points in the former is smaller (which may be directly linked to the fact that the number of concerned model points is lower), and the fact that the dark matter



(a) Bino

(b) Bino

Figure 7.17: Figure (a): the fraction of the excluded pMSSM model points is shown for the different annihilation and co-annihilation mechanisms for the bino-like LSP (as black points) and the number of model points generated (in blue). In Figure (b) the same is shown for the saturated DM relic density constraint. The LSP is bino-like for all the presented model points.

constraint drives this effect. For this reason, the plot of the maximal CLs value in each bin is also given in Figure 7.18b, where most of the excluded bins are part of the SM-like Higgs and Z funnel but where no fully excluded region shows up. Above $M_1 > 700$ GeV, the CLs of the model points are all between 0.5 and 1, far from being excluded by the 0-lepton analysis: this is compatible with the Sfitter results [145] for which a lot of model points compatible with the data were found. The number of model points when the LSP is wino-like saturating the DM is null, and the number of higgsino-like ones is too small to be exploited.

One can also look at the NLSP type of the non-excluded model points for a LSP saturating the DM which do not correspond to the SM-like Higgs and Z funnel to point out the still opened annihilation channels. In Figure 7.17b the fraction of the excluded pMSSM model points is shown for the different annihilation and co-annihilation mechanisms for the bino-like LSP (as black points) and the number of model points generated (in blue), in the case when the DM is saturated. When comparing with Figure 7.17a, one can observe that there is higher number of model points with the gaugino NLSP when the DM is saturated, and also that there is less model points with the NLSP belonging to light flavour bin. There is also difference in the fraction of model points excluded for the case of light flavour NLSP (around 45% when the DM is not saturated, compared to 25% when it is saturated). The reason for this is in the fact that the neutralino mass is higher when the DM is saturated (the average is higher than 750 GeV while the same average for non saturated DM is around 650 GeV). The difference in mass between the NLSP and LSP is somewhat higher when the DM is saturated (~ 10 GeV), making the mass spectrum of these model points less compressed, but this does not seem to make a considerable effect on the exclusion of model points.

7.5 Conclusion

In this Chapter the results of the pMSSM analysis are discussed, first by considering the overall exclusion of the ATLAS searches, and then by exploring the mass and parameters planes in details. Also the complementarity of the ATLAS searches is presented, and it is shown that the 0-lepton analysis is clearly prominent when the fraction of excluded model points and also the coverage of parameters planes are explored. The power of the 0-lepton analysis permits to use it alone to identify both the excluded parts of the parameter planes (by considering the maximal

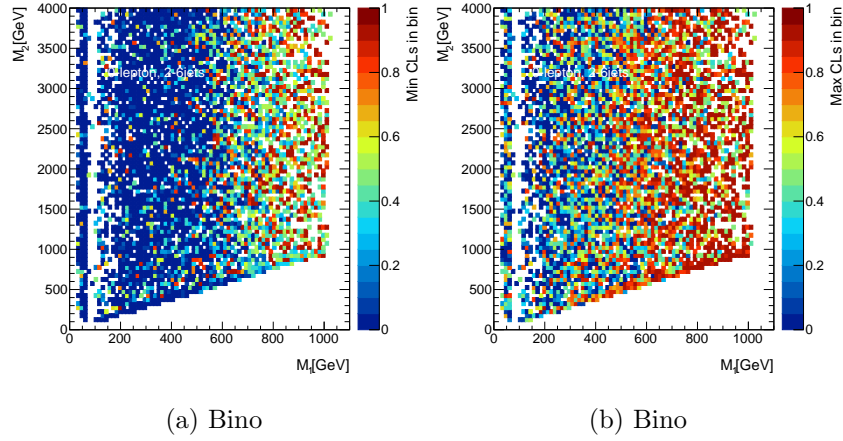


Figure 7.18: Figure (a): The minimal CLs value of the 0-lepton analysis is shown in each bin in the $M_1 - M_2$ parameter plane when the dark matter relic density is saturated. Figure (a): The maximal CLs value of the 0-lepton analysis is shown in each bin in the $M_1 - M_2$ parameter plane when the dark matter relic density is saturated. The LSP is bino-like for all the presented model points.

CLs value in each bin), and the areas where the exclusion power is low (when exploring its impact by showing the minimal CLs value in each bin). The impact of the ATLAS searches is further explored in the context of the dark matter, to see if there is a preference for certain LSP type or annihilation mechanism. In addition, the possibility of restricting the model set to the model points that saturate the dark matter relic density, is examined to try to identify the parameter values that are less excluded. The ATLAS searches permit to exclude more than 40% of the considered pMSSM model points, restraining even further the sparticle masses and the parameters values where one may expect to discover SUSY.

Conclusion

This thesis has been performed within the context of the 0-lepton analysis which focuses on squarks and gluinos decays, and tackles final states with many jets, no electron or muon and large missing transverse energy (coming from the production of the lightest supersymmetric particle (LSP)). It is performed with 20.3 fb^{-1} of data collected by the ATLAS experiment in 2012.

The first part of the work described in this document has been to design Validation Regions (VR) to further check the outcome of the fit which leads to the final results of the 0-lepton analysis. The background processes coming from tau leptons (from the W -boson and top quark decays) are studied in details, as it is dominant at the end of the selection process. The validation of their modeling has been assessed. This work has been used in [2] for the final exclusion limit results on sparticle masses in several rather constrained models. For instance, since no significant excess above Standard Model expectation has been observed, the exclusion limits at the 95% confidence level on the mass of the gluino has been set to 1330 GeV for a simplified model incorporating only a gluino and the (massless) lightest neutralino. In the mSUGRA/CMSSM models with $\tan\beta = 30$, $A_0 = -2m_0$ and $\mu > 0$, squarks and gluinos of equal mass have been excluded for masses below 1700 GeV. A possible addition of a veto on the events containing tau leptons was also explored by assessing its impact on the exclusion reach of the analysis.

The second part of this thesis work was to perform an interpretation of the results of the 0-lepton analysis in a less restricted phenomenological Minimal SuperSymmetric Model (pMSSM) described with 19 parameters where the neutralino is assumed to be the LSP and the R parity is conserved. The parameter space was chosen to take into account the pre-LHC constraints: B-physics results, precision measurements, the mass of the observed Higgs boson, limits from the direct searches for Dark Matter and the upper limit on the cold dark matter energy density of the Universe (Ω_{cdm}). It is part of the full ATLAS analysis that has been published in [3]. The goal was to make a final statement on the status of the supersymmetry searches after Run 1 of the LHC. The 0-lepton analysis has a decisive role in this effort as it provides the best exclusion power. In parallel the final states accessible within the pMSSM are very numerous, pushing the analysis toward configurations that have never been studied before. A comparison of the truth and reconstructed yields as well as the CLs determination has been checked extensively in order to ascertain the validity of the derived results. The pMSSM parameter space is mainly driven by the Higgs mass constraint, Ω_{cdm} and the correlation between both. Thus the final interpretation which leads to limits on the masses of neutralinos, gluinos and squarks are discussed as a function of the type of the LSP (bino/wino/higgsino). Using only the results of the 0-lepton analysis, which is the only analysis that allows to set statistically well defined limits, the comparison of simplified models vs. full SUSY models results have been addressed. The determination of the favoured/disfavoured areas of the SUSY parameters are further discussed.

Bibliography

- [1] ATLAS Collaboration, *Search for squarks and gluinos with the ATLAS detector in final states with jets and missing transverse momentum and 20.3 fb⁻¹ of $\sqrt{s} = 8$ TeV proton-proton collision data*, [ATLAS-CONF-2013-047](#), 2013.
- [2] ATLAS Collaboration, G. Aad et al., *Search for squarks and gluinos with the ATLAS detector in final states with jets and missing transverse momentum using $\sqrt{s} = 8$ TeV proton-proton collision data*, [JHEP 09 \(2014\) 176](#), [arXiv:1405.7875 \[hep-ex\]](#).
- [3] ATLAS Collaboration, G. Aad et al., *Summary of the ATLAS experiment's sensitivity to supersymmetry after LHC Run 1 ? interpreted in the phenomenological MSSM*, [JHEP 10 \(2015\) 134](#), [arXiv:1508.06608 \[hep-ex\]](#).
- [4] S. P. Martin, *A Supersymmetry primer*, [Adv.Ser.Direct.High Energy Phys. 21 \(2010\) 1–153](#), [arXiv:hep-ph/9709356 \[hep-ph\]](#).
- [5] M. E. Peskin and D. V. Schroeder, *An Introduction to Quantum Field Theory*. Westview Press, 1995. Reading, USA: Addison-Wesley (1995) 842 p.
- [6] S. L. Glashow, *Partial Symmetries of Weak Interactions*, [Nucl. Phys. 22 \(1961\) 579–588](#).
- [7] S. Weinberg, *A Model of Leptons*, [Phys. Rev. Lett. 19 \(1967\) 1264–1266](#).
- [8] A. Salam, *Weak and Electromagnetic Interactions*, [Conf. Proc. C680519 \(1968\) 367–377](#).
- [9] S. L. Glashow, J. Iliopoulos, and L. Maiani, *Weak Interactions with Lepton-Hadron Symmetry*, [Phys. Rev. D2 \(1970\) 1285–1292](#).
- [10] F. Englert and R. Brout, *Broken Symmetry and the Mass of Gauge Vector Mesons*, [Phys. Rev. Lett. 13 \(1964\) 321–323](#).
- [11] P. W. Higgs, *Broken symmetries, massless particles and gauge fields*, [Phys. Lett. 12 \(1964\) 132–133](#).
- [12] P. W. Higgs, *Broken Symmetries and the Masses of Gauge Bosons*, [Phys. Rev. Lett. 13 \(1964\) 508–509](#).
- [13] G. S. Guralnik, C. R. Hagen, and T. W. B. Kibble, *Global Conservation Laws and Massless Particles*, [Phys. Rev. Lett. 13 \(1964\) 585–587](#).
- [14] P. W. Higgs, *Spontaneous Symmetry Breakdown without Massless Bosons*, [Phys. Rev. 145 \(1966\) 1156–1163](#).
- [15] T. W. B. Kibble, *Symmetry breaking in nonAbelian gauge theories*, [Phys. Rev. 155 \(1967\) 1554–1561](#).

- [16] UA1 Collaboration, G. Arnison et al., *Experimental Observation of Isolated Large Transverse Energy Electrons with Associated Missing Energy at $s^{**}(1/2) = 540\text{-GeV}$* , *Phys. Lett.* **B122** (1983) 103–116.
- [17] UA1 Collaboration, G. Arnison et al., *Experimental Observation of Lepton Pairs of Invariant Mass Around $95\text{-GeV}/c^{**2}$ at the CERN SPS Collider*, *Phys. Lett.* **B126** (1983) 398–410.
- [18] UA2 Collaboration, M. Banner et al., *Observation of Single Isolated Electrons of High Transverse Momentum in Events with Missing Transverse Energy at the CERN anti- p p Collider*, *Phys. Lett.* **B122** (1983) 476–485.
- [19] CDF Collaboration, F. Abe et al., *Observation of top quark production in $\bar{p}p$ collisions*, *Phys. Rev. Lett.* **74** (1995) 2626–2631, [arXiv:hep-ex/9503002 \[hep-ex\]](#).
- [20] D0 Collaboration, S. Abachi et al., *Observation of the top quark*, *Phys. Rev. Lett.* **74** (1995) 2632–2637, [arXiv:hep-ex/9503003 \[hep-ex\]](#).
- [21] N. Cabibbo, *Unitary Symmetry and Leptonic Decays*, *Phys. Rev. Lett.* **10** (1963) 531–533.
- [22] M. Kobayashi and T. Maskawa, *CP Violation in the Renormalizable Theory of Weak Interaction*, *Prog. Theor. Phys.* **49** (1973) 652–657.
- [23] Super-Kamiokande Collaboration, Y. Fukuda et al., *Measurements of the solar neutrino flux from Super-Kamiokande's first 300 days*, *Phys.Rev.Lett.* **81** (1998) 1158–1162, [arXiv:hep-ex/9805021 \[hep-ex\]](#).
- [24] KamLAND Collaboration, T. Araki et al., *Measurement of neutrino oscillation with KamLAND: Evidence of spectral distortion*, *Phys.Rev.Lett.* **94** (2005) 081801, [arXiv:hep-ex/0406035 \[hep-ex\]](#).
- [25] Planck Collaboration, P. Ade et al., *Planck 2015 results. XIII. Cosmological parameters*, [arXiv:1502.01589 \[astro-ph.CO\]](#).
- [26] H. Flacher, M. Goebel, J. Haller, A. Hocker, K. Monig, and J. Stelzer, *Revisiting the Global Electroweak Fit of the Standard Model and Beyond with Gfitter*, *Eur. Phys. J.* **C60** (2009) 543–583, [arXiv:0811.0009 \[hep-ph\]](#). [Erratum: *Eur. Phys. J.* **C71**,1718(2011)].
- [27] ATLAS Collaboration, G. Aad et al., *Observation of a new particle in the search for the Standard Model Higgs boson with the ATLAS detector at the LHC*, *Phys.Lett.* **B716** (2012) 1–29, [arXiv:1207.7214 \[hep-ex\]](#).
- [28] CMS Collaboration, S. Chatrchyan et al., *Observation of a new boson at a mass of 125 GeV with the CMS experiment at the LHC*, *Phys. Lett.* **B716** (2012) 30–61, [arXiv:1207.7235 \[hep-ex\]](#).
- [29] Gfitter Group Collaboration, M. Baak, J. Cth, J. Haller, A. Hoecker, R. Kogler, K. Mnig, M. Schott, and J. Stelzer, *The global electroweak fit at NNLO and prospects for the LHC and ILC*, *Eur. Phys. J.* **C74** (2014) 3046, [arXiv:1407.3792 \[hep-ph\]](#).
- [30] M. E. Peskin and T. Takeuchi, *Estimation of oblique electroweak corrections*, *Phys. Rev.* **D46** (1992) 381–409.

- [31] J. Wess and B. Zumino, *Supergauge Transformations in Four-Dimensions*, *Nucl. Phys.* **B70** (1974) 39–50.
- [32] E. W. Kolb and M. S. Turner, *The Early Universe*. Addison-Wesley, 1990. *Frontiers in Physics*, 69.
- [33] G. Belanger, F. Boudjema, and A. Pukhov, *micrOMEGAs : a code for the calculation of Dark Matter properties in generic models of particle interaction*, in *The Dark Secrets of the Terascale*, pp. 739–790. 2013. [arXiv:1402.0787 \[hep-ph\]](https://arxiv.org/abs/1402.0787).
<http://inspirehep.net/record/1280091/files/arXiv:1402.0787.pdf>.
- [34] *Report on the Direct Detection and Study of Dark Matter*, http://science.energy.gov/~media/hep/pdf/files/pdfs/dmsagreportjuly18_2007.pdf.
- [35] C. Arina, M. E. C. Catalan, S. Kraml, S. Kulkarni, and U. Laa, *Constraints on sneutrino dark matter from LHC Run 1*, *JHEP* **05** (2015) 142, [arXiv:1503.02960 \[hep-ph\]](https://arxiv.org/abs/1503.02960).
- [36] H. Pagels and J. R. Primack, *Supersymmetry, Cosmology and New TeV Physics*, *Phys. Rev. Lett.* **48** (1982) 223.
- [37] T. Stefaniak, *Neutralino annihilation processes in the minimal supergravity model*, [arXiv:0806.2214 \[hep-ph\]](https://arxiv.org/abs/0806.2214).
- [38] R. D. Ball et al., *Parton distributions with LHC data*, *Nucl. Phys.* **B867** (2013) 244–289, [arXiv:1207.1303 \[hep-ph\]](https://arxiv.org/abs/1207.1303).
- [39] W. Beenakker, R. Hopker, M. Spira, and P. M. Zerwas, *Squark and gluino production at hadron colliders*, *Nucl. Phys.* **B492** (1997) 51–103, [arXiv:hep-ph/9610490](https://arxiv.org/abs/hep-ph/9610490).
- [40] W. Beenakker, M. Kramer, T. Plehn, M. Spira, and P. Zerwas, *Stop production at hadron colliders*, *Nucl. Phys.* **B515** (1998) 3–14, [arXiv:hep-ph/9710451 \[hep-ph\]](https://arxiv.org/abs/hep-ph/9710451).
- [41] W. Beenakker, M. Klasen, M. Kramer, T. Plehn, M. Spira, et al., *The Production of charginos / neutralinos and sleptons at hadron colliders*, *Phys.Rev.Lett.* **83** (1999) 3780–3783, [arXiv:hep-ph/9906298 \[hep-ph\]](https://arxiv.org/abs/hep-ph/9906298).
- [42] M. Spira, *Higgs and SUSY particle production at hadron colliders*, [arXiv:hep-ph/0211145 \[hep-ph\]](https://arxiv.org/abs/hep-ph/0211145).
- [43] T. Plehn, *Measuring the MSSM Lagrangean*, *Czech.J.Phys.* **55** (2005) B213–B220, [arXiv:hep-ph/0410063 \[hep-ph\]](https://arxiv.org/abs/hep-ph/0410063).
- [44] A. Collaboration, *ATLAS Run 1 Pythia8 tunes*, Tech. Rep. ATL-PHYS-PUB-2014-021, CERN, Geneva, Nov, 2014. <http://cds.cern.ch/record/1966419>.
- [45] T. Gleisberg, S. Hoeche, F. Krauss, M. Schonherr, S. Schumann, et al., *Event generation with SHERPA 1.1*, *JHEP* **0902** (2009) 007, [arXiv:0811.4622 \[hep-ph\]](https://arxiv.org/abs/0811.4622).
- [46] G. Corcella et al., *HERWIG 6.5: an event generator for Hadron Emission Reactions With Interfering Gluons (including supersymmetric processes)*, *JHEP* **01** (2001) 010, [arXiv:hep-ph/0011363](https://arxiv.org/abs/hep-ph/0011363).
- [47] G. Corcella et al., *HERWIG 6.5 release note*, 2002. [arXiv:hep-ph/0210213](https://arxiv.org/abs/hep-ph/0210213).

- [48] T. Sjostrand, S. Mrenna, and P. Z. Skands, *A Brief Introduction to PYTHIA 8.1*, *Comput. Phys. Commun.* **178** (2008) 852–867, [arXiv:0710.3820](#).
- [49] J. Alwall, M. Herquet, F. Maltoni, O. Mattelaer, and T. Stelzer, *MadGraph 5 : Going Beyond*, *JHEP* **1106** (2011) 128, [arXiv:1106.0522 \[hep-ph\]](#).
- [50] M. L. Mangano, M. Moretti, F. Piccinini, R. Pittau, and A. D. Polosa, *ALPGEN, a generator for hard multiparton processes in hadronic collisions*, *JHEP* **07** (2003) 001, [arXiv:hep-ph/0206293](#).
- [51] S. Frixione and B. R. Webber, *Matching NLO QCD computations and parton shower simulations*, *JHEP* **06** (2002) 029, [arXiv:hep-ph/0204244](#).
- [52] S. Frixione, P. Nason, and B. R. Webber, *Matching NLO QCD and parton showers in heavy flavour production*, *JHEP* **08** (2003) 007, [arXiv:hep-ph/0305252](#).
- [53] P. Nason, *A New method for combining NLO QCD with shower Monte Carlo algorithms*, *JHEP* **0411** (2004) 040, [arXiv:hep-ph/0409146 \[hep-ph\]](#).
- [54] S. Frixione, P. Nason, and C. Oleari, *Matching NLO QCD computations with parton shower simulations: the POWHEG method*, *JHEP* **0711** (2007) 070, [arXiv:0709.2092 \[hep-ph\]](#).
- [55] S. Alioli, P. Nason, C. Oleari, and E. Re, *A general framework for implementing NLO calculations in shower Monte Carlo programs: the POWHEG BOX*, *JHEP* **1006** (2010) 043, [arXiv:1002.2581 \[hep-ph\]](#).
- [56] J. M. Butterworth, J. R. Forshaw, and M. H. Seymour, *Multiparton interactions in photoproduction at HERA*, *Z. Phys.* **C72** (1996) 637–646, [arXiv:hep-ph/9601371](#).
- [57] B. P. Kersevan and E. Richter-Was, *The Monte Carlo event generator AcerMC version 2.0 with interfaces to PYTHIA 6.2 and HERWIG 6.5*, [arXiv:hep-ph/0405247 \[hep-ph\]](#).
- [58] L. Evans and P. Bryant, *LHC Machine*, *JINST* **3** (2008) S08001.
- [59] ATLAS Collaboration, *The ATLAS Experiment at the CERN Large Hadron Collider*, 2008. *JINST* **3** (2008) S08003.
- [60] CMS Collaboration, S. Chatrchyan et al., *The CMS experiment at the CERN LHC*, *JINST* **3** (2008) S08004.
- [61] LHCb Collaboration, A. A. Alves, Jr. et al., *The LHCb Detector at the LHC*, *JINST* **3** (2008) S08005.
- [62] ALICE Collaboration, K. Aamodt et al., *The ALICE experiment at the CERN LHC*, *JINST* **3** (2008) S08002.
- [63] TOTEM Collaboration, G. Anelli et al., *The TOTEM experiment at the CERN Large Hadron Collider*, *JINST* **3** (2008) S08007.
- [64] LHCf Collaboration, O. Adriani et al., *The LHCf detector at the CERN Large Hadron Collider*, *JINST* **3** (2008) S08006.
- [65] GEANT4 Collaboration, S. Agostinelli et al., *GEANT4: A simulation toolkit*, *Nucl. Instrum. Meth.* **A506** (2003) 250–303.

- [66] A. Collaboration, *The ATLAS Simulation Infrastructure*, *The European Physical Journal C* **70** (2010) no. 3, 823–874.
<http://dx.doi.org/10.1140/epjc/s10052-010-1429-9>.
- [67] ATLAS Collaboration Collaboration, *Performance of the ATLAS Inner Detector Track and Vertex Reconstruction in the High Pile-Up LHC Environment*, Tech. Rep. ATLAS-CONF-2012-042, CERN, Geneva, Mar, 2012.
<https://cds.cern.ch/record/1435196>.
- [68] *Alignment of the ATLAS Inner Detector and its Performance in 2012*, Tech. Rep. ATLAS-CONF-2014-047, CERN, Geneva, Jul, 2014.
<http://cds.cern.ch/record/1741021>.
- [69] ATLAS Collaboration Collaboration, G. Aad et al., *Jet energy measurement with the ATLAS detector in proton-proton collisions at $\sqrt{s} = 7$ TeV*, [arXiv:1112.6426](https://arxiv.org/abs/1112.6426) [[hep-ex](https://arxiv.org/archive/hep)].
- [70] W. Lampl et al., *Calorimeter Clustering Algorithms: Description and Performance*, Tech. Rep. ATL-LARG-PUB-2008-002, CERN, 2011 .
- [71] M. Cacciari, G. P. Salam, and G. Soyez, *The anti- k_t jet clustering algorithm*, *JHEP* **04** (2008) 063, [arXiv:0802.1189](https://arxiv.org/abs/0802.1189).
- [72] M. Cacciari and G. P. Salam, *Dispelling the N^3 myth for the k_t jet-finder*, *Phys. Lett. B* **641** (2006) 57, [arXiv:hep-ph/0512210](https://arxiv.org/abs/hep-ph/0512210).
- [73] ATLAS Collaboration, *Commissioning of the ATLAS high-performance b-tagging algorithms in the 7 TeV collision data*, *ATLAS-CONF-2011-102*, 2011.
- [74] ATLAS Collaboration, *Measuring the b-tag efficiency in a top-pair sample with 4.7 fb^{-1} of data from the ATLAS detector*, *ATLAS-CONF-2012-097*, 2012.
- [75] ATLAS Collaboration, G. Aad et al., *Electron performance measurements with the ATLAS detector using the 2010 LHC proton-proton collision data*, *Eur. Phys. J. C* **72** (2012) 1909, [arXiv:1110.3174](https://arxiv.org/abs/1110.3174) [[hep-ex](https://arxiv.org/archive/hep)].
- [76] ATLAS Collaboration Collaboration, *Improved electron reconstruction in ATLAS using the Gaussian Sum Filter-based model for bremsstrahlung*, Tech. Rep. ATLAS-CONF-2012-047, CERN, Geneva, May, 2012.
<https://cds.cern.ch/record/1449796>.
- [77] ATLAS Collaboration Collaboration, G. Aad et al., *Performance of Missing Transverse Momentum Reconstruction in Proton-Proton Collisions at 7 TeV with ATLAS*, *Eur.Phys.J. C* **72** (2012) 1844, [arXiv:1108.5602](https://arxiv.org/abs/1108.5602) [[hep-ex](https://arxiv.org/archive/hep)].
- [78] M. Capeans, G. Darbo, K. Einsweiler, M. Elsing, T. Flick, M. Garcia-Sciveres, C. Gemme, H. Pernegger, O. Rohne, and R. Vuillermet, *ATLAS Insertable B-Layer Technical Design Report*, Tech. Rep. CERN-LHCC-2010-013. ATLAS-TDR-19, CERN, Geneva, Sep, 2010. <https://cds.cern.ch/record/1291633>.
- [79] ATLAS Collaboration, G. Aad et al., *Search for squarks and gluinos with the ATLAS detector in final states with jets and missing transverse momentum using 4.7 fb^{-1} of $\sqrt{s} = 7$ TeV proton-proton collision data*, *Phys. Rev. D* **87** (2013) 012008, [arXiv:1208.0949](https://arxiv.org/abs/1208.0949) [[hep-ex](https://arxiv.org/archive/hep)].

- [80] ATLAS Collaboration, G. Aad et al., *Search for squarks and gluinos using final states with jets and missing transverse momentum with the ATLAS detector in $\sqrt{s} = 7$ TeV proton-proton collisions*, *Phys. Lett. B* **710** (2012) 67–85, [arXiv:1109.6572 \[hep-ex\]](#).
- [81] ATLAS Collaboration, G. Aad et al., *Search for squarks and gluinos using final states with jets and missing transverse momentum with the ATLAS detector in $\sqrt{s} = 7$ TeV proton-proton collisions*, *Phys. Lett. B* **701** (2011) 186–203, [arXiv:1102.5290 \[hep-ex\]](#).
- [82] CMS Collaboration, S. Chatrchyan et al., *Search for supersymmetry in hadronic final states with missing transverse energy using the variables α_T and b-quark multiplicity in pp collisions at 8 TeV*, *Eur. Phys. J. C* **73** (2013) 2568, [arXiv:1303.2985 \[hep-ex\]](#).
- [83] CMS Collaboration, S. Chatrchyan et al., *Inclusive search for supersymmetry using the razor variables in pp collisions at $\sqrt{s} = 7$ TeV*, *Phys. Rev. Lett.* **111** (2013) 081802, [arXiv:1212.6961 \[hep-ex\]](#).
- [84] CMS Collaboration, S. Chatrchyan et al., *Search for supersymmetry in hadronic final states using MT_2 in pp collisions at $\sqrt{s} = 7$ TeV*, *JHEP* **10** (2012) 018, [arXiv:1207.1798 \[hep-ex\]](#).
- [85] CMS Collaboration, S. Chatrchyan et al., *Search for new physics in the multijet and missing transverse momentum final state in proton-proton collisions at $\sqrt{s} = 7$ TeV*, *Phys. Rev. Lett.* **109** (2012) 171803, [arXiv:1207.1898 \[hep-ex\]](#).
- [86] S. Amoroso, M. Baak, G. J. Besjes, R. Bruneliere, S. Caron, V. Consorti, L. Dufлот, G. Fletcher, S. Henrot-Versille, M. Hodgkinson, N. Kanaya, T. Javurek, Y. Kataoka, T. J. Khoo, T. LeCompte, R. van der Leeuw, N. Makovec, M. Marjanovic, J. Mamuzic, Y. Nakahama, M. A. Parker, M. Ronzani, Z. Rurikova, D. R. Tovey, and M. Vranjes Milosavljevic, *Search for squarks and gluinos with the ATLAS detector in final states with jets and missing transverse momentum and 20.3 fb⁻¹ of $\sqrt{s} = 8$ TeV proton-proton collision data: supporting documentation*, Tech. Rep. ATL-COM-PHYS-2013-1224, CERN, Geneva, Aug, 2013. <https://cds.cern.ch/record/1595965>.
- [87] ATLAS Collaboration, *Performance of the Reconstruction and Identification of Hadronic Tau Decays in ATLAS with 2011 Data*, Tech. Rep. ATLAS-CONF-2012-142, CERN, Geneva, Oct, 2012. <https://cds.cern.ch/record/1485531>.
- [88] ATLAS Collaboration, G. Aad et al., *Identification and energy calibration of hadronically decaying tau leptons with the ATLAS experiment in pp collisions at $\sqrt{s} = 8$ TeV*, *Eur. Phys. J. C* **75** (2015) no. 7, 303, [arXiv:1412.7086 \[hep-ex\]](#).
- [89] ATLAS Collaboration, *Expected Performance of the ATLAS Experiment - Detector, Trigger and Physics*, CERN-OPEN-2008-020. [arXiv:0901.0512 \[hep-ex\]](#).
- [90] A. Collaboration, *Improved luminosity determination in pp collisions at $\sqrt{s} = 7$ TeV using the ATLAS detector at the LHC*, [arXiv:1302.4393 \[hep-ex\]](#).
- [91] ATLAS Collaboration, *Further ATLAS tunes of PYTHIA 6 and Pythia 8*, 2011. [ATL-PHYS-PUB-2011-014](#).
- [92] A. Martin, W. Stirling, R. Thorne, and G. Watt, *Parton distributions for the LHC*, *Eur.Phys.J.* **C63** (2009) 189–285, [arXiv:0901.0002 \[hep-ph\]](#).

- [93] H.-L. Lai et al., *New parton distributions for collider physics*, *Phys. Rev.* **D82** (2010) 074024, [arXiv:1007.2241 \[hep-ph\]](#).
- [94] S. Catani, F. Krauss, R. Kuhn, and B. Webber, *QCD matrix elements + parton showers*, *JHEP* **0111** (2001) 063, [arXiv:hep-ph/0109231 \[hep-ph\]](#).
- [95] F. Krauss, *Matrix elements and parton showers in hadronic interactions*, *JHEP* **0208** (2002) 015, [arXiv:hep-ph/0205283 \[hep-ph\]](#).
- [96] S. Hoeche, F. Krauss, S. Schumann, and F. Siegert, *QCD matrix elements and truncated showers*, *JHEP* **0905** (2009) 053, [arXiv:0903.1219 \[hep-ph\]](#).
- [97] J. Alwall, S. Hoeche, F. Krauss, N. Lavesson, L. Lonnblad, et al., *Comparative study of various algorithms for the merging of parton showers and matrix elements in hadronic collisions*, *Eur.Phys.J.* **C53** (2008) 473–500, [arXiv:0706.2569 \[hep-ph\]](#).
- [98] J. Pumplin et al., *New generation of parton distributions with uncertainties from global QCD analysis*, *JHEP* **07** (2002) 012, [arXiv:hep-ph/0201195](#).
- [99] S. Catani et al., *Vector boson production at hadron colliders: A Fully exclusive QCD calculation at NNLO*, *Phys. Rev. Lett.* **103** (2009) 082001, [arXiv:0903.2120 \[hep-ph\]](#).
- [100] B. Cooper, J. Katzy, M. Mangano, A. Messina, L. Mijovic, et al., *Monte Carlo tuning in the presence of Matching*, [arXiv:1109.5295 \[hep-ph\]](#).
- [101] P. Z. Skands, *Tuning Monte Carlo Generators: The Perugia Tunes*, *Phys.Rev.* **D82** (2010) 074018, [arXiv:1005.3457 \[hep-ph\]](#).
- [102] ATLAS Collaboration, *Further ATLAS tunes of PYTHIA6 and Pythia 8*, .
- [103] ATLAS Collaboration, G. Aad et al., *First tuning of HERWIG/JIMMY to ATLAS data*, 2010. ATL-PHYS-PUB-2010-014.
- [104] M. Czakon, P. Fiedler, and A. Mitov, *Total Top-Quark Pair-Production Cross Section at Hadron Colliders Through $O(\frac{4}{S})$* , *Phys.Rev.Lett.* **110** (2013) no. 25, 252004, [arXiv:1303.6254 \[hep-ph\]](#).
- [105] M. Czakon and A. Mitov, *Top++: A Program for the Calculation of the Top-Pair Cross-Section at Hadron Colliders*, [arXiv:1112.5675 \[hep-ph\]](#).
- [106] T. Sjöstrand, S. Mrenna, and P. Z. Skands, *PYTHIA 6.4 Physics and Manual*, *JHEP* **0605** (2006) 026, [arXiv:hep-ph/0603175](#).
- [107] N. Kidonakis, *Next-to-next-to-leading-order collinear and soft gluon corrections for t-channel single top quark production*, *Phys.Rev.* **D83** (2011) 091503, [arXiv:1103.2792 \[hep-ph\]](#).
- [108] N. Kidonakis, *NNLL resummation for s-channel single top quark production*, *Phys.Rev.* **D81** (2010) 054028, [arXiv:1001.5034 \[hep-ph\]](#).
- [109] N. Kidonakis, *Two-loop soft anomalous dimensions for single top quark associated production with a W- or H-*, *Phys.Rev.* **D82** (2010) 054018, [arXiv:1005.4451 \[hep-ph\]](#).
- [110] A. Lazopoulos, T. McElmurry, K. Melnikov, and F. Petriello *Phys. Lett.* **B666** (2008) 62–65, [arXiv:0804.2220 \[hep-ph\]](#).

- [111] M. V. Garzelli, A. Kardos, C. G. Papadopoulos, and Z. Trocsanyi, *$t\bar{t}W^{+-}$ and $t\bar{t}Z$ Hadroproduction at NLO accuracy in QCD with Parton Shower and Hadronization effects*, *JHEP* **11** (2012) 056, [arXiv:1208.2665 \[hep-ph\]](#).
- [112] J. M. Campbell and R. K. Ellis, *$t\bar{t}W^{+-}$ production and decay at NLO*, .
- [113] J. M. Campbell and R. K. Ellis, *An Update on vector boson pair production at hadron colliders*, *Phys.Rev.* **D60** (1999) 113006, [arXiv:hep-ph/9905386 \[hep-ph\]](#).
- [114] J. M. Campbell, R. K. Ellis, and C. Williams, *Vector boson pair production at the LHC*, *JHEP* **1107** (2011) 018, [arXiv:1105.0020 \[hep-ph\]](#).
- [115] A. Djouadi, M. Muhlleitner, and M. Spira, *Decays of supersymmetric particles: The Program SUSY-HIT (SUSpect-SdecaY-Hdecay-InTerface)*, *Acta Phys.Polon.* **B38** (2007) 635–644, [arXiv:hep-ph/0609292 \[hep-ph\]](#).
- [116] B. Allanach, *SOFTSUSY: a program for calculating supersymmetric spectra*, *Comput.Phys.Commun.* **143** (2002) 305–331, [arXiv:hep-ph/0104145 \[hep-ph\]](#).
- [117] S. Gieseke, C. Rohr, and A. Siodmok, *Colour reconnections in Herwig++*, *Eur. Phys. J.* **C72** (2012) 2225, [arXiv:1206.0041 \[hep-ph\]](#).
- [118] A. Kulesza and L. Motyka, *Threshold resummation for squark-antisquark and gluino-pair production at the LHC*, *Phys.Rev.Lett.* **102** (2009) 111802, [arXiv:0807.2405 \[hep-ph\]](#).
- [119] A. Kulesza and L. Motyka, *Soft gluon resummation for the production of gluino-gluino and squark-antisquark pairs at the LHC*, *Phys.Rev.* **D80** (2009) 095004, [arXiv:0905.4749 \[hep-ph\]](#).
- [120] W. Beenakker, S. Brensing, M. Kramer, A. Kulesza, E. Laenen, et al., *Soft-gluon resummation for squark and gluino hadroproduction*, *JHEP* **0912** (2009) 041, [arXiv:0909.4418 \[hep-ph\]](#).
- [121] W. Beenakker, S. Brensing, M. Kramer, A. Kulesza, E. Laenen, and I. Niessen, *Supersymmetric top and bottom squark production at hadron colliders*, *JHEP.* **1008** (2010) 098, [arXiv:1006.4771 \[hep-ph\]](#).
- [122] W. Beenakker, S. Brensing, M. Kramer, A. Kulesza, E. Laenen, et al., *Squark and gluino hadroproduction*, *Int.J.Mod.Phys.* **A26** (2011) 2637–2664, [arXiv:1105.1110 \[hep-ph\]](#).
- [123] ATLAS Jet Trigger Group Collaboration, ATLAS, *The Design and Performance of the ATLAS Jet Trigger for the Event Filter*, 2011.
- [124] D. Casadei et al., *The implementation of the ATLAS missing Et triggers for the initial LHC operation*, Feb, 2011.
- [125] S. Owen, *Data-driven estimation of the QCD multijet background to SUSY searches with jets and missing transverse momentum at ATLAS using jet smearing*, Tech. Rep. ATL-PHYS-INT-2012-008, CERN, Geneva, Feb, 2012. <https://cds.cern.ch/record/1423310>.
- [126] G. Cowan, K. Cranmer, E. Gross, and O. Vitells, *Asymptotic formulae for likelihood-based tests of new physics*, *Eur. Phys. J.* **C71** (2011) 1554.

- [127] A. Read, *Presentation of search results: the CLs technique*, Journal of Physics G: Nucl. Part. Phys. **28** (2002) 2693–2704.
- [128] ATLAS, CMS Collaboration, G. Aad et al., *Combined Measurement of the Higgs Boson Mass in pp Collisions at $\sqrt{s} = 7$ and 8 TeV with the ATLAS and CMS Experiments*, [arXiv:1503.07589](https://arxiv.org/abs/1503.07589) [hep-ex].
- [129] ATLAS Collaboration, *First look at pp collisions data at $\sqrt{s}=13\text{TeV}$ in preparation for a search for squarks and gluinos in final states with jets and missing transverse momentum with the ATLAS detector*, Tech. Rep. ATL-PHYS-PUB-2015-028, CERN, Geneva, Jul, 2015. <https://cds.cern.ch/record/2037905>.
- [130] ATLAS Collaboration, *Expected sensitivity studies for gluino and squark searches using the early LHC 13 TeV Run-2 dataset with the ATLAS experiment*, Tech. Rep. ATL-PHYS-PUB-2015-005, CERN, Geneva, Mar, 2015. <https://cds.cern.ch/record/2002608>.
- [131] Particle Data Group Collaboration, K. Olive et al., *Review of Particle Physics*, Chin.Phys. **C38** (2014) 090001.
- [132] L. Breiman et al., *Classification and Regression Trees*. Chapman & Hall, New York, 1984. <http://www.crcpress.com/catalog/C4841.htm>. new edition of [221]?
- [133] Y. Freund and R. E. Schapire, *A Decision-Theoretic Generalization of On-Line Learning and an Application to Boosting*, Journal of Computer and System Sciences **55** (1997) no. 1, 119 – 139. <http://www.sciencedirect.com/science/article/pii/S002200009791504X>.
- [134] ATLAS Collaboration Collaboration, G. Aad et al., *Search for squarks and gluinos with the ATLAS detector in final states with jets and missing transverse momentum using $\sqrt{s} = 8$ TeV proton–proton collision data*, JHEP **09** (2014) 176, [arXiv:1405.7875](https://arxiv.org/abs/1405.7875) [hep-ex].
- [135] G. Cowan, K. Cranmer, E. Gross, and O. Vitells, *Asymptotic formulae for likelihood-based tests of new physics*, Eur. Phys. J. **C71** (2011) 1554, [arXiv:1007.1727](https://arxiv.org/abs/1007.1727) [physics.data-an]. [Erratum: Eur. Phys. J.C73,2501(2013)].
- [136] ATLAS Collaboration, *Search for squarks and gluinos using final states with jets and missing transverse momentum with the ATLAS detector in $\sqrt{s} = 7$ TeV proton-proton collisions*, 2011. [arXiv:1109.6572](https://arxiv.org/abs/1109.6572) [hep-ex]. [arXiv:1109.6572](https://arxiv.org/abs/1109.6572)[hep-ex].
- [137] C. F. Berger, J. S. Gainer, J. L. Hewett, and T. G. Rizzo, *Supersymmetry Without Prejudice*, JHEP **0902** (2009) 023, [arXiv:0812.0980](https://arxiv.org/abs/0812.0980) [hep-ph].
- [138] M. W. Cahill-Rowley, J. L. Hewett, S. Hoeche, A. Ismail, and T. G. Rizzo, *The New Look $p\text{MSSM}$ with Neutralino and Gravitino LSPs*, Eur. Phys. J. **C72** (2012) 2156, [arXiv:1206.4321](https://arxiv.org/abs/1206.4321) [hep-ph].
- [139] M. Cahill-Rowley, R. Cotta, A. Drlica-Wagner, S. Funk, J. Hewett, et al., *Complementarity and Searches for Dark Matter in the $p\text{MSSM}$* , [arXiv:1305.6921](https://arxiv.org/abs/1305.6921) [hep-ph].
- [140] M. Cahill-Rowley, R. Cotta, A. Drlica-Wagner, S. Funk, J. Hewett, et al., *Complementarity of dark matter searches in the phenomenological MSSM*, Phys.Rev. **D91** (2015) no. 5, 055011, [arXiv:1405.6716](https://arxiv.org/abs/1405.6716) [hep-ph].

- [141] P. Bechtle, K. Desch, and P. Wienemann, *Fittino, a program for determining MSSM parameters from collider observables using an iterative method*, *Comput. Phys. Commun.* **174** (2006) 47–70, [arXiv:hep-ph/0412012 \[hep-ph\]](#).
- [142] O. Buchmueller et al., *The CMSSM and NUHM1 in Light of 7 TeV LHC, $B_s \rightarrow \mu^+ \mu^-$ and XENON100 Data*, *Eur. Phys. J.* **C72** (2012) 2243, [arXiv:1207.7315 \[hep-ph\]](#).
- [143] K. de Vries, E. Bagnaschi, O. Buchmueller, R. Cavanaugh, M. Citron, et al., *The pMSSM10 after LHC Run 1*, [arXiv:1504.03260 \[hep-ph\]](#).
- [144] C. Streye, G. Bertone, G. Besjes, S. Caron, R. Ruiz de Austri, et al., *Profile likelihood maps of a 15-dimensional MSSM*, *JHEP* **1409** (2014) 081, [arXiv:1405.0622 \[hep-ph\]](#).
- [145] S. Henrot-Versillé, R. Lafaye, T. Plehn, M. Rauch, D. Zerwas, et al., *Constraining Supersymmetry using the relic density and the Higgs boson*, *Phys.Rev.* **D89** (2014) no. 5, 055017, [arXiv:1309.6958 \[hep-ph\]](#).
- [146] M. Chakraborti, U. Chattopadhyay, A. Choudhury, A. Datta, and S. Poddar, *The Electroweak Sector of the pMSSM in the Light of LHC - 8 TeV and Other Data*, *JHEP* **1407** (2014) 019, [arXiv:1404.4841 \[hep-ph\]](#).
- [147] S. S. AbdusSalam, *LHC-7 supersymmetry search interpretation within the phenomenological MSSM*, *Phys. Rev.* **D87** (2013) no. 11, 115012, [arXiv:1211.0999 \[hep-ph\]](#).
- [148] S. S. AbdusSalam and D. Choudhury, *Higgs boson discovery versus sparticles prediction: Impact on the pMSSM's posterior samples from a Bayesian global fit*, [arXiv:1210.3331 \[hep-ph\]](#).
- [149] M. Carena, J. Lykken, S. Sekmen, N. R. Shah, and C. E. Wagner, *The pMSSM Interpretation of LHC Results Using Renormalization Group Invariants*, *Phys.Rev.* **D86** (2012) 075025, [arXiv:1205.5903 \[hep-ph\]](#).
- [150] A. Arbey, M. Battaglia, and F. Mahmoudi, *Light Neutralino Dark Matter in the pMSSM: Implications of LEP, LHC and Dark Matter Searches on SUSY Particle Spectra*, *Eur. Phys. J.* **C72** (2012) 2169, [arXiv:1205.2557 \[hep-ph\]](#).
- [151] A. Strubig, S. Caron, and M. Rammensee, *Constraints on the pMSSM from searches for squarks and gluinos by ATLAS*, *JHEP* **1205** (2012) 150, [arXiv:1202.6244 \[hep-ph\]](#).
- [152] A. Arbey, M. Battaglia, and F. Mahmoudi, *Implications of LHC Searches on SUSY Particle Spectra: The pMSSM Parameter Space with Neutralino Dark Matter*, *Eur.Phys.J.* **C72** (2012) 1847, [arXiv:1110.3726 \[hep-ph\]](#).
- [153] B. C. Allanach, A. J. Barr, A. Dafinca, and C. Gwenlan, *Discovery reach for generic supersymmetry at the LHC: $MT2$ versus missing transverse momentum selections for pMSSM searches*, *JHEP* **1107** (2011) 104, [arXiv:1105.1024 \[hep-ph\]](#).
- [154] J. A. Conley, J. S. Gainer, J. L. Hewett, M. P. Le, and T. G. Rizzo, *Supersymmetry Without Prejudice at the LHC*, *Eur.Phys.J.* **C71** (2011) 1697, [arXiv:1009.2539 \[hep-ph\]](#).
- [155] S. S. AbdusSalam, B. C. Allanach, F. Quevedo, F. Feroz, and M. Hobson, *Fitting the Phenomenological MSSM*, *Phys. Rev.* **D81** (2010) 095012, [arXiv:0904.2548 \[hep-ph\]](#).

- [156] CMS Collaboration, *Phenomenological MSSM interpretation of the CMS 2011 5fb-1 results*, Tech. Rep. CMS-PAS-SUS-12-030, CERN, Geneva, 2013. <https://cds.cern.ch/record/1552402>.
- [157] CMS Collaboration, *Phenomenological MSSM interpretation of the CMS 7 and 8 TeV results*, Tech. Rep. CMS-PAS-SUS-13-020, CERN, Geneva, 2014. <https://cds.cern.ch/record/1693148>.
- [158] CMS Collaboration, *Reinterpreting the results of the search for long-lived charged particles in the pMSSM and other BSM scenarios*, Tech. Rep. CMS-PAS-EXO-13-006, CERN, Geneva, 2014. <https://cds.cern.ch/record/1648902>.
- [159] CMS Collaboration, V. Khachatryan et al., *Constraints on the pMSSM, AMSB model and on other models from the search for long-lived charged particles in proton-proton collisions at $\sqrt{s} = 8$ TeV*, *Eur. Phys. J.* **C75** (2015) no. 7, 325, [arXiv:1502.02522](https://arxiv.org/abs/1502.02522) [[hep-ex](#)].
- [160] A. Barr, B. Petersen, T. Rizzo, W. J. Fawcett, Y. Abulaiti, P. Bechtle, M. I. Besana, C. Bock, R. Caminal Armadans, A. Cortes-Gonzalez, D. Cote, O. Dale, C. David, D. Delgove, C. Deluca Silberberg, P. Dondero, L. Dufflot, L. Escobar Sawa, E. Feng, S. Gadatsch, T. Gillam, B. K. Gjelsten, Z. J. Grout, L. Heinrich, S. Henrot-Versille, T. Javurek, A. Kastanas, S. Kazama, D. Krauss, T. Lari, F. Legger, W. Liebig, A. Lipniacka, J. Lorenz, C. M. Macdonald, A. Mann, M. Marjanovic, B. Martin dit Latour, M. Martinez-Perez, A. Marzin, J. Maurer, F. Meloni, P. Pani, C. Potter, J. Poveda, O. Ricken, N. Rompotis, P. F. Salvatore, H. Sandaker, A. De Santo, I. Santoyo Castillo, S. Schaepe, M. J. Schultens, L. Smestad, V. Tudorache, R. Ueno, P. Urrejola, C. Wanotayaroj, D. Xu, S. Yamamoto, T. Yamanaka, X. Zhuang, and K. Suruliz, *Summary of the ATLAS experiment's sensitivity to supersymmetry after LHC Run 1 - interpreted in the phenomenological MSSM*, Tech. Rep. ATL-COM-PHYS-2014-952, CERN, Geneva, Aug, 2014. <https://cds.cern.ch/record/1747267>.
- [161] G. D'Ambrosio, G. Giudice, G. Isidori, and A. Strumia, *Minimal flavor violation: An Effective field theory approach*, *Nucl.Phys.* **B645** (2002) 155–187, [arXiv:hep-ph/0207036](https://arxiv.org/abs/hep-ph/0207036) [[hep-ph](#)].
- [162] S. Heinemeyer, W. Hollik, and G. Weiglein, *FeynHiggs: A Program for the calculation of the masses of the neutral CP even Higgs bosons in the MSSM*, *Comput.Phys.Commun.* **124** (2000) 76–89, [arXiv:hep-ph/9812320](https://arxiv.org/abs/hep-ph/9812320) [[hep-ph](#)].
- [163] T. Hahn, S. Heinemeyer, W. Hollik, H. Rzehak, and G. Weiglein, *High-precision predictions for the light CP-even Higgs Boson Mass of the MSSM*, *Phys.Rev.Lett.* **112** (2014) 141801, [arXiv:1312.4937](https://arxiv.org/abs/1312.4937) [[hep-ph](#)].
- [164] A. Djouadi, J. Kalinowski, and M. Spira, *HDECAY: A Program for Higgs boson decays in the standard model and its supersymmetric extension*, *Comput.Phys.Commun.* **108** (1998) 56–74, [arXiv:hep-ph/9704448](https://arxiv.org/abs/hep-ph/9704448) [[hep-ph](#)].
- [165] J. Alwall, R. Frederix, S. Frixione, V. Hirschi, F. Maltoni, et al., *The automated computation of tree-level and next-to-leading order differential cross sections, and their matching to parton shower simulations*, *JHEP* **1407** (2014) 079, [arXiv:1405.0301](https://arxiv.org/abs/1405.0301) [[hep-ph](#)].

- [166] A. Djouadi, J.-L. Kneur, and G. Moultaka, *SuSpect: A Fortran code for the supersymmetric and Higgs particle spectrum in the MSSM*, *Comput.Phys.Commun.* **176** (2007) 426–455, [arXiv:hep-ph/0211331](#) [[hep-ph](#)].
- [167] G. Belanger, F. Boudjema, A. Pukhov, and A. Semenov, *MicrOMEGAs 2.0: A Program to calculate the relic density of dark matter in a generic model*, *Comput.Phys.Commun.* **176** (2007) 367–382, [arXiv:hep-ph/0607059](#) [[hep-ph](#)].
- [168] G. Belanger, F. Boudjema, A. Pukhov, and A. Semenov, *micrOMEGAs: A Tool for dark matter studies*, *Nuovo Cim.* **C033N2** (2010) 111–116, [arXiv:1005.4133](#) [[hep-ph](#)].
- [169] M. Baak, M. Goebel, J. Haller, A. Hoecker, D. Kennedy, et al., *The Electroweak Fit of the Standard Model after the Discovery of a New Boson at the LHC*, *Eur.Phys.J.* **C72** (2012) 2205, [arXiv:1209.2716](#) [[hep-ph](#)].
- [170] T. Aoyama, M. Hayakawa, T. Kinoshita, and M. Nio, *Complete Tenth-Order QED Contribution to the Muon $g-2$* , *Phys.Rev.Lett.* **109** (2012) 111808, [arXiv:1205.5370](#) [[hep-ph](#)].
- [171] Heavy Flavor Averaging Group Collaboration, Y. Amhis et al., *Averages of B-Hadron, C-Hadron, and tau-lepton properties as of early 2012*, [arXiv:1207.1158](#) [[hep-ex](#)].
- [172] K. De Bruyn, R. Fleischer, R. Knegjens, P. Koppenburg, M. Merk, et al., *Probing New Physics via the $B_s^0 \rightarrow \mu^+ \mu^-$ Effective Lifetime*, *Phys.Rev.Lett.* **109** (2012) 041801, [arXiv:1204.1737](#) [[hep-ph](#)].
- [173] CMS Collaboration, LHCb Collaboration Collaboration, V. Khachatryan et al., *Observation of the rare $B_s^0 \rightarrow \mu^+ \mu^-$ decay from the combined analysis of CMS and LHCb data*, [arXiv:1411.4413](#) [[hep-ex](#)].
- [174] F. Mahmoudi, *SuperIso v2.3: A Program for calculating flavor physics observables in Supersymmetry*, *Comput.Phys.Commun.* **180** (2009) 1579–1613, [arXiv:0808.3144](#) [[hep-ph](#)].
- [175] BaBar Collaboration, B. Aubert et al., *A Search for $B^+ \rightarrow \ell^+ \nu_\ell$ Recoiling Against $B^- \rightarrow D^0 \ell^- \bar{\nu} X$* , *Phys. Rev.* **D81** (2010) 051101, [arXiv:0912.2453](#) [[hep-ex](#)].
- [176] Belle Collaboration, K. Hara et al., *Evidence for $B^- \rightarrow \tau^- \bar{\nu}$ with a Semileptonic Tagging Method*, *Phys. Rev.* **D82** (2010) 071101, [arXiv:1006.4201](#) [[hep-ex](#)].
- [177] Belle Collaboration, I. Adachi et al., *Evidence for $B^- \rightarrow \tau^- \bar{\nu}_\tau$ with a Hadronic Tagging Method Using the Full Data Sample of Belle*, *Phys. Rev. Lett.* **110** (2013) no. 13, 131801, [arXiv:1208.4678](#) [[hep-ex](#)].
- [178] BaBar Collaboration, J. Lees et al., *Evidence of $B^+ \rightarrow \tau^+ \nu$ decays with hadronic B tags*, *Phys. Rev.* **D88** (2013) no. 3, 031102, [arXiv:1207.0698](#) [[hep-ex](#)].
- [179] CKMfitter Group Collaboration, J. Charles et al., *CP violation and the CKM matrix: Assessing the impact of the asymmetric B factories*, *Eur. Phys. J.* **C41** (2005) 1–131, [arXiv:hep-ph/0406184](#) [[hep-ph](#)]. Updated result as of summer 2014 from <http://ckmfitter.in2p3.fr>.
- [180] ALEPH, DELPHI, L3, OPAL, SLD, LEP Electroweak Working Group, SLD Electroweak Group, SLD Heavy Flavour Group Collaboration, S. Schael et al., *Precision electroweak measurements on the Z resonance*, *Phys. Rept.* **427** (2006) 257–454, [arXiv:hep-ex/0509008](#) [[hep-ex](#)].

- [181] *LEPSUSYWG, ALEPH, DELPHI, L3 and OPAL experiments, note LEPSUSYWG/01-03.1*, [Http://lepsusy.web.cern.ch/lepsusy](http://lepsusy.web.cern.ch/lepsusy).
- [182] CDF Collaboration, T. Aaltonen et al., *Inclusive Search for Squark and Gluino Production in $p\bar{p}$ Collisions at $\sqrt{s} = 1.96\text{-TeV}$* , *Phys. Rev. Lett.* **102** (2009) 121801, [arXiv:0811.2512](https://arxiv.org/abs/0811.2512) [[hep-ex](#)].
- [183] D0 Collaboration, V. M. Abazov et al., *Search for squarks and gluinos in events with jets and missing transverse energy using 2.1 fb^{-1} of $p\bar{p}$ collision data at $\sqrt{s} = 1.96\text{-TeV}$* , *Phys. Lett.* **B660** (2008) 449–457, [arXiv:0712.3805](https://arxiv.org/abs/0712.3805) [[hep-ex](#)].
- [184] LUX Collaboration Collaboration, D. Akerib et al., *First results from the LUX dark matter experiment at the Sanford Underground Research Facility*, *Phys.Rev.Lett.* **112** (2014) 091303, [arXiv:1310.8214](https://arxiv.org/abs/1310.8214) [[astro-ph.CO](#)].
- [185] COUPP Collaboration Collaboration, E. Behnke et al., *First Dark Matter Search Results from a 4-kg CF_3I Bubble Chamber Operated in a Deep Underground Site*, *Phys.Rev.* **D86** (2012) 052001, [arXiv:1204.3094](https://arxiv.org/abs/1204.3094) [[astro-ph.CO](#)].
- [186] XENON100 Collaboration Collaboration, E. Aprile et al., *Limits on spin-dependent WIMP-nucleon cross sections from 225 live days of XENON100 data*, *Phys.Rev.Lett.* **111** (2013) no. 2, 021301, [arXiv:1301.6620](https://arxiv.org/abs/1301.6620) [[astro-ph.CO](#)].
- [187] R. Ruiz de Austri and C. Prez de los Heros, *Impact of nucleon matrix element uncertainties on the interpretation of direct and indirect dark matter search results*, *JCAP* **1311** (2013) 049, [arXiv:1307.6668](https://arxiv.org/abs/1307.6668) [[hep-ph](#)].
- [188] A. Freitas, *Status of Constraints on Supersymmetry*, in *Hadron collider physics. Proceedings, 19th Symposium, HCP2008, Galena, USA, May 27-31, 2008*. 2008. [arXiv:0808.0136](https://arxiv.org/abs/0808.0136) [[hep-ph](#)]. <http://inspirehep.net/record/792099/files/arXiv:0808.0136.pdf>.
- [189] R. Lafaye, T. Plehn, M. Rauch, and D. Zerwas, *Measuring Supersymmetry*, *Eur. Phys. J.* **C54** (2008) 617–644, [arXiv:0709.3985](https://arxiv.org/abs/0709.3985) [[hep-ph](#)].
- [190] G.-C. Cho and K. Hagiwara, *Supersymmetric contributions to muon $g-2$ and the electroweak precision measurements*, *Phys. Lett.* **B514** (2001) 123–130, [arXiv:hep-ph/0105037](https://arxiv.org/abs/hep-ph/0105037) [[hep-ph](#)].
- [191] G. Belanger, F. Boudjema, A. Cottrant, A. Pukhov, and S. Rosier-Lees, *Lower limit on the neutralino mass in the general MSSM*, *JHEP* **03** (2004) 012, [arXiv:hep-ph/0310037](https://arxiv.org/abs/hep-ph/0310037) [[hep-ph](#)].
- [192] ATLAS collaboration Collaboration, G. Aad et al., *Search for new phenomena in final states with large jet multiplicities and missing transverse momentum at $\sqrt{s} = 8\text{ TeV}$ proton-proton collisions using the ATLAS experiment*, *JHEP* **10** (2013) 130, [arXiv:1308.1841](https://arxiv.org/abs/1308.1841) [[hep-ex](#)].
- [193] ATLAS Collaboration, ATLAS Collaboration, *Search for squarks and gluinos in events with isolated leptons, jets and missing transverse momentum at $\sqrt{s} = 8\text{ TeV}$ with the ATLAS detector*, *JHEP* **1504** (2015) 116, [arXiv:1501.03555](https://arxiv.org/abs/1501.03555) [[hep-ex](#)].
- [194] ATLAS Collaboration Collaboration, G. Aad et al., *Search for supersymmetry in events with large missing transverse momentum, jets, and at least one tau lepton in 20 fb^{-1} of $\sqrt{s} = 8\text{ TeV}$ proton-proton collision data with the ATLAS detector*, *JHEP* **1409** (2014) 103, [arXiv:1407.0603](https://arxiv.org/abs/1407.0603) [[hep-ex](#)].

- [195] ATLAS Collaboration Collaboration, G. Aad et al., *Search for supersymmetry at $\sqrt{s}=8$ TeV in final states with jets and two same-sign leptons or three leptons with the ATLAS detector*, *JHEP* **1406** (2014) 035, [arXiv:1404.2500 \[hep-ex\]](#).
- [196] ATLAS Collaboration Collaboration, G. Aad et al., *Search for strong production of supersymmetric particles in final states with missing transverse momentum and at least three b-jets at $\sqrt{s} = 8$ TeV proton-proton collisions with the ATLAS detector*, *JHEP* **1410** (2014) 24, [arXiv:1407.0600 \[hep-ex\]](#).
- [197] ATLAS Collaboration, G. Aad et al., *Search for new phenomena in final states with an energetic jet and large missing transverse momentum in pp collisions at $\sqrt{s} = 8$ TeV with the ATLAS detector*, [arXiv:1502.01518 \[hep-ex\]](#).
- [198] ATLAS Collaboration Collaboration, G. Aad et al., *Search for direct pair production of the top squark in all-hadronic final states in proton-proton collisions at $\sqrt{s} = 8$ TeV with the ATLAS detector*, *JHEP* **1409** (2014) 015, [arXiv:1406.1122 \[hep-ex\]](#).
- [199] ATLAS Collaboration Collaboration, G. Aad et al., *Search for top squark pair production in final states with one isolated lepton, jets, and missing transverse momentum in $\sqrt{s} = 8$ TeV pp collisions with the ATLAS detector*, *JHEP* **11** (2014) 118, [arXiv:1407.0583 \[hep-ex\]](#).
- [200] ATLAS Collaboration Collaboration, G. Aad et al., *Search for direct top-squark pair production in final states with two leptons in pp collisions at $\sqrt{s} = 8$ TeV with the ATLAS detector*, *JHEP* **1406** (2014) 124, [arXiv:1403.4853 \[hep-ex\]](#).
- [201] ATLAS Collaboration, *Search for pair-produced third-generation squarks decaying via charm quarks or in compressed supersymmetric scenarios in pp collisions at $\sqrt{s} = 8$ TeV with the ATLAS detector*, *Phys. Rev. D* **90** (2014) 052008, [arXiv:1407.0608 \[hep-ex\]](#).
- [202] ATLAS Collaboration Collaboration, G. Aad et al., *Search for direct top squark pair production in events with a Z boson, b-jets and missing transverse momentum in $\sqrt{s}=8$ TeV pp collisions with the ATLAS detector*, *Eur.Phys.J.* **C74** (2014) no. 6, 2883, [arXiv:1403.5222 \[hep-ex\]](#).
- [203] ATLAS Collaboration, G. Aad et al., *Search for direct third-generation squark pair production in final states with missing transverse momentum and two b-jets in $\sqrt{s} = 8$ TeV pp collisions with the ATLAS detector*, *JHEP* **10** (2013) 189, [arXiv:1308.2631 \[hep-ex\]](#).
- [204] ATLAS Collaboration, ATLAS Collaboration, *ATLAS Run 1 searches for direct pair production of third-generation squarks at the Large Hadron Collider*, Submitted to *Eur.Phys.J.* (2015) , [arXiv:1506.08616 \[hep-ex\]](#).
- [205] ATLAS Collaboration, G. Aad et al., *Search for direct pair production of a chargino and a neutralino decaying to the 125 GeV Higgs boson in $\sqrt{s} = 8$ TeV pp collisions with the ATLAS detector*, [arXiv:1501.07110 \[hep-ex\]](#).
- [206] ATLAS Collaboration Collaboration, G. Aad et al., *Search for direct production of charginos, neutralinos and sleptons in final states with two leptons and missing transverse momentum in pp collisions at $\sqrt{s} = 8$ TeV with the ATLAS detector*, *JHEP* **1405** (2014) 071, [arXiv:1403.5294 \[hep-ex\]](#).

- [207] ATLAS Collaboration Collaboration, G. Aad et al., *Search for the direct production of charginos, neutralinos and staus in final states with at least two hadronically decaying taus and missing transverse momentum in pp collisions at $\sqrt{s} = 8$ TeV with the ATLAS detector*, [arXiv:1407.0350 \[hep-ex\]](#).
- [208] ATLAS Collaboration Collaboration, G. Aad et al., *Search for direct production of charginos and neutralinos in events with three leptons and missing transverse momentum in $\sqrt{s} = 8$ TeV pp collisions with the ATLAS detector*, *JHEP* **1404** (2014) 169, [arXiv:1402.7029 \[hep-ex\]](#).
- [209] ATLAS Collaboration Collaboration, G. Aad et al., *Search for supersymmetry in events with four or more leptons in $\sqrt{s} = 8$ TeV pp collisions with the ATLAS detector*, *Phys.Rev.* **D90** (2014) 052001, [arXiv:1405.5086 \[hep-ex\]](#).
- [210] ATLAS Collaboration Collaboration, G. Aad et al., *Search for charginos nearly mass degenerate with the lightest neutralino based on a disappearing-track signature in pp collisions at $\sqrt{s} = 8$ TeV with the ATLAS detector*, *Phys.Rev.* **D88** (2013) no. 11, 112006, [arXiv:1310.3675 \[hep-ex\]](#).
- [211] ATLAS Collaboration, G. Aad et al., *Searches for heavy long-lived sleptons and R-Hadrons with the ATLAS detector in pp collisions at $\sqrt{s} = 7$ TeV*, *Phys.Lett.* **B720** (2013) 277–308, [arXiv:1211.1597 \[hep-ex\]](#).
- [212] ATLAS Collaboration, G. Aad et al., *Searches for heavy long-lived charged particles with the ATLAS detector in proton-proton collisions at $\sqrt{s} = 8$ TeV*, *JHEP* **1501** (2015) 068, [arXiv:1411.6795 \[hep-ex\]](#).
- [213] ATLAS Collaboration Collaboration, G. Aad et al., *Search for neutral Higgs bosons of the minimal supersymmetric standard model in pp collisions at $\sqrt{s} = 8$ TeV with the ATLAS detector*, *JHEP* **1411** (2014) 056, [arXiv:1409.6064 \[hep-ex\]](#).
- [214] M. Kramer, A. Kulesza, R. van der Leeuw, M. Mangano, S. Padhi, et al., *Supersymmetry production cross sections in pp collisions at $\sqrt{s} = 7$ TeV*, [arXiv:1206.2892 \[hep-ph\]](#).
- [215] J. Alwall et al., *MadGraph/MadEvent v4: The New Web Generation*, *JHEP* **09** (2007) 028, [arXiv:0706.2334 \[hep-ph\]](#).
- [216] M. W. Cahill-Rowley, J. L. Hewett, A. Ismail, and T. G. Rizzo, *More energy, more searches, but the phenomenological MSSM lives on*, *Phys.Rev.* **D88** (2013) no. 3, 035002, [arXiv:1211.1981 \[hep-ph\]](#).
- [217] *Performance assumptions based on full simulation for an upgraded ATLAS detector at a High-Luminosity LHC*, Tech. Rep. ATL-PHYS-PUB-2013-009, CERN, Geneva, Sep, 2013. <https://cds.cern.ch/record/1604420>.
- [218] C. J. Geyer and M. U. M. S. O. Statistics, *Markov Chain Monte Carlo Maximum Likelihood*. Defense Technical Information Center, 1992. <http://www.worldcat.org/oclc/228023754>.
- [219] H. Baer and M. Brhlik, *QCD improved $b \rightarrow s$ gamma constraints on the minimal supergravity model*, *Phys. Rev.* **D55** (1997) 3201–3208, [arXiv:hep-ph/9610224 \[hep-ph\]](#).

- [220] D. Stockinger, *The Muon Magnetic Moment and Supersymmetry*, *J. Phys.* **G34** (2007) R45–R92, [arXiv:hep-ph/0609168](#) [hep-ph].
- [221] L. Breiman, J. Friedman, R. Olshen, and C. Stone, *Classification and Regression Trees*. Wadsworth and Brooks, Monterey, CA, 1984. new edition [132]?

Remerciements

The work presented here would not have been possible without the enormous help from a lot of people!

I would like to thank the referees Andreas Hoecker and Tilman Plehn for devoting time to read and evaluate my manuscript, and write a report on it. Also huge thanks for the members of my jury Achille Stocchi and Petar Adžić for accepting to come and assess the work that went into this thesis.

Merci aussi à Achille pour m'accueillir au laboratoire. J'aimerais aussi remercier Marie-Hélène pour le temps passé à Petnica, et pour tous les bons conseils que tu m'as donné. Merci aussi à Fabien pour toujours trouver le temps pour me voir, même quand j'arrive à la dernière minute avec trop de documents. Merci aussi à l'Institut Français de Serbie, en particulier à Vesna Adamović, pour me donner la possibilité de faire cette thèse en France. Merci à l'Université Paris Sud, et à l'École Doctorale.

Le plus grand merci à Sophie, pour me traiter comme sa gosse, même quand j'étais complètement insupportable. Merci pour toutes les fois où je t'ai interrompu pour poser les questions bêtes, aussi pour tous les explications de physique, et la vie. Tu est pour moi beaucoup plus que ma directrice de thèse, et je pense qu'on a formé une bande qui va être présente pour toute ma vie.

Hvala Mariji, što si prihvatila da budeš moja mentorka i što je uvek htela da me sasluša i da mi pomogne. Zahvalna sam ti na svim lepim trenucima koje smo provele na raznim putovanjima, i na svojoj pomoći koju si mi pružila tokom godina, na svim komentarima i sugestijama.

Merci à Dudu, qui est vraiment aussi l'un de co-directeurs de ma thèse. Tu a passé trop de temps à m'aider qu'il n'a pas eu de temps d'écrire son HDR, et moi je me sens responsable. Si je prends tous les corrections que tu m'as fait ça peut être une HDR entière! Merci pour tout ton aide à physique, mais surtout que tu es un vrai ami, qui m'écoute et qui était toujours là pour moi. Merci pour tous nos discussions, et pour ton soutien constant.

Thank to the whole 0-lepton analysis team, especially to Renaud.

A very special thanks to Brian. Thank you for always having time to listen, to reply to all my questions, for being so patient and always nice. I appreciate all the time you spent discussing with me and explaining me everything. I am also deeply grateful for you believing in me and giving me so many opportunities. Most importantly, thanks for the ice cream.

I would also like to express how it was great working with you Valentina. Thanks to laughing with me when all the others were serious and for having so great attitude towards our work, and life. With you I realised how everyone can find some common things everywhere and how we all complement each other. I enjoyed so much each time we met and hope that we will meet again soon.

Merci à Geneviève pour m'offrir tellement chaleur dans tous nos interactions. Tu es toujours allée au delà des limites pour m'aider et trouver les solutions à tous mes problèmes. Merci de partager avec moi les choses mals mais aussi les choses biens, et de prendre soin de moi.

Merci aussi à tous qui était là pour le café du matin: Bruno, Dudu, Seb, Sophie, Stéphane. Pour être là, j'ai toujours couru au labo le matin, et j'étais souvent en retard. J'ai eu beaucoup plaisir d'écouter toutes les discussions et j'ai appris beaucoup. Merci pour faire ces moments de début de journée si agréable, et désolée de toujours vous faire attendre pour finir ma café

pour commencer le travail.

La pause dans l'après-midi était aussi vraiment important pour moi: il faut avoir les moments dans la journée quand on peut se détendre. Merci à Dudu, Laurent, Nikola, Sophie, pour toujours être très rigoureux quand c'est le moment de pauser. Merci pour tous les petits plaisirs: les bombons, les brioches, et surtout les conversations. Merci à Nikola pour tous le temps qu'il m'a donné pour m'expliquer la physique, même si mon manière de poser les questions n'était pas toujours très claire. Je te remercie aussi pour être mon chaperon à Amsterdam. Merci à Laurent pour ton bon humour et pour corriger une partie de ma thèse.

Merci à Dirk pour avoir été si sympa avec moi, de me montrer la communauté plus large, à Les Houches et au GDR, de lire et commenter tous ces chapitres pMSSM de ma thèse, merci, j'ai appris beaucoup.

Je remercie tellement le groupe Weekend et Soir de Rédaction: avec vous la rédaction était presque agréable, mais c'est sûr que c'était amusant et passionnant. Merci de me supporter pendant tous mes hauts et mes bas, surtout mes bas. Merci à Alexis, Camille, Cyril, François, Laura, Renato, et particulièrement à Marta de nous organiser et nous motiver chaque fois de venir et passer du temps ensemble. Tous est beaucoup plus simple avec des gens qui te comprennent et te soutiennent.

Merci à tous les jeunes de labo: Baptiste, Charles, Christophe, Dima, Marta, Olga, Sandra, Vangelis pour les pti-dej, pour les soirs au Gramophone et pour les jeux de carte. Merci à Baptiste aussi pour la visite guidée d'Oxford. Vangelis, merci pour être toujours sincère. Merci à Mhamad d'être tellement gentil, c'était toujours un vrai plaisir de passer du temps avec toi. Merci à Ahmed, pour la compassion et soutien pendant des weekends au labo. Merci à Anja et Guillaume pour être si positive.

Merci à David et RD pour m'accueillir au groupe ATLAS du LAL, et de me considérer comme une de la groupe de première année.

Merci à Lydia pour toujours trouver les mots pour m'encourager et de me donner de bons conseils. Merci à Louis pour son bon humour de se rigoler de moi, et pour tous les photos. J'espère que j'ai grossi aussi pour occuper plus qu'un pixel.

Merci à Luc pour être un collègue de bureau extraordinaire. Toujours prêt à bien rigoler, c'était un immense plaisir de partager tous les petits trucs quotidiens.

Thank you Clara for having the patience to listen to me, and for time spent together in Paris and also for introducing me to running.

Thank you Lan for being a true friend always, someone I can rely on and call anytime. I enjoyed immensely our dinners, wine and long discussions about life and all that. Thank you for your hospitality, I spent so much time at your place, and thanks for making me feel at home with you.

I want also to thank Natasha for the evenings spent in great company, for walks in Paris, and for being such a good friend.

Hvala Majo na velikoj pomoći oko realizacije ove teze i podršci. Hvala također i Mirzeti što je uvek izlazila u susret svim mojim molbama. Hvala i Mirjani na pomoći koju mi je pružila u rešavanju svih administrativnih problema.

Hvala i ATLAS grupi u Beogradu. Hvala profesoru Popoviću što je uvek vodio računa o meni, i čijim sam zalaganjem i dobila priliku da radim ovaj doktorat u saradnji sa grupom u Francuskoj. Hvala mu na tome što je uspevao da izvuče najbolje iz svih nas. Hvala profesore Šijački na uvek interesantnim predavanjima, kojima ste me zainteresovali za fiziku visokih energija i pre nego što sam došla u grupu. Hvala profesore Adžiću što ste mi pomogli da odem prvi put u CERN i vidim šta je stvarno rad na velikom eksperimentu.

Hvala Ljiljo na velikoj pomoći, što ste mi dozvolili da biram šta ću da radim, i na tome što uvek imate interese grupe u vidu. Hvala i na vašem angažovanju oko saradnje sa Francuskom, sve je počelo od te vaše ideje! Hvala i Vama Jelena što ste me podržavali i bili u svim mojim

većima. Lidiya, hvala ti što si uvek imala korisne sugestije i ideje, što si sa mnom delila svoja iskustva i na tvojim savetima. Nenade, hvala ti na svim zanimljivim razgovorima i gostoprimstvu.

Alek, hvala ti što sam uvek mogla da ti ispričam svoje probleme, na prijateljstvu i zanimljivom vremenu koje smo provele zajedno. Uživala sam na našim izletima po Parizu, ručkovima, kao i u kolačima i kafi. Hvala i svim kolegama: Ivani, Ivanu, Igoru, Marku, Petru, Danijeli i Tanji.

Marko, hvala ti na svemu, ja ne mogu da opišem koliko je sve što sam do sada uradila bilo zahvaljujući tebi.

Nemanja, hvala ti na šetnjama i razgovorima o poslu i životu po Parizu i Amsterdamu, na uživanju u umetnosti, vinu i malim stvarima. Kolega Milanče, hvala na razumevanju, dobro je što još možemo zajedno da se smejemo.

Sanja, hvala ti što si imala strpljenja da slušaš o svemu, mada su moje priče bile prilično dosadne, na podršci u svakom trenutku.

Hvala i mojoj porodici na razumevanju za sve moje probleme i što su ih slušali iako nisu imali pojma o čemu pričam. Hvala na svojoj ljubavi i podršci.